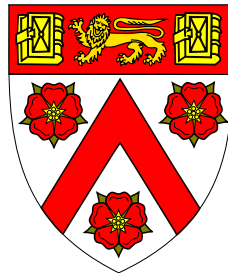


# Studying Accretion Disc Winds with X-ray Spectroscopy



**Peter Kosec**

Under the supervision of:

Prof. A. C. Fabian

Prof. C. S. Reynolds

&

Dr. C. Pinto

Institute of Astronomy

University of Cambridge

This thesis is submitted for the degree of

*Doctor of Philosophy*

Trinity College

March 2020



# Declaration

This thesis is the result of my own work and includes nothing which is the outcome of work done in collaboration except as declared in the Preface and specified in the text. It is not substantially the same as any that I have submitted, or, is being concurrently submitted for a degree or diploma or other qualification at the University of Cambridge or any other University or similar institution except as declared in the Preface and specified in the text. I further state that no substantial part of my thesis has already been submitted, or, is being concurrently submitted for any such degree, diploma or other qualification at the University of Cambridge or any other University or similar institution except as declared in the Preface and specified in the text. This dissertation contains fewer than 60,000 words including abstract, appendices, footnotes, tables and equations.

The chapters of this thesis based on published or submitted work are as follows:

- **Chapter 2**

P. Kosec, C. Pinto, A. C. Fabian and D. J. Walton, “Searching for outflows in ultraluminous X-ray sources through high-resolution X-ray spectroscopy,” *Monthly Notices of the Royal Astronomical Society*, Vol. 473, Issue 4, p. 5680-5697, February 2018.

- **Chapter 3**

P. Kosec, C. Pinto, D. J. Walton, A. C. Fabian, M. Bachetti, M. Brightman, F. Fürst and B. W. Greffenstette, “Evidence for a variable Ultrafast Outflow in the newly discovered Ultraluminous Pulsar NGC 300 ULX-1,” *Monthly Notices of the Royal Astronomical Society*, Vol. 479, Issue 3, p. 3978-3986, September 2018.

- **Chapter 4**

P. Kosec, A. Zoghbi, D. J. Walton, C. Pinto, A. C. Fabian, M. L. Parker and C. S. Reynolds, “Detection of a variable ultra-fast outflow in the Narrow Line Seyfert 1 galaxy PG 1448+273” submitted to *Monthly Notices of the Royal Astronomical Society*, March 2020.

- **Chapter 5**

P. Kosec, D. J. K. Buisson, M. L. Parker, C. Pinto, A. C. Fabian and D. J. Walton, “A stratified ultrafast outflow in 1H0707-495?” *Monthly Notices of the Royal Astronomical Society*, Vol. 481, Issue. 1, p. 947-953, November 2018.

- **Chapter 6**

P. Kosec, A. C. Fabian, C. Pinto, D. J. Walton, S. Dyda and C. S. Reynolds, “An ionised accretion disc wind in Hercules X-1,” *Monthly Notices of the Royal Astronomical Society*, Vol. 491, Issue. 3, p.3730-3750, January 2020.

Peter Kosec

March 2020

# Abstract

## Studying Accretion Disc Winds with X-ray Spectroscopy

Peter Kosec

In this thesis I present the results of my PhD research into the physics of accretion (infall) and ejection (outflow) of matter in compact objects.

Accretion disc winds are formed of hot and ionised material launched by magnetic forces, radiation pressure or thermally from the discs of accretors. They have been discovered in most types of accreting systems including supermassive black holes, classical X-ray binaries and Ultraluminous X-ray sources. Outflows form a ubiquitous and important part of the accretion flow, carrying away a considerable fraction of the originally infalling mass. With velocities as high as 30 per cent of the speed of light, their kinetic energy budget can also be significant and have a strong impact on the accretor surroundings. Ultra-fast outflows from supermassive black holes could contribute to or even drive active galactic nucleus feedback in galaxies.

Accretion disc winds can be observed through Doppler-shifted spectral lines in the X-ray part of the electromagnetic spectrum, the wind physical properties can thus be studied with X-ray spectroscopy. In this work, I present the detection of disc winds and I study their physics in a number of accreting systems. I particularly make use of the high-spectral resolution Reflection Grating Spectrometer onboard the *XMM-Newton* observatory. For efficient data analysis I develop and use systematic automated routines for search of wind signatures in X-ray spectra.

The first two chapters of this thesis introduce the theory of accretion and describe different accreting systems, as well as the X-ray observatories and data analysis methods used in this study. The third chapter contains a systematic search for disc winds in a sample of Ultraluminous X-ray sources, powered by super-Eddington accretion onto

stellar-mass black holes and neutron stars. In the fourth chapter I achieve the first discovery of an ultra-fast wind in a neutron star Ultraluminous X-ray source.

In the following two chapters I present the detection of ultra-fast outflows from two accreting supermassive black holes PG 1448+273 and 1H 0707-495. The outflow energetics show that these winds are more than capable to drive feedback in the accretor host galaxies. Furthermore, both show evidence for a multi-phase wind structure, PG 1448+273 also exhibiting variability in time.

In the seventh chapter, I present the discovery of a disc wind in the unique X-ray binary Hercules X-1 known for a precessing, warped accretion disc. I leverage the warped disc precession to sample the vertical distribution of the disc wind, constraining its launching angle as well as the total mass outflow rate, two crucial quantities which are difficult to measure in other accreting systems.

The final chapter contains the conclusions of the thesis as well as potential future research avenues in this field and the promising upcoming X-ray observatories.

## Acknowledgements

First and foremost, I would like to thank my primary supervisor Andy Fabian for his help, advice and patience with me. This would not be a successful PhD without his guidance. I would also like to thank him for offering me my first research internship, back in the summer of 2013, which introduced me into astronomical research in the first place.

Secondly, I would like to acknowledge my secondary supervisor Chris Reynolds for his useful advice in the last two years of my PhD. My deepest gratitude goes to Ciro Pinto, who has been supervising me since the start of my PhD. I would especially like to thank him for the incredible effort with making sure that my papers, proposals, reports and applications were the best they could have been.

Thirdly, I would like to acknowledge Dom Walton for helping me whenever necessary, and for his in-depth comments and suggestions on my work. Special thanks to everyone else from the X-ray group thanks to whom my time at the IoA was incredible: George, Will, Sergei, Sergey, James, Becky, Annabelle, Payton, Haonan, Naoki and all the others.

Next, I would like to thank Jiachen Jiang and Douglas Buisson for being great office mates during the first three years of my PhD. I cannot forget my course mates either: Tom, Lewis, Inigo, Laura, Aneesh, GuyChul, John and Ed.

My scientific results would not be possible without the IT support of Roderick Johnstone on the X-ray computer cluster. I would also like to acknowledge Jeremy Sanders for developing the Veusz plotting package which I made great use of during my PhD. Additionally, I would like to thank Paul Hewett, Debbie Peterson and the rest of the admins at the IoA for their great work, as well as Mandy and the other IoA staff for running IoA as smoothly as feasible. I have thoroughly enjoyed everyday coffee and tea breaks, and without the work of staff they would not be possible.

I would like to express my gratitude to the Science and Technology Facilities Council for funding my PhD project, as well as to Trinity College for sponsoring several of my conference travels.

Next, I would like to acknowledge some of the people which introduced me into science and astronomy in the first place. I am very grateful to Zdenka Baxova who taught me astronomy and physics from the beginning and made sure I signed up for all the possible competitions and olympiads. Without her, I would have probably not found my way into astronomy. I would also like to thank Stephen Walker, Steve Allen, Norbert Werner, Ondrej Urban, Fiona Harrison, Mislav Baloković and Murray Brightman for supervising me during summer internships and for teaching me how to ‘do science’.

Most importantly, I would like to thank my family. Special thanks to my parents for supporting me all the way despite my laziness, and for allowing me to leave Slovakia to pursue my dreams. I would not be in Cambridge today had it not been for all your hard work over the years. I am grateful to my sister Zuzka for all the thematic astronomical gifts over the years.

And finally, I would like to thank Pet’ka for her unconditional support and for motivating me to do my best everyday. Without you, none of this would be possible.

Ďakujem.

# Table of contents

<b>List of figures</b>	<b>xiii</b>
<b>List of tables</b>	<b>xvii</b>
<b>1 Introduction</b>	<b>1</b>
1.1 The physics of accretion onto compact objects . . . . .	1
1.1.1 Compact objects . . . . .	1
1.1.2 Theory of accretion . . . . .	2
1.1.3 Accretion disc winds . . . . .	4
1.2 Accretion and ejection of matter in different systems . . . . .	8
1.2.1 Active galactic nuclei . . . . .	8
1.2.2 Classical X-ray binaries . . . . .	15
1.2.3 Ultraluminous X-ray sources . . . . .	19
1.3 X-ray observatories . . . . .	22
1.3.1 <i>XMM-Newton</i> . . . . .	22
1.3.2 <i>NuSTAR</i> . . . . .	27
1.4 X-ray spectroscopy . . . . .	28
1.4.1 Spectral modelling . . . . .	30
1.4.2 X-ray spectra of accreting objects and commonly used spectral continuum models . . . . .	30
1.4.3 Ionised plasma modelling . . . . .	34
1.5 This thesis . . . . .	36
<b>2 Data reduction and analysis methods</b>	<b>39</b>
2.1 <i>XMM-Newton</i> data reduction . . . . .	39
2.1.1 RGS . . . . .	39
2.1.2 EPIC . . . . .	40
2.2 Spectral search methods . . . . .	41

2.2.1	Gaussian line search . . . . .	41
2.2.2	Physically motivated model search . . . . .	43
<b>3</b>	<b>Searching for outflows in ultraluminous X-ray sources</b>	<b>47</b>
3.1	Introduction . . . . .	49
3.2	Observations and data reduction . . . . .	51
3.3	Methods . . . . .	53
3.3.1	Continuum spectral fitting . . . . .	53
3.3.2	Gaussian line search . . . . .	54
3.3.3	Spectral model search . . . . .	54
3.4	Results . . . . .	55
3.4.1	Holmberg IX X-1 . . . . .	55
3.4.2	Holmberg II X-1 . . . . .	58
3.4.3	NGC 5643 X-1 . . . . .	59
3.4.4	NGC 4190 ULX1 . . . . .	60
3.4.5	M33 X-8 . . . . .	60
3.4.6	NGC 1313 X-2 . . . . .	61
3.4.7	NGC 5204 X-1 . . . . .	62
3.4.8	NGC 6946 X-1 . . . . .	64
3.4.9	NGC 4631 ULX1 and IC 342 X-1 . . . . .	65
3.5	Discussion . . . . .	65
3.5.1	Strongest features . . . . .	66
3.5.2	Attempting to identify the spectral features . . . . .	66
3.5.3	Physical model search . . . . .	69
3.5.4	ULX comparison within the sample and with previous work . . . . .	73
3.5.5	Contamination by host galaxy . . . . .	76
3.5.6	Further studies . . . . .	79
3.6	Conclusions . . . . .	81
<b>4</b>	<b>A variable ultrafast outflow in NGC 300 ULX-1 pulsar</b>	<b>83</b>
4.1	Introduction . . . . .	85
4.2	Observations and data reduction . . . . .	86
4.2.1	<i>XMM-Newton</i> . . . . .	87
4.2.2	<i>NuSTAR</i> . . . . .	88
4.3	Methods and results . . . . .	89
4.3.1	Broadband modelling . . . . .	89
4.3.2	Line search . . . . .	90

4.3.3	Physical model search . . . . .	91
4.3.4	Significance of the wind detection . . . . .	95
4.3.5	The first <i>XMM-Newton</i> observation . . . . .	97
4.4	Discussion . . . . .	98
4.5	Conclusions . . . . .	101
<b>5</b>	<b>A variable ultra-fast outflow in the AGN PG 1448+273</b>	<b>103</b>
5.1	Introduction . . . . .	105
5.2	Observation and data reduction . . . . .	107
5.3	Results . . . . .	109
5.3.1	Broadband X-ray continuum . . . . .	109
5.3.2	Ionised wind search . . . . .	112
5.3.3	Ultrafast outflow and warm absorption . . . . .	118
5.3.4	Residual structure in the spectrum - a multiphase outflow? . . .	121
5.4	Discussion . . . . .	123
5.5	Conclusions . . . . .	125
<b>6</b>	<b>A stratified ultrafast outflow in the AGN 1H 0707-495?</b>	<b>127</b>
6.1	Introduction . . . . .	129
6.2	Observations and data reduction . . . . .	131
6.3	Methods and results . . . . .	132
6.3.1	Broadband fitting . . . . .	132
6.3.2	Emission lines fitted with Gaussians . . . . .	134
6.3.3	Physical models of photoionised emission . . . . .	135
6.3.4	UFO absorption signatures . . . . .	136
6.3.5	Time and flux variability of spectral features . . . . .	139
6.4	Discussion and conclusions . . . . .	140
<b>7</b>	<b>An ionised accretion disc wind in Hercules X-1</b>	<b>147</b>
7.1	Introduction . . . . .	149
7.1.1	Hercules X-1 . . . . .	150
7.2	Observations and data reduction . . . . .	151
7.2.1	Orbital and super-orbital phases . . . . .	153
7.3	Results . . . . .	155
7.3.1	Continuum modelling . . . . .	155
7.3.2	Photoionised wind modelling . . . . .	159
7.3.3	Short-on and Low state observations . . . . .	166

7.4	Elemental abundances in the wind . . . . .	167
7.5	Discussion . . . . .	171
7.5.1	Wind evolution with luminosity, orbital and super-orbital phase . . . . .	171
7.5.2	Location of the wind absorption . . . . .	177
7.5.3	Mass outflow rate . . . . .	180
7.5.4	Possible wind launching mechanisms . . . . .	183
7.5.5	Are observations over the super-orbital period probing different lines of sight? . . . . .	187
7.6	Conclusions . . . . .	190
<b>8</b>	<b>Conclusions and future research</b>	<b>193</b>
8.1	Conclusions . . . . .	193
8.1.1	Ultraluminous X-ray sources . . . . .	193
8.1.2	Active galactic nuclei . . . . .	194
8.1.3	Classical X-ray binaries . . . . .	195
8.2	Future research . . . . .	196
8.2.1	Efficient ionised outflow search . . . . .	196
8.2.2	Understanding the vertical structure of accretion disc winds . .	197
8.3	Future X-ray observatories . . . . .	198
8.3.1	X-ray Imaging and Spectroscopy Mission ( <i>XRISM</i> ) . . . . .	198
8.3.2	Advanced Telescope for High Energy Astrophysics ( <i>ATHENA</i> ) . . . . .	200
8.3.3	<i>Arcus</i> . . . . .	201
	<b>References</b>	<b>203</b>
	<b>Appendix A Complete Gaussian line search results from chapter 2</b>	<b>241</b>
	<b>Appendix B PG 1448-273: Additional short <i>XMM-Newton</i> observa- tion</b>	<b>243</b>
	<b>Appendix C Pile-up in <i>XMM-Newton</i> Her X-1 observations</b>	<b>247</b>
C.1	Analysis with RGS 1 and 2 . . . . .	249
C.2	Analysis with RGS 1 only . . . . .	250

# List of figures

1.1	Simulation of a supercritical radiation-driven wind . . . . .	5
1.2	Simulation of a line pressure-driven wind . . . . .	7
1.3	The AGN unification model . . . . .	10
1.4	UFO absorption in the X-ray spectrum of PDS 456 . . . . .	13
1.5	Kinetic powers of AGN outflows . . . . .	14
1.6	The hardness-intensity diagram of black hole X-ray binary outbursts . .	16
1.7	Ionised winds in X-ray binaries . . . . .	18
1.8	Detection of an ultra-fast outflow in a ULX . . . . .	21
1.9	Artist's impression of <i>XMM-Newton</i> in orbit . . . . .	23
1.10	The combined effective area of the RGS 1 and RGS 2 instruments . . .	25
1.11	Artist's impression of <i>NuSTAR</i> in orbit . . . . .	27
1.12	The collecting area of <i>NuSTAR</i> . . . . .	28
1.13	Example of an X-ray line spectrum . . . . .	29
1.14	Example X-ray reflection spectrum . . . . .	32
1.15	A schematic of a ULX system . . . . .	35
3.1	PN spectra of ULXs . . . . .	56
3.2	Gaussian line search results for Holmberg IX X-1 . . . . .	57
3.3	Gaussian line search results for Holmberg II X-1 . . . . .	59
3.4	Gaussian line search results for NGC 5204 X-1 . . . . .	62
3.5	Histogram of $\Delta C$ -stat of real and simulated searches of NGC 5204 X-1 .	63
3.6	Gaussian line search results for NGC 6946 X-1 . . . . .	65
3.7	Histogram of $\Delta C$ -stat of real and simulated searches of NGC 6946 X-1 .	66
3.8	The CIE scan results of the stacked NGC 5204 X-1 RGS spectrum . . .	70
3.9	The RGS spectrum of NGC 5204 X-1 . . . . .	71
3.10	Histogram of $\Delta C$ -stat of real and simulated CIE searches of NGC 5204 X-1	72
3.11	Example CIE searches of the simulated datasets of NGC 5204 X-1 . . .	73
3.12	X-ray spectra of NGC 5204 X-1 and SS 433 . . . . .	74

3.13	Comparison between Gaussian line searches of hard ULXs . . . . .	75
3.14	Comparison between Gaussian line searches of soft ULXs . . . . .	77
3.15	Source (background not subtracted) spectrum of NGC 6946 X-1 . . . . .	78
3.16	The significance of the strongest feature of ULXs . . . . .	80
4.1	RGS extraction regions . . . . .	88
4.2	Gaussian line search of NGC 300 ULX-1 RGS data . . . . .	90
4.3	Photoionised absorber automated scan . . . . .	92
4.4	<i>XMM-Newton</i> EPIC and <i>NuSTAR</i> spectrum of NGC 300 ULX-1 . . . . .	94
4.5	RGS spectrum of NGC 300 ULX-1 . . . . .	95
4.6	Histogram of $\Delta C$ -stat of real and simulated XABS searches of NGC 300 ULX-1 . . . . .	98
4.7	Gaussian line search of the first <i>XMM-Newton</i> observation . . . . .	99
5.1	Image of the EPIC pn exposure . . . . .	108
5.2	EPIC spectra fitted with a phenomenological AGN model . . . . .	112
5.3	RGS spectrum fitted with a phenomenological AGN model . . . . .	113
5.4	Systematic scan for ionised outflow features . . . . .	115
5.5	Histogram of $\Delta C$ -stat of real and simulated XABS searches . . . . .	117
5.6	EPIC spectra fitted with the ionised outflow model . . . . .	119
5.7	RGS spectrum fitted with the ionised outflow model . . . . .	120
5.8	Systematic scan for multi-phase ionised outflow features . . . . .	122
6.1	Lightcurve of 1H 0707-495 . . . . .	132
6.2	Low flux X-ray spectrum of 1H 0707-495 . . . . .	133
6.3	O VIII region of the 2008 and 2010 campaign low flux spectra . . . . .	141
6.4	Outflow velocity of ions versus peak ionisation parameter . . . . .	144
6.5	Two possible interpretations of 1H0707 outflows . . . . .	145
7.1	Example <i>XMM-Newton</i> pn spectrum of Her X-1 . . . . .	156
7.2	Example <i>XMM-Newton</i> RGS spectrum of Her X-1 . . . . .	157
7.3	Schematic of Her X-1 spectral components . . . . .	159
7.4	N VII, O VIII, Ne X and Fe XXV/XXVI energy bands from observation 0673510501 . . . . .	162
7.5	Same plot as Fig. 7.4 but for observation 0673510601. . . . .	163
7.6	Same plot as Fig. 7.4 but for observation 0673510901. . . . .	163
7.7	Same plot as Fig. 7.4 but for observation 0783770501. . . . .	164
7.8	Same plot as Fig. 7.4 but for observation 0783770601. . . . .	164

---

7.9	Ionising luminosity for each observation versus the super-orbital phase .	172
7.10	Ionised wind parameters versus ionising luminosity . . . . .	173
7.11	Ionised wind parameters versus orbital phase . . . . .	175
7.12	Ionised wind parameters versus super-orbital phase . . . . .	176
7.13	Maximum distance of absorption from the ionising source versus the ionising luminosity . . . . .	178
7.14	A scheme of the Her X-1 system . . . . .	179
7.15	Mass outflow rate of the wind for each observation . . . . .	182
7.16	Mass outflow rate versus the super-orbital phase . . . . .	188
8.1	Example of a wavelet-based emission line spectral search . . . . .	197
8.2	Artist's impression of the <i>XRISM</i> X-ray observatory . . . . .	199
8.3	Artist's impression of the <i>ATHENA</i> X-ray observatory . . . . .	200
8.4	500 ks <i>XRISM</i> and 20 ks <i>ATHENA</i> simulation of NGC 300 ULX-1 . .	201
A.1	Gaussian line search of all ULXs . . . . .	242
B.1	EPIC spectra of the second <i>XMM-Newton</i> observation . . . . .	244
B.2	RGS spectrum of the second <i>XMM-Newton</i> observation . . . . .	245
C.1	Average RGS count rates during the highest count rate observation . .	248
C.2	Best-fitting spectral models for observation 0673510501 using only RGS 1 first and second orders . . . . .	251



# List of tables

3.1	Coordinates, distance and hardness ratio of ULXs used in this chapter .	52
3.2	Log of the observations used in this chapter . . . . .	53
3.3	The most prominent residuals found by the Gaussian line search . . . .	67
4.1	Log of the observations used in this chapter . . . . .	87
4.2	Best-fitting spectral parameters of NGC 300 ULX-1 . . . . .	93
5.1	Best-fitting X-ray continuum parameters . . . . .	111
6.1	Best-fitting photoionised emission and absorption models . . . . .	137
6.2	The strongest absorption residuals fitted with a Gaussian . . . . .	139
7.1	Log of the observations used in this chapter . . . . .	152
7.2	Modified Julian dates, orbital and super-orbital phases for each <i>XMM-Newton</i> observation . . . . .	154
7.3	Best-fitting wind parameters for each observation of Her X-1 . . . . .	161
7.4	Best-fitting abundances of elements and elemental ratios . . . . .	169
7.5	Maximum absorption distances and mass outflow rates . . . . .	180
7.6	Inverse Compton temperatures and wind launching radii . . . . .	185
C.1	Best-fitting wind parameters using only RGS instruments . . . . .	250



# Chapter 1

## Introduction

### 1.1 The physics of accretion onto compact objects

#### 1.1.1 Compact objects

Astrophysical objects much denser or heavier than common stars and planets are usually described as ‘compact objects’. This class traditionally contains three flavours of objects.

The most extreme compact objects are black holes [245]. Their gravity is so strong that even light cannot escape from their surfaces. They are described by Einstein’s General Relativity [90], with the exception of their centres (called the singularity) where even General Relativity breaks down. An astrophysical black hole can be described with just two properties: its mass, and its spin, the latter indicating how much angular momentum it possesses. Black holes can be split into two categories based on their dimensionless spin  $a$ : static Schwarzschild black holes [358] with zero spin, and rotating Kerr black holes [19, 284] with a non-zero spin value between -1 and 1. The radius of a Schwarzschild black hole can be expressed as:

$$R_S = 2R_G = \frac{2GM}{c^2} \approx 3\left(\frac{M}{M_\odot}\right) \text{ km} \quad (1.1)$$

where  $R_G$  is the gravitational radius,  $G$  is the gravitational constant,  $M$  is the black hole mass,  $c$  is the speed of light and  $M_\odot$  is the mass of the Sun. The spin  $a$  of a black hole is defined such that:

$$a = \frac{cJ}{GM^2} \quad (1.2)$$

where  $J$  is the magnitude of the black hole angular momentum [336].

Black holes are observed to come in two flavours in our Universe. On one hand, stellar-mass black holes have masses of the order of  $10 M_{\odot}$  [431] and are the remnants of heavy [ $M > 25 M_{\odot}$ , 150] stars. On the other hand, supermassive black holes [225, 328] reside in the centres of most galaxies in the Universe and have masses between  $10^6 M_{\odot}$  and  $10^{10} M_{\odot}$ . They could be formed either by a direct collapse of matter in the Early Universe [23], from stellar-mass black holes which increased their mass by accretion, or by merging of smaller black holes [264]. Finally, between these two flavours, there is a third, hypothetical class of intermediate-mass black holes (with masses between 100 and  $10000 M_{\odot}$ ), however the observational evidence for this class of objects is elusive [262, 312, 107].

Neutron stars, the second class of compact objects, are lighter than black holes, with masses between  $1.4 M_{\odot}$  [49] and  $3 M_{\odot}$  [287, 391] and sizes around  $\sim 10$  km [263, 342]. They are the endpoints of life of stars lighter than those which produce black holes, but heavy enough to explode in supernovae [150]. Neutron stars are so dense that their internal pressure forces electrons inside atomic nuclei, forming matter primarily made of neutrons with nuclear density. They can also have very strong surface magnetic fields, which might reach values as high as  $10^{15}$  G [202, 242].

White dwarfs are the endpoints of stellar evolution of stars with masses below  $9 M_{\odot}$  [160] including our Sun. With masses of less than  $1.4 M_{\odot}$  [49] and radii similar to the Earth's radius, they are composed of degenerate matter and held together by the balance of the gravitational force and the electron degeneracy pressure. They are not studied in this thesis.

### 1.1.2 Theory of accretion

Accretion (infall) of material onto compact objects is one of the most energetic phenomena in our Universe. Compact objects have such a strong gravitational pull that they can attract material from their surroundings, such as gas in their neighbourhood or from a stellar companion. Since the infalling material has non-zero angular momentum, it cannot simply fall onto the compact object but instead begins to orbit the central object. Interactions and collisions between the particles of the accreting material result in the formation of an accretion disc around the compact object.

The accretion disc is viscous and turbulent, which results in loss of gravitational energy and angular momentum of most particles in the disc, and thus the bulk of the material in-spirals towards the accretor. Mechanical viscosity is insufficient to explain the observed luminosity of accreting systems [320], so the effect responsible for viscosity is likely magnetic, via the magneto-rotational instability [MRI, 15, 16]. A

standard, widely accepted accretion disc model was described by Shakura and Sunyaev [363], according to which the disc is optically thick but geometrically thin, and each radius within the disc has a characteristic temperature. Such a disc therefore emits multi-color thermal blackbody radiation<sup>1</sup>.

Alternative models of accretion have been developed, e.g. the slim, advection-dominated thick disc model [1] which could be applicable to high mass accretion rate systems, the Advection Dominated Accretion Flow [ADAF, 277, 278, 434] model, most likely applicable in the very low mass accretion rate regime, and the unified accretion-ejection model which could explain collimated jet launching in accreting systems [114].

The temperature of the accretion disc increases closer to the compact object<sup>2</sup> and depends on the mass accretion rate through the disc, but also on the mass of the accretor [363]. The inner disc regions of supermassive black holes have temperatures of 10 – 100 eV ( $10^5 - 10^6$  K), whereas the inner discs of neutron stars and stellar-mass black holes can reach temperatures as high as 1 keV ( $10^7$  K)<sup>3</sup>. Such discs emit extreme amounts of energy through thermal radiation. The total luminosity of the disc can be expressed as:

$$L = \epsilon \dot{m} c^2 \tag{1.3}$$

where  $\dot{m}$  is the mass accretion rate through the disc and  $\epsilon$  is the accretion efficiency. Most of the energy is emitted in the innermost regions of the disc which are the hottest, and therefore  $\epsilon$  depends strongly on the size of the inner radius of the accretion disc. For an accreting black hole, the smallest radius of the disc can be the innermost stable circular orbit (ISCO). The radius of the ISCO depends highly on the black hole spin parameter. For a Schwarzschild black hole, the ISCO radius is  $6R_G$ . For a maximally spinning Kerr black hole, the ISCO radius is much smaller at  $1.2R_G$  [284]. For neutron stars, the innermost disc radius can be as small as the neutron star radius. However, neutron star magnetospheres can truncate accretion discs at radii as large as  $1000 R_G$  [e.g. 206] by forcing material onto accretion columns which follow the magnetic field lines of the neutron star.

---

<sup>1</sup>The integrated luminosity of each patch of the disc follows the Stefan-Boltzmann's law:  $L = \sigma T^4 A$ , where  $\sigma$  is the Stefan-Boltzmann's constant,  $T$  is the temperature of the patch and  $A$  is its area.

<sup>2</sup>The temperature of a stationary accretion disc scales approximately as  $T \propto r^{-3/4}$  where  $r$  is the distance from the central object.

<sup>3</sup>The temperature of accretion discs of objects with the same fractional (with respect to mass) mass accretion rates scales as  $T \propto M^{-1/4}$ .

The accretion efficiency  $\epsilon$  is 5.7% for a non-rotating, Schwarzschild black hole, and can be as high as 40% for a maximally rotating Kerr black hole [389, 209].  $\epsilon$  is usually taken to be of the order of 10% for neutron stars since they have solid surfaces. The kinetic energy of matter accreting onto them does not disappear the moment it crosses the ISCO [364] as in the case of black holes but a fraction of it is radiated away from the star's surface.

Accreting compact objects therefore emit huge amounts of energy since their efficiency  $\epsilon$  is much higher than, for example, that of nuclear fusion or fission (for both  $\epsilon < 1\%$ ).

The radiation emitted during accretion in turn provides an outward radiation pressure which acts against gravity. The balance of gravity and radiation pressure then sets the maximum theoretical luminosity (and mass accretion rate) of an accreting system, under the assumption of spherical symmetry. This is defined by the Eddington limit [88]:

$$L_{\text{Edd}} = \frac{4\pi GMm_p c}{\sigma_T} = 1.3 \times 10^{38} \frac{M}{M_\odot} \text{ erg/s} \quad (1.4)$$

where  $M$  is the mass of the accretor,  $m_p$  is the mass of the proton ( $\approx$ hydrogen mass) and  $\sigma_T$  is the Thomson scattering cross-section for electrons. The Eddington ratio is then defined as the ratio of the accretor bolometric luminosity to its Eddington luminosity. In principle, there should be no accreting systems in excess of this luminosity. In practice, it is possible to exceed the limit by breaking spherical symmetry or with strong magnetic fields (which can suppress the electron scattering cross-section).

### 1.1.3 Accretion disc winds

The material in the accretion disc loses energy and angular momentum via MRI and thus in-spirals towards the compact object. However, there are mechanisms that can accelerate it outwards instead and drive it away from the disc. Such mechanisms can give rise to an outflow from the disc, possibly to infinity, in the form of a so-called accretion disc wind. Alternatively, if the material is not sufficiently accelerated, it can return to the disc in the form of a 'failed' wind.

The material circulating in the accretion disc has approximately Keplerian velocity:

$$v_{\text{Kep}} = \sqrt{\frac{GM}{R}} \quad (1.5)$$

where  $R$  is the distance from the compact object. The material has to reach the escape velocity to successfully leave the accreting system in the form of a wind:

$$v_{\text{esc}} = \sqrt{\frac{2GM}{R}} \quad (1.6)$$

This means that a disc wind, successfully launched from the inner accretion flow ( $R \sim 10 - 100 R_G$ ) of neutron stars and black holes can reach velocities of more than 10% of the speed of light. Such a wind carries considerable kinetic energy and can strongly influence the surroundings of the compact object.

There are multiple mechanisms able to drive an accretion disc wind. The first mechanism is the radiation pressure on electrons. If the luminosity (and the mass accretion rate) of a compact object approaches or crosses the Eddington limit, isotropic radiation pressure can exceed the gravitational force on some fraction of the accreting material, and such material is launched away from the disc as a radiation-driven wind (see Fig. 1.1 for a radiation-driven wind simulation).

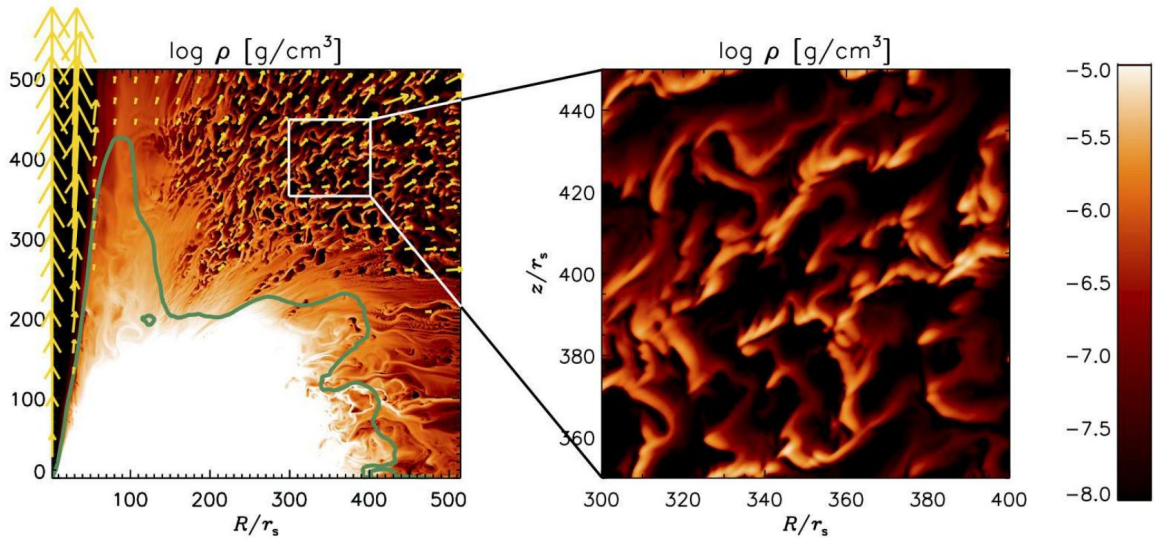


Fig. 1.1 Simulation of a radiation-driven wind in a super-Eddington accreting system. The figure shows the density of the material (according to the colour bar on the right) versus its location, as well as its velocity (yellow arrows). This figure is taken from Takeuchi et al. [385].

If the material in the accretion disc is not fully ionised, the gas opacity can be much higher than the electron scattering cross-section. The gas opacity is enhanced via bound-free and bound-bound transitions, thus at lower ionisations the wind can be ‘line’ driven using the many elemental transitions in the UV band. These transitions may

amplify the effective scattering cross-section by a factor as high as 1000 compared to the Thomson cross-section [48, 290]. An outflow can therefore be launched at luminosities much lower than the Eddington luminosity.

However, this wind driving mechanism relies on the presence of the numerous UV transitions providing the amplification of the gas opacity. The outflowing material therefore cannot be over-ionised by X-ray radiation (for example from the inner accretion flow) and at the same time it requires sufficient UV flux to launch the wind. Such winds have been observed in hot stars [207]. This driving mechanism is unlikely to work in X-ray binaries, the spectra of which are very hard with most of the flux being emitted in the X-ray energy band. Alternatively, the accelerating gas must be shielded from the hard X-ray radiation which would over-ionise it before it reaches the escape velocity. This has been shown to work in some hydrodynamical simulations [Fig. 1.2, 67, 322, 321] of accreting supermassive black holes thanks to failed inner disc winds which can shield the outer colder, UV-line rich disc regions.

Magnetic fields are an important component of accretion because they drive MRI [15, 16]. It is therefore possible that under a favourable magnetic configuration, magnetic tension or magnetic pressure could drive an outflow from the disc. Blandford and Payne [30] have indeed shown that a disc wind can appear for some magnetic field configurations. Importantly, magnetic driving does not rely on radiation pressure and could thus be important in low luminosity objects. However, magnetic wind models in general do not predict the wind properties such as the mass loss rates and are hence difficult to test against observations.

In some cases, the wind can also be driven by Compton heating [21]. If the outer disc is irradiated by a hard X-ray spectrum (from the inner accretion flow), some fraction of the material will be heated to the inverse Compton temperature<sup>4</sup> of the heating spectrum. At this temperature, the thermal velocity of the heated particles can be large enough to escape the gravity of the compact object (i.e. the thermal velocity is larger than the escape velocity at that radius), if the situation occurs at a large enough distance from the object. According to Begelman et al. [21], this happens for radii in the accretion disc larger than:

$$R \gtrsim 0.1 \times R_{\text{IC}} = \frac{2GM}{v_{\text{th}}^2} = \frac{GM\mu m_{\text{p}}}{kT_{\text{IC}}} \quad (1.7)$$

---

<sup>4</sup>The inverse Compton temperature of a spectrum is one quarter of the average energy of the photons of the spectrum [21]. It can therefore be expressed as:  $kT_{\text{IC}} = \frac{1}{4}\langle\epsilon\rangle = \frac{1}{4}L^{-1} \int_0^\infty EL_{\text{E}}dE$ , where  $L$  is the total luminosity and  $L_{\text{E}}$  is the luminosity at energy  $E$ .

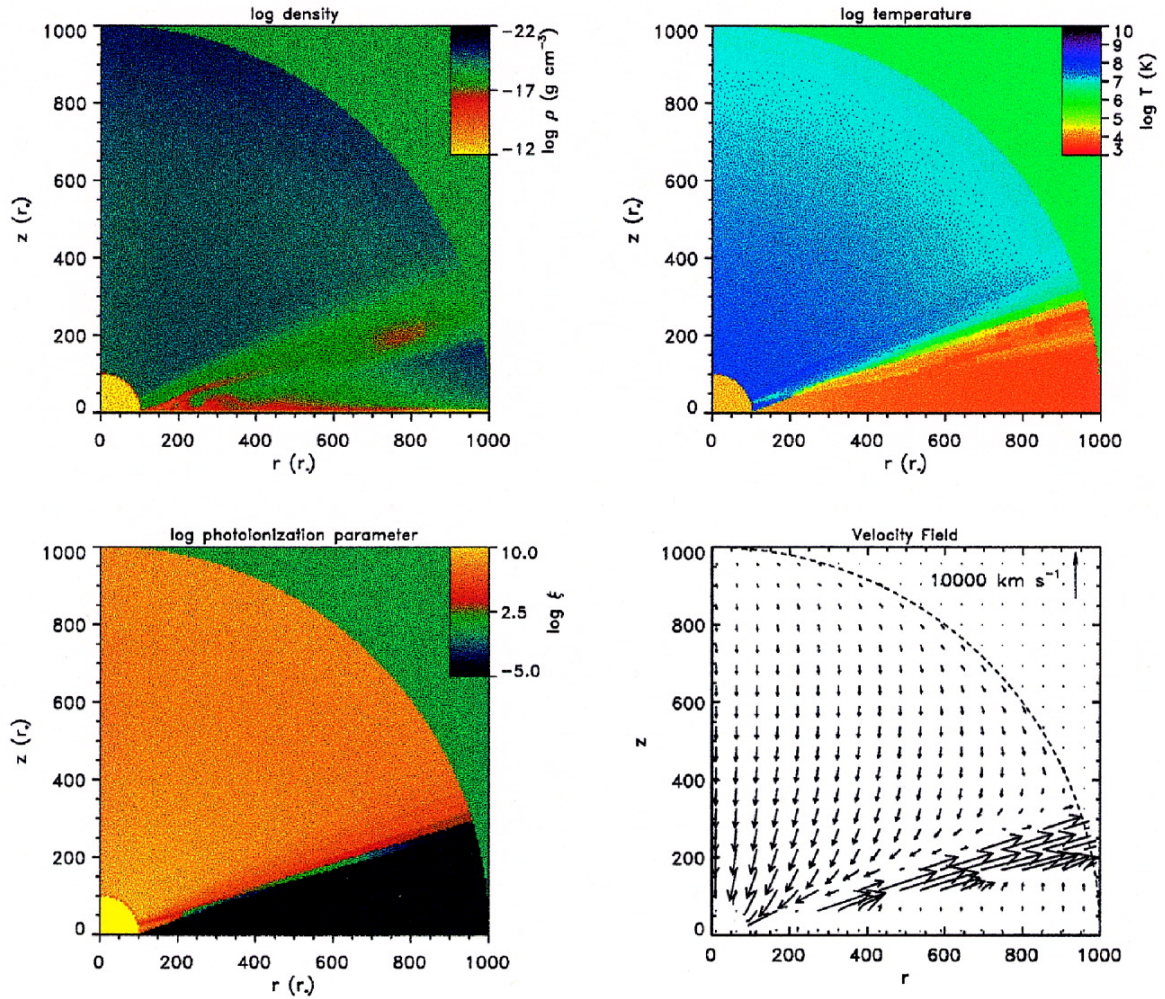


Fig. 1.2 Simulation of a line pressure-driven outflow from the accretion disc of a supermassive black hole. The top-left plot shows the density of the material versus its location, the top-right plot shows its temperature. The bottom-left and bottom-right plots contain the photoionisation parameter and the velocity of the material, respectively. This figure is taken from Proga et al. [322].

where  $\mu$  is the mean atomic mass of the particles and  $k$  is the Boltzmann constant. At the same time, the critical luminosity of the hard X-ray radiation required for a significant mass flux within a Compton heating driven wind is:

$$L_{\text{cr}} = 0.030 (T_{\text{IC}}/10^8 \text{ K})^{-1/2} L_{\text{Edd}} \quad (1.8)$$

Hence the object must be luminous but does not need to reach the Eddington luminosity  $L_{\text{E}}$ , and it also must have a strong hard X-ray spectrum (with a high inverse Compton temperature). Any winds driven by this mechanism are also naturally much slower than

those launched by the previous phenomena since the thermal velocity of a  $T_{\text{IC}} \sim 10^8$  K ( $\sim 9$  keV) particle is only of the order of 1000 km/s ( $\sim 0.003c$ ).

Finally, it is possible that an accretion disc wind might be driven by a combination of multiple of the effects described above. In particular, radiation pressure alone might be ineffective in driving powerful winds in sub-Eddington accreting systems, however in combination with either Compton heating or magnetic fields the driving force could be sufficient.

There is also a second class of outflows from accretion disc called jets. These are collimated narrow-angle outflows of high-velocity particles (hadronic or leptonic), launched by magnetic fields [31] along the axis of rotation of the accretion disc. Their main observational signature is radio emission from the synchrotron emission of particles within the jet [29]. I do not study the jet phenomena in this thesis, focusing only on wide angle disc outflows which are best studied through X-ray observations.

## 1.2 Accretion and ejection of matter in different systems

Accretion disc winds have been discovered in most types of accreting systems. Below I describe the physics of accretion and disc winds in the systems studied in the research chapters of this thesis.

### 1.2.1 Active galactic nuclei

Most galaxies in our Universe host a supermassive black hole with a mass between  $10^6$  and  $10^{10} M_{\odot}$  in their centre [341, 112, 154]. At any time, in a majority of galaxies, this black hole is inactive, i.e. it is not accreting [195]. If the black hole is accreting significant amounts of material, it shines across the whole electromagnetic spectrum and so these galaxies are called active galaxies and their nuclear regions are known as active galactic nuclei (AGN). AGN can be broadly split into three main categories according to their brightness: quasars [356], where the nuclear regions by far dominate the radiative output of the whole host galaxy, Seyfert galaxies [362], where the AGN component is an important fraction of the host's energetic output but it does not completely shadow it, and Low Luminosity AGN (LLAGN) where the nucleus emits a small fraction of the radiative output of the galaxy.

AGN are also classified as broad line AGN (type 1) and narrow line AGN (type 2) depending on the presence of broad ( $\sim 5000$  km/s) lines in their optical and UV

spectra. The broad lines originate in the ionised clouds of the so-called broad line region close to the black hole where the orbital velocities are large. At larger radii, narrow optical and UV lines are produced in the so-called narrow line region where the orbital velocities are much lower (line widths of  $\sim 1000$  km/s or less). Between these two regions, there is a dusty, clumpy, torus-like structure [141, 282, 165, 93] orbiting the central engine. The two optical classes of AGN can be unified into a single model by the varying torus inclination to the observer (Fig. 1.3). This is the AGN unification scheme [6]. In broad line AGN, the inclination angle between the axis of the dusty torus and our line of sight is such that the broad line region (closer to the AGN than the torus) is not obscured by the dust. At high inclination angles, the torus obscures our view of the broad line region, and therefore only narrow lines are observed.

Approximately 10% – 20% of all AGN also show persistent radio emission likely associated with relativistic jets and are classified as radio-loud AGN. A similar AGN unification scheme based on the observer inclination towards the jet direction was proposed for radio-loud AGN [405].

How supermassive black holes in galactic nuclei grew to their present mass is still an open question [411]. Nowadays, most AGN are observed to accrete significantly below the Eddington limit [173, 4]. However, recent observational discoveries of massive ( $10^9 - 10^{10} M_{\odot}$ ) black holes at very high redshifts [269, 432, 11] imply that these black holes did not have enough time since Big Bang to reach their masses through sub-Eddington accretion from small stellar-mass black holes. Such a fast growth of supermassive black holes can be explained by three main possibilities: (a) they grew from Population III star remnants with initial masses of  $\sim 100 M_{\odot}$  but had to experience prolonged periods of super-Eddington accretion [228, 412]; (b) they could have formed by direct collapse into  $10^4 - 10^6 M_{\odot}$  black hole seeds in the very Early Universe and grew by Eddington-limited accretion since then [23]; (c) they grew by frequent black hole - black hole mergers.

Considering the high efficiency of accretion from Eq. (1.3), the energy released during the formation and accretion of a supermassive black hole is very significant. It is so large that, if efficiently coupled to the stars and gas in its host galaxy, it would gravitationally unbind the host [97]. The fact that this is not observed suggests that the coupling is very inefficient.

Nevertheless, it has been found that there is a tight relation between the masses of the supermassive black holes and the velocity dispersion (a proxy of the total stellar mass) of the spheroidal components of their hosts [113, 130, 397, 144, 194]. Such a tight correlation suggests a strong relationship and interaction between central black

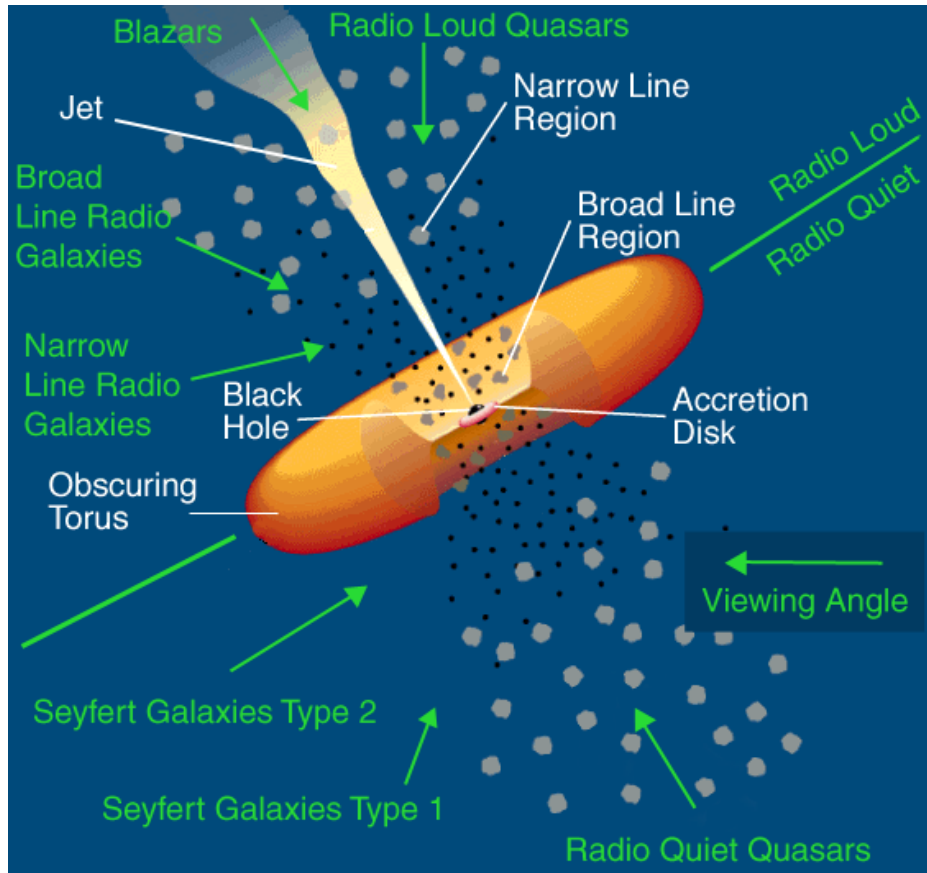


Fig. 1.3 The AGN unification model. The appearance of an AGN strongly depends on our line of sight towards the system. If the line of sight passes through the obscuring dusty torus, we do not observe the broad line region and only narrow optical/UV lines are seen in the AGN spectrum. Additionally, significant part of the X-radiation is absorbed by the torus and the AGN is classed as Type 2. Otherwise, the AGN is classed as Type 1. AGN can also be split into two classes based on the presence of a radio jet: radio-quiet and radio-loud. (image credit: NASA, based on Urry and Padovani [405]).

holes and their hosts, even though the masses and especially the sizes of black holes are insignificant compared to their hosts [black hole masses are only about 0.1% of their host masses, 146]. The relationship and interaction is likely with the gas and dust of the host (which in turn is the main stellar forge of the galaxy), which better couples with the AGN energy output than stars themselves.

At the same time, the observed galaxy luminosity function differs from the theoretical predictions of the Press-Schechter function [319, 355]. It was found that the number of galaxies at both the low and the high luminosity ends of the function is lower than

expected [26, 59]. The lack of small galaxies could be attributed to supernova feedback [184]. On the other hand, the lack of massive galaxies is likely due to their nuclear activity [59].

Last but not least, observational studies of galaxies in the Universe found that galaxies can be broadly split into two groups: blue and star-forming, and red and ‘dead’, with little star formation [24, 17, 71].

All of these observations can be explained if the supermassive black holes in the centres of galaxies have a profound effect on their environments, in the form of a feedback loop limiting the star formation in their hosts, which in turn hinders the growth of the central black holes. This effect is called the AGN feedback [97].

AGN feedback has been unambiguously observed in the massive brightest cluster galaxies (BCG) in the centres of galaxy clusters and is likely mediated via the highly collimated jets launched by the supermassive black holes of BCGs, preventing efficient cooling of the intracluster medium [239, 300, 103, 238]. In smaller galaxies, jets are likely not the source of feedback since they do not deposit energy efficiently into the host galaxies of AGN. Instead, the energy released through accretion could couple to their hosts via wide-angle accretion disc winds launched from the discs of AGN [366, 188]. Such wide-angle outflows can in theory establish the  $M$ - $\sigma$  relation [187] by heating and pushing the host’s gas and dust out of the galaxy. As a result, the host’s star formation can be quenched.

Alternatively, AGN feedback could be mediated via radiation pressure on dust [162, 340], which can increase the effective scattering cross-section by a factor as large as 100 [163], and push dust and gas outside of the AGN hosts, thus preventing star formation.

AGN outflows could therefore be of great importance. They have been observed in AGN for decades [58] and can be broadly classified into six main categories: powerful winds observed through the blueshifted UV absorption lines in some quasars, cold molecular outflows observed in the sub-millimetre band, neutral interstellar medium outflows, warm ionised outflows observed in the optical and infrared bands, warm absorbers mostly seen in the soft X-ray spectra of AGN at low outflow velocities ( $<5000$  km/s) and the ultrafast outflows (UFOs), observed in the AGN X-ray spectra with very high velocities between  $0.05c$  and  $0.5c$ .

The first category of winds is observed in the so-called broad absorption line quasars [BALs, 226], which show UV absorption troughs thousands of km/s wide, with velocities as high as  $0.1c$ . BALs form about 10% of all known quasars [118]. The

discoveries of line-locking<sup>5</sup> in the UV spectra of BALs [119, 425, 193] suggest that these winds are powered by radiation line driving.

The second category are cold, molecular outflows with velocities up to a few 1000 km/s, discovered recently in a number of galaxies in the sub-millimetre band [115, 379, 117]. Their mass outflow rates and kinetic powers are extreme, and so they very likely originate in AGN activity [230, 55].

Neutral ISM outflows can be powered by AGN and are observed through absorption features in the optical and UV bands [349, 348]. They are also traced by neutral hydrogen 21 cm absorption [268] and can reach velocities up to  $\sim 1000$  km/s.

Warm ionised outflows are traced by nebular emission lines and have been detected in many powerful AGN [147, 41, 43] at moderate velocities (100s of km/s to  $\sim 2000$  km/s) with large observed spatial extents (up to 10 kpc).

Warm absorbers [338] are ionised outflows observed in the soft X-ray and UV spectra of AGN with relatively low ionisation parameters, and at small to moderate velocities (0-5000 km/s). They have been discovered in many Seyfert 1 galaxies and studied in great detail [133, 175, 183, 372, 73]. Their mass outflow rates are large [33] but with low velocities, the kinetic powers of warm absorbers are typically not sufficient to drive AGN feedback in galaxies (Fig. 1.5).

In this thesis I mainly focus on the last and the most extreme category of wide-angle outflows in AGN. Ultrafast outflows are observed in the X-ray spectra of AGN with velocities in excess of  $0.05c$ , and as large as  $\sim 0.5c$  [316, 395, 393, 330]. They are often detected through highly blueshifted high ionisation Fe XXV and Fe XXVI absorption lines in the hard X-ray band (7-10 keV, see Fig. 1.4 for an example UFO absorption feature). Tombesi et al. [393] claim that about one third of all AGN shows signatures of UFOs.

There is evidence that some UFOs are multi-phase - they show distinct velocity and ionisation components [223, 313, 314, 204, 34]. In at least one case, IRAS 13224-3809, a time-resolved study showed that the UFO absorption strength responds to the X-ray flux of the AGN, and anti-correlates with it [297, 294, 303].

The large velocity of the UFOs necessarily means that their kinetic powers are considerable (Fig. 1.5) and therefore they are strong candidates for driving AGN feedback in galaxies [188]. Theoretical studies predict that the outflow needs to carry

---

<sup>5</sup>Line-locking is the observational signature of velocity separation of different ionised absorption components being similar to the velocity separation of two prominent absorption lines or a doublet. In the framework of radiation line pressure-driven winds, if an outer cloud is being accelerated by line pressure and is shielded by an inner cloud, the reduction of flux at specific line energies which provide the line pressure on the outer cloud can result in the two clouds being locked together in velocities [354, 39].

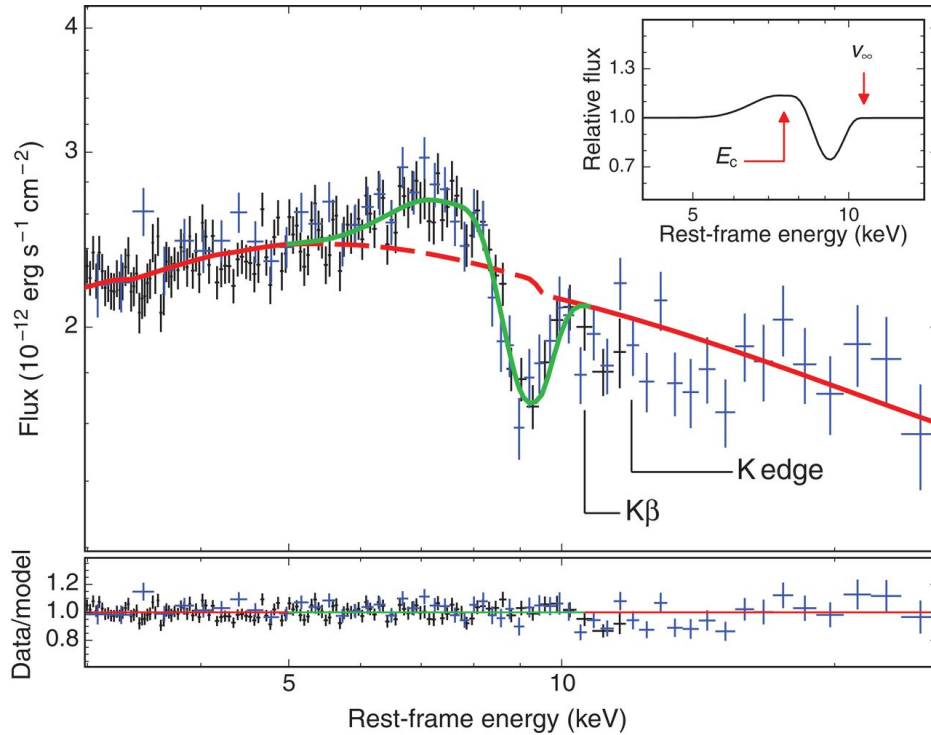


Fig. 1.4 An example spectrum showing UFO absorption in the 7 – 10 keV band. The absorption signature is likely imprinted by a powerful wind outflowing at a velocity of  $\sim 0.25c$  from the accretion disc of the highly accreting AGN PDS 456. This figure was taken from Nardini et al. [279].

at least around 5% of the radiative energy of the AGN [77, 190, 57]. Such kinetic powers are indeed observed in UFOs [394, 279], assuming they do not have negligible covering fractions and volume filling factors (unlikely if they are wide-angle outflows). Furthermore, some AGN hosting these outflows also show powerful molecular outflows with significant mass outflow rates [408, 394] and energetics comparable to UFOs. Molecular outflows could be evolved UFOs at large, galactic scales and at late times following the AGN activity.

UFOs are often observed in Narrow Line Seyfert 1 galaxies (NLS1s), a subclass of Seyfert 1 galaxies with relatively narrow permitted optical emission lines [ $\lesssim 2000$  km/s, 289, 236]. These AGN usually host lower mass ( $10^6 M_{\odot}$ ) supermassive black holes [35] accreting close to, or possibly in excess of the Eddington limit [172]. UFOs in NLS1s could therefore be driven by radiation pressure, although alternative mechanisms including magnetic driving [121, 124] or a combination of the two mechanisms have been proposed. UFOs have also been detected in the highly accreting massive ( $\sim 10^9$

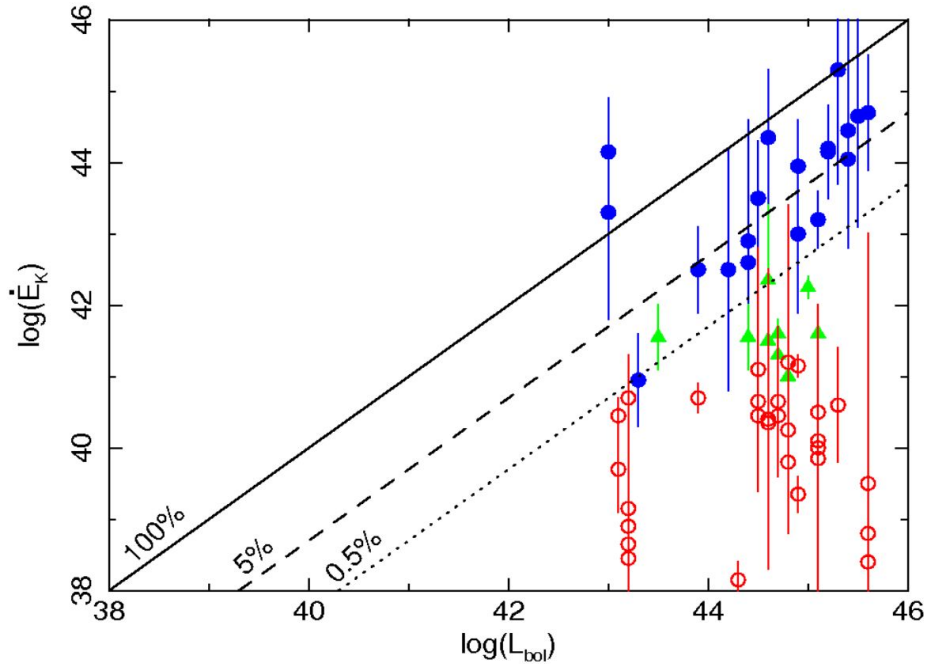


Fig. 1.5 The kinetic power of ionised outflows observed in different AGN versus their bolometric luminosity. UFOs (blue colour) show extreme kinetic powers, usually larger than 5% of  $L_{\text{bol}}$ , sufficient to drive AGN feedback in their galaxies [77]. Warm absorbers (red colour) have much less significant kinetic powers ( $< 0.5\%$ ) due to smaller velocities. Outflows with velocities between those of UFOs and warm absorbers (green colour) have intermediate powers. This figure was taken from Tombesi et al. [392].

$M_{\odot}$ ) quasar PDS 456 [332, 279, 330, 34], and in strongly lensed quasars [51, 50, 52], hence they are not exclusive to NLS1s.

An alternative novel explanation for UFOs is that they are not in fact unbound flows. Instead the blueshifted absorption features could originate in low-density gas co-rotating with the inner accretion flow, where velocities up to  $0.5c$  are present [127, 102]. This interpretation and model is not investigated throughout this thesis. I focus on the outflowing wind interpretation as it can simultaneously explain AGN feedback in galaxies. Furthermore, the co-rotating gas interpretation cannot explain ionised outflows observed in other objects such as the Ultraluminous X-ray sources and X-ray binaries.

If the UFOs truly are accretion disc winds accelerated to tens of % of the speed of light, they are potentially powerful enough to drive AGN feedback in galaxies and are of great importance in the Universe. However, the UFO spectral features are often weak due to high ionisation of the outflowing material, and the inference of the wind

physical properties can be complicated by other spectral features in AGN. The UFO physics and launching mechanisms are therefore not completely understood. To address these issues, I developed an automated, systematic routine for detecting outflows in accreting systems. In this thesis I use the method to achieve an unambiguous detection of UFOs in two highly accreting NLS 1 galaxies PG 1448+273 (Chapter 5) and 1H 0707-495 (Chapter 6).

### 1.2.2 Classical X-ray binaries

Most stars in the Universe have at least one or more stellar companions - they exist in binaries, triples and multiples [2, 87, 351]. In a fraction of binary systems, the separation of the components is small enough that they gravitationally interact and can exchange matter [159, 299, 158]. If one of the components is a compact object such as a neutron star, stellar-mass black hole or a white dwarf, accretion onto the compact object can occur and the system becomes a so-called X-ray binary, shining brightly in the X-ray energy band.

X-ray binaries can be broadly separated into two classes: high mass X-ray binaries and low mass X-ray binaries. The former consist of a compact object and a high mass star with a strong wind. The accretion onto the compact object then occurs mostly via wind capture [424]. The second class consists of a compact object and a lower mass star, which fills the Roche lobe of the system [89]. The accretion of material onto the compact object then occurs through the first Lagrangian point between the two components of the binary.

X-ray binaries show different behaviour based on the nature of the compact object in the system.

#### Black hole X-ray binaries

Black hole X-ray binaries [334], particularly those in low mass X-ray binaries show strongly transient behaviour. Normally, they spend prolonged periods of time in a quiescent state during which very little X-ray emission is seen [237, 275, 288, 241]. Then they enter into short outbursts with lengths of 10s-100s of days [95]. During these outbursts, the binary is known to follow a ‘Q’ shaped hardness-intensity diagram (Fig 1.6). The outburst begins in a hard state, when the total luminosity is low ( $L \lesssim 0.01 \times L_E$ ), the X-ray spectrum is very hard and dominated by emission from an optically thin corona [390] which might be the base of a jet [234], and a stable and compact radio jet is present [126]. The accretion disc might be truncated at  $\sim 100 R_G$  in

the hard state and the emission shows rich time variability behaviour [82]. Sometimes the binary can enter into a bright hard state when the X-ray luminosity is at or above 10% of its Eddington luminosity [84].

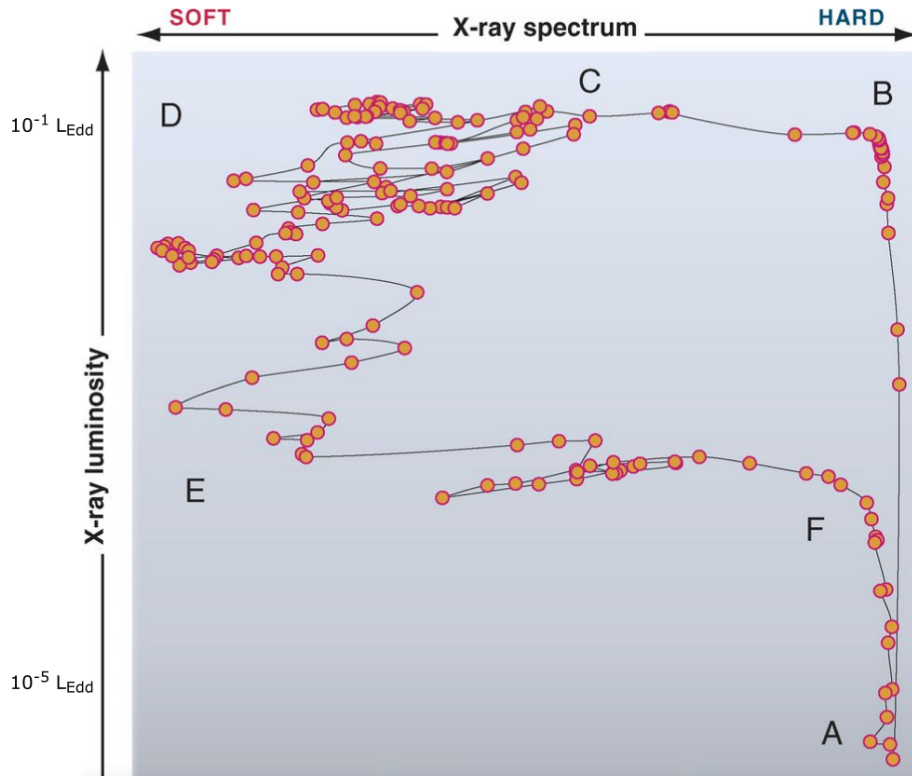


Fig. 1.6 The hardness-intensity (Q) diagram of black hole X-ray binary outbursts. The outburst starts in a hard state (A, B). The binary can then transition into a soft state (D, E) through an intermediate state (C), followed by a transition back into a hard state (F) and return into quiescence. This figure is adapted from Fender and Belloni [108].

The X-ray binary can then transition into a soft state [387] or alternatively it can drop back down into quiescence after a so-called ‘failed’ outburst [156]. In the soft state, the hard powerlaw emission from the corona is much weaker. Instead, accretion disc multicolour thermal emission dominates its X-ray spectrum [219]. During the soft state, the accretion disc is known to extend down to the ISCO, and the luminosity of the system is around  $\sim 0.1 \times L_E$  or even higher. The time variability is also weaker and a compact jet is usually replaced with discrete jetted ejecta [109, 56]. Last but not least, accretion disc winds are observed in some black hole X-ray binaries in the soft state.

Ionised disc winds were first discovered in GRO J1655-40 [403] and GRS 1915+105 [200], but have since been detected in about 10 black hole binaries, exclusively in their soft states [78]. The signatures of these disc winds are highly ionised absorption lines, usually of iron, in the hard X-ray band (around 7 keV), however transitions of other ions such as silicon and sulphur have also been detected. The observed outflow velocities measured from the line blueshifts are in the range between 300 and 3000 km/s. The inferred mass outflow rates are large and in the range between 1% and 100% of the mass accretion rate, so disc winds can be an important component of the accretion flow in X-ray binaries. They are most likely driven by Compton heating [280, 79] or by magnetic fields [259, 261, 122]. X-ray luminosities of binaries are too low for isotropic radiation driving and their spectra are too hard for radiation line driving.

Such winds might be present in all soft state black hole binaries [298] but their structure is likely not spherically symmetric and thus not always observable in absorption. Instead, they are probably concentrated towards the accretion disc as all the wind detections were made in high inclination systems, and conversely low inclination binaries do not appear to show signatures of disc winds [Fig. 1.7, 310]. In some cases, since the apparent outflow velocities are quite low, these winds could be ‘failed’ outflows, i.e. they could be bound flows [283].

### Neutron star X-ray binaries

Accreting neutron star binaries can be broadly split into two categories based on the strength of the surface magnetic field of the neutron star.

Weakly magnetised accreting neutron stars, with  $\sim 10^9$  G surface magnetic fields are usually observed with very small rotational periods in the range of milliseconds [428, 407]. They can be classified into two categories based on their behaviour in the colour-colour diagram, as Atoll sources (following elongated curved branches sometimes resembling a geographical ‘atoll’ in the colour-colour diagram) and Z sources (following three branches which resemble a letter Z) [270, 149, 357]. These systems show similar hard/soft state behaviour to black hole X-ray binaries [227]. In their soft states, particularly the brightest Z sources show luminosities approaching their Eddington luminosity ( $2 \times 10^{38}$  erg/s for a  $1.4 M_{\odot}$  neutron star).

Accretion disc winds have been discovered in multiple neutron star X-ray binaries including GX 13+1 [402, 365, 404] and Cir X-1 [40]. Their properties are very similar to that of disc winds observed in black hole X-ray binaries, suggesting the same driving mechanism [79]. The wind driving can therefore occur either through Compton heating

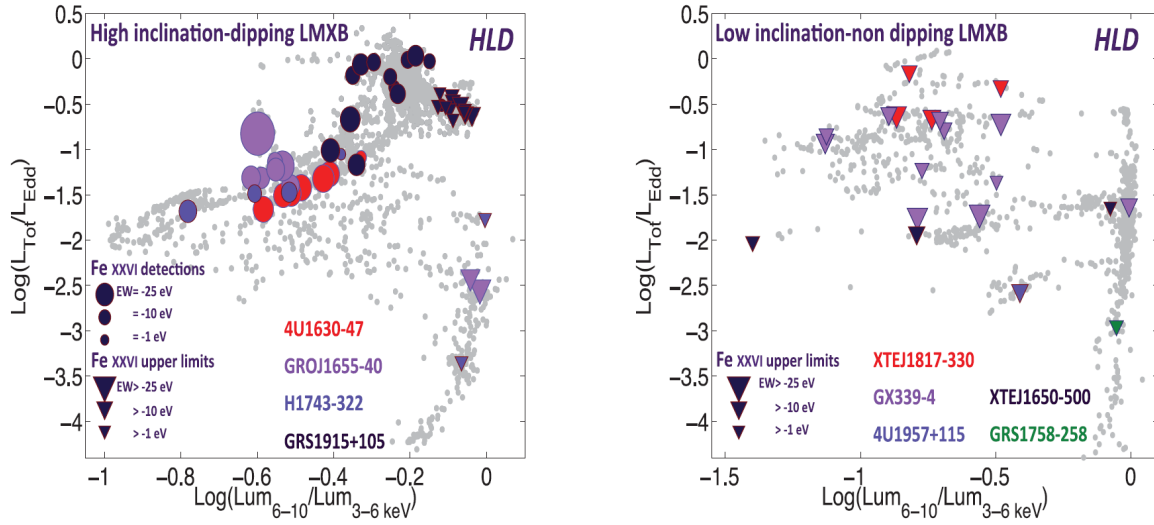


Fig. 1.7 Ionised wind detections (coloured circles) and non-detections (coloured triangles) of high inclination (left plot) and low inclination (right plot) X-ray binaries placed on the hardness-luminosity diagram (HLD). Disc winds are only detected in high inclination binaries in the soft state, suggesting an equatorial wind structure. This figure is taken from Ponti et al. [310].

or with magnetic fields, possibly with a contribution from the radiation pressure in the luminous  $Z$  sources. At the same time, there is a class of lower luminosity neutron star binaries which show static ionised absorption from atmospheres above their accretion discs [78]. These objects also show the so-called accretion disc coronae of highly ionised material, revealing themselves through rich X-ray emission line spectra [170, 324].

Highly magnetised accreting neutron stars are also called the X-ray pulsars [427, 272, 27]. The most famous objects of this class are Centaurus X-3 and Hercules X-1, both discovered in the early 1970s with the first X-ray satellite Uhuru [137, 138, 387, 136]. The surface magnetic field of the neutron star, which can have a strength of  $\sim 10^{12}$  G [measured via the cyclotron scattering feature, 398, 426] dominates the inner accretion flow in these systems [206, 135]. It creates a magnetosphere [244] truncating the accretion disc to as far as  $1000 R_G$ , inside which the accreting matter is channelled along the magnetic field lines towards the neutron star. As the matter approaches the neutron star's magnetic poles, it forms an accretion column co-rotating with the neutron star [65]. The accretion column emits anisotropic radiation, hence a fraction of the pulsar's radiation is pulsed at the rotation frequency of the neutron star (typically  $\sim 1$  s). Beyond the magnetosphere, there is a standard accretion disc, however if it is

truncated at  $\sim 1000 R_G$ , its temperature is low ( $< 0.1$  keV) and it is not observed in the X-rays.

Until recently, there has been very little evidence for disc winds from accreting pulsars. In Chapter 7 of this thesis, I present the first discovery of an ionised outflow in the famous X-ray pulsar Hercules X-1.

### 1.2.3 Ultraluminous X-ray sources

Ultraluminous X-ray sources (ULXs) are off-nuclear X-ray point sources with X-ray luminosities in excess of  $10^{39}$  erg/s (i.e. the Eddington luminosity of a  $10 M_\odot$  accretor) [for a recent review, see 174]. They are most abundant in smaller, star-forming and metal-poor galaxies [232, 435]. The origin and nature of ULXs has been disputed for decades, since their original discovery with the *Einstein* X-ray observatory in the 1980s [222, 96]. As ULXs do not lie in galactic nuclei, they are not powered by supermassive black holes. At the same time, their luminosities (if assumed isotropic) exceed the Eddington limit of standard stellar-mass ( $\sim 10 M_\odot$ ) black holes found in Galactic X-ray binaries. Three main explanations have been proposed to solve this discrepancy.

One of the propositions to explain the existence of ULXs is that their X-ray radiation is strongly beamed, and their total X-ray luminosity is much lower. However, with apparent luminosities as high as  $10^{41}$  erg/s, the beaming factors would have to be extreme for the brightest objects of the ULX class. Secondly, several ULXs are located in large (10 – 100 pc) bubbles of ionised plasma, approximately isotropic in their shape [292, 291, 142]. These ionised bubbles require consistently high fluxes of isotropic soft X-ray radiation to remain ionised, strongly arguing against extreme beaming in ULXs.

Alternatively, ULXs could be powered by a class of intermediate-mass black holes (IMBHs) with masses between 100 and 10000  $M_\odot$ , accreting below the Eddington limit [254, 107]. This hypothesis has been supported by the discovery of a soft X-ray blackbody spectral component in ULX spectra with temperatures from 0.1 to 0.3 keV [252, 255, 66]. The temperature of this component, if originating from multi-color accretion disc emission of the ULX, would lie directly in-between the temperatures of accretion discs of X-ray binaries and discs of AGN, as expected if ULXs were powered by IMBHs. A second piece of evidence for the IMBH nature of ULXs is the discovery of quasi-periodic oscillations (QPOs) in the power density spectra of multiple ULXs [375, 74, 377, 376, 110]. The frequencies, if associated with the orbital frequency at the innermost stable circular orbit (ISCO) of the ULX accretion disc, would correspond to expected ISCO orbital frequencies of IMBHs [76, 46, 68].

The third and the most accepted hypothesis for the nature of ULXs is that they are powered by super-Eddington accretion onto stellar-mass compact objects [191, 318, 140]. There are multiple arguments for this explanation. First, the ULX population appears to be a direct extension of the normal X-ray binary population in galaxies, only to higher luminosities, with no break in the population function at  $10^{39}$  erg/s [381, 265]. Secondly, the X-ray spectrum of ULXs significantly differs from that of sub-Eddington accretors such as X-ray binaries and AGN. In particular, ULXs show a very low energy roll-over in the spectrum at less than 10 keV, whereas the high-energy cut-off in sub-Eddington systems is only observed above 50-100 keV [99]. This was initially observed with *XMM-Newton* ULX observations [3, 140, 75] and later unambiguously confirmed with the high energy coverage of the *NuSTAR* telescope [13, 416, 418].

The third, and by far the strongest evidence of super-Eddington accretion in ULXs is the detection of X-ray pulsations in a number of ULXs [12, 125, 164, 45, 353, 346]. The pulsations are unambiguously associated with emission from an accretion column, confirming that at least these 6 ULXs are powered by neutron stars. These systems thus must be accreting significantly in excess of the Eddington limit (one of these objects, NGC 5907 ULX-1 exceeds the Eddington limit by a factor of  $\sim 500$ ). Neutron stars form an unknown, but likely significant fraction of the ULX population [429].

The final important piece of evidence for the super-Eddington scenario is the discovery of ultra-fast outflows in a handful of ULXs. Powerful winds, launched by the extreme radiation pressure are naturally expected if ULXs accrete above the Eddington limit. The first, tentative evidence for UFOs in ULXs was achieved by detecting broad residuals in soft X-ray low spectral resolution data from CCD instruments onboard the *XMM-Newton* and *Chandra* telescopes, in multiple ULX systems [374]. These residuals are likely not associated with nearby star formation [352]. Furthermore, in one of the ULXs, NGC 1313 X-1, the strength of these residuals anti-correlates with the X-ray flux of the ULX [249], and therefore the residuals must be associated with the object. They also cannot originate in relativistic reflection where a direct correlation would be expected.

Pinto et al. [306] used the high-spectral resolution Reflection Grating Spectrometers onboard *XMM-Newton* to resolve the soft X-ray spectra of ULXs and detected UFOs in two ULXs NGC 1313 X-1 (Fig. 1.8) and NGC 5408 X-1. The UFO spectral features are narrow, significantly blueshifted ( $\sim 0.2c$ ) photoionised absorption lines of elements such as iron, oxygen, neon and nitrogen. Additionally, iron K absorption at a similar blueshift was found in the hard X-ray spectrum of NGC 1313 X-1 [417]. Similar features were later detected in a third system NGC 55 ULX [304]. Due to the extreme velocity,

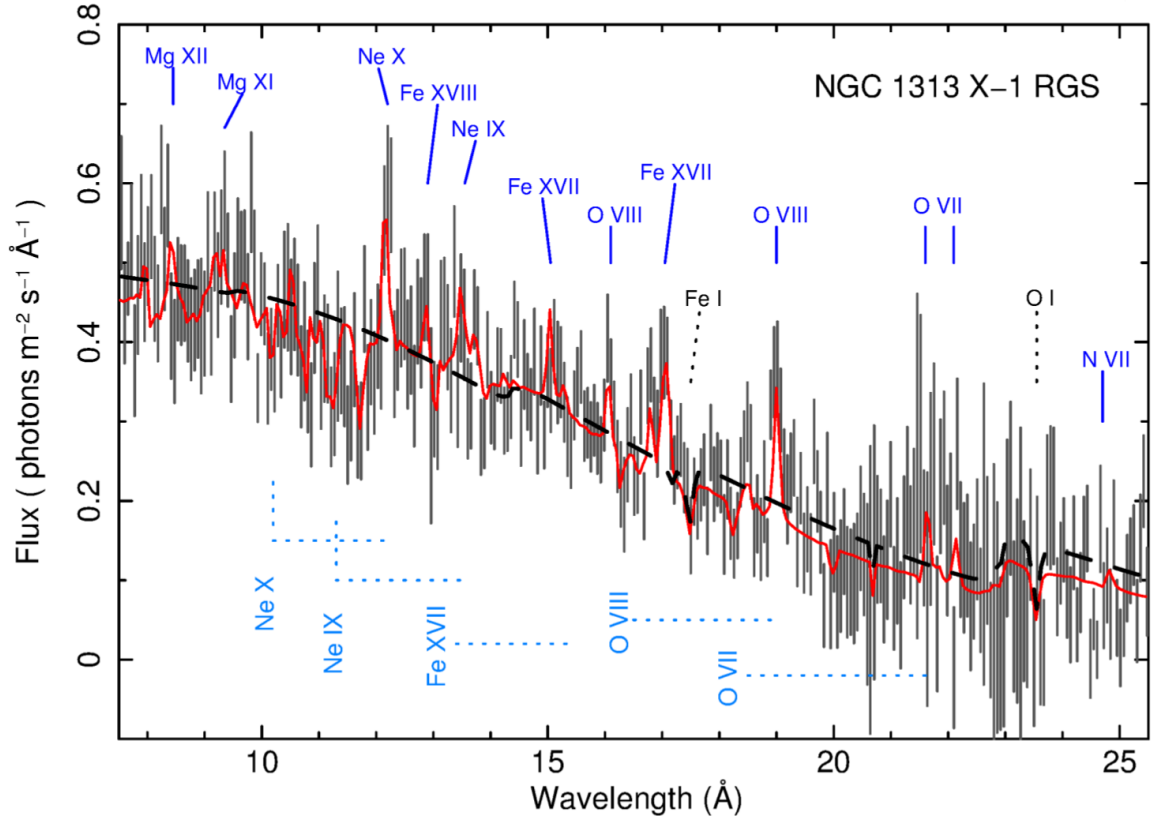


Fig. 1.8 Detection of an ultra-fast outflow in the ULX NGC 1313 X-1. The signatures of the outflow are the narrow, strongly blueshifted absorption lines of neon, iron and oxygen. This figure is taken from Pinto et al. [306].

the kinetic power of these outflows is very significant and could be comparable to the radiative output of the ULXs, and could be sufficient to power the inflation of the ionised superbubbles in which many ULXs reside [306].

If ULXs are powered by super-Eddington accretion, radiation-driven outflows should be present in all of them and should have a great impact on these systems and their surroundings. However, up to date these outflows have only been detected in a small number of cherry-picked ULXs with the best-quality datasets, and have not been studied systematically as a sample. I performed a systematic search for outflows and other narrow spectral features in a sample of 10 ULXs with usable *XMM-Newton* RGS data. The results of the analysis are described in Chapter 3. Chapter 4 of this thesis contains the discovery and detailed study of a UFO in the newly discovered neutron star ULX NGC 300 ULX-1.

We observe no persistent ULXs in our Galaxy. However, we know of a persistent super-Eddington stellar-mass accretor called SS 433 [233]. SS 433 is a microquasar which launches powerful jets with kinetic power in excess of  $10^{40}$  erg/s [22], despite the mass of the compact accretor being smaller than  $20 M_{\odot}$  [105], suggesting that the accretion rate is strongly super-Eddington. Nevertheless, its X-ray luminosity is much lower than  $10^{39}$  erg/s [361]. From the blue and red sides of its jet, we know that the system is oriented almost edge-on towards us [the inclination angle of the rotation axis is around 80 degrees and periodically precesses, 153]. It is therefore possible that SS 433 is a ULX misaligned from our point of view such that the luminous X-ray emitting regions are completely obscured by the outer accretion disc [23, 106].

### 1.3 X-ray observatories

In this thesis, I study accreting systems and the physics of their accretion disc winds with X-ray spectroscopic observations. X-rays are not observable from the Earth's surface because they are absorbed by the Earth's atmosphere. Therefore all of the X-ray instruments must be placed above the main bulk of the atmosphere, either in a high altitude balloon, on a sounding rocket, or on a satellite orbiting the Earth. A great majority of the modern X-ray observatories are carried by satellites. The following section describes the X-ray observatories which collected the data used in my analysis.

#### 1.3.1 *XMM-Newton*

The X-ray Multi-Mirror Mission [*XMM-Newton*, 166] is an X-ray satellite built and launched by the European Space Agency in December 1999 (see Fig. 1.9 for an artist's impression). *XMM-Newton* carries a wide range of X-ray instruments covering a wide energy band (0.3 to 10 keV) as well as a smaller optical/UV telescope. *XMM-Newton* offers instruments with the highest photon collecting area from all of the current X-ray missions with the exception of *NICER* (in the 1-2 keV band) and the recently launched *eROSITA*. However, *NICER* offers a much poorer spatial resolution than *XMM-Newton* and both *NICER* and *eROSITA* lack high-spectral resolution instruments as opposed to *XMM-Newton*.

Importantly, all of the successful *XMM-Newton* observations for which the (1 year) proprietary period has expired are accessible on-line on the *XMM-Newton* Science Archive<sup>6</sup> (XSA). XSA allows interactive access and a quick look at the science products

---

<sup>6</sup>[www.cosmos.esa.int/web/xmm-newton/xsa](http://www.cosmos.esa.int/web/xmm-newton/xsa)

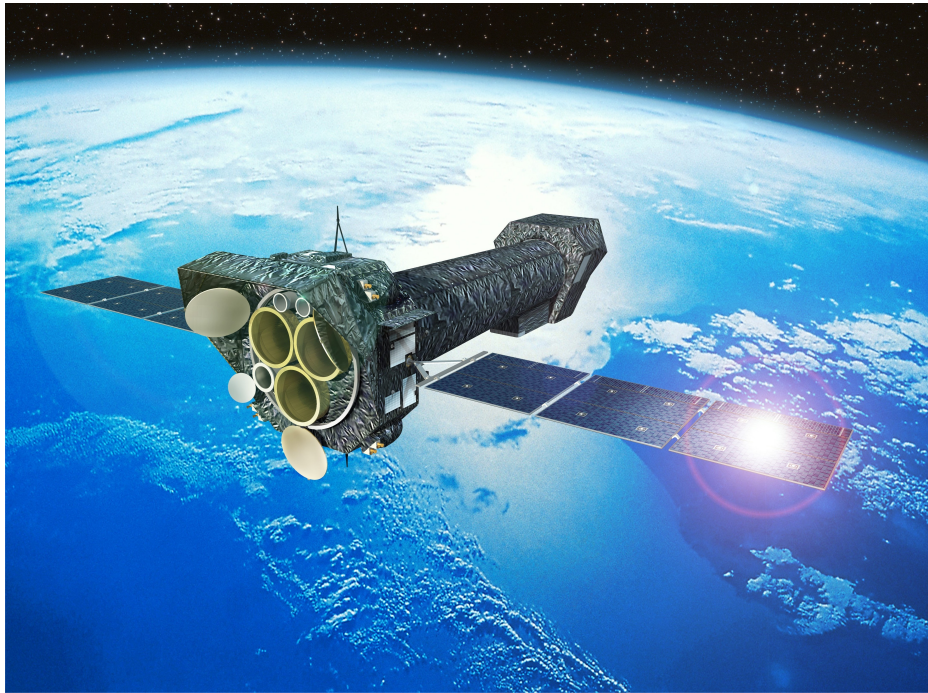


Fig. 1.9 Artist's impression of *XMM-Newton* in orbit (credit: ESA/D. Ducros).

from *XMM-Newton* instruments. The desired observations can be downloaded to local storage directly from XSA.

*XMM-Newton* carries three X-ray telescopes, each of which is composed of 58 paraboloid-hyperboloid Wolter I grazing-incidence mirrors, nested in a co-axial and co-focal configuration. The grazing angle of the mirrors is just around 30 arcmin (depending on the X-ray energy) to provide reflectivity across a wide energy band including the hard X-rays between 5 and 10 keV. The focal length of each telescope is 7.5m, and the spatial resolution of the mirrors is around 6 arcsec [full width half maximum, or 15 arcsec half energy width, 10].

The X-ray instruments onboard *XMM-Newton* offer a wide range of scientific possibilities. The European Photon Imaging Camera (EPIC) instrument consists of three CCD cameras with wide band capability and moderate energy resolution. The two Reflection Grating Spectrometers (RGS 1 and 2) offer high spectral resolution in the soft X-ray band (0.3 keV to 1.8 keV).

### Reflection Grating Spectrometers

Each of the two Reflection Grating Spectrometers [RGS, 72] consists of an array of reflection gratings placed in the converging beam at the exit from the X-ray telescope.

An array of 9 large format CCDs is placed in the reflection direction and records the position and energy of each photon reflected from the gratings. The photon position along the dispersion direction is used to calculate the energy of the reflected photon according to the dispersion equation:

$$m\lambda = d(\cos\beta - \cos\alpha) \quad (1.9)$$

where  $m$  is the spectral order of the diffraction,  $d$  is the groove spacing of the grating,  $\beta$  is the angle between the outgoing ray and the grating plane, and  $\alpha$  is the angle between the incoming ray and the grating plane.

The position in the cross-dispersion direction (perpendicular to the dispersion direction) shows the spatial position of the X-ray source in the direction perpendicular to the roll angle of *XMM-Newton* (the field-of-view in this direction is 5 arcmin). The measured energy of the photon is used to separate events of different spectral orders. As RGS is a slit-less spectrometer, the roll angle of the spacecraft is of great importance since any X-ray photons coming from the direction parallel to the dispersion axis but off the center point will be assigned an incorrect wavelength. This is particularly a problem for diffuse sources such as galaxy clusters but contamination can also occur if there are multiple bright point sources along the roll angle from the center point.

The source spectrum is extracted from a region along the dispersion axis from all working CCDs (CCD 7 is disabled in RGS 1 and CCD 4 is disabled in RGS 2). The background spectrum is extracted from two rectangular regions offset from the source region in the cross-dispersion direction so that they lie outside of the main source point spread function. For crowded fields or extended sources with contaminated background regions it is possible to use a ‘model’ background scaled to the expected background flux.

The instrument achieves a high resolving power in the soft X-ray band (0.3-1.8 keV, 7-38 Å) with a resolution of between 120 and 700 in the first spectral order. The spectral resolution in the wavelength units is approximately constant ( $\sim 0.06$  Å in the first order, full width half maximum), as opposed to CCD instruments where the resolution is roughly constant in energy units. The second order offers double the resolution of the first order, but also has a much poorer effective area and a limited wavelength band (5 to 20 Å).

The collecting area of RGS in comparison with other high-spectral resolution instruments is shown in Fig. 1.10. The figure shows that RGS is by far the best current instrument to use for faint source spectroscopy below  $\sim 1.3$  keV (above 10 Å). The wavelength band between 10 and 35 Å contains many important transitions of ionised

elements, in particular the transitions of oxygen, nitrogen, neon and iron. RGS is therefore greatly suited for studies of ionised plasma and accretion disc winds. RGS also has a high pile-up limit<sup>7</sup>, only observations of the brightest X-ray sources in the sky will result in distorted spectra. The gratings' resolving power is more than  $10\times$  higher than the resolution of non-dispersive CCD cameras (see the following subsection), even for extended objects up to 1 arcmin in angular size.

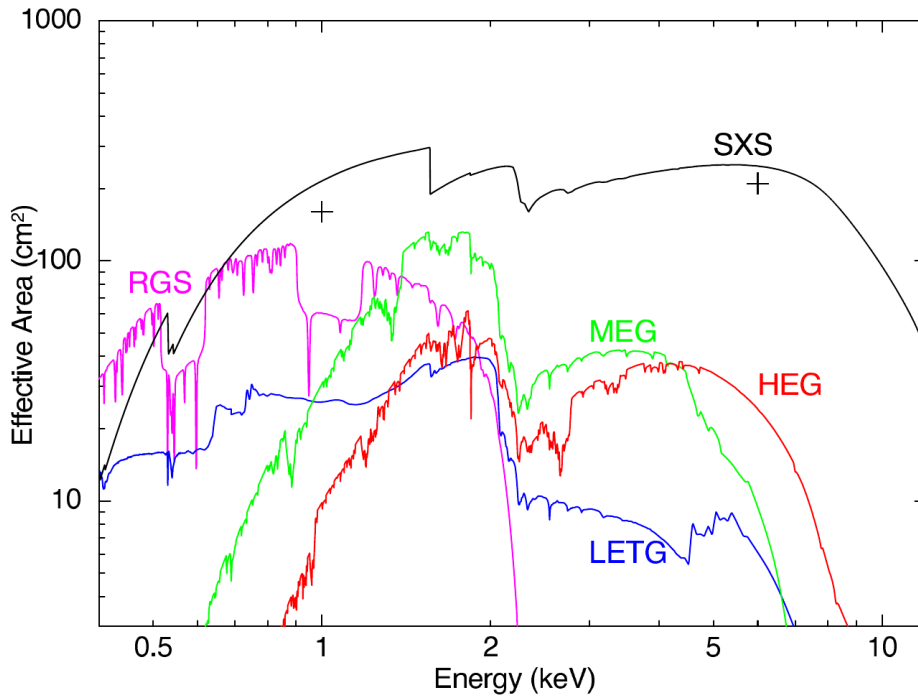


Fig. 1.10 The combined effective area of the RGS 1 and RGS 2 instruments (magenta colour) onboard *XMM-Newton* compared with other high-spectral resolution X-ray instruments. LETG (blue), MEG (green) and HEG (red) are grating instruments onboard the *Chandra* X-ray observatory. SXS (black) was the high-resolution instrument onboard the *Hitomi* X-ray observatory (lost in 2016), a copy of which will be re-flown onboard the X-ray Imaging and Spectroscopy Mission (*XRISM*, to be launched in 2022). This figure is taken from Takahashi et al. [382].

<sup>7</sup>Pile-up is the effect of two photons arriving at the same CCD pixel during the same read-out cycle. They are effectively registered as a single event with the energy equal to the sum of the photon energies. In RGS this means that two first order photons arriving at the same time will be registered as a single second order photon, distorting the final source spectrum in both orders.

## European Photon Imaging Camera

In addition to the RGS instruments, *XMM-Newton* also carries three broadband X-ray (0.3-10 keV) instruments based on Charge-Coupled Device (CCD) technology. Two of the CCDs, Metal Oxide Semi-conductor (MOS) 1 and 2 [400] are front-illuminated and virtually identical, the third one, the pn camera [378] is back-illuminated. The collecting areas of the cameras are much higher than those of the RGS instruments. The pn collecting area exceeds 1000 cm<sup>2</sup> in the 0.7 to 2.5 keV range and is stable up to 7 keV. pn is therefore particularly effective for studies of the iron K energy region (5 – 8 keV). The area of each MOS camera reaches up to 500 cm<sup>2</sup> (50% of X-rays from their mirrors are reflected towards the RGS instruments), depending on the photon energy, but its response below 1 keV is poorer than that of pn as MOS is front-illuminated.

The energy resolution of the three cameras is comparable and is between 50 and 100 eV over the whole energy band. The spectral resolution is therefore quite poor at low energies ( $R \sim 10$ ) but improves considerably at the higher end of the band ( $R \sim 50-100$ ). The angular resolution of the detectors is roughly 6 arcsec (FWHM), *XMM-Newton* is therefore the second best X-ray observatory in terms of spatial resolution, the first being the *Chandra* observatory.

The EPIC cameras can be operated in different modes depending on the source requirements. They are operated in Full Frame mode (pn additionally offers Extended Full Frame mode) with a field of view of  $\sim 30$  arcmin for observations of extended sources or for wide field studies. In these modes the event read-out time is very long and bright point sources will cause pile-up<sup>8</sup> and distortion of the source spectra. For brighter point sources with a count rate of above  $\sim 0.5$  ct/s in MOS and above 2 ct/s in pn, it is possible to use Large Window mode which reduces the field of view and decreases the read-out time. For even brighter sources (above 1.5 ct/s in MOS and 3 ct/s in pn), Small Window mode must be used, reducing the FOV to just 2 arcmin with MOS and 4 arcmin with pn. Usage of Small Window mode also reduces the live-time of the pn camera to about 70% of the exposure because of telemetry limitations.

The brightest sources (e.g. nearby X-ray binaries) with count rates in pn above 25 ct/s, must be observed in Timing mode, or if they exceed 800 ct/s, in Burst Mode. Burst mode allows for observation of sources as bright as 60000 ct/s but with a small live-time of 3%. In both modes only limited spatial information of the photon events is preserved, they are therefore only useful for observations of very bright point sources. MOS cameras are not usually used in Timing mode due to poor calibration.

---

<sup>8</sup>In EPIC, pile-up results in events moving from lower energies to higher energies, distorting the overall source spectral shape.

The wide energy band, good spectral and spatial resolution and the various science modes of the EPIC cameras mean that the instruments excel in studies of all accreting systems.

### 1.3.2 *NuSTAR*

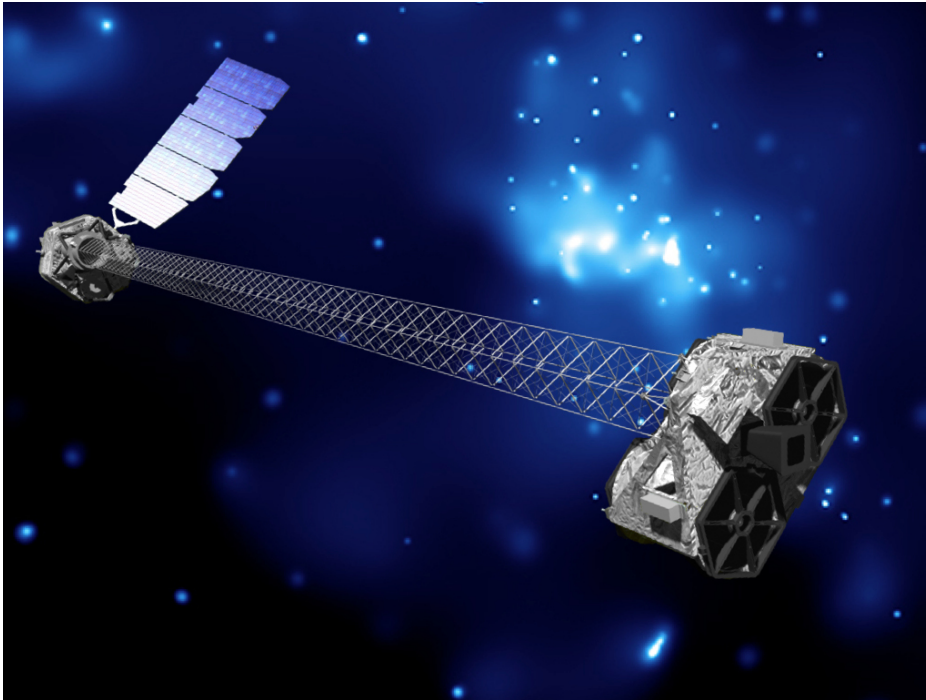


Fig. 1.11 Artist's impression of *NuSTAR* in orbit (credit: California Institute of Technology).

The Nuclear Spectroscopic Telescope Array [*NuSTAR*, 148] is a hard X-ray telescope built and launched by the National Aeronautics and Space Administration (NASA) in 2012 (see Fig. 1.11 for an artist's impression). It is the first focusing hard X-ray (3 – 79 keV) observatory. *NuSTAR* consists of two independent X-ray telescopes FPMA and FPMB (focal plane modules) with a focal length of 10 m. Each telescope uses a conical approximation to the Wolter I design with 'depth-graded multilayer' coatings<sup>9</sup> on the mirrors. The focusing optics offer a high spatial resolution (for a hard X-ray instrument) of 18 arcsec (FWHM, 58 arcsec half-energy width). Each telescope uses a

<sup>9</sup>Multilayers are thin coatings of two alternating materials deposited one on top of the other. *NuSTAR* uses Pt/SiC and W/Si multilayers, allowing its mirrors to reflect X-rays with energies up to 79 keV.

CZT detector with triggered read-out (and negligible pile-up) and has a field-of-view of about 10 arcmin.

The collecting area in comparison with other X-ray instruments is shown in Fig. 1.12. *NuSTAR* is the only focusing instrument effective above 10 keV. At the same time, it is also effective in the 3-10 keV band providing a useful overlap with other X-ray observatories. The spectral resolution is 400 eV at 10 keV and 900 eV at 68 keV, somewhat poorer than that of the EPIC cameras onboard *XMM-Newton* at the same energies. The very high pile-up limit (400 ct/s) allows *NuSTAR* to observe the brightest X-ray sources in the sky with no spectral distortion. The instrument is therefore very well suited for studies of nearby X-ray binaries, and for studies of X-ray reflection [101, 315, 132] as well as coronae [99] in both X-ray binaries and AGN. Other notable uses are studies of accretion columns and cyclotron scattering features [398] in accreting magnetised pulsars.

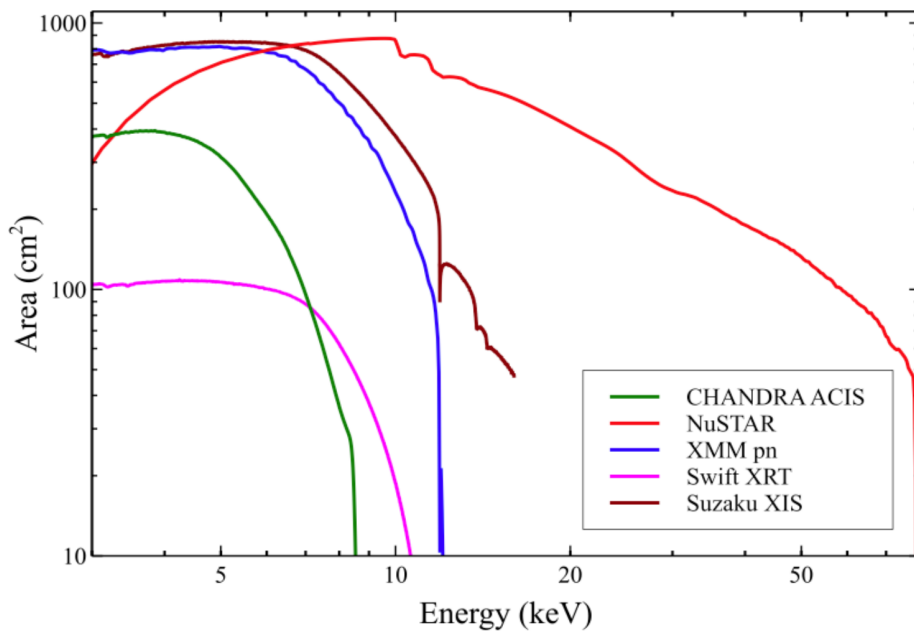


Fig. 1.12 The collecting area of *NuSTAR* in comparison with other X-ray instruments (credit: *NuSTAR* observatory guide).

## 1.4 X-ray spectroscopy

Highly energetic processes in the Universe such as accretion result in very high temperatures of plasmas, which can often be in the range between  $10^6 - 10^8$  K. Matter at

such high temperatures shines brightly in the X-ray energy band. X-ray observations are thus an important tool in studying the physical conditions of these high energy processes and their host systems.

At the same time, the 0.3 – 10 keV X-ray band also contains many elemental transitions of most elements abundant in the Universe including iron, sulphur, silicon, magnesium, neon, oxygen and nitrogen. X-ray spectroscopy is therefore a very powerful means of studying ionised astrophysical plasmas across a very large range of ionisation states. Fig. 1.13 contains an example of an X-ray line spectrum showing the large abundance of X-ray features which can be used for X-ray studies.

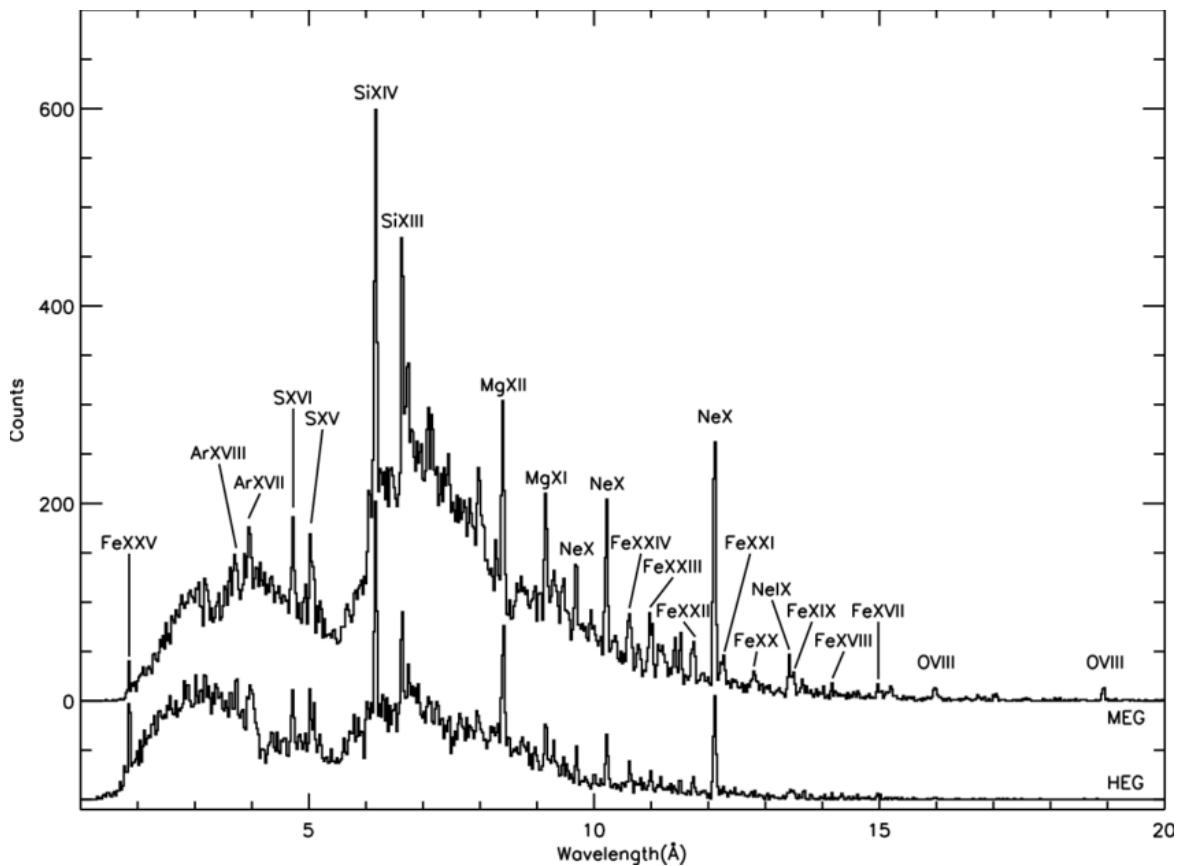


Fig. 1.13 The rich X-ray line spectrum of the Wolf-Rayet binary star WR140, taken with the HETG instrument (MEG grating data on top, HEG grating data on the bottom) onboard *Chandra*. This figure is taken from Pollock et al. [309].

### 1.4.1 Spectral modelling

X-ray instruments collect data in the form of photon counts registered in different energy channels (the exact mechanism differs between individual instruments). The channels are converted into an energy scale using the redistribution matrix of the instrument. The photon counts per channel can be converted into a flux at each energy channel using the knowledge of the energy-dependent effective collecting area of the instrument. This requires a complex and accurate instrument and mirror calibration.

The desired dataset is extracted from a certain source region (a subset of the full dataset) and is usually composed of the source flux and the background flux. The background flux can be physical (other X-ray sources in the source extraction region) but it can also be instrumental. It can be subtracted from the source+background dataset by choosing a background region and subtracting the background region photon counts (scaled by the ratio of the source and background areas) from the source region photon counts. One therefore obtains a background-subtracted source spectrum.

The spectrum is then analysed and fitted to theoretical models with a spectral fitting package. In this thesis, I employ the SPEX fitting package [177]. Alternative fitting packages are available, e.g. XSPEC [7] and ISIS [157].

It is important to choose appropriate fitting statistics to minimize during the fitting procedure. In case the source data have Gaussian uncertainties, which is usually the case if the number of photon counts per energy bin/channel are large ( $>25$ ),  $\chi^2$  statistics are appropriate. This usually holds for bright sources and observations with low-resolution instruments such as CCDs. If the source data have low photon counts per energy channel, the errors are likely Poissonian, and Cash statistics [C-stat, 47] must be applied. This is usually the necessary treatment of high-spectral resolution data and is often applied in this thesis. Cash statistics are still appropriate even in the high count limit.

### 1.4.2 X-ray spectra of accreting objects and commonly used spectral continuum models

Spectral models can be broadly split into two categories: continuum (or additive) models and multiplicative models. Continuum models are additive and correspond to independent components in the spectra of sources, such as thermal blackbody emission or powerlaw-like inverse Compton emission. Multiplicative models modify continuum models according to specific laws which may include atomic lines, e.g. absorption

models, which reduce the transmitted continuum X-ray flux at certain energies by a multiplicative factor.

### Active galactic nuclei

The bulk of the accretion disc emission falls outside the X-ray band as the temperatures in the inner accretion disc are of the order of  $\sim 10$  eV and so the AGN discs emit most prominently in the extreme UV (EUV) band (0.01 – 0.1 keV). It is normally impossible to observe this band as all of the radiation is absorbed by Galactic neutral hydrogen along the line of sight towards the sources, and hence it is challenging to estimate the true bolometric luminosities of AGN. The exception are a few AGN with lower black hole masses of  $\sim 10^6 M_{\odot}$  [325, 81], where the emission from the inner edge of the accretion disc likely peeks into the very soft X-ray band (0.3 – 0.5 keV).

The strongest X-ray spectral component of AGN is the emission from a hot corona of electrons which has approximately powerlaw shape (in the 0.3 – 10 keV band), with a slope between 1.5 – 2.5 depending on the AGN [302]. The emission originates in Compton up-scattering of disc photons by energetic electrons in the corona. The temperature of the corona introduces an exponential high-energy roll-over of the powerlaw emission, but the energy of the roll-over can be of the order of 100 keV so the only instrument capable of observing this effect is *NuSTAR* [99]. This emission is therefore often described with a simple POWERLAW model if using just the 0.3 – 10 keV energy band. Given its temperature and high variability, the corona is likely very close to the black hole [within  $10 R_G$ , 52, 99].

The second component originates in the ionised reflection of coronal emission off the accretion disc [132, 386, 339]. The most prominent features of this component are the iron K line at 6.4 – 7.0 keV (depending on the ionisation of the reflecting material) which is usually blurred by the fast motion in the inner accretion flow and affected by gravitational redshift [209, 208, 251, 274], the Compton hump at 20 – 30 keV and the edge at 7.1 keV. A schematic reflection spectrum showing these components is shown in Fig. 1.14.

The shape of the X-ray reflection spectrum is an important diagnostic of the properties of the inner accretion flow [101]. Amongst the properties which can be inferred from the X-ray reflection and particularly from the shape of the iron K line is the inner accretion disc radius. Assuming the disc is truncated at the ISCO, the spin of the black hole can be directly measured [336]. Furthermore, the reflection can be used to estimate the accretion disc inclination, the ionisation state of the inner disc as

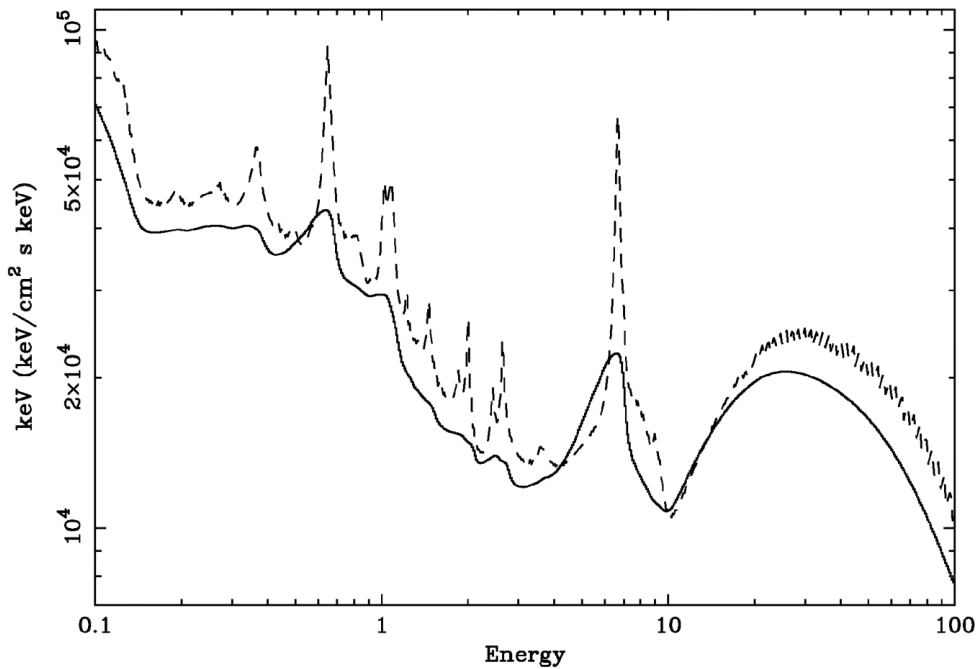


Fig. 1.14 An example X-ray reflection spectrum. Its most important components are the iron K line at  $\sim 6.4$  keV, an iron edge at 7.1 keV and a Compton hump above 10 keV. The dashed line shows the spectrum in the rest-frame. The solid line shows the same spectrum after gravitational redshift and blurring effects due to the fast motion of gas in the inner accretion flow are applied. This figure is taken from Ross and Fabian [347].

well as the elemental abundances of the accretion flow. Finally, in special cases the density of the accretion disc can be measured too [129, 168].

There are many models describing ionised and relativistic reflection, starting from simple models describing just the blurred iron K line (LAOR), through more complex models that include the reflected continuum like PEXRAV [229] and PEXMON [274], to physical models which include all of the reflected emission such as REFLIONX [347] and RELXILL [128].

Additionally, AGN often exhibit a soft X-ray component called the soft excess [8, 413, 35, 333]. It is well described by a thermal BLACKBODY model with a temperature of  $\sim 0.1$  keV [302], however its true nature is still an open question. It could originate in reflection of the coronal emission off the accretion disc [60, 419]. Alternatively, it could be produced in a warm comptonisation region with temperatures much lower than the corona itself (about 1 keV) but hotter than the accretion disc, with an optical depth of  $\sim 10$  [81, 301, 18], possibly constituting the atmosphere of the inner disc. Finally, the

soft excess shape could be explained as a spectral artefact if the AGN is absorbed by a partial covering absorber [401].

The AGN emission is often absorbed by neutral and ionised absorbers (for more details see the subsection on ionised wind modelling) in the line of sight towards the AGN. Neutral absorption is particularly important in Type 2 AGN, where a dusty torus obscures our direct view of the inner accretion flow. All of the AGN analysed in this thesis are Type 1 hence I do not focus on neutral absorption with the exception of Galactic neutral absorption [430, 179].

### **Black hole X-ray binaries**

The X-ray spectra of sub-Eddington X-ray binaries show similarities with AGN spectra. They also exhibit a powerlaw-like coronal emission with properties resembling the AGN (particularly in the hard state). They also show ionised reflection not unlike that observed in AGN [101]. However, the density of their discs is expected to be significantly higher which likely has important consequences for the spectral modelling of ionised reflection [129, 396, 168].

The accretion disc of X-ray binaries is much hotter than in AGN and it is especially dominant in the soft state (and is much brighter than the coronal emission in the soft state), with temperatures of about 1 keV [139, 54]. It is usually described with a multi-colour blackbody model like DBB, or with a physical model such as KERRBB [219]. In the hard state, the disc emission is much weaker than the coronal emission and with a lower temperature ( $<1$  keV) perhaps owing to disk truncation.

### **Neutron star X-ray binaries**

Sub-Eddington neutron star X-ray binary spectra differ strongly based on the strength of their surface fields.

Weakly magnetised neutron stars such as the Z sources in the soft state show X-ray spectra dominated by thermal blackbody emission from their strongly heated surfaces with temperatures of  $\sim 3$  keV [266], as well as strong multicolour thermal emission from the accretion discs ( $T \sim 1 - 2$  keV) extending down to small radii (in  $R_G$ ). They can also show relativistic reflection [42].

Strongly magnetised neutron stars, the X-ray pulsars, do not show any disc thermal emission in the X-ray band as their discs are highly truncated and thus emit mainly in the EUV band. The most important component is the emission from the accretion column which reprocesses thermal photons from the neutron star surface [64] and creates a comptonisation spectrum, with a high energy roll-over usually observed at

30-60 keV [272, 27]. Additionally, the accretion column component pulsates in time as the neutron star rotates. There is often a second, soft X-ray component, well fitted with a  $\sim 0.1$  keV BLACKBODY model but which does not originate in thermal disc emission as it is also pulsed [151].

### Ultraluminous X-ray sources

The 0.3 – 10 keV spectra of ULXs can usually be described with two BLACKBODY or DISCBLACKBODY components [345, 374, 343]. The softer of the two components, with a temperature of  $\sim 0.2$  keV likely originates in the outer, sub-Eddington part of the accretion disc, or in an optically thick outflow. The hotter of the two components, with a temperature around 1 – 2 keV is usually associated with the inner, super-Eddington part of the accretion disc and is well fitted with a simple BLACKBODY or a broadened blackbody (MBB, a blackbody modified by coherent Compton scattering). The two components appear with different ratios of fluxes, separating ULXs into three main classes: soft ultraluminous, hard ultraluminous, and broadened disc ULXs [380]. Finally, a third continuum, powerlaw-like (i.e. well fitted with a POWERLAW model) component appears to be universally present in ULXs [416]. It dominates above 10 keV, and could be associated with an accretion column in case of a neutron star accretor [415], or with a corona-like structure in the case of a black hole accretor [421]. Fig. 1.15 contains a simple schematic of a ULX system.

### 1.4.3 Ionised plasma modelling

If a beam of X-ray radiation is passed through a slab of ionised plasma, the slab will absorb part of the original radiation at specific elemental transition energies depending on its ionisation state or temperature, and on average scatter it into directions other than the initial beam direction. If we are observing along the beam direction, we observe absorption lines imprinted on the continuum spectrum. If we are looking from another direction, we observe emission lines of radiation scattered from the original beam. In reality, if we are observing the X-ray radiation from an accreting system, passing through an ionised outflow, the resulting spectrum will be a superposition of both of the above situations.

The absorption and emission lines produced in the ionised outflow are calculated theoretically by simulating a slab of photo-ionized plasma, where all ionic line column densities are linked through a photo-ionisation model. An ionisation balance for each element is calculated based on the properties of the slab of plasma, and in turn the

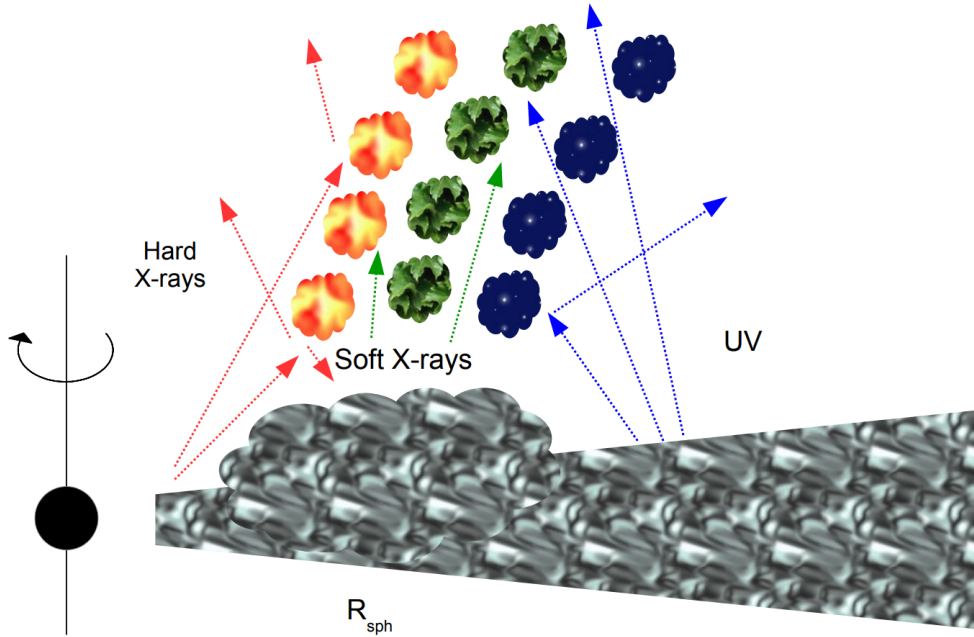


Fig. 1.15 A schematic sketch of a ULX system (with a black hole accretor). The hardest X-rays are produced in the innermost regions of the accretion system by either a Comptonised corona (in the case of a black hole accretor) or by an accretion column (in the case of a magnetised neutron star accretor). The supercritical, geometrically thick part of the disc produces the higher temperature blackbody component with temperatures around 1 keV. Finally, the soft blackbody component ( $T \sim 0.1 - 0.2$  keV) originates either in the outer (subcritical) accretion disc or in an optically thick part of the radiation-driven outflow. This figure is taken from Pinto et al. [305].

column densities in each relevant line are calculated. The main property of the plasma is its ionisation parameter  $\xi$  [205], defined as:

$$\xi = \frac{L}{nr^2} \quad (1.10)$$

where  $L$  is the ionising (typically 13.6 eV to 13.6 keV) luminosity,  $n$  is the density of the material and  $r$  is the distance from the ionising source.  $\xi$  defines how strongly the plasma is ionised, indicating the number of photo-ionising photons per particle or the photo-ionising flux density. Another important property is the shape of the ionising spectrum, i.e. its Spectral Energy Distribution (SED), which modifies the ionisation balance. Other relevant parameters are the column density, defining the depth of absorption/emission features, the turbulent width, defining the line widths and the elemental abundances, which modify the relative strengths of different elements

with respect to each other. Finally, the ionised absorber can be in motion relative to the observer and the radiation source, so the absorption model can be blueshifted or redshifted accordingly.

There are multiple spectral models which can reproduce ionised absorption. The most widely used model is `XSTAR` in `XSPEC` which uses pre-calculated ionisation tables. In this thesis I choose to apply the `XABS` and `PION` models within `SPEX`, which calculate the ionisation states and absorption line strengths within the fitting package and do not require any preparation before dataset fitting.

`XABS` and `PION` are similar spectral models with one major distinction. `XABS` assumes a fixed SED, based on the broadband spectrum of the AGN NGC 5548 [373, 372] and is thus more appropriate for AGN than for ULXs and X-ray binaries. `XABS` can also only reproduce absorption lines from an ionised plasma. `PION` [256, 240], on the other hand, does not assume a specific SED but instead takes the real SED of the currently loaded continuum spectral model to instantly calculate the ionisation balance and the line strengths of all ions. It can reproduce both absorption and emission lines. This means that `PION` is more accurate than `XABS`, however at a much higher computational cost as the SED, the ionisation balance and the ionic level population are recalculated during each step of the fitting. In this thesis, I apply both spectral models, choosing whichever is more applicable in the current scientific scenario depending on the requirements (computation speed versus accuracy).

## 1.5 This thesis

Outflows have been known to exist in accreting systems for decades, however many questions about their physics, launching mechanisms and their impact on the accretors and their surroundings are still unanswered. In this thesis I employ X-ray spectroscopy, particularly using the high-resolution instrument RGS onboard *XMM-Newton* to detect and study disc winds in different types of accretors.

The first goal of my PhD project was to study and understand what happens to objects accreting close to or in excess of the Eddington limit: how much matter and energy (if any) they lose into the wind and how this depends on their physical properties including masses and accretion rates. The second goal was to study whether such winds explain some other observables e.g. the properties of ULX nebulae, the AGN-bulge relationship and the fast growth of supermassive black holes in the early Universe.

In the first two research chapters I study ULXs which are known to accrete at super-Eddington rates and have been shown to launch powerful radiation-driven outflows. Understanding these winds can make a helpful comparison with winds in other objects such as AGN where the outflows could also be radiation-driven. The conditions of ULXs could also be relevant to the accretion of massive black holes in the early Universe, when the accretion fuel was much more abundant.

Secondly, in chapters 5 and 6 I study two NLS1 AGN, supermassive black holes likely accreting around or just above the Eddington limit and their powerful ultra-fast outflows. I particularly focus on the possibility that these outflows are multi-phase, which can be levered to understand their energetics and launching mechanisms. Furthermore, in chapter 5, I analyse multiple X-ray observations of the AGN to show that its disc wind properties must be time variable. In chapter 6 I make use of the multi-wavelength observations of the object to study the wind phases across a broad range of ionisation states.

Thirdly, in chapter 7 I study the physics of accretion in Hercules X-1, a unique neutron star X-ray binary which is known to possess a warped, precessing accretion disc. The warped disc precession can be used to study the 3D structure and the energetics of the accretion disc wind in this system, to understand wind physics in X-ray binaries.

Finally, in chapter 8 I conclude and outline potential avenues for further research in this field. I also describe the upcoming X-ray missions which can achieve future breakthroughs in the field of accretion disc winds.

In this thesis, I study accretion disc winds in very different physical systems. The research chapters are ordered by the decreasing Eddington ratio of accretors. This way I will track the properties of accretion disc winds in accreting systems with progressively lower importance of radiation pressure. In the first two chapters I study ULXs, where the mass accretion rates strongly exceed the Eddington limit. The following two chapters focus on NLS1 AGN, likely accreting just around the Eddington limit. Finally, I study Hercules X-1, a sub-Eddington accretor with an Eddington ratio of  $0.1 - 0.2$  where radiation pressure cannot be the dominant force but could contribute to wind launching.



# Chapter 2

## Data reduction and analysis methods

This chapter introduces some of the analysis methods used throughout the thesis. First, I describe *XMM-Newton* data reduction and processing techniques. Secondly, I introduce two automated spectral scan methods which I use to search for the signatures of ionised plasma in the X-ray spectra of accreting systems.

### 2.1 *XMM-Newton* data reduction

All the publicly available *XMM-Newton* data can be found on the XSA archive<sup>1</sup>. After downloading, the datasets are processed using a standard pipeline software called SAS. The method of data reduction depends on the instrument, the data of which is being processed into science quality. The reduction procedure for RGS and EPIC detectors is explained below.

#### 2.1.1 RGS

RGS data are processed using a routine called RGSPROC. First, the intervals of high background flaring are identified. A lightcurve is created using only events from CCD 9 which is the most affected by flaring. All the time intervals exceeding a background flux threshold are filtered out. Following the standard guidelines, the threshold is usually taken to be 0.15 or 0.25 cts/s.

Afterwards, the source and background regions are chosen. Since RGS is a dispersive grating, the source region is usually a rectangle along the dispersion direction centred

---

<sup>1</sup>[nxsas.esac.esa.int/nxsas-web/](http://nxsas.esac.esa.int/nxsas-web/)

on the satellite pointing. However, the region can be adjusted if necessary. The background regions are usually two rectangles along the dispersion direction of the grating, but shifted in the cross-dispersion direction, towards the edges of the RGS detectors, thus avoiding the source PSF. If the default background regions are partly contaminated, custom regions can be selected. Alternatively, a background template can be used if both background regions are completely unusable.

Finally, the source and background spectra can be extracted from the selected regions. The second order spectra have twice the spectral resolution of the first order but also have a much smaller effective area, and so they are rarely used in analysis. The RGS 1 and RGS 2 data can be stacked with the `RGSCOMBINE` routine, but this is not recommended for other than plotting purposes.

If the fitting will be done with the `SPEX` fitting package, the spectra must be converted from the `OGIP` format to `SPEX` format using the `TRAFO` tool<sup>2</sup>. The raw spectra heavily oversample the instrument resolution. This can be solved by binning the spectrum by a factor of 3 directly in `SPEX`, resulting in a reasonable oversampling of the spectral resolution by roughly a factor of 3. The effective wavelength range of RGS is between 7 and 37 Å. However, in practice the usable range heavily depends on the background flux. Especially the upper end of the wavelength range is often heavily affected by the background and so the data are not useful above a much lower threshold wavelength (e.g. 20 – 25 Å).

### 2.1.2 EPIC

The EPIC data reduction depends on the detector and the mode used. First, pn data are pre-processed using the `EPPROC` routine and MOS data are pre-processed using the `EMPROC` routine. Secondly, background lightcurves are created for each of the detectors using only 10 – 12 keV (for pn) and > 10 keV (for MOS) events to identify flaring intervals. The standard flaring thresholds are around 0.5 ct/s for pn and 0.25 ct/s for MOS. Intervals of time exceeding these thresholds are filtered out.

Afterwards, the images of the pn and MOS exposures are created for source and background region selection. In imaging modes, the source regions are usually circles with a radius of 30 – 40 arcsec which capture most of the PSF. The high energy signal to noise ratio can be enhanced by using a smaller region size (e.g. 20 arcsec) which decreases the importance of background subtraction (background is usually stronger in the high energy band). The background regions are usually chosen to be as large as

---

<sup>2</sup>[xmm2.esac.esa.int/docs/documents/CAL-TN-0083.pdf](http://xmm2.esac.esa.int/docs/documents/CAL-TN-0083.pdf)

possible, while avoiding the source PSF and other X-ray point sources. They should also be located on the same chip as the source region, avoid chip gaps, out-of-time events in the pn exposure<sup>3</sup> as well as the ‘copper ring’ on the pn chip<sup>4</sup>.

In EPIC pn Timing mode, only 1D spatial information of the incoming photons is preserved. The source region is thus a rectangle centred on the source position. The background region is usually a small rectangle as far away from the source as possible. However, the source PSF covers the whole chip and hence can contaminate the background region. Therefore the background subtraction must be treated cautiously.

Finally, the spectra can be extracted. Following the standard guidelines, only events of PATTERN $\leq$ 4 (single/double) are usually accepted for pn data, and events of PATTERN $\leq$ 12 (single-quadruple) are accepted in MOS datasets<sup>5</sup>.

Following the data preparation, the spectra can be converted from the OGIP format to SPEX format using the TRAFO tool. The raw EPIC spectra are heavily oversampled. The SPECGROUP routine can be used to bin the spectra to at least 25 counts per bin to achieve Gaussian statistics, and simultaneously to oversample the spectral resolution by a factor of 3 at maximum. The EPICSPECCOMBINE routine can be used to stack the EPIC spectra if required.

The useful spectral range of EPIC detectors is between 0.3 and 10 keV. Sometimes this range has to be slightly adjusted, e.g. in Timing mode it is not recommended to use data below 0.5 keV. It is also known that the pn Timing mode calibration is imperfect around the Au edge at 2.3 keV [308].

## 2.2 Spectral search methods

### 2.2.1 Gaussian line search

A Gaussian line search can be performed to find any spectral lines, both absorption and emission, that ionised plasma (either at rest or moving) might have imprinted on the X-ray continuum of the source. This process can be fully scripted and ran in an automated fashion.

The search is composed of individual steps. Each step follows the same pattern. First, the best-fitting continuum spectral model of the object is taken. Then another component, a single Gaussian line located at a certain energy, with a predefined line width is added. Both the line energy and its width are fixed to ensure a simple C-stat

---

<sup>3</sup>[xmm-tools.cosmos.esa.int/external/xmm\\_user\\_support/documentation/uhb/epicot.html](http://xmm-tools.cosmos.esa.int/external/xmm_user_support/documentation/uhb/epicot.html)

<sup>4</sup>[xmm-tools.cosmos.esa.int/external/xmm\\_user\\_support/documentation/uhb/epicintbkgd.html](http://xmm-tools.cosmos.esa.int/external/xmm_user_support/documentation/uhb/epicintbkgd.html)

<sup>5</sup>[xmm-tools.cosmos.esa.int/external/xmm\\_user\\_support/documentation/uhb/epic\\_evgrades.html](http://xmm-tools.cosmos.esa.int/external/xmm_user_support/documentation/uhb/epic_evgrades.html)

parameter space. The original continuum is kept frozen except in the case of high quality datasets, where it is possible to free its overall normalisation without running into unconstrained fits in SPEX. Then the normalisation of the added Gaussian line is fitted. The best-fitting normalisation can be both positive or negative, to reproduce an emission and absorption line, respectively. The width of the line is calculated based on a grid of velocity dispersions of the gas to be described.

After the fit, the  $1\sigma$  error on the normalisation of the line is calculated and saved as well as the  $\Delta C$ -stat improvement of the fit compared to original C-stat value. The approximate significance of the line in  $\sigma$  can be calculated as a ratio of the line normalization to the average of its  $1\sigma$  errors (upper and lower). Alternatively, the  $\Delta C$ -stat value is a good guideline as to whether the detection is significant. This is a fit for 1 additional free parameter (the line normalisation) compared with the original continuum fit, hence an improvement of  $\Delta C$ -stat=9 would give a significance of  $3\sigma$ . These approaches are however only approximate because they ignore the large amount of trials performed to find features across the whole energy grid (the look-elsewhere effect) and so they overestimate the real significance.

Afterwards, the search proceeds as described above step-by-step for a grid of line energies spanning the desired energy range. The grid ideally slightly oversamples the energy resolution of the instrument. In the case of RGS, I choose steps of  $0.01\text{\AA}$ , which works out to about 2000 steps across the 7 to  $26\text{\AA}$  wavelength range. This still makes the Gaussian scan computationally reasonable (each search does not take more than a few hours). The search can be repeated for different line widths/turbulent velocities. Typically, I search for lines with 3 different velocity dispersions (line widths) simulating different physical scenarios: 500 km/s, 1000 km/s and 5000 km/s. In the end I obtain a table of  $\Delta C$ -stat values, normalisations and significances of Gaussian lines for the whole energy band.

It should be kept in mind that the  $\Delta C$ -stat values only give approximate  $\sigma$  significances because they do not take into account the "look-elsewhere" effect. Only Monte Carlo simulations can give a rigorous answer about the actual significance of a line. For each simulation a fake spectrum is simulated with the same response matrix and using the template model of the continuum as the original spectrum. The simulation should in principle produce a spectrum which is identical to the real data but only contains Poisson noise around the continuum spectral model. Then an identical line search is performed as done for the original data.

The simulation is repeated as many times as desired, and I count the number of occurrences of lines in simulated data at the same or higher significance as the  $\Delta C$ -stat

of the line found in real data. The real significance (probability) of a line found in the original data is then the ratio of simulations that do not find a line with the same or higher  $\Delta C$ -stat value to all performed simulations. For a  $3\sigma$  search (99.7 % probability), the need arises to perform well over 1000 simulations. Computational time necessary for the task therefore can be of the order of 1000 hours or even more.

### 2.2.2 Physically motivated model search

If the residuals found in an X-ray spectrum originate in plasma which is not at rest, their identification can be challenging. In principle, the plasma could have any physical properties (Doppler shift, temperature, ionisation/temperature, turbulent velocity) resulting in a large possible parameter space. A physically motivated spectral model search can be performed to find the best-fitting solution to the data as well as the statistical significance of any detection. Effectively, it is a routine to scan a large parameter space of a plasma absorption or emission grid, to locate the best-fitting ionised absorber/emitter properties.

The ionised plasma model is always added to the best-fitting broadband continuum spectral model of the object, similarly as done during a Gaussian spectral scan. Depending on the properties of the plasma, different models can be used to describe its spectral features. If it produces emission lines, an additive spectral model can describe its features. One example of such models is the collisional ionisation equilibrium model CIE [176] in SPEX which can describe the emission from a shocked (collisionally ionised) plasma, as found e.g. in jets and in the intracluster medium.

Alternatively, if the plasma is located along our line of sight towards the X-ray source, it can imprint absorption features on the X-ray spectrum of the source object. In this case a multiplicative plasma model can be applied to the baseline continuum. If the plasma is in photoionisation equilibrium, as expected for example for an ionised disc wind, its spectral features can be described by a photoionisation grid such as XABS [373, 372] or PION [256, 240] in SPEX.

Below, the physical model search is illustrated on an example scan with the XABS photoionisation model, which was performed on the X-ray spectrum of the NLS1 PG 1448+273 in chapter 5 of this thesis.

The main parameters of the XABS model are the column density  $N_{\text{H}}$ , ionisation parameter  $\log \xi$ , systematic velocity  $z$  and turbulent velocity (or simply velocity broadening)  $v_{\text{turb}}$  of the ionised absorber. An ionised outflow in the X-ray spectrum of an object can in principle have any blueshift, ionisation parameter, column density and turbulent velocity. This large parameter range has to be searched in an automated way

to avoid missing the parameter space with the best-fitting solution. As an added bonus, performing a systematic search in this way will allow us to constrain the statistical significance of any outflow detection in the X-ray spectrum.

First, we create a grid of photoionisation models which spans a large space of ionisation parameters, between  $\log(\xi/\text{erg cm s}^{-1}) = -1.0$  and  $\log(\xi/\text{erg cm s}^{-1}) = 4.8$  with a grid spacing of  $\Delta \log \xi = 0.2$  [in line with the recommendation of 337], with three fixed turbulent velocities of  $v_{\text{turb}} = 100 \text{ km/s}$ ,  $v_{\text{turb}} = 1000 \text{ km/s}$  and  $v_{\text{turb}} = 10000 \text{ km/s}$ . The turbulent velocity space grid is chosen to be coarse to decrease the computational cost of the automated search. The abundances of all elements are fixed to Solar values in the photoionisation grids.

Afterwards a range of realistic systematic absorber velocities (blueshifts) is chosen. We choose to search for an absorber with a systematic velocity between  $+20000 \text{ km/s}$  (to account for possible infalling gas) and  $-100000 \text{ km/s}$  (blueshift of roughly  $0.4c$ , after relativistic correction). The step size is  $150 \text{ km/s}$  for turbulent broadening of  $100 \text{ km/s}$  and  $300 \text{ km/s}$  for turbulent broadening of  $1000 \text{ km/s}$ . This is chosen so that in each case the step size is not much larger than the broadening and at the same time is not much larger than the spectral resolution of our detectors, RGS being the best of our instruments with a spectral resolution of roughly  $\sim 300 \text{ km/s}$  in velocity units. In the case of turbulent velocity equal to  $10000 \text{ km/s}$ , the features are so broad that such detailed sampling is not necessary, instead we sample by  $1000 \text{ km/s}$ .

We generate an absorption grid for every possible systematic velocity, ionisation parameter and broadening within the selected range, add this model to the baseline source continuum, and fit for the column density of the absorber (with the remaining absorber parameters fixed), leaving the continuum parameters free to vary. If an absorber of such parameters is disfavoured by the data, the resulting column density will be 0, i.e. the best-fitting solution is the null (baseline continuum) model. Otherwise we recover the best-fitting absorber column density as well as the  $\Delta C$ -stat fit improvement obtained by adding the photoionisation grid to the (null) baseline continuum model. Any improvement in the  $\Delta C$ -stat fit statistics compared to the null model is recorded for every point in the multi-dimensional search grid.

The  $\Delta C$ -stat value determines how strongly the spectral model including the wind absorption is preferred to the baseline continuum model. However, due to the look-elsewhere effect, since we are searching through a large parameter space, it is not trivial to assign directly a ‘wind detection significance’ to a specific value of  $\Delta C$ -stat [323]. Monte Carlo simulations must be employed to rigorously ‘map’ the C-stat fit improvement to a specific false alarm probability for each wind detection. However,

such simulations, especially for non-trivial baseline continuum models, can be very expensive if performed over the full parameter space.

The formal statistical significance of any detection needs to be estimated by running simulations tailored to match the particular search performed. A fake continuum spectrum is simulated using the real source continuum model (accounting for uncertainties in continuum parameters when simulating the spectrum). Afterwards, the same automated search is performed on the simulated data and the number of wind detections stronger than the one found in real data is counted. The real significance (probability) of the detection found in the original data is the ratio of simulations that do not find a detection with the same or higher  $\Delta C$ -stat value to all performed simulations.

As it is very computationally expensive to run 1000s of physical model searches on simulated datasets, some simplifications can be made to the simulated searches which make them cheaper to run. These are described in chapters 4 and 5.



## Chapter 3

Searching for outflows in  
ultraluminous X-ray sources  
through high-resolution X-ray  
spectroscopy



# Abstract

Ultraluminous X-ray sources are non-nuclear point sources exceeding the Eddington luminosity of a 10 Solar mass black hole. The modern consensus for a majority of the ULX population is that they are powered by stellar-mass black holes or neutron stars accreting well above the Eddington limit. Theoretical models of super-Eddington accretion predict existence of powerful outflows of moderately ionised gas at mildly relativistic velocities. So far, these winds have been found in 3 systems: NGC 1313 X-1, NGC 5408 X-1, NGC 55 ULX. In this work, we create a sample of all ULXs with usable archival high resolution X-ray data, with 10 sources in total, in which we aim to find more signatures of outflows. We perform Gaussian line scans to find any narrow spectral signatures, and physical wind model scans where possible. We tentatively identify an outflow in NGC 5204 X-1, blueshifted to  $0.34c$ , which produces emission features with a total significance of at least  $3\sigma$ . Next we compare ULXs with similar hardness ratios. Holmberg IX X-1 shows absorption features which could be associated with a photoionised outflowing absorber, similar to that seen in NGC 1313 X-1. The spectrum of Holmberg II X-1 possesses features similar to NGC 5408 X-1 and NGC 6946 X-1 shows O VIII rest-frame emission. All other sources from the sample also show tentative evidence of spectral features in their high resolution spectra. Further observations with the *XMM-Newton* and *Chandra* gratings will place stronger constraints. Future missions like *XRISM* and *ATHENA* will be able to detect them at larger distances and increase our sample.

## 3.1 Introduction

The true nature of the compact objects powering ULXs has been disputed for decades. Two explanations are most plausible. ULXs could either be intermediate mass black holes ( $\sim 10^3 - 10^4 M_\odot$ ) accreting at sub-Eddington rates, or super-Eddington accretors of smaller mass. The first explanation might as well be the case for the more luminous objects at or above  $\sim 10^{41}$  erg/s [107, 423]. However, the modern consensus for a

majority of the ULX population seems to prefer the second hypothesis [189, 248, 380, 13, 247]. In addition 3 of the ULXs were recently identified as neutron stars with extremely high accretion rates [12, 125, 164]. At luminosities of several times  $10^{40}$  erg/s, they surpass the Eddington luminosity by a factor of more than hundred (not taking possible geometric beaming into account).

Physical models of super-Eddington accretion (up to  $\sim 100$  times the critical mass accretion rate) imply a geometrically and optically thick disc around the central accretor [363, 318, 116]. Theoretical simulations are also consistent with this concept [385, 276]. The main prediction of these models are massive radiatively driven outflows of ionised gas launched from regions close to the accretor, at mildly relativistic velocities. At high inclination angles from the rotation axis of the system, these outflows gradually become optically thick [the opacity also depends on the mass accretion rate of the source, see 247]. At a low angle from the rotation axis, the outflow is optically thin, effectively forming an evacuated funnel. For a current idea of structure of the system, see Fig. 1.15. This means that the spectral hardness of a source could be directly related to the viewing angle under which it is being observed. At low inclination angles, the observer looks right into the evacuated funnel and sees the innermost parts of the thick accretion disc, which are thought to produce the hardest X-ray radiation. At higher angles, these regions are partially obscured by the disc itself and the outflowing wind. At very high inclination angles, only the Compton thick wind and outer parts of the accretion disc are visible, which produces a very soft X-ray spectrum - possibly an ultraluminous supersoft X-ray source (ULS) spectrum, and may resemble microquasars such as SS 433 [235] if it possesses jets. In general, it is thought that the higher the inclination angle, the softer the ULX appears [247, 111, 304].

ULX outflows are hence a major prediction of this theory, however they are much more difficult to observe in practice as it requires searching for weak absorption and emission features in X-ray spectra. This is particularly complicated by the fact that most ULXs reside in low metallicity environments which decreases the equivalent widths of X-ray lines. Additionally, even if winds are present in all ULXs, they might not be observable at all viewing angles. After the *XMM-Newton* and *Chandra* launch, strong residuals were spotted in ULX X-ray spectral fits [374, and references therein]. Middleton et al. [249] noticed these residuals appear to anti-correlate with spectral hardness, supporting the picture that they are associated with an outflow rather than reflection of a primary continuum. A confirmed detection was finally achieved in 2016 by Pinto et al. [306] thanks to the use of high resolution spectroscopy with the Reflection Grating Spectrometer onboard the *XMM-Newton* mission. As of August

2017, outflows have been discovered in 3 different ULXs, with the first two being NGC 1313 X-1 and NGC 5408 X-1, thanks to very high quality RGS data (300-700 ks each), both mildly relativistic at a speed of about  $0.2c$ . A weaker detection has been reported in NGC 55 ULX [304]. The most notable spectral features of these winds are highly blueshifted Ne X, Fe XVII, O VII and O VIII absorption lines, and low velocity emission lines of the same elements. Walton et al. [417] found evidence for a similar velocity outflow in iron K absorption.

In this work, we aim to search for similar signatures of outflows in a sample of ULXs using archival *XMM-Newton* data. This can be achieved by identifying any robust emission or absorption features in their X-ray spectra. We hope to collect as large a sample of ULXs with suitable (RGS) data and good enough statistics as possible (as of April 2017). We also try to span a range of different spectral categories of ULXs: soft ultraluminous, hard ultraluminous and broadened disc [380].

The structure of the chapter is as follows. In sections 2 and 3 we describe our data reduction techniques and methods for outflow detection, respectively. Section 4 contains the results of the in-depth search for emission and absorption features in ULX RGS spectra. Section 5 discusses the validity and implications of our results. We summarize the work done in section 6.

## 3.2 Observations and data reduction

All observations in this work were carried out by the *XMM-Newton* [166] satellite. We use data from both the EPIC PN [378] and the RGS detectors [72]. We select all objects with suitable and public RGS data that do not yet have a reported detection of an outflow. Suitable RGS data means the object is correctly aligned with an appropriate roll angle and not offset by more than 2 arcmin from the optical axis of the spectrometer. The source also needs to have enough counts (at least  $\sim 1000$  in total) and a high enough count rate (above  $\sim 0.1$  count/s with PN in the 0.3-10 keV band) to be able to detect any spectral features. In the end, our sample consists of 8 ULXs with different spectral properties: Holmberg IX X-1, Holmberg II X-1, NGC 1313 X-2, NGC 4190 ULX1, NGC 5204 X-1, NGC 5643 X-1, NGC 6946 X-1 and M33 X-8. We also study NGC 4631 ULX1 but given its brightness, detection of any spectral features does not seem feasible. IC 342 X-1 is bright enough for the analysis but its RGS data are contaminated by another X-ray source in the source region.

All objects studied in this analysis are listed with their properties such as the distance and coordinates in Table 3.1. We obtain the source distances by averaging

Table 3.1 Coordinates, distance and hardness ratio of ULXs used in this work.

Object name	RA			Dec			Distance Mpc	Hardness ratio <sup>1</sup>
	hh	mm	ss	dd	mm	ss		
NGC 5643 X-1	14	32	42	-44	09	36	16.9	0.639
Holmberg IX X-1	09	57	53	+69	03	48	3.7	0.603
NGC 4190 ULX1	12	13	45	+36	37	55	2.9	0.569
M33 X-8	01	33	51	+30	39	36	0.85	0.532
NGC 4631 ULX1	09	57	53	+69	03	48	7.4	0.521
NGC 1313 X-2	03	18	22	-66	36	04	4.3	0.509
IC 342 X-1	03	45	56	+68	04	55	3.3	0.500
NGC 5204 X-1	13	29	39	+58	25	06	5.6	0.403
Holmberg II X-1	08	19	29	+70	42	19	3.3	0.242
NGC 6946 X-1	20	35	01	+60	11	31	5.6	0.237

<sup>1</sup>The average (absorption-corrected) hardness ratio for each source, defined as  $H/(H+S)$  where H is the X-ray flux in 2-10 keV band and S is the X-ray flux in 0.3-2 keV band.

newer measurements shown in the NED database. It should be kept in mind that due to low distances of ULXs, the assumption of exact distances does not actually affect the following analysis. Absolute luminosity measurements would be affected, but they are not used in this work. The coordinates and source names are obtained from SIMBAD. We calculate an average hardness ratio for each source. We fit the broadband PN spectrum with the standard continuum model (as described in Sect. 3.3.1) and calculate the X-ray flux between 0.3-2 keV (S) and 2-10 keV (H). The hardness ratio is then defined as  $H/(H+S)$ . Finally we use all individual observations of a source to calculate an average hardness ratio. This way the ratio takes into account different neutral obscuration levels for each source.

The observational info such as exposures and Obs IDs are shown in Table 3.2. For some of the objects in our sample, more *XMM-Newton* data are available but they are unsuitable for RGS analysis due to a low S/N ratio or a bad roll angle.

All the data were downloaded from the XSA archive and reduced with a standard pipeline using SAS v15.0, CalDB as of April 2017. We follow the data reduction pipelines for RGS and PN data described in section 2.1. The source regions for PN were selected as circles centred on the ULX with a radius of 30 arcsec. The background regions were circles located in the same region of the chip, avoiding the copper ring, chip gaps and out of time events from the source. We used the default selection of source and background regions in RGS where possible. In several cases we had to do custom background selection for the RGS data through RGS masks, for example in NGC 5643 X-1 due to contamination of default background regions by other sources.

Table 3.2 Log of the observations used in this work.

Object name	Number of exposures	Total duration <sup>1</sup> ks	Observations used Obs ID
NGC 5643 X-1	1	108	0744050101
Holmberg IX X-1	9	159	0112521001 0112521101 0200980101 0693850801 0693850901 0693851001 0693851101 0693851701 0693851801
NGC 4190 ULX1	3	43.3	0654650101 0654650201 0654650301
M33 X-8	2	20.5	0102640101 0141980801
NGC 4631 ULX1	1	44	0110900201
NGC 1313 X-2	2	102.5	0764770101 0764770401
IC 342 X-1	2	87.5	0693850601 0693851301
NGC 5204 X-1	9	162.1	0142770101 0142770301 0150650301 0405690101 0405690201 0405690501 0693850701 0693851401 0741960101
Holmberg II X-1	2	99.5	0200470101 0561580401
NGC 6946 X-1	1	109.9	0691570101

<sup>1</sup>Total clean RGS exposure (per detector) of all pointings used in this analysis, after subtracting solar flaring periods.

PN data were grouped by a minimum of 25 counts per bin and RGS data were binned by a factor of 3 directly in SPEX. All RGS observations were later stacked for plotting purposes, making sure the selection regions were identical to avoid any energy shifts. The PN observations were also stacked using the EPICSPECCOMBINE task. The spectral range used was 0.3 to 10 keV for EPIC PN (limited by the effective area and calibration uncertainties) and 7 to 26 Å (or 20 Å where necessary) for RGS data (limited by the background).

## 3.3 Methods

### 3.3.1 Continuum spectral fitting

We use SPEX [177] for spectral fitting, and Cash statistics [47] as there are not enough data points per bin in RGS data for a  $\chi^2$  analysis. After reaching the best-fitting solution, all model parameters are checked extensively with the ‘error’ function within SPEX in case there are multiple minima in the C-stat function.

We fit PN data between 0.3 and 10 keV with a  $\text{HOT}^*(\text{POW}+\text{MBB}+\text{BB})$  model where possible. HOT reproduces mostly neutral (gas temperature of about 0.5 eV) galactic ISM absorption plus any additional absorption near the source itself [see 178, for an example of similar usage of the model]. POW (standard powerlaw) and MBB (colour corrected black body) model X-ray emission from close to the compact object. BB is a standard blackbody model which represents the photosphere at larger distances from the accretor. Similar X-ray continuum models were used by Gladstone et al. [140] and Walton et al. [416].

The RGS continuum is easier to fit with a case-by-case approach. Where counts are sufficient (long observations of Holmberg II X-1 and IX X-1, and stacked data of NGC 5204 X-1), we fit RGS data with the standard model, only checking PN data for any discrepancies. For sources with less counts, we take the model from PN spectral fitting, freeze all its parameters except for the overall normalization (using parameter coupling) and fit this model to RGS data of the source. The only exception from these 2 approaches is NGC 5643 X-1, where a simple  $\text{HOT}^*\text{POW}$  spectral model provided a satisfactory fit.

### 3.3.2 Gaussian line search

We perform a Gaussian line search in SPEX to find any spectral lines, both absorption and emission, that a possible outflow might have imprinted on the X-ray continuum of the source. We use the continuum spectral model obtained following the procedure above, and follow the steps described in section 2.2.1. The wavelength step size is 0.01 Å, and use 3 different velocity dispersions (line widths) simulating different physical scenarios: 500 km/s, 1000 km/s and 5000 km/s. We perform Monte Carlo simulations for the most promising datasets to assess the significance of the detected features rigorously. The computational time necessary for simulations can be of the order of 1000 hours, so a rigorous analysis of all objects in our sample using this method is not currently feasible.

### 3.3.3 Spectral model search

In the last part of this work, we use a physical model of ionised plasma to describe a potential outflow. The first model we make use of is XABS (see section 1.4.3 for more details about the model), which reproduces absorption by photoionised gas. We follow the steps described in section 2.2.2. This search is mainly motivated by detection of an absorption line around 12.5 Å in Holmberg IX X-1 and around 15 Å in Holmberg II

X-1, a similar spectral feature to what was found in NGC 1313 X-1 and NGC 5408 X-1 [306], albeit at smaller  $\Delta\lambda$  from their rest-frame wavelengths. This could imply a smaller (or more projected out of our line of sight) outflow velocity.

To fit any potential emission features, we use a collisionally ionised emission model, CIE in SPEX. The model is similar to MEKAL in XSPEC, but with many recent updates to atomic data [particularly after the Hitomi observation of the Perseus cluster, see 152]. This model could reproduce plasma emission from a shocked region in case the ULX possesses jets, just as observed in SS433. We add a CIE component to the continuum model and fit its temperature and normalization for a specific blueshift (similarly as done during a XABS search described in section 2.2.2). To apply blueshift to the CIE component, we have to make use of the REDS model in SPEX. We also freeze the dispersion velocity of the collisionally ionised gas to a particular value, e.g. 250 or 1000 km/s. Subsequently, we vary the blueshift of the CIE component in a grid between 0c and 0.4c. We find any potential statistical fit improvements by checking the  $\Delta C$ -stat value at each step. Then we can obtain the real significance of a detection with Monte Carlo simulations.

## 3.4 Results

All the broadband PN spectra of the sources from our sample are shown in Fig. 3.1. The detailed results from the RGS Gaussian line search for each source are shown in Fig. A.1 in Appendix A. Detailed comparisons are done for sources with similar hardness ratio such as Holmberg IX X-1 versus NGC 1313 X-1, and Holmberg II X-1 versus NGC 5204 X-1 versus NGC 5408 X-1. In this section we discuss the analysis performed for each source individually.

### 3.4.1 Holmberg IX X-1

There are 9 observations of this well known ULX in total, including a very long exposure (0200980101) at 120 ks. Unfortunately, the source was caught in a lower flux state during this observation so the total count number is not as good as expected, but still much better than any other observation. Initially, we fit the broadband PN spectrum for each observation separately. The spectral shape can usually be fitted with a  $\text{HOT}^*(\text{BB}+\text{MBB}+\text{POW})$  model (see Section 3.3.1 for more information). We start by performing a full line search on all observations separately, however we find that only the 120 ks observation has good enough S/N ratio to be analysed separately.

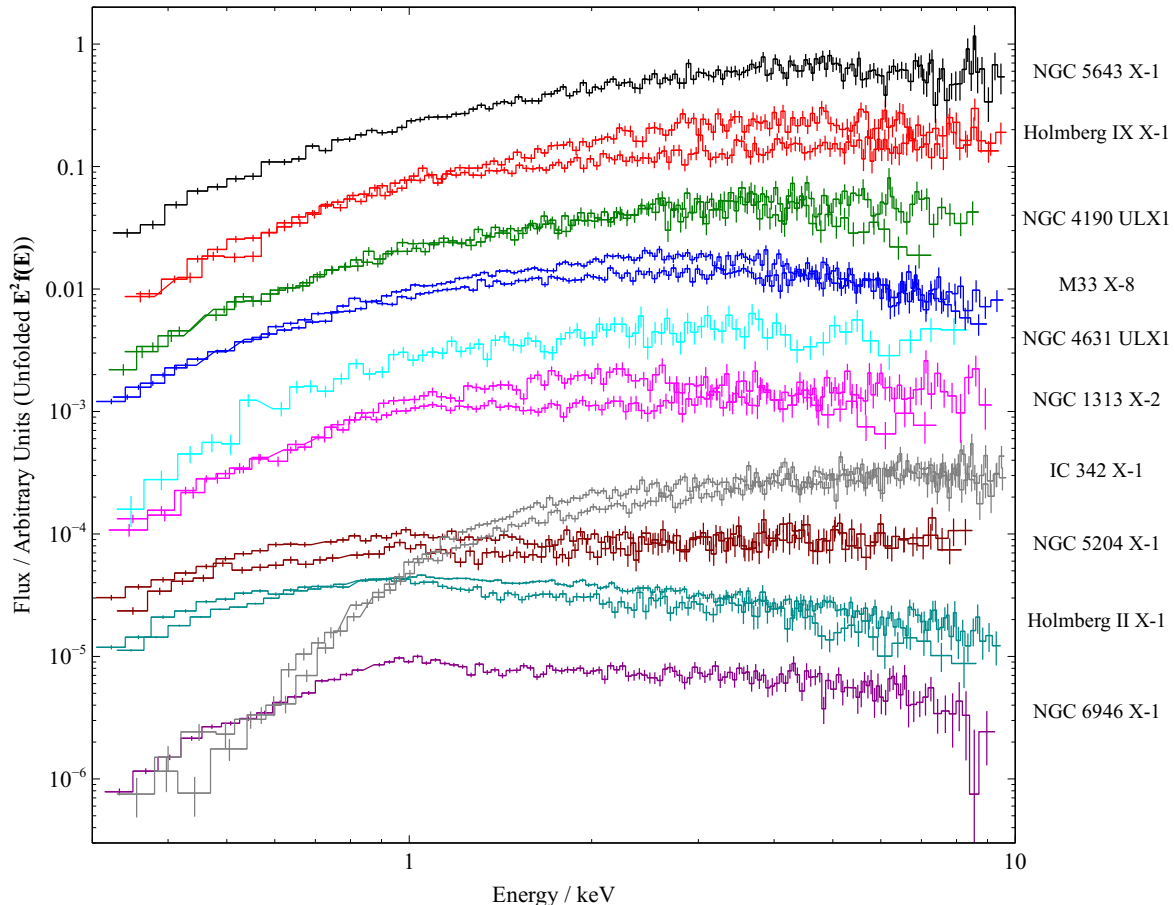


Fig. 3.1 Unfolded ( $E^2 f(E)$ ) PN spectra of ULXs used in this analysis, between 0.3 and 10.0 keV. Y axis is in arbitrary units (fluxes are rescaled for plotting purposes). Sources are ordered by increasing hardness  $H/(H+S)$ , where  $H$  is the 2.0-10.0 keV flux and  $S$  is the 0.3-2.0 keV flux, from bottom to top of the plot (see also Sect. 3.2). Different objects are plotted in different colours, and where multiple observations are available, we plot only the 2 observations with most different hardness ratios, both with the same colour. Sources plotted are: black - NGC 5643 X-1, red - Holmberg IX X-1, dark green - NGC 4190 ULX1, dark blue - M33 X-8, cyan - NGC 4631 ULX1, pink - NGC 1313 X-2, grey - IC 342 X-1, dark red - NGC 5204 X-1, dark cyan - Holmberg II X-1, purple - NGC 6946 X-1. The spectra are not corrected for absorption.

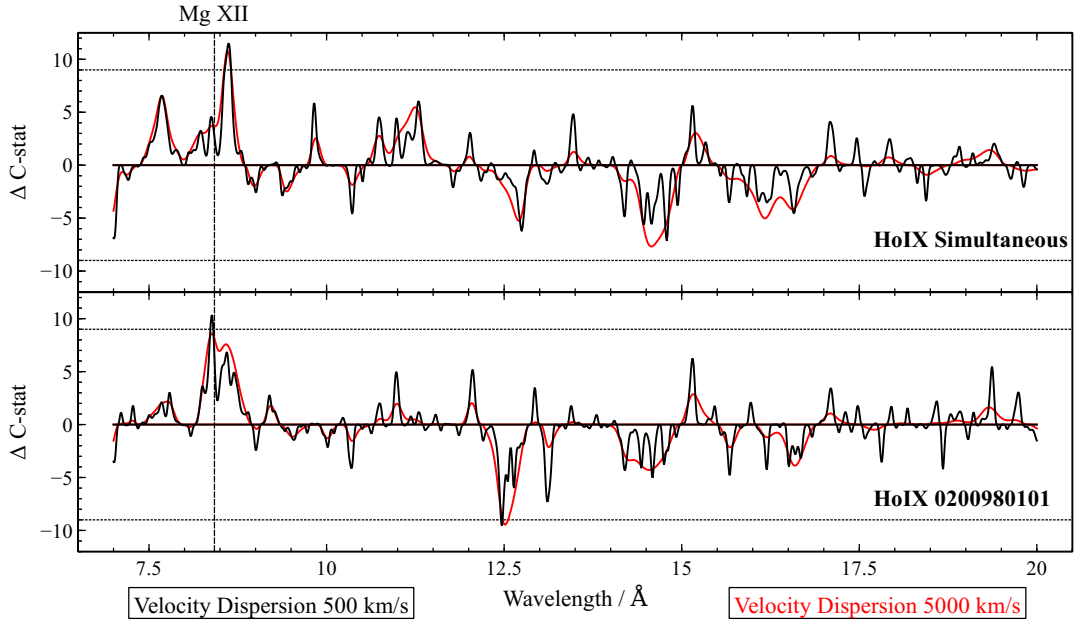


Fig. 3.2 Gaussian line search results for Holmberg IX X-1. The Y axis is defined as  $\Delta C\text{-stat}$  times the sign of normalisation of the line to show the difference between absorption and emission features. Horizontal dotted lines show the values of  $\Delta C\text{-stat}=9$  and  $-9$ .

We first analyse the highest quality observation (0200980101). Initially we fit the broadband continuum of the source between 0.3 and 10 keV using PN data. We use a double blackbody (a simple blackbody model plus a color-corrected blackbody) plus a powerlaw model. All these components are absorbed by neutral absorption, which is reproduced by the H<sub>0</sub>T component in SPEX. We obtain the following results: The temperatures of the blackbody components are  $T_{BB} = 0.204 \pm 0.10$  keV and  $T_{MBB} = 3.94^{+0.16}_{-0.15}$  keV. The powerlaw slope gamma is  $2.0 \pm 0.2$  and the absorber column density near the source plus galactic ISM absorption is  $1.36^{+0.17}_{-0.16} * 10^{21} \text{ cm}^{-2}$ .

The RGS spectrum has about 7000 source counts in total, but the background is quite high and limits our analysis to the 7.0 to 20.0 Å region only. The line search does not find any lines at very high significance, see Fig. 3.2. There is an emission spectral feature with a strength of over 10  $\Delta C\text{-stat}$  at 8.5 Å and an absorption feature with  $\Delta C\text{-stat}$  of over 9 located at 12.5 Å. Otherwise the spectrum is clean of any strong features.

The other 8 observations each individually do not have enough counts to do a full line search therefore we did a combined line search using all 9 observations. The source varies between observations, hence we cannot use a single broadband spectral

model. We group the observations into several spectral groups based on their flux and the time of observation. These groups share the same spectral model. We end up with 6 different spectral models: group 1 - observation 0112521001 + 0112521101, group 2 - 0200980101, group 3 - 0693850801, group 4 - 0693850901 + 0693851001, group 5 - 0693851101 and group 6 - 0693851701 + 0693851801. We fit the broadband spectral model for each group separately based on their PN spectra. We then follow by a simultaneous Gaussian line search on all these fits without any stacking of the data itself. This way we are looking for spectral features that are present in all of the observations, taking into account the variability of the source itself.

The simultaneous line search does not bring any conclusive results either. The 12.5 Å absorption feature gets weaker than in the 0200980101 observation (now at  $\Delta C\text{-stat}=6$ ), but does not disappear completely hence it could still be present in some observations (and not present in others). On the other hand, the emission feature at 8.5 Å is now stronger at  $\Delta C\text{-stat}$  of almost 12, therefore it must be present at least in a fraction of other observations. Its width also diminishes. Finally a not very strong, but quite wide absorption feature appears at around 14.5 Å with  $\Delta C\text{-stat}$  of about 8.

### 3.4.2 Holmberg II X-1

There are 2 observations of Holmberg II X-1 usable for RGS analysis, one high quality pointing with 56 ks of clean exposure and the source in a higher flux state (3 count/s in PN), and a second one with 44 ks and the source in a lower state (1.2 count/s).

First we analyse the long observation. The data quality is very good with almost 13000 source counts in RGS and we are able to fit the continuum based just on RGS data (hence a PN continuum is not necessary). A reasonable fit is obtained with a single blackbody plus powerlaw model with a temperature of  $0.25_{-0.03}^{+0.04}$  keV and a powerlaw slope of  $1.7 \pm 0.3$ . We perform a Gaussian line search over the 7 to 26 Å band where the continuum flux is significantly above the background. The data quality allows us to unfreeze the overall normalisation of the continuum and we fit it in addition to Gaussian line normalisation. This could increase the line strength found by the line search, but it sometimes crashes the fitting program if the data quality is not sufficiently high.

The analysis shows multiple strong residuals (Fig. 3.3). Two emission features are found at 11.8 Å with  $\Delta C\text{-stat}=11$ , and at 22 Å with  $\Delta C\text{-stat}=12$ . There are also multiple absorption features: an absorption doublet around 14.5 Å and  $\Delta C\text{-stat}$  of 12 and 8, around 22.3 Å with  $\Delta C\text{-stat}=10$ , and two weaker but broad features at 9 and 10 Å with  $\Delta C\text{-stat}$  of 8.

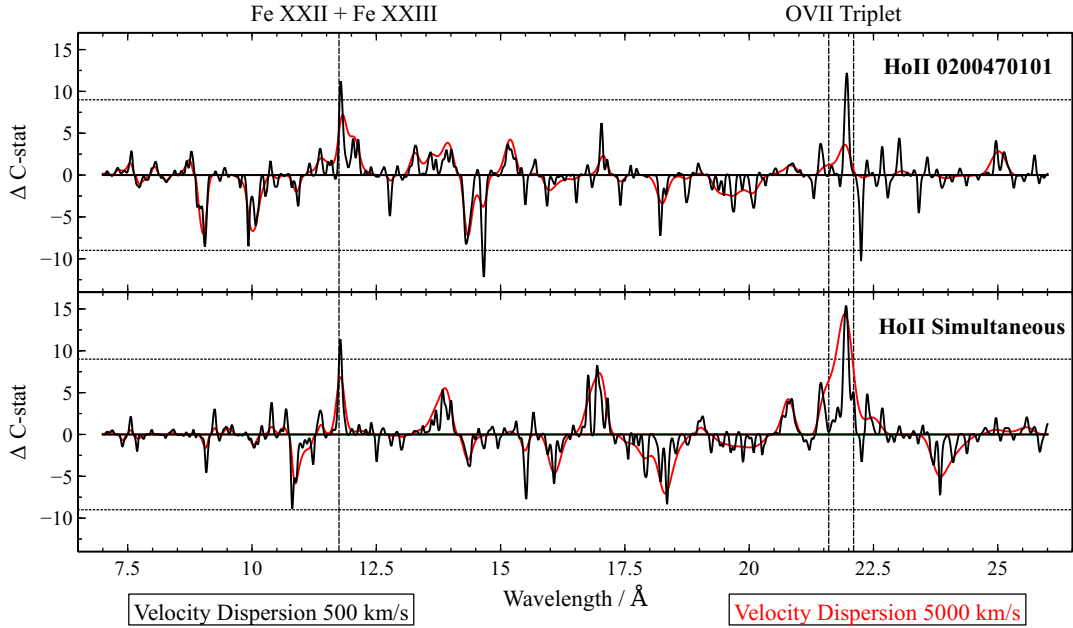


Fig. 3.3 Line search results for Holmberg II X-1. Axes are defined as in Fig. 3.2.

To quantify the actual probability of the detected spectral features we perform 1000 simulations of fake spectra as described in Section 3.3.2. Out of the total number of simulations, 2 have 2 absorption lines with  $\Delta C$ -stat higher than the real data detections. This suggests the combined significance of our detection is about  $3\sigma$ .

The second observation is much shorter and the source is at lower flux, hence it is not good enough for an individual RGS analysis, particularly for an absorption line search. We therefore perform a simultaneous line search in both observations at once. As before, both spectra have their continua fitted separately, to which we add the same Gaussian line. The line search finds that the absorption features at  $14.5 \text{ \AA}$  weaken considerably, suggesting they are not present in the second spectrum. Alternatively they could be dominated by the background. However, some of the emission features remain. The  $11.8 \text{ \AA}$  line stays at the same  $\Delta C$ -stat=11 level meaning it is present in the second observation at least partially, and the  $22 \text{ \AA}$  line increases in significance to  $\Delta C$ -stat of over 15 suggesting it is definitely present in both spectra.

### 3.4.3 NGC 5643 X-1

NGC 5643 X-1 is the hardest ULX in our sample and has a single long exposure which is well centred for RGS use. It is also the most distant ULX studied here at 17 Mpc, so its count rate is relatively low ( $\sim 0.25$  counts/s in PN data). The broadband 0.3 to 10 keV

spectrum can be well fitted with a blackbody and a second colour-corrected blackbody at temperatures of  $0.31 \pm 0.03$  and  $2.29 \pm 0.07$  keV, respectively (no powerlaw needed).

However, fitting the RGS data with this model results in a relatively poor fit and is not re-normalisable as there is slope difference between the PN and RGS data, most likely caused by high RGS background. We therefore adopt a completely different, simple powerlaw model for our line search analysis. This results in a reasonable fit (C-stat of 514 for 432 degrees of freedom), with a hard powerlaw coefficient of  $1.28 \pm 0.14$ . Due to strong background above  $20 \text{ \AA}$  in RGS data, we are forced to perform the line search in the  $7$  to  $20 \text{ \AA}$  range.

The line search finds a potential emission line at  $\sim 13.8 \text{ \AA}$  at  $\Delta C$ -stat of almost 12. There are more residuals between  $18$  and  $20 \text{ \AA}$  but these are most likely caused by the background or random fluctuations. The line search results are shown in Fig. A.1.

#### 3.4.4 NGC 4190 ULX1

There are 3 observations of the source in total, but given their statistics an individual line search would not likely be successful. Initially we fit the PN data with our standard model. One of the PN spectra is not usable as the detector has been swamped with flares for practically the whole exposure time, but we fit the other two observations with a double blackbody (first observation) and a blackbody plus powerlaw (second observation) model. For the observation without any continuum model, we use the PN model from the first observation which was taken only 2 days apart and their RGS continua are super-imposable.

Now we renormalise the PN continua to the RGS spectrum and search for spectral features in all 3 observations simultaneously. We have about 2500 RGS counts in total. Overall the search does not find any very significant features, but we find a broad emission residual peaking at  $18.7 \text{ \AA}$  with  $\Delta C$ -stat=12. The feature is suspiciously broad, but at the same time the counts are well above the background level in this spectral range. There are other residuals found by the line search but none are stronger than  $\Delta C$ -stat=10. The line search results for NGC 4190 ULX1 can be found in Fig. A.1.

#### 3.4.5 M33 X-8

M33 X-8 is atypical for our sample as it only barely reaches the luminosity to be considered a ULX. At the same time, the source is located directly in the core of M33 [221, 86]. However, the X-ray spectrum of M33 X-8 is very atypical for an AGN as its high-energy folding energy is just around 2 keV if fitted with a standard powerlaw [384].

Furthermore, no activity was revealed from the nucleus of M33 at other wavelengths, and kinematic and photometric studies of the core reveal that the mass of its central black hole (if there is any) is of the order of  $10^3 M_{\odot}$  or less [131, 243]. The nucleus therefore does not host a supermassive black hole and thus M33 X-8 is a ULX.

We possess 2 observations of the source, which are short but the source is very bright thanks to its proximity (count rate of about 5 count/s with PN). We fit the broadband spectrum as usual and find a good fit with the standard double blackbody and a powerlaw model.

The RGS spectra have about 7000 counts combined. We renormalise the PN spectra to the RGS level and search for any spectral features simultaneously in both observations between 7 and 26 Å. The simultaneous search finds an emission feature at 12.5 Å with a strength of about  $\Delta C\text{-stat}=11$ , but other than that the spectrum is relatively clean. It is very unlikely that this feature is caused by the background given the high count rate of the source. The feature found by our line search is shown in Fig. A.1.

### 3.4.6 NGC 1313 X-2

We are using the newly public data on NGC 1313 X-2, which is the only existing data of this source well centred for an RGS analysis with sufficient exposure time. Two exposures of 110 ks in total show that the source has varied significantly - increasing the PN count rate from 0.24 count/s during the first, longer observation, to 0.41 count/s during the second observation. We fit the first spectrum with a full broadband model, while the second one only requires a double blackbody (BB + MBB) fit.

Each observation only contains about 800 RGS counts (both RGS detectors combined). The background is stronger than the source above  $\sim 20$  Å, so we search in the usual 7 to 20 Å range. We fit the RGS spectra and renormalise them to avoid any constant residuals in the line search. Then we perform a simultaneous line search for both observations at once, i.e. we are looking for residuals that are present at both times. We find absorption residuals at 8, 9.6 and 13 Å, and a bit weaker but a very broad feature at 15.5 Å. There are potential emission line features at 10, 14.5 and 16.2 Å, and it seems that the background affects our results at least above 18 Å. A plot of these features can be seen in A.1.

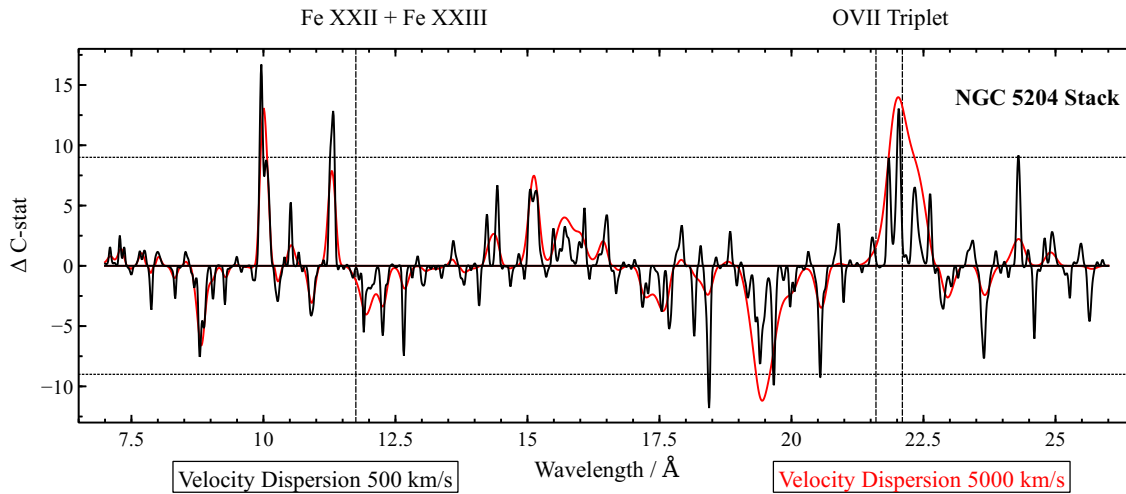


Fig. 3.4 Line search results for NGC 5204 X-1. Axes are defined as in Fig. 3.2.

### 3.4.7 NGC 5204 X-1

There are 9 observations of NGC 5204 X-1 in total that are pointed well enough for RGS analysis, with a total raw exposure of 250 ks (160 ks filtered). The object varies in flux between about 0.5 count/s to 1.2 count/s (with PN), but as the observations are rather short, none of them is of high enough quality to be searched individually. We perform a custom RGS data reduction and extraction for each observation to avoid any possible errors such as energy shift and then stack them into a single spectrum. This simplifies the analysis greatly. We are able to get away with stacking despite the long-term variability of the source. It varies in normalisation but its spectral hardness does not change considerably. The spectrum is fitted with a single blackbody plus a powerlaw model (the second blackbody not necessary) with a temperature of  $0.21^{+0.06}_{-0.05}$  keV and a gamma index of  $1.9^{+0.4}_{-0.3}$ .

We have 9000 counts in total which gives very good statistics compared to some other sources in our sample. The line search (see Fig. 3.4) finds a very strong emission feature at 10 Å, with  $\Delta C$ -stat of over 16, and weaker features at 11.3 Å ( $\Delta C$ -stat=13) and at 22 Å ( $\Delta C$ -stat=14). The last feature is very broad and might be caused by background contamination, but the first two features are located at low wavelengths where source counts clearly dominate the background. There are potential absorption features at 18.5 and 19.5 Å with strengths of about  $\Delta C$ -stat=11.

We perform 2009 Monte Carlo simulations to quantify the significance of these spectral residuals. We focus on the 3 strongest emission lines, each of them with at least  $\Delta C$ -stat=13. We find 97 simulated emission features stronger than this threshold,

so the confidence of the weakest of our features is  $\sim 95\%$  each. Furthermore, we find 13 emission features with  $\Delta C\text{-stat} > 16.7$ , which is the strength of the most prominent emission residual in real spectrum (confidence level of 99.35%). Finally, we want to quantify the confidence on multiple spectral features present in a fake spectrum with  $\Delta C\text{-stat} > 13$  (as a lower limit of confidence on our emission residuals). We find 11 occurrences of two lines in a single fake spectrum with such strength, but only 1 case of two emission lines which gives a confidence level of roughly 99.9% (even though we are definitely still in the discrete regime here given the total number of simulations). Therefore it seems extremely unlikely that all 3 emission features observed in the spectrum of NGC 5204 X-1 are caused by noise.

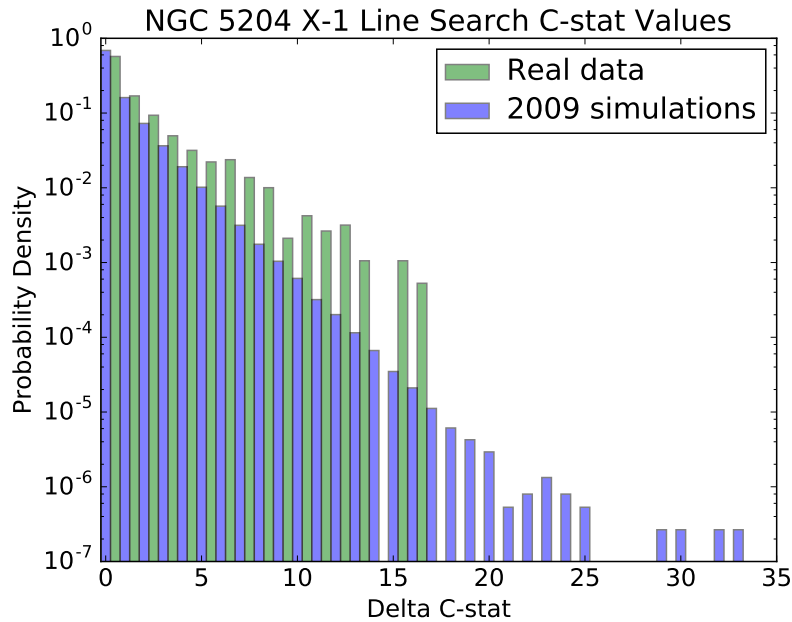


Fig. 3.5 Histogram of  $\Delta C\text{-stat}$  of a real Gaussian line scan of NGC 5204 X-1 (green) and of line scans of 2009 Monte Carlo simulated datasets (blue). The Y axis is the probability density function, the integral of which is 1, and the X axis is the  $\Delta C\text{-stat}$  value.

The significance of our detections can also be shown in a different way. We can plot a histogram of  $\Delta C\text{-stat}$  values (the fit improvement) using all energy bins in our band for a certain Gaussian line scan. A bin of  $\Delta C\text{-stat} = X$  is then equal to the number of occurrences of  $\Delta C\text{-stat}$  between  $X$  and  $X+1$  in this line scan. We can also rescale the bin values to obtain the probability density of  $\Delta C\text{-stat}$  - in our case, this is achieved by simply dividing all bin values by 2000 (the number of energy bins). This is plotted in

Fig. 3.5. In green, the histogram of the real Gaussian line scan of NGC 5204 X-1 (with a dispersion velocity of 1000 km/s) versus the  $\Delta C$ -stat value is shown, while the average histogram of line scans on 2009 Monte Carlo simulated spectra of NGC 5204 X-1 is in blue. The y axis in the histogram is the probability density of the  $\Delta C$ -stat value (the integral of which is 1). Note that the real data histogram does not contain a value at  $\Delta C$ -stat=14 - this simply means there were no occurrences of  $\Delta C$ -stat between 14 and 15 in the line scan. One can notice that the probability density of simulated data resembles very much a powerlaw function. In comparison, there is clear excess of higher  $\Delta C$ -stat data in our real search. One should however keep in mind that the last bin of real data (in green) corresponds to exactly 1 occurrence (hence 1 case  $\sim 0.5 \times 10^{-3}$  in the histogram) so the last few bins are affected by small number statistics. It seems very unlikely that the real data line scan distribution of  $\Delta C$ -stat values comes purely from noise which creates the blue histogram.

### 3.4.8 NGC 6946 X-1

NGC 6946 X-1 was already studied in Pinto et al. [306], but without a rigorous Gaussian line scan, hence we include it in our analysis. It is the softest ULX in the sample. At a distance of 5.6 Mpc, its PN count rate is only about 0.36 count/s, but luckily it has a full orbit 120 ks exposure (110 ks of clean data). We can fit it with a standard double blackbody plus a powerlaw model with temperatures  $T_{\text{BB}} = 0.17 \pm 0.09$  keV and  $T_{\text{MBB}} = 1.68^{+0.13}_{-0.20}$  keV and a gamma index of  $2.7 \pm 0.4$ , although the fit is not very good at C-stat=195 with 118 degrees of freedom mostly due to a prominent residual at around 1 keV [250].

The observation has about 3000 RGS source counts in total. We had to use a custom background since one of the 2 default background regions was contaminated by multiple bright X-ray binaries within the host galaxy. We use the PN spectral model which we renormalise as we did with other sources and search for spectral lines between 7 and 20 Å. The line search finds a narrow emission feature at 13.5 Å with  $\Delta C$ -stat=14 and a very strong and broad emission feature at 19 Å with a strength of over 17.5  $\Delta C$ -stat. There is also an absorption residual at 16.5 Å with  $\Delta C$ -stat of about 10 and other potential weaker features. The Gaussian line scan results are shown in Fig. 3.6.

We perform 1070 Monte Carlo simulations and Gaussian line scan them. We focus on the prominent signature at 19.3 Å with a width of about 3000 km/s. In total we find 4 fake spectral features stronger than the real feature. This suggests the feature is significant at about  $3\sigma$ , but further simulations would be necessary to constrain its

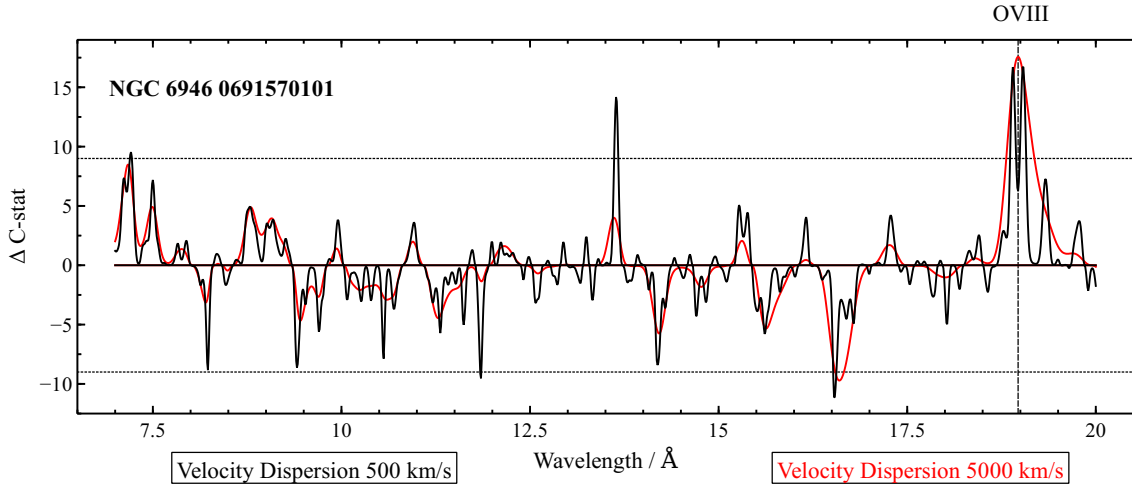


Fig. 3.6 Line search results for NGC 6946 X-1. Axes are defined as in Fig. 3.2.

significance more accurately. The histogram comparing the probability of occurrence of each  $\Delta C$ -stat value in the real search and in the simulated scans is shown in Fig. 3.7.

### 3.4.9 NGC 4631 ULX1 and IC 342 X-1

A thorough search on the XSA archive shows that also NGC 4631 ULX1 and IC 342 X-1 have suitable pointings for RGS analysis. Unfortunately, NGC 4631 ULX1 is relatively distant at over 7 Mpc and has a flux of only about 0.1 count/s with PN. Even though its observation has a relatively long exposure of 55 ks, this only results in about 650 RGS counts in total. We consider these data to be too low in quality to be able to detect any spectral features because the source flux is at the same level as the background flux.

IC 342 X-1 has 2 observations with good enough pointing for RGS with a total exposure of 120 ks and a sufficient flux of  $\sim 0.5$  count/s with PN. Unfortunately, the RGS spectrum is contaminated by another source with  $\sim$ half the X-ray luminosity (in the 0.3 to 10 keV band) of IC 342 X-1 along the dispersion direction of the spectrometer and hence it is unusable for subtle analysis like a spectral line search.

## 3.5 Discussion

We have collected all available *XMM-Newton* RGS X-ray ULX data with good enough quality for spectral line searches. Then we searched for residuals in the continua of their spectra by performing Gaussian line scans. The statistical significance of some

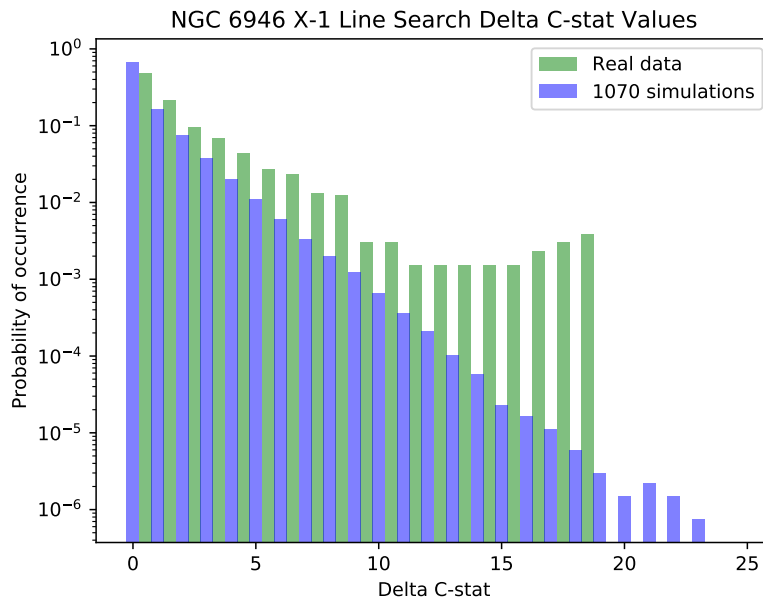


Fig. 3.7 Histogram of  $\Delta C$ -stat of a real Gaussian line scan of NGC 6946 X-1 (green) and of line scans of 1070 Monte Carlo simulated datasets (blue). The Y axis is the probability density function, the integral of which is 1, and the X axis is the  $\Delta C$ -stat value.

among the most prominent features was quantified by Monte Carlo simulations of source spectra.

### 3.5.1 Strongest features

Table 3.3 shows the strongest residuals found in the RGS spectra of ULXs in our sample. This means their  $\Delta C$ -stat difference is higher than 9 for at least one value of the line width (we have searched using the line width equivalents of 500 km/s, 1000 km/s and 5000 km/s). We found that there is usually little difference between the results from searches with the line widths of 500 and 1000 km/s.

### 3.5.2 Attempting to identify the spectral features

In NGC 6946 X-1, we detect an emission residual located at the rest-frame wavelength of O VIII (19.0 Å) with a significance of at least  $3\sigma$ . The line is moderately broad with a width of 0.2 Å ( $\sim 3000$  km/s).

Table 3.3 The most prominent residuals found by the Gaussian line search, ordered by the source hardness ratio as defined earlier.

Object	Obs.	$\lambda$	Line type	$\Delta C^1$ 500 km/s	$\Delta C^1$ 5000 km/s	Preliminary identification	Signif. <sup>2</sup> %
		Å					
NGC 5643 X-1	0744050101	13.79	Em.	11.43	6.42		
Holmberg IX X-1	0200980101	8.40	Em.	10.29	8.61	Mg XII (1s-2p)	
Holmberg IX X-1	0200980101	12.48	Abs.	-9.56	-9.45		~98
Holmberg IX X-1	Simult.	8.63	Em.	11.52	10.78	Mg XII (1s-2p)	
NGC 4190 ULX1	Simult.	17.07	Em.	9.04	6.95	Fe XVII (2p-3s)	
NGC 4190 ULX1	Simult.	18.62	Em.	9.01	12.20	O VII (1s-3p) O VIII (1s-2p)	
M33 X-8	Simult.	12.57	Em.	10.73	9.69		
NGC 1313 X-2	Simult.	18.94	Em.	10.50	7.15	O VIII (1s-2p)	
NGC 1313 X-2	Simult.	8.99	Abs.	-9.16	-9.78		
NGC 1313 X-2	Simult.	9.58	Abs.	-13.90	-10.58		
NGC 1313 X-2	Simult.	12.98	Abs.	-11.42	-4.84		
NGC 5204 X-1	Stack	9.97	Em.	16.70	13.07		$\gtrsim 99.35$
NGC 5204 X-1	Stack	11.33	Em.	12.85	7.87		95
NGC 5204 X-1	Stack	18.44	Abs.	-11.18	-2.4		
NGC 5204 X-1	Stack	19.67	Abs.	-9.88	-11.19		
NGC 5204 X-1	Stack	20.55	Abs.	-9.24	-3.48		
NGC 5204 X-1	Stack	22.04	Em.	13.04	13.99	O VII triplet	95
Holmberg II X-1	0200470101	11.79	Em.	11.18	7.21	Fe XXII (2p-3d) Fe XXIII (2p-3d)	
Holmberg II X-1	0200470101	14.67	Abs.	-12.18	-3.80		
Holmberg II X-1	0200470101	21.97	Em.	12.20	3.61	O VII triplet	93
Holmberg II X-1	0200470101	22.26	Abs.	-10.28	-0.24		
Holmberg II X-1	Simult.	11.79	Em.	11.36	6.88	Fe XXII (2p-3d) Fe XXIII (2p-3d) O VII triplet	
Holmberg II X-1	Simult.	21.96	Em.	15.40	14.42		
NGC 6946 X-1	0691570101	7.22	Em.	9.54	8.50		
NGC 6946 X-1	0691570101	11.86	Abs.	-9.53	-1.36		
NGC 6946 X-1	0691570101	13.65	Em.	14.18	4.01		
NGC 6946 X-1	0691570101	16.55	Abs.	-11.13	9.72		
NGC 6946 X-1	0691570101	18.98	Em.	16.69	17.57	O VIII (1s-2p)	$\gtrsim 99.7$

<sup>1</sup> $\Delta C$ -stat value using 2 different line widths, i.e. using 2 different gas dispersion velocities: 500 km/s and 5000 km/s.<sup>2</sup>Statistical significance of the feature obtained by Monte Carlo simulations.

In NGC 5204 X-1, we find 3 emission features. A broad emission line at  $\sim 22 \text{ \AA}$  (approximate rest-frame wavelength of the O VII triplet) with a significance of 95 %. The remaining 2 emission lines do not correspond to a rest-frame wavelength of any expected (i.e. strong enough) elemental transition from photoionised plasma or plasma in collisional equilibrium. However, they are most likely not resulting from noise: the significance of the stronger one (at  $10 \text{ \AA}$ ) is about 99.35 %, and of the weaker one (at  $11.3 \text{ \AA}$ ) is  $\sim 95$  %. These 2 features were already noticed by Roberts et al. [344] in *Chandra* data, although due to poor spectral resolution, they blend into a single broad emission line in CCD spectra. The fact that the lines are not located at the rest-frame wavelength of a transition makes their identification much more challenging. We manually experimented with photoionisation models such as PION and collisional equilibrium models like CIE to represent emitters at different blueshifts or redshifts but were unable to identify the lines this way without an automated approach (see Sect. 3.3.3).

Holmberg II X-1 shows 2 strong emission residuals, both in the highest quality observation (0200470101) and in the simultaneous analysis of 2 observations at once. The residuals are located at the rest-frame wavelengths of iron and oxygen: the first one corresponds to Fe XXII and/or Fe XXIII at  $\sim 11.8 \text{ \AA}$ , and the second one is at the rest-frame wavelength of the O VII triplet. Both features are narrow in the single observation, while the O VII feature becomes wide if we include all observations available. The long observation also shows multiple absorption features, with a combined significance of the strongest 2 being about  $3\sigma$  based on Monte Carlo simulations. These features are much weaker in the simultaneous line scan.

Holmberg IX X-1 seems to possess only 1 strong emission feature. In the highest quality observation (0200980101) search, this feature is centred on the rest-frame wavelength of Mg XII ( $8.42 \text{ \AA}$ ). Curiously, in the simultaneous search with all observations available, the feature is much weaker but there is a strong emission line shifted by  $0.23 \text{ \AA}$  ( $\sim 8000 \text{ km/s}$ ) at  $8.63 \text{ \AA}$ . This could either be the same feature observed in the long observation or a completely different signature. The one notable absorption feature is only present in the long observation search at  $12.48 \text{ \AA}$ . It is a broad feature, resembling the absorption lines found in NGC 1313 X-1, albeit at a different velocity shift. If this is a signature of an outflow, it could suggest a different outflow velocity or simply a different viewing angle of the ULX and its wind. Monte Carlo simulations show we are detecting this feature at about 98 % confidence level.

### 3.5.3 Physical model search

Where the spectral residuals are not located at a rest-frame wavelength of any expected elemental transition, we need to use SPEX models to identify any redshifted or blueshifted lines (for more details, see Sect. 3.3.3).

We follow-up with a search for spectral features in Holmberg IX X-1 using an ionised absorber model (see section 2.2.2 for more details about the search method). We adopt a grid of velocities from 0 to -100000 km/s with a step of 500 km/s (which is comparable to the RGS resolution). First we adopt a velocity broadening in XABS of 150 km/s, then do the same for 750 and 1500 km/s. We find the best fit is obtained for a blueshift of either 0.06c or 0.26c. The best fit improvement is about  $\Delta C$ -stat of 15, which is not a high enough significance to conclusively claim a wind detection. Further deep and uninterrupted exposures are needed for a firmer conclusion.

We apply the same procedure to the highest quality observation of Holmberg II X-1. Adopting a velocity dispersion of 500 km/s (based on the narrow shape of residuals found by line search) gives the best fit at a blueshift of  $\sim 0.2$ - $0.25c$ , albeit at a lower significance than obtained for Holmberg IX X-1. The best fit photoionisation parameter in this case is  $\log(\xi/\text{erg cm s}^{-1}) = 3.0 \pm 0.2$ , similar to outflows that have been found in NGC 1313 X-1 and NGC 5408 X-1.

#### A jet detection in NGC 5204 X-1?

NGC 5204 X-1 shows multiple emission features, the most prominent ones being at 10 and 11.3 Å. To explain them with a physical model, we perform a CIE model scan between 0 and 0.4c blueshift on the stacked data (see section 3.3.3 for more details about the scan). The results of the scan are shown in Fig. 3.8. We find a significant fit improvement for an outflow velocity of -0.337c with  $\Delta C$ -stat=25.08, a temperature of about 0.5 keV and a dispersion velocity of 1000 km/s. To follow up, we fit the RGS spectrum directly with a blueshifted CIE model plus continuum. The fit is shown in Fig. 3.9, now on a narrower band between 7.5 and 20 Å, which is less affected by the background. The collisionally ionised plasma model fits both emission features very well. These features are produced by Fe XVII in our model. The fit improvement is  $\Delta C$ -stat=25.87 for 4 degrees of freedom (normalisation, temperature and velocity dispersion of the CIE component, plus its blueshift). The best fit is achieved for a velocity broadening of  $\lesssim 1000$  km/s.

The fit can be further improved by freeing some of the abundances. Since the CIE component is mostly driven by the two Fe XVII lines (and not continuum collisionally

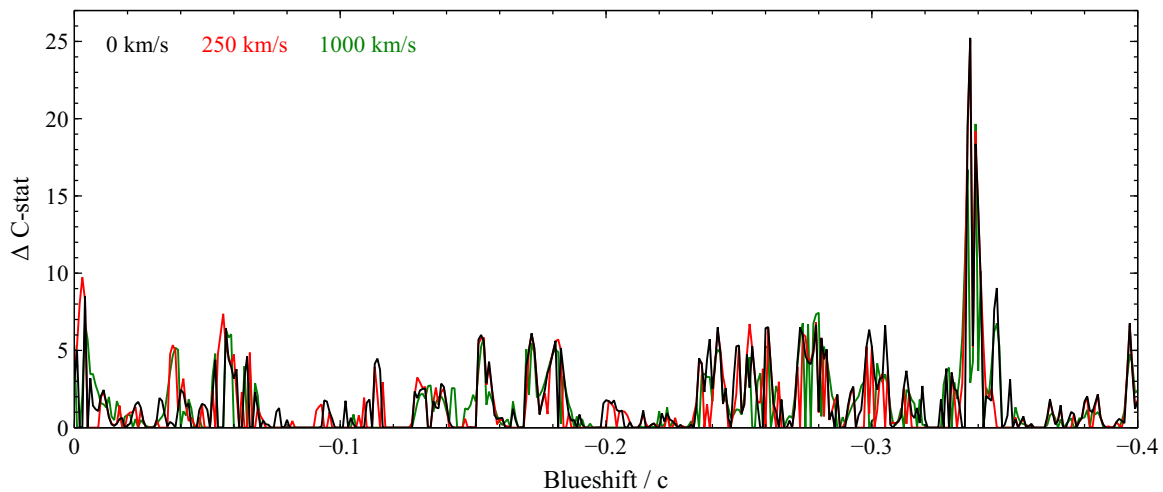


Fig. 3.8 The CIE scan results of the stacked NGC 5204 X-1 RGS spectrum for 3 different velocity broadening values.

ionised emission from hydrogen bremsstrahlung), it is impossible to obtain any reliable results if we free the iron abundance. We thaw nitrogen and oxygen abundances. Then we couple neon and magnesium abundances to that of oxygen as they are thought to have a similar core-collapse supernova origin [69], and it is not recommended to fit all elements separately due to low statistics. In the end, the addition of the CIE component improves the fit by  $\Delta C$ -stat of 39.2 for 6 additional degrees of freedom - normalisation, temperature, velocity broadening, blueshift, and 2 abundances. The temperature of emitting gas is  $0.60^{+0.08}_{-0.09}$  keV and the  $1\sigma$  upper limit on its velocity broadening is 335 km/s. The nitrogen abundance (with respect to iron)  $N/Fe$  is rather high but poorly constrained at  $N/Fe \gtrsim 4$  and the coupled oxygen, neon and magnesium abundance  $O/Fe = Ne/Fe = Mg/Fe \lesssim 0.8$ . The blueshift of the CIE component is  $-0.3371^{+0.0006}_{-0.0005} c$  (116800 km/s).

We perform Monte Carlo simulations to quantify the significance of these features. We simulate a fake RGS spectrum with comparable statistics and continuum model as the NGC 5204 X-1 spectrum. Then we launch the same CIE scan procedure as we used for real data. We repeat the same process as many times as possible and look for any cases where a fake feature produces a stronger ( $\Delta C$ -stat) fit improvement than we found in the real spectrum. We performed 2112 simulations in total and found 6 outliers stronger than the feature found in measured data. This gives the significance of 99.7 %, which is about  $3\sigma$ . Fig. 3.10 contains a histogram comparison of the  $\Delta C$ -stat values of the real and simulated CIE searches showing a clear deviation of the real data from Monte Carlo simulations. Fig. 3.11 contains two example searches of simulated

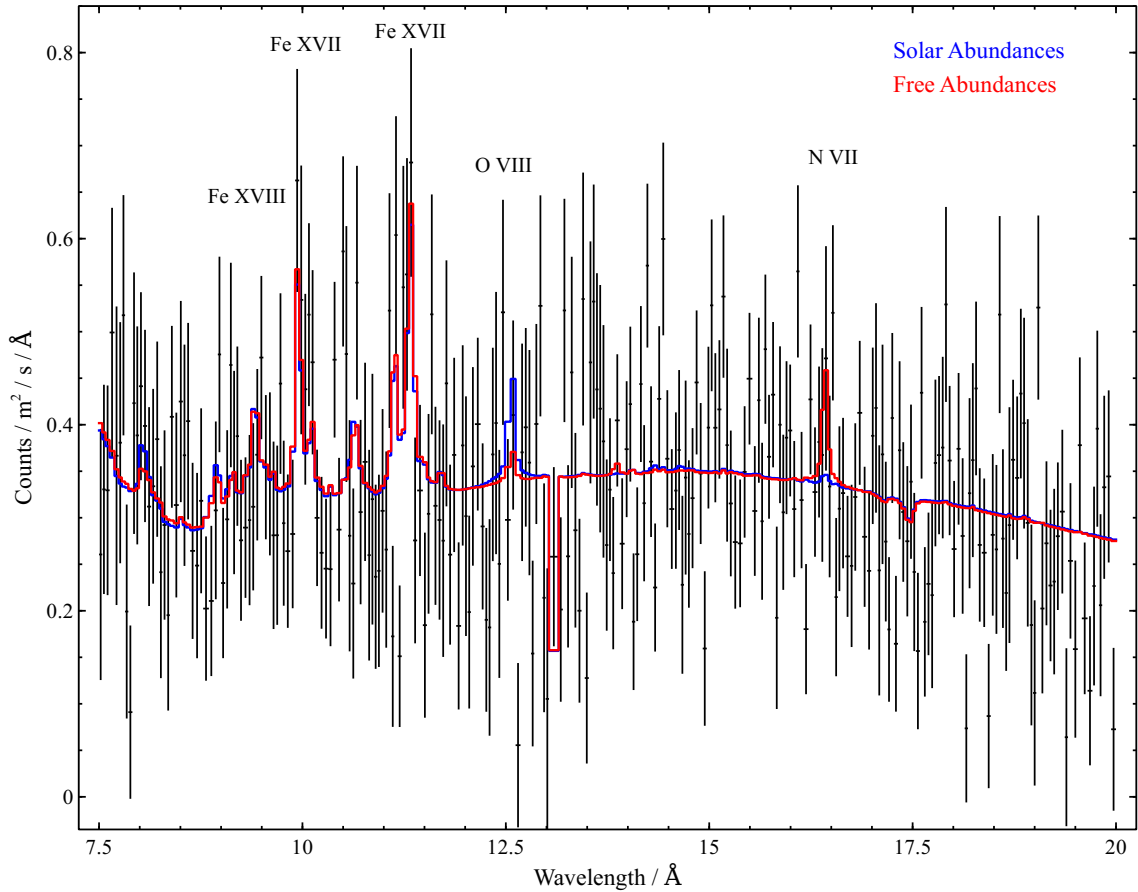


Fig. 3.9 The RGS spectrum of NGC 5204 X-1 between 7.5 and 20 Å, using all available *XMM-Newton* observations (stacked). The model is composed of a continuum fit with a powerlaw and a blackbody component (plus neutral absorption). On top of the continuum, a blueshifted collisionally ionised gas in equilibrium model CIE is added. In blue, the model is shown with default abundances. In red, the abundances of nitrogen and oxygen are freed, and the abundances of neon and magnesium are tied to oxygen.

NGC 5204 X-1 datasets which resulted in stronger detections (with higher  $\Delta C$ -stat values) than the CIE search on the real data.

Our findings are very similar to the X-ray emission lines of SS 433, the Galactic microquasar [233], albeit the emission lines in NGC 5204 X-1 are observed at much higher blueshift (Fig. 3.12). Most of the SS 433 X-ray emission comes from plasma ionised by its jets, which produces prominent emission lines throughout the X-ray band [235]. The gas producing these lines is accelerated to  $0.27c$ , which, accounting for projection effects, results into emission from the blue jet being blueshifted by about  $0.08c$ , and the red jet being redshifted by  $\sim 0.16c$ . Unfortunately, due to the higher blueshift of lines seen in NGC 5204 X-1, the elemental transitions seen in SS 433 (with

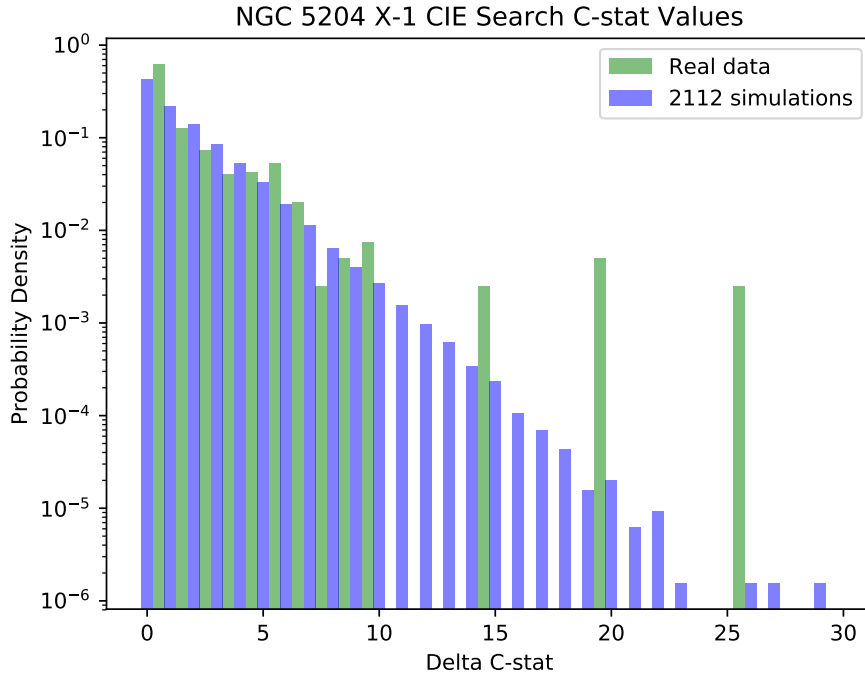


Fig. 3.10 Histogram of  $\Delta C$ -stat of a real CIE outflow scan of NGC 5204 X-1 (green) and of CIE scans of 2112 Monte Carlo simulated datasets (blue). The Y axis is the probability density function, the integral of which is 1, and the X axis is the  $\Delta C$ -stat value.

*Chandra* gratings) are mostly blueshifted out of the RGS energy band ( $7 \text{ \AA}$  and higher). The only line seen both in our spectrum and the [235] analysis of SS 433 is the Ne X Ly  $\alpha$  and Fe XXIII line with the rest frame wavelength of  $12.134 \text{ \AA}$ . In SS 433, the line is seen at  $11.194 \text{ \AA}$  originating from the blue jet, and should be at  $8.05 \text{ \AA}$  in NGC 5204 X-1. Emission residuals can indeed be seen around  $8 \text{ \AA}$  in its spectrum (see Fig. 3.9), but they are too weak to make any claims. Further residuals in NGC 5204 X-1 are seen at higher energies in CCD PN and *Chandra* data [344].

The blueshift of the emission lines seen in NGC 5204 X-1 is higher than in SS 433 (0.34c plus any projection effects versus 0.27c), but the terminal jet velocity might be source dependent. The spatial orientation of both sources is also most likely quite different with SS 433 being seen practically edge-on, while NGC 5204 X-1 is probably at a much lower inclination angle (but higher inclination than, say, NGC 1313 X-1 or Holmberg IX X-1 due to its softer spectrum). The X-ray continuum of SS 433 is much harder, and not super-Eddington (SS 433 does not look like a ULX from our point of

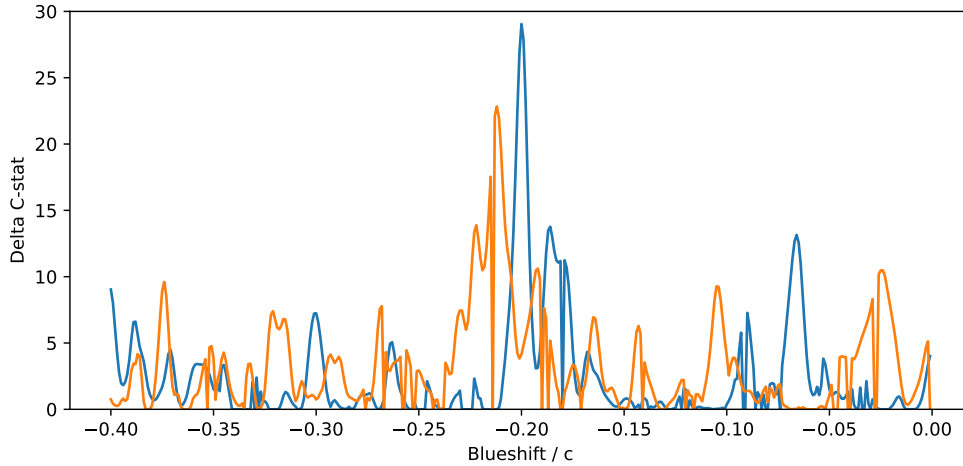


Fig. 3.11 Two example CIE searches of the simulated NGC 5204 X-1 datasets which resulted in stronger detections than the one achieved in the real data.

view) due to inclination and heavy absorption. Hence most of the continuum emission of SS 433 actually comes from its jets (the kinetic power of which is super-Eddington) and not the accretion disk as we observe in ULXs. Therefore a hardness comparison of SS 433 with other ULXs does not make sense. The temperature of the plasma observed in NGC 5204 X-1 is rather low at  $\sim 0.6$  keV, which is at the lower limit of estimates from the line strengths in SS 433 (0.5-10 keV). However, the NGC 5204 X-1 plasma temperature could be an underestimate as we can only see a few lines (most importantly Fe XVII) that are not blueshifted out of the RGS energy band. Future *Chandra* grating or calorimeter observations will be able to determine whether the source has other prominent emission lines at higher energies, as observed in SS 433. It is worth mentioning that NGC 5204 X-1 and SS 433 also exhibit very similar He I (6678 Å), He II (4686 Å) and H $\alpha$  (6563 Å) line emission in the optical band [106].

### 3.5.4 ULX comparison within the sample and with previous work

Holmberg II X-1 and NGC 5204 X-1 have similar spectral hardnesses (Table 3.1) so are good candidates for a comparison within our sample. Looking at their line scans, Fig. 3.3 and 3.4, we notice that both sources have strong detections of the O VII line at rest frame. We also do not see any O VIII detection. At lower wavelengths, the line scans show emission residuals, but they are not exactly at the same energy. In Holmberg

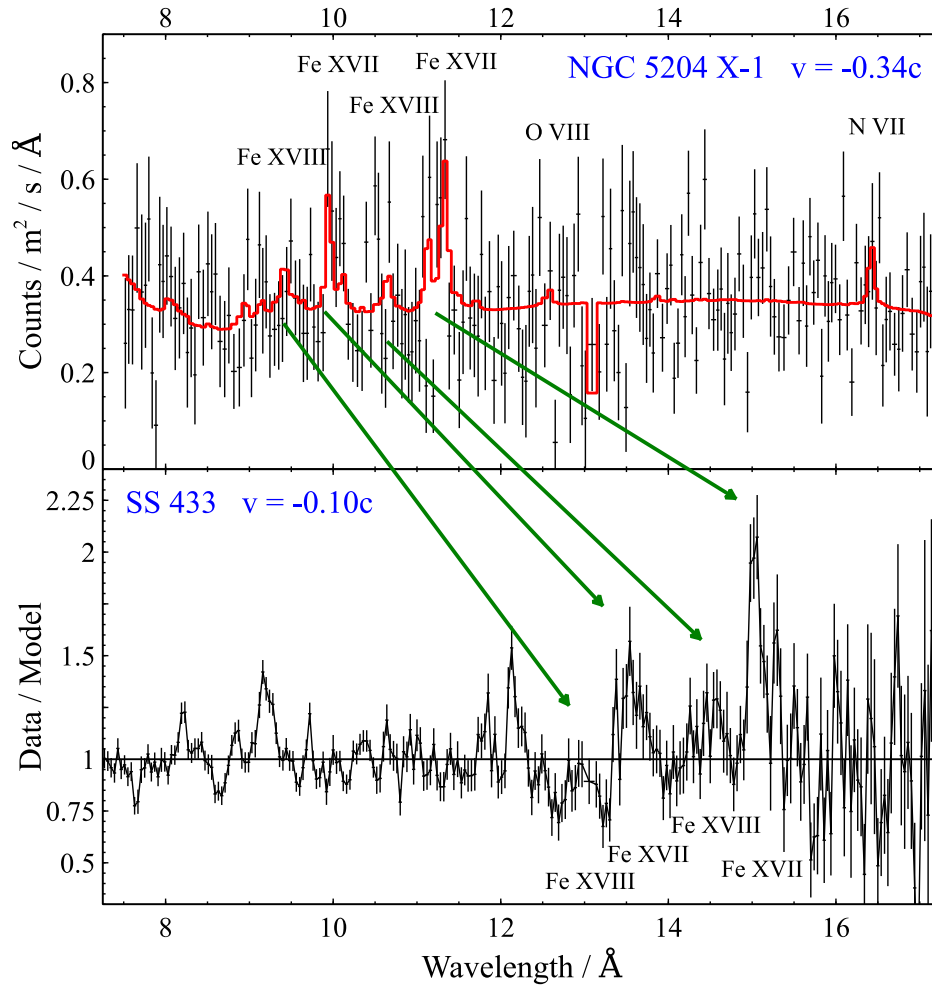


Fig. 3.12 A comparison between the RGS spectra of NGC 5204 X-1 and SS 433. Top: RGS spectrum of NGC 5204 X-1 in the 7.5 – 17 Å range, using all archival *XMM-Newton* observations (stacked). The model is composed of a continuum fit with a powerlaw and a blackbody component (plus neutral absorption). On top of the continuum, a model of blueshifted, collisionally ionised gas in equilibrium (CIE) is added. Bottom: RGS spectrum of SS 433, using the longest *XMM-Newton* observation of the source. The Y-axis is defined as the ratio of data versus a simple powerlaw model for plot clarity. Green arrows correspond to the same atomic features (at different blueshifts) in both objects.

II X-1, we find a strong emission feature at 11.8 Å, which could be associated with an iron transition. NGC 5204 X-1 does not show any residuals at this wavelength. Instead, it has 2 prominent emission features at lower wavelengths (10 and 11.3 Å), which are difficult to associate with any rest-frame transitions but are likely produced

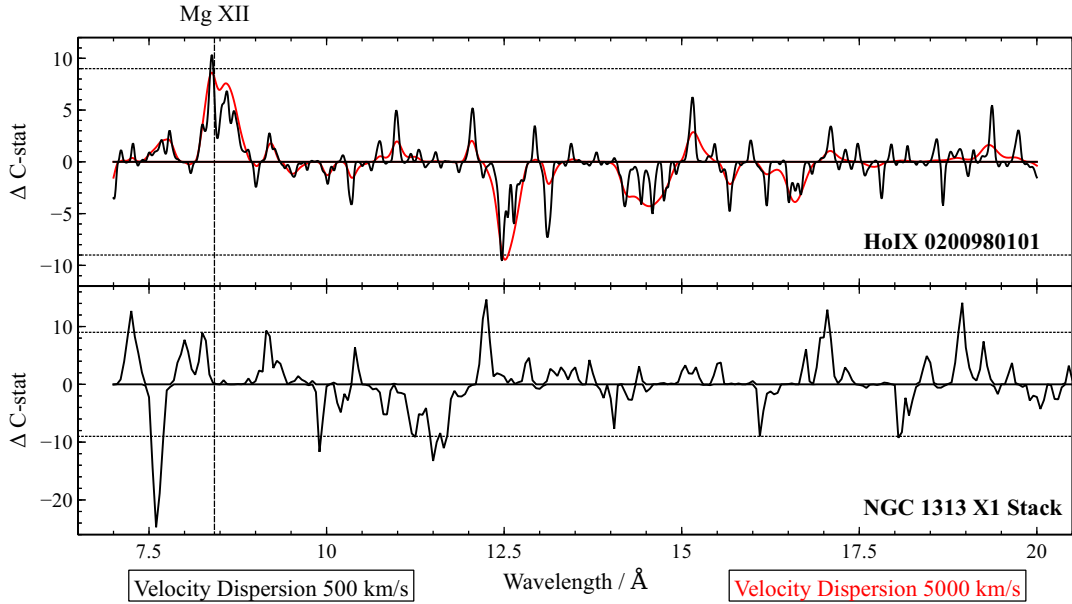


Fig. 3.13 Comparison between a Gaussian line search of the highest quality single observation of Holmberg IX X-1 and the stacked results of NGC 1313 X-1. Axes are defined as in Fig. 3.2.

by blueshifted collisionally ionised gas. There are no obvious absorption features that these 2 sources would have in common.

Next we would like to compare our findings with the ULXs that have already been shown to possess outflows [306, 304]. There are 3 such sources in total, as of June 2017: NGC 1313 X-1, NGC 5408 X-1 and NGC 55 ULX.

Holmberg IX X-1 (average hardness ratio of 0.6) is one of the hardest sources in our sample (Table 3.1). Its spectrum resembles that of NGC 1313 X-1 (hardness ratio 0.49), which was the first source with an outflow that was identified thanks to its shifted, broad absorption signature at around 11.5 Å (Fig. 3.13). Holmberg IX X-1 does not have such a prominent absorption line, however it does show a broad residual at 12.5 Å. If these 2 features are a result of the same transition, the projected velocity difference of outflows in these 2 sources needs to be about  $\sim 0.08c$  (the one in NGC 1313 X-1 has a velocity of about  $0.2c$ ). Other than this, the line scans of these 2 sources do not have much in common.

NGC 5408 X-1 (hardness ratio 0.19) has a softer X-ray spectrum than NGC 1313 X-1 or Holmberg IX X-1, similar to Holmberg II X-1 and NGC 6946 X-1 (both with HR  $\sim 0.24$ ) and (less similar) to the spectrum of NGC 5204 X-1 (HR = 0.4). Comparing these 4 sources (Fig. 3.14), we find their line scans give quite different results. While both NGC 5204 X-1 and Holmberg II X-1 show strong emission residuals at the O VII

transition ( $22 \text{ \AA}$ ), there seems to be only a very small hint of O VII in the line scan of NGC 5408 X-1. Conversely, where NGC 5408 X-1 and NGC 6946 X-1 show a prominent emission line of O VIII ( $19 \text{ \AA}$ ), NGC 5204 X-1 and Holmberg II X-1 have little or no residuals. At lower wavelengths, most of these sources exhibit emission residuals in the 10 to 15  $\text{\AA}$  range, but they are all shifted differently in each ULX. Holmberg II X-1 has one of the emission features exactly at the rest-frame wavelength of Fe XXII and Fe XXIII, and the 12.1  $\text{\AA}$  feature in NGC 5408 X-1 can be explained by the Ne X transition. The other residuals do not seem to align with any expected rest-frame elemental transitions. However, the emission features of these 3 ULXs look curiously similar - they are at  $9.954^{+0.018}_{-0.003} \text{ \AA}$  and  $11.33^{+0.04}_{-0.02} \text{ \AA}$  in NGC 5204 X-1, at  $11.78 \pm 0.02$  and  $13.87^{+0.08}_{-0.21} \text{ \AA}$  in Holmberg II X-1 and at  $12.07 \pm 0.03$  and  $14.09^{+0.02}_{-0.03} \text{ \AA}$  in NGC 5408 X-1 (errors obtained by fitting Gaussian lines to ULX spectra). Unfortunately, despite the similarity, all sources have slightly different relative ratios of wavelengths of their residuals:  $0.881^{+0.003}_{-0.004}$  for NGC 5204 X-1,  $0.849^{+0.015}_{-0.007}$  for Holmberg II X-1 and  $0.857 \pm 0.004$  for NGC 5408 X-1. The line ratios of Holmberg II X-1 and NGC 5408 X-1 are consistent, but mostly because the 13.9  $\text{\AA}$  feature in Holmberg II X-1 is rather weak and broad, hence the errors on its wavelength are large. The ratios of the first two objects are inconsistent with the line ratio of NGC 5204 X-1. Hence it seems very unlikely that the residuals correspond to identical elemental transitions in all 3 sources, (blue/red)shifted differently in each ULX as one could hope.

NGC 6946 X-1 has the softest spectrum from our ULX sample (Table 3.1), resembling that of the ULX/ULS source in NGC 55 (hardness ratio  $\sim 0.11$ ). In Fig. 3.14, we can see that both objects show a prominent O VIII emission line, which is blueshifted in NGC 55 ULX by a few hundred km/s. In the case of NGC 6946 X-1, the line is much wider but seems to be centred exactly on the rest-frame wavelength of O VIII. Additionally, both objects show other emission and absorption residuals, but none of them appear at the same wavelengths.

### 3.5.5 Contamination by host galaxy

Most of our sources have emission residuals right at the rest-frame wavelengths of oxygen VII and VIII transitions. The host galaxies of these ULXs emit in O VII and VIII and can potentially contaminate our results if the background subtraction is imperfect. This could be the case especially for galaxies with high star formation rates like NGC 6946, which are bright in this band ( $<1 \text{ keV}$ ). To check for such possibility, we take NGC 6946 X-1 as an example. We extract the source (background not subtracted) and the background spectrum, which is shown in Fig. 3.15. There is a small excess

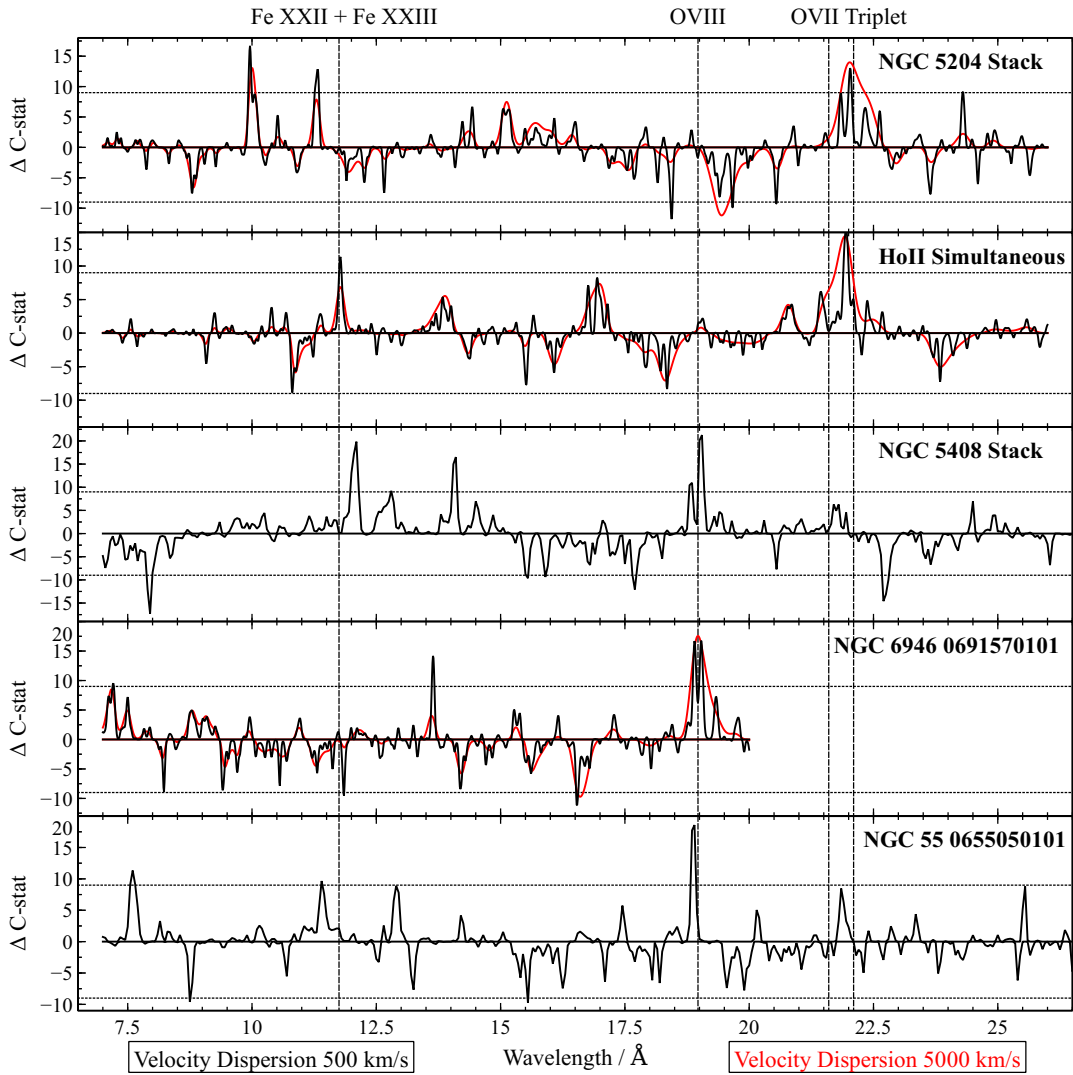


Fig. 3.14 Comparison between a Gaussian line search of the stacked scan of NGC 5204 X-1, the simultaneous scan of Holmberg II X-1, the stacked results of NGC 5408 X-1, and results from single observations of NGC 6946 X-1 and NGC 55 ULX. Axes are defined as in Fig. 3.2.

of flux around  $19 \text{ \AA}$  in the background spectrum, which is where the oxygen VIII transition is located, and also where we detect a significant emission residual in the ULX spectrum. However, the excess is too small to cause such a strong emission feature in our line scans even if partially underestimated (comparing with its strength in the NGC 6946 X-1 source spectrum). The source flux is about 2 times higher than the background flux in this energy band, hence it is unlikely that imperfect subtraction of galaxy emission could produce such a prominent spike in source spectrum.

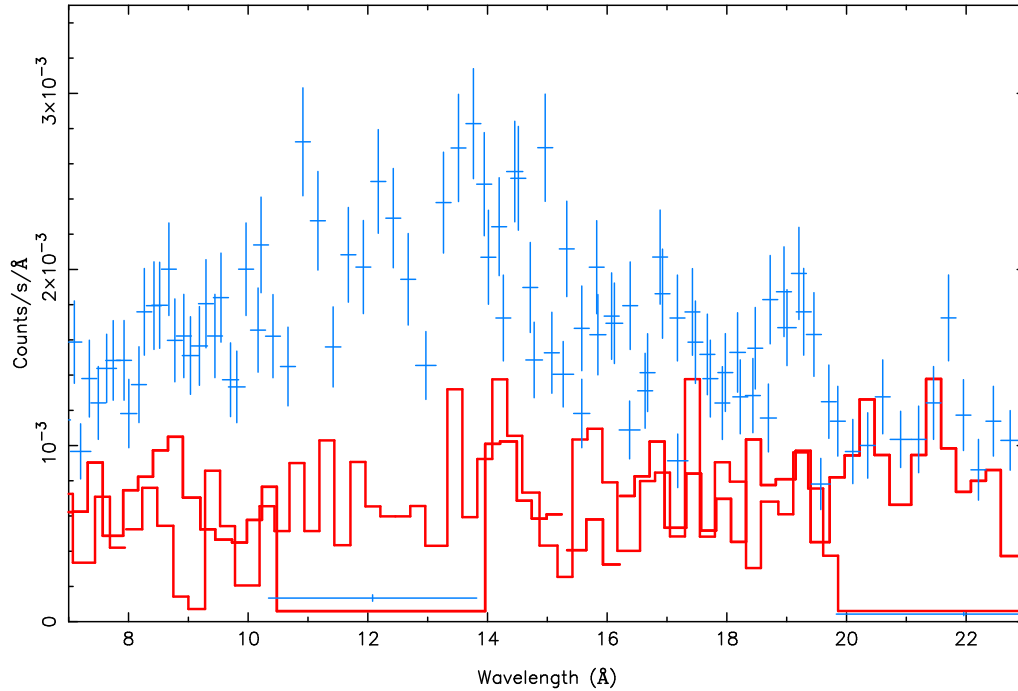


Fig. 3.15 Blue - source (background not subtracted) spectrum of NGC 6946 X-1 between 7 and 23 Å, red - background spectrum of the same object. Both RGS 1 and RGS 2 detector spectra are shown.

We perform a further check to be sure that the oxygen features do not originate in galaxy emission only. We extract a MOS 1 detector image of the NGC 6946 X-1 pointing and use the `rgsvprof`<sup>1</sup> procedure to create a total flux profile along the RGS slit, in the RGS energy band from 0.35 to 1.77 keV. Based on this, we obtain the expected spectral broadening of a line created by such flux profile. The broadening is caused by sources off-axis in the dispersive spectrograph (in the wavelength direction) whose spectrum is then shifted in energy/wavelength. We create the flux profile for both source and background slits and compare them. Based on the line profiles, we estimate a 10 % upper limit on galaxy contamination in the O VIII band.

<sup>1</sup><http://var.sron.nl/SPEX-doc/manual/manuale105.html>

### 3.5.6 Further studies

Our results show that with the current archival *XMM-Newton* data, we are able to tentatively detect narrow spectral features in most out of the 10 or so brightest ULXs in the sky. It also seems that, with one exception (NGC 5204 X-1), data available at the moment are insufficient in quality to distinguish between different emission and absorption models describing these features.

ULXs with well described outflows have been monitored for considerable amounts of time: over 400 ks of raw data in the case of NGC 1313 X-1 and  $\sim 800$  ks in the case of NGC 5408 X-1. The current generation of X-ray observatories is able to make a difference for the brightest ULXs given enough observing time. Unfortunately, no other ULX has been observed for such long periods of time up to date, and most have total exposures of only about 100 ks (but usually not a full uninterrupted *XMM-Newton* orbit) or below.

It is clear that more data are necessary to put further constraints on the presence of outflows in the spectra of ULXs. At the moment, we struggle with 2 issues using the RGS *XMM-Newton* data: not enough counts in spectra for narrow line studies, and high background levels below  $10 \text{ \AA}$  and above  $20 \text{ \AA}$ . The first problem is solved purely by further exposures, the second one requires long, uninterrupted observations. The latter can be partially compensated by stacking separate observations, but potential long-term variability issues may compromise the results (especially for the most variable ULXs). It would be also useful to re-observe some objects (like IC 342 X-1), which have already been observed by *XMM-Newton*, but with a roll angle that makes the RGS analysis impossible, for example due to contamination by other sources.

Observational time aside, if we believe the funnel theory of the accretion in ULXs [Fig. 13 of 304], some sources seem to be better candidates for a detection of outflow signatures than others. In Fig. 3.16, the  $\Delta C$ -stat significance of the strongest spectral feature found by the Gaussian line scan is shown versus the total clean exposure time of the source. The color scheme here defines the hardness ratio of the source as defined in Table 3.1. There are many different factors that affect the detection significance of features other than just the exposure time, yet we can see that all the soft sources from our sample (NGC 6946 X-1, Holmberg II X-1 and NGC 5204 X-1) have strong detections of features, while the harder sources show weaker detections despite some of them having enough observing time, like Holmberg IX X-1 (or counts like M33 X-8). It is difficult to draw any firm conclusions from the plot (which needs to be more densely populated with new observations and other sources), but soft ULXs seem to be good candidates for future spectral line and outflow searches.

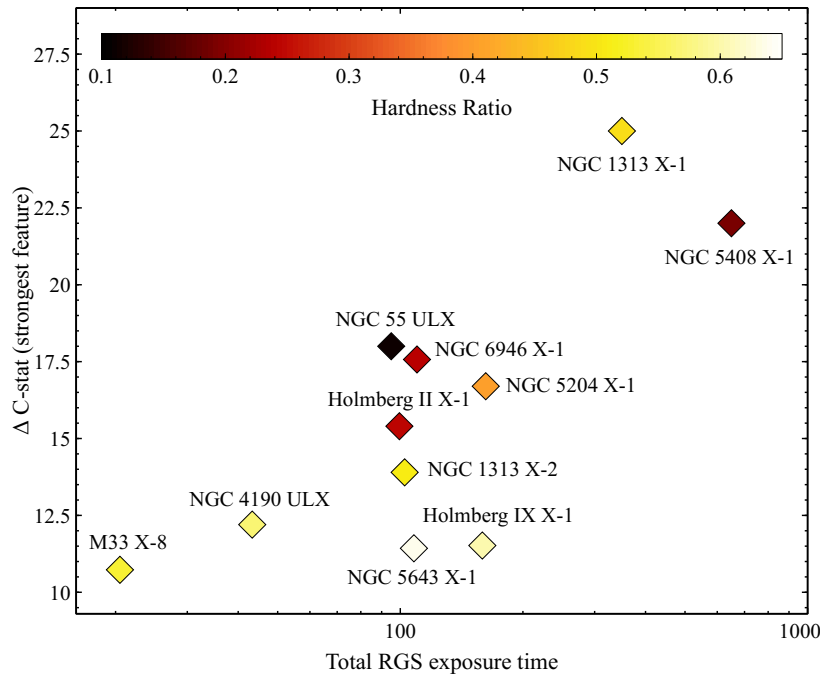


Fig. 3.16 Plot showing the significance (in  $\Delta C\text{-stat}$ ) of the strongest feature of a particular ULX versus the total clean RGS exposure time. Heat map shows the hardness ratio of the ULX (see Table 3.1). NGC 1313 X-1, NGC 5408 X-1 and NGC 55 ULX are not a part of our sample as they were studied by Pinto et al. [306] and Pinto et al. [304].

NGC 5204 X-1 is naturally the best source to start with. Our simulations show that a few hundred additional ks of *XMM-Newton* data should be sufficient to describe the observed spectral features to very high detail and significance. If the feature is indeed the blue side of a jet, the data should be of high enough quality to tentatively locate the red jet. This could be used to accurately determine the actual spatial orientation of the ULX. *Chandra* gratings, despite their lower collecting area, could be used to scan the higher energy band, where residuals (in CCD spectra) are seen as well, currently at a lower statistical significance. Similar approach could be chosen for other promising sources. Most importantly, full-orbit *XMM-Newton* observations (with proper alignment for the RGS detectors) will be crucial for further studies of ULX outflows, to both achieve the necessary total count amount, and constrain the background as well as possible.

A drawback of current instruments is that they both are dispersive spectrographs. Proper care is required when planning the observations to avoid contamination by other point sources in the field such as galactic binaries and AGN. Additionally, in

some cases the host galaxy contamination can also be an issue in the softest band ( $<0.7$  keV), especially when it is difficult to obtain a representative background region that would accurately constrain the galactic emission.

Future missions such as *XRISM* [Hitomi replacement, 383] and *ATHENA* [273] will be able to overcome this difficulty thanks to their calorimeters, albeit in the harder X-ray band ( $>1$  keV). *Arcus*<sup>2</sup>, if approved, despite being a dispersive spectrograph, would prove crucial in characterising ULX outflows thanks to its unprecedented spectral resolution and collecting area in the soft X-ray band ( $<1.2$  keV). These missions will naturally also require much less exposure time to achieve the expected results. They will also be capable of detecting outflows in ULXs at larger distances, thus increasing our sample size considerably.

## 3.6 Conclusions

We collected all the usable archival high spectral resolution data of ULXs. Aiming to find spectral features or directly outflows in ULX spectra, we performed Gaussian line scans, followed by Monte Carlo simulations of spectra and physical model scans for the most promising sources. We compared our results with the previous achievements in this field. Our results show that:

- In some sources, we discover several potential lines located at similar wavelengths to the rest-frame positions of the strongest lines of magnesium, iron and oxygen. Emission lines of these elements were previously detected in other ULXs such as NGC 1313 X-1 and NGC 5408 X-1.
- We find multiple strong emission residuals in the spectrum of NGC 5204 X-1. Most of these can be described by collisionally ionised plasma blueshifted to  $-0.34c$ . The significance of this detection is at least  $3\sigma$ . The detected features resemble the X-ray line emission from the Galactic microquasar SS 433, suggesting that this outflow might not be a UFO as observed in other ULXs but instead a collimated jet.
- Holmberg IX X-1 exhibits 2 interesting features. An emission residual at around  $8.5 \text{ \AA}$ , which could correspond to rest-frame Mg XII emission, and an absorption residual at around  $12.5 \text{ \AA}$ . We were able to fit the spectrum with a photoionised absorption model with outflow velocity of  $\sim 0.25c$ .

---

<sup>2</sup><http://www.arcusxray.org/>

- Holmberg II X-1 shows both absorption and emission residuals. The absorption features are only present in the highest quality observation, and when combined they are significant at about  $3\sigma$ . The two emission features are present in both observations and might correspond to iron (Fe XXII and/or Fe XXIII) and O VII emission.
- The spectrum of NGC 6946 X-1 shows a broad emission feature at  $19 \text{ \AA}$ , the rest-frame wavelength of an O VIII transition. The line is detected at over  $3\sigma$  in high resolution data. A similar, but narrower feature was previously detected in other ULXs such as NGC 5408 X-1 and NGC 55 ULX.
- All remaining sources show moderately strong emission or absorption residuals. However, at this stage we prefer not to claim identification of these features with outflows as more Monte Carlo simulations and new data are required.
- At the moment, we are limited by the data quality, more specifically by high background and low count number. Further uninterrupted and long observations are required to overcome both of these limitations. Full-orbit *XMM-Newton* observations and deep *Chandra* data will be crucial in further studies to discover and study ULX outflows in more detail. Future missions such as *XRISM*, *Arcus* and *ATHENA* will also be able to achieve much better results with considerably less exposure time and for a larger sample of ULXs.
- The limited statistics on outflows in ULXs and the current data quality do not allow us to estimate the occurrence of UFO phenomena in ULXs. However, this work is an important pilot programme for future studies in this area which will utilise larger and deeper high spectral resolution X-ray datasets.

## Chapter 4

**Evidence for a variable ultrafast  
outflow in the newly discovered  
ultraluminous pulsar NGC 300  
ULX-1**



# Abstract

Ultraluminous pulsars are a definite proof that persistent super-Eddington accretion occurs in nature. They support the scenario according to which most ULXs are super-Eddington accretors of stellar mass rather than sub-Eddington intermediate mass black holes. An important prediction of theories of supercritical accretion is the existence of powerful outflows of moderately ionized gas at mildly relativistic speeds. In practice, the spectral resolution of X-ray gratings such as RGS onboard *XMM-Newton* is required to resolve and unambiguously identify their observational signatures in ULXs. Using RGS, outflows have been discovered in the spectra of 3 ULXs (none of which are currently known to be pulsars). Most recently, the fourth ultraluminous pulsar was discovered in NGC 300. In this chapter, I present the detection of an ultrafast outflow in the X-ray spectrum of the object, with a significance of more than  $3\sigma$ , during one of the two simultaneous observations of the source by *XMM-Newton* and *NuSTAR* in December 2016. The outflow has a projected velocity of 65000 km/s ( $0.22c$ ) and a high ionisation factor  $\log(\xi/\text{erg cm s}^{-1})$  of 3.9. This is the first direct evidence for a UFO in a neutron star ULX and also the first time that this its evidence in a ULX spectrum is seen in both soft and hard X-ray data simultaneously. We find no evidence of the UFO during the other observation of the object, which could be explained by either clumpy nature of the absorber or a slight change in our viewing angle of the accretion flow.

## 4.1 Introduction

As of the end of 2017, none of the neutron star ULXs were known to possess ultrafast outflows. This was probably caused by observational difficulties - out of the 3 PULXs known by the end of 2017, only 1 was suitable for a high-resolution X-ray analysis with the current generation of instruments. The remaining 2 are either too distant or located in a crowded field. Furthermore, the ULXs with detected pulsations are likely the most face-on oriented ULXs (i.e. the inclination between our line of sight

and the ULX accretion disc axis is small) as this orientation simplifies the detection of pulsations since it offers a clear view towards the central accretion column. This could mean that any potential outflows in PULXs might not cross our line of sight towards the inner accretion flow due to the system inclination, in which case they would not produce any absorption lines in ULX spectra.

However, in January 2018, the 4th ultraluminous pulsar was discovered in NGC 300 [44, 45] and named NGC 300 ULX-1. The object was originally mis-identified as a supernova and named SN2010da [267, 92] but later identified as a likely supergiant B[e] high-mass X-ray binary [28, 210, 410]. It has only recently been observed at ULX luminosities, and is experiencing an extremely fast spin-up [186], having spun-up from a rotational period of 45 s to just 20 s in less than 2 years. Furthermore, Walton et al. [415] discovered a potential cyclotron resonant scattering feature in the hard X-ray spectrum of the object.

Here we perform a rigorous, in-depth analysis of the coordinated *XMM-Newton* and *NuSTAR* data on NGC 300 ULX-1 from December 2016, searching for spectral signatures of an ultrafast outflow in this system. We use simple Gaussian line scans as well as automated searches with physical models of outflowing photoionised absorbers and quantify the statistical significance of detections with Monte Carlo simulations. We detect a variable UFO with a projected velocity of  $0.22c$  in the spectrum of the object with a significance of more than  $3\sigma$ .

The structure of this chapter is as follows. Section 4.2 contains information about the observations of the source and data reduction. We present the methods and results in section 4.3 and discuss their implications in section 4.4. Finally, section 4.5 summarizes our findings.

## 4.2 Observations and data reduction

We used data from *XMM-Newton* and *NuSTAR*. There are multiple observations of the object by the *Swift* satellite, but their data quality (photon counts) is not sufficient for a search for ultrafast wind in a ULX.

As of February 2018, there are two simultaneous observations of the source by *NuSTAR* and *XMM-Newton* taken very shortly within each other in December 2016. The *XMM-Newton* exposures are separated by a 10 hour window because of the satellite's orbit. The first one is about 140 ks of raw time long, the exposure of the second one is about 80 ks of raw time. *NuSTAR* observed the object at the same time, for a total duration of about 320 ks ( $\sim 160$  ks exposure time). We extracted the

Table 4.1 Log of the observations used in this work.

Instrument	Obs ID	Start time	Clean exposure <sup>a</sup> ks
<i>XMM-Newton</i>	0791010101	2016-12-17 08:52	134/96/120
<i>XMM-Newton</i>	0791010301	2016-12-19 08:44	77/46/65
<i>NuSTAR</i>	30202035002	2016-12-16 15:31	163

<sup>a</sup>*XMM-Newton* exposures are listed as RGS/PN/MOS exposure.

spectra of each of the *XMM-Newton* observations separately, without any stacking during the analysis, and also extracted 2 *NuSTAR* spectra from time intervals that are simultaneous with the *XMM-Newton* observations to take into account possible variability of the object (albeit its count rate,  $\sim 0.9$  counts/s with the PN instrument, is very similar during both observations). Further info about the exposures is shown in Table 4.1.

We obtained the object distance of 2 Mpc by averaging newer measurements on the NED database.

#### 4.2.1 *XMM-Newton*

All the *XMM-Newton* [166] data were downloaded from the XSA archive and reduced using a standard pipeline with SAS v16, CalDB as of January 2018. We follow the standard routines for data reduction described in section 2.1. We use data from all X-ray instruments onboard *XMM-Newton*: the EPIC PN [378] and MOS [400] CCDs, and the RGS detectors [72]. The source regions for PN and MOS 1,2 were circles centred on the ULX with a radius of 40 arcsec. Unfortunately, the position of the ULX is right on a chip gap of the PN chip, so the data might be partly compromised. This is why we also use MOS 1 and 2 data which are unaffected by this issue. However, the agreement between PN and MOS spectra is very good, hence the PN chip gap position is probably not a problem. The background regions were circles located in the same region of the chip (and avoiding the copper ring and out of time events on the PN chip), with a radius of 50 arcsec.

*XMM-Newton* was not pointed directly at the object and therefore we cannot use the default selection of source and background regions for the RGS detectors. The default source region is pointed on the X-ray binary NGC 300 X-1 (at a distance of about 1.1 arcmin from NGC 300 ULX-1). We chose a source region centred on the position of NGC 300 ULX-1 (Fig. 4.1), with a size such that it covers 90 per cent of the instrument PSF in the cross-dispersion direction. The background region is

a rectangle shifted by 1.4 arcmin in the cross-dispersion direction, with a size that includes 95 percent of the PSF, avoiding the flux from NGC 300 X-1 and at the same time maximizing its area to constrain the background as well as possible.

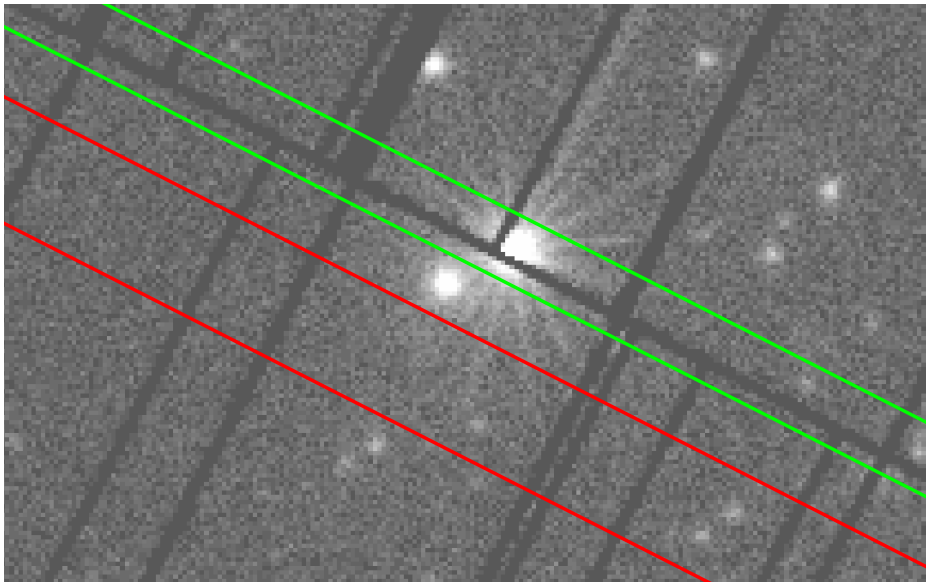


Fig. 4.1 RGS extraction regions shown on the EPIC PN image of the exposure (0791010301). The source extraction region is in green colour, the background region is in red. Both regions avoid contamination by the X-ray binary NGC 300 X-1 (in the centre of the image).

We grouped the PN, MOS 1 and MOS 2 data to at least 25 counts per bin and also rebinned the original EPIC channels by at least a factor of 3. RGS data were binned by a factor of 3 to oversample the spectral resolution by about a factor of 3. The spectral range used was: 0.3 to 10 keV for PN data, 0.3 to 9.8 keV for MOS, initially 7 Å (1.8 keV) to 26 Å (0.5 keV), and later only 7 to 20.5 Å (0.6 keV) for RGS data, mostly limited by the background level and the calibration uncertainties of the instruments.

#### 4.2.2 *NuSTAR*

We reduced the *NuSTAR* [148] data following standard procedures using the *NuSTAR* Data Analysis Software (NUSTARDAS, v1.8.0) and instrumental calibration files from CalDB v20171204. We first cleaned the data with NUPIPELINE, using the standard depth correction, which significantly reduces the internal high-energy background, and also removed passages through the South Atlantic Anomaly (using the settings SAA-CALC=3, TENTACLE=NO and SAAMODE=OPTIMIZED). Source and background spectra and instrumental responses were then produced for each of the two focal plane

modules (FPMA/B) using NUPRODUCTS. Source products were extracted from circular regions of radius  $40''$ , and background was estimated from larger regions of blank sky on the same detector as ULX-1. In order to maximise the signal-to-noise (S/N), in addition to the standard ‘science’ (mode 1) data, we also extracted the ‘spacecraft science’ (mode 6) data following the method outlined in Walton et al. [422]. In this case, mode 6 provides  $\sim 10\%$  of the good *NuSTAR* exposure.

## 4.3 Methods and results

In this section, we describe the methods we used to study the data and show the results of our analysis. We note that all the subsections except for the last one only use the data taken during the second *XMM-Newton* observation of the object (ID 0791010301) alongside with simultaneous *NuSTAR* data. We also performed the same analysis on the first dataset (ID 0791010101) but find no evidence for ultrafast wind.

### 4.3.1 Broadband modelling

We use the SPEX fitting package [177] for spectral fitting, and C-statistics [47] as there are not enough counts per bin in RGS data for a  $\chi^2$  analysis. All the model parameters are checked extensively with a proper error search in case there are multiple minima in the C-stat function. The statistical error intervals are calculated at  $1\sigma$  level (68 per cent confidence).

We fit the broadband X-ray spectrum of the object with a phenomenological model which consists of a powerlaw (POW in SPEX) plus a simple blackbody (BB) plus a color corrected blackbody (MBB). Similar spectral models have been used by Gladstone et al. [140] and Walton et al. [416] and describe the ULX continuum reasonably well. We also test alternative descriptions of continuum such as a disk blackbody component and find that the results of our analysis do not change significantly. All the emission is absorbed by Galactic and host galaxy (mostly) neutral interstellar medium (ISM) accounted for by the HOT component [see 178, for an example of similar usage of the model]. The Leiden/Argentine/Bonn Survey of Galactic HI [179] shows that there should be a column density of about  $4 \times 10^{20} \text{ cm}^{-2}$  towards the host galaxy NGC 300.

We use all available data for this observation from RGS, PN, MOS (1 and 2) and FPM (A and B) detectors to constrain the broadband continuum as well as possible. A cross-normalisation constant is added for each instrument to account for small ( $< 10$  per cent) calibration uncertainties of each detector. The best-fit model is a powerlaw

with a hard slope of  $1.51_{-0.21}^{+0.12}$ , a soft blackbody with a temperature of  $0.231_{-0.007}^{+0.008}$  keV and a color-corrected blackbody with a temperature of  $2.67 \pm 0.07$  keV. We obtain the ISM column density of  $2.7_{-1.3}^{+1.1} \times 10^{20}$  cm $^{-2}$ . The fit statistic is C-stat=1545.87 for 1347 degrees of freedom. The unabsorbed 0.3 to 10 keV luminosity of the ULX during this epoch inferred by fitting the spectral components is about  $3 \times 10^{39}$  erg s $^{-1}$ .

### 4.3.2 Line search

Initially, we performed a simple Gaussian scan using the RGS data only by following the steps in section 2.2.1. We aimed to find any possible narrow absorption and emission features that an outflow might imprint on the continuum spectrum of NGC 300 ULX-1. We used the EPIC broadband coverage to anchor the spectral continuum outside the RGS band, between 0.3 and 10 keV with the exception of the 7 to 26 Å region (approximately 0.5 to 1.8 keV).

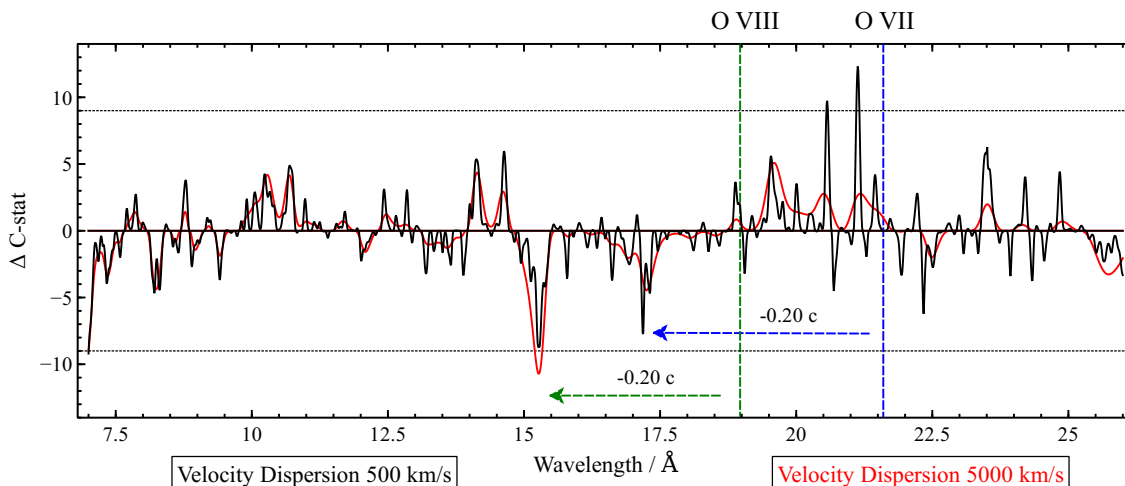


Fig. 4.2 Gaussian line search results of RGS data from the second *XMM-Newton* observation (0791010301). The black curve shows the line search using a velocity dispersion of 500 km/s, while the red curve shows the search assuming 5000 km/s. The Y axis is defined as  $\Delta$ C-stat times the sign of the line normalisation to show the difference between absorption and emission features. Horizontal dotted lines show the values of  $\Delta$ C-stat=9 and -9. The rest-frame wavelengths of emission lines of the O VIII and O VII ions (taking the average of the triplet wavelength) are shown with green and blue dashed lines. Green and blue dashed arrows show the potential blueshift of the absorber if the potential features are produced by O VII and O VIII absorption.

We perform the Gaussian line scan on the RGS data of the second *XMM-Newton* observation (ID 0791010301) of the object using 2 different turbulent velocities: 500

km/s and 5000 km/s. The results are shown in Fig. 4.2. We notice that there are no very strong features ( $\Delta C\text{-stat} > 15$ ) in the spectrum. However, there is an absorption signature at around  $15.3 \text{ \AA}$  (0.81 keV) that could originate in blueshifted oxygen VIII absorption. The rest-frame wavelength of this transition is  $19 \text{ \AA}$  so the corresponding blueshift would be around  $0.2c$ . Curiously, there is another, weaker absorption feature at  $17.2 \text{ \AA}$  (0.72 keV), that, if produced by O VII ions, would give the absorber blueshift of around  $0.2c$  as well (see Fig. 4.2), assuming that the resonant line at the rest-frame wavelength of  $21.6 \text{ \AA}$  would dominate the absorption. This motivates us to follow-up with a more rigorous search, using a physical model of the absorber.

Additionally, there seem to be a few emission lines between 20 and  $22 \text{ \AA}$  in the line scan, however they are quite narrow and located in the energy band ( $>20 \text{ \AA}$ ) which is partially affected by the background. They are also not located on a rest-frame wavelength of any expected transition.

### 4.3.3 Physical model search

Finding two features that could correspond to the same blueshift encourages us to try to fit the features with a physical photoionised absorption model. We use the XABS model in SPEX to describe the absorption of outflowing photoionised gas [372] and find the best fit at a speed of  $66000 \pm 1000 \text{ km/s}$  ( $0.220 \pm 0.003 c$ ), with a column density of about  $10^{21} \text{ cm}^{-2}$ , the ionisation parameter with a  $\log(\xi/\text{erg cm s}^{-1})$  of 2.1 and a turbulent velocity of  $\sim 2000 \text{ km/s}$ . The  $\Delta C\text{-stat}$  fit improvement is relatively modest at about 13.5.

However, upon closer inspection of the data we also notice weak absorption features in the  $>2 \text{ keV}$  PN spectrum (Fig. 4.4). These could be unresolved absorption lines of higher energy transitions, not unlike those seen in some AGN, for example IRAS 13224-3809 [294]. This suggests the possibility that the wind might actually be much more ionised than the best-fit RGS solution and that more information could be hidden in the higher energy CCD data. For this reason, we use all the data available: PN, MOS 1 and 2 data from the second *XMM-Newton* observation of the object, plus we extract spectra from *NuSTAR* FPMA and FPMB instruments for the time duration of this observation.

To locate any possible solutions, we perform an automated scan with the XABS model by following the steps described in section 2.2.2. We use the broadband continuum obtained in section 4.3.1. The parameter space we search through is the following: the blueshift of the absorber between 0 and 120000 km/s, its ionisation parameter between 1.5 and 4.5, and its turbulent velocity between 250 and 5000 km/s. We choose

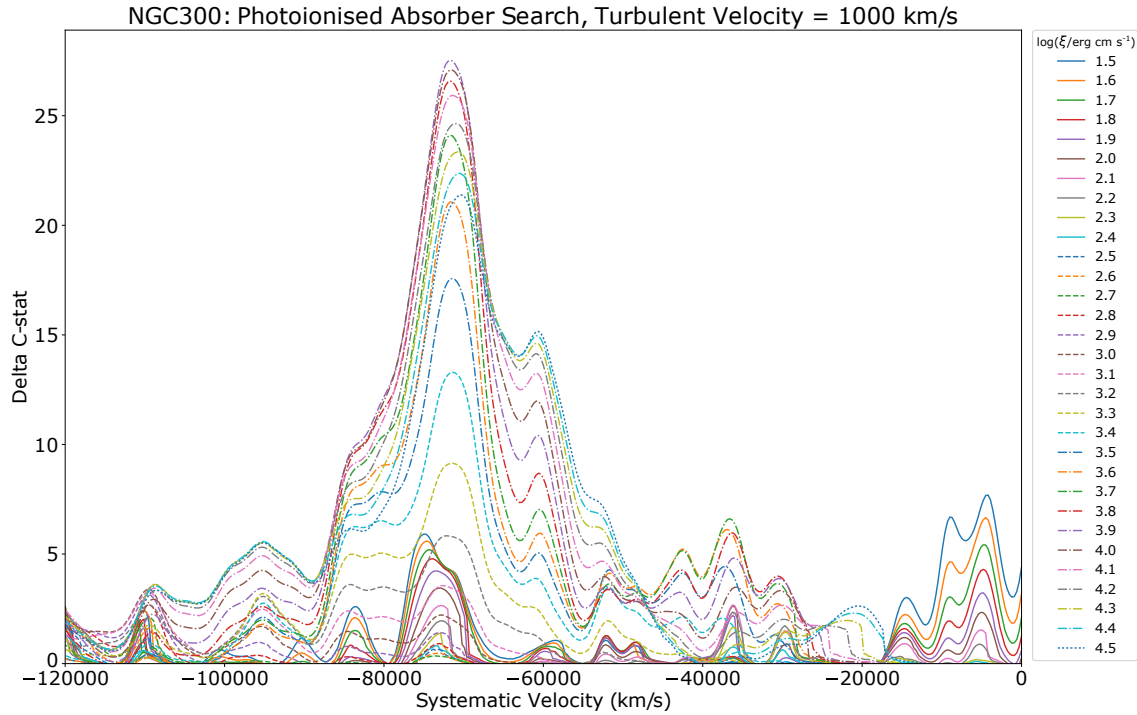


Fig. 4.3 Automated scan of all available data using a photoionised absorber model XABS with a fixed turbulent velocity of 1000 km/s. The X-axis shows the systematic velocity of the absorber, while the Y-axis gives the  $\Delta C$ -stat statistical fit improvement achieved by adding this component to the broadband continuum spectrum. Curves of different colours show automated searches with different values of the ionisation parameter which is kept frozen during the search.

the blueshift grid steps of 300 km/s, which oversamples slightly the RGS detector resolution, ionisation parameter steps of 0.1 and use 3 turbulence velocities: 250, 1000 and 5000 km/s. The results of the 1000 km/s turbulence velocity search are shown in Fig. 4.3. One can immediately notice the large fit improvement of about  $\Delta C\text{-stat}=27.5$  at  $\sim 70000$  km/s ( $\sim 0.23c$ ), for a scan with the ionisation parameter of  $\log(\xi/\text{erg cm s}^{-1}) = 3.9$ . The scans with other turbulent velocities do not show such large fit improvements at any systematic velocity and for any ionisation parameter.

We explore this solution in more detail by direct fitting in SPEX using all the available data. All the uncertainties are reported at  $1\sigma$  level. The results are shown in Table 4.2. The best-fit solution shows the absorber outflowing at a projected (relativistically-corrected) speed of  $65100_{-2200}^{+1000}$  km/s ( $0.217_{-0.007}^{+0.004} c$ ). Its column density is  $1.2_{-0.6}^{+1.9} \times 10^{23}$  cm $^{-2}$ , ionisation parameter is  $\log(\xi/\text{erg cm s}^{-1}) = 3.92_{-0.13}^{+0.19}$  and the

Table 4.2 Best-fitting spectral parameters of NGC 300 ULX-1.

Ionised wind			
$N_{\text{H}}$ $\text{cm}^{-2}$	$\log(\xi/\text{erg cm s}^{-1})$	Turbulent velocity km/s	Systematic velocity km/s
$1.2_{-0.6}^{+1.9} \times 10^{23}$	$3.92_{-0.13}^{+0.19}$	$800_{-500}^{+1100}$	$65100_{-2200}^{+1000}$
Broadband continuum			
ISM $N_{\text{H}}$ $\text{cm}^{-2}$	$\Gamma$	Soft blackbody keV	Hard blackbody keV
$(3.6 \pm 1.2) \times 10^{20}$	$1.61_{-0.13}^{+0.11}$	$0.231_{-0.008}^{+0.007}$	$2.73_{-0.07}^{+0.08}$

turbulent velocity is  $800_{-500}^{+1100}$  km/s. The continuum parameters are: powerlaw slope of  $1.61_{-0.13}^{+0.11}$ , blackbody temperatures  $0.231_{-0.008}^{+0.007}$  keV and  $2.73_{-0.07}^{+0.08}$  keV, and ISM column density of  $(3.6 \pm 1.2) \times 10^{20} \text{ cm}^{-2}$ . We find the statistical fit improvement of  $\Delta\text{C-stat}=27.59$ . The spectrum fitted with the photoionised absorber is shown in Fig. 4.4 (CCD data) and Fig. 4.5 (RGS data). The strongest features of the absorber are iron absorption at 8-9 keV and oxygen absorption at 0.8 keV. We assume Solar abundances of elements [220] when fitting the XABS model.

To explore whether each detector agrees with this wind solution, we remove one instrument in turn from our analysis and perform the continuum and the continuum + wind spectral fit, calculating the  $\Delta\text{C-stat}$  fit improvement between these 2 fits. Removing RGS data reduces our fit improvement upon adding the wind to the broadband continuum to  $\Delta\text{C-stat}=22.31$ . Removing PN data alone reduces the fit improvement to  $\Delta\text{C-stat}=21.76$ , removing both MOS detectors decreases it to just  $\Delta\text{C-stat}=17.44$  and finally removing only FPM data decreases the fit improvement to  $\Delta\text{C-stat}=21.33$ . The fact that removing any of the individual instruments from the analysis reduces the fit improvement  $\Delta\text{C-stat}$  suggests that the wind signatures are present in all instruments, and hence they are not just Poisson noise.

The ultrafast wind is variable on relatively short timescales of tens of ks (see section 4.3.5) and it is possible that the wind is only present for a fraction of the observation (albeit the lightcurves do not show any significant flux change during the observation). To explore this possibility, we split the observation into halves by exposure time. Then we fit each half separately with the continuum and the continuum + wind model (as done with full data). We find that the wind signatures are slightly stronger in the second half of the observation, but the fit improvement is much lower due to decreased

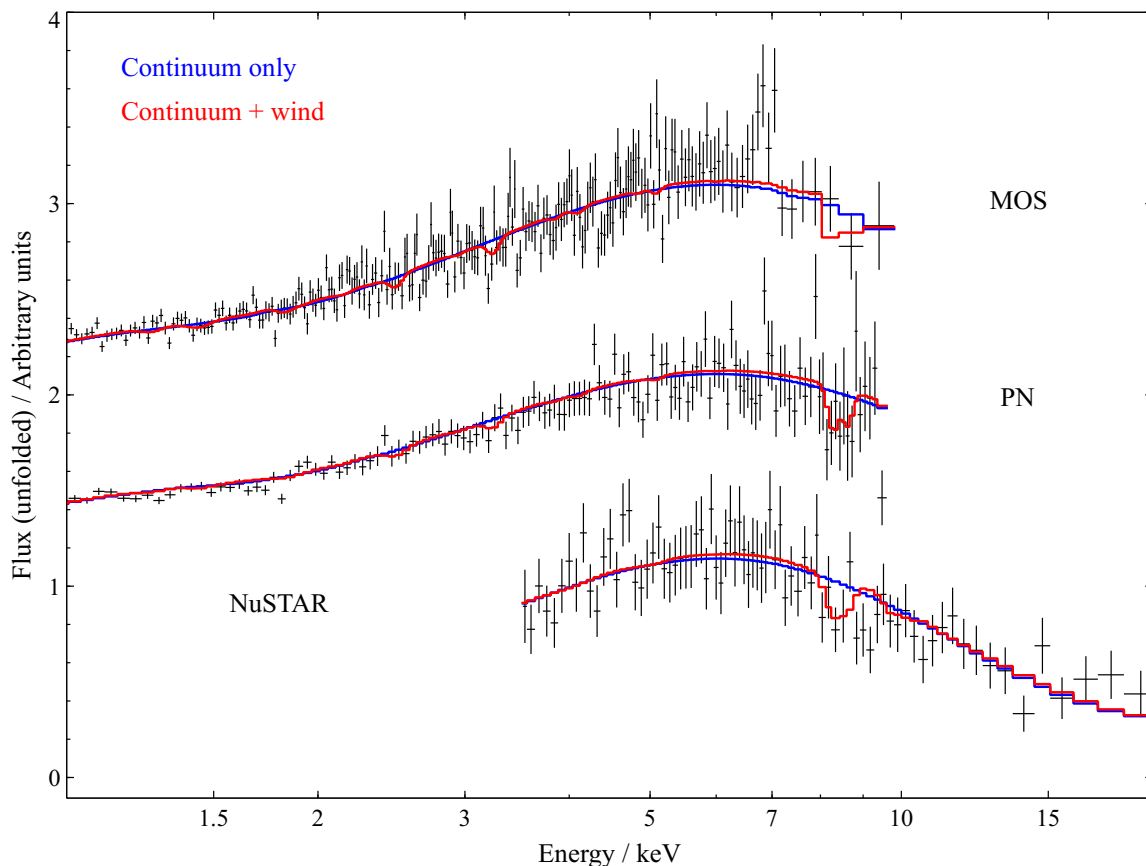


Fig. 4.4 The X-ray spectrum of the source during the second *XMM-Newton* observation with simultaneous *NuSTAR* data. The Y-axis shows the source flux unfolded (with a constant), different instruments are shifted by constant amounts for plotting purposes. The continuum only model is shown in blue colour, the continuum plus outflow model is in red. Data are stacked (MOS, FPM) and overbinned for plotting purposes.

statistics. Hoping to increase the S/N ratio, we also cut out the first quarter and only fit the last 3 quarters of the observation exposure. This does not help either, the fit improvement is still weaker compared to the result achieved using the full dataset.

The MOS and PN spectra of the source also show hints of emission features, maybe with a P-Cygni profile. To see if they can be fitted with a consistent systematic velocity, we perform automated scans using physical emission models. We use a photoionised emitter model, PHOTEMIS in XSPEC, to represent emission from photoionised outflowing gas. Similarly, we use a collisionally ionised emitter model, CIE in SPEX, to describe emission from shocked gas. We run the automated scans in the same fashion as the photoionised absorber search. However, none of these show a significant statistical fit improvement. The maximum fit improvement obtained was  $\Delta C\text{-stat} \sim 14$  only.

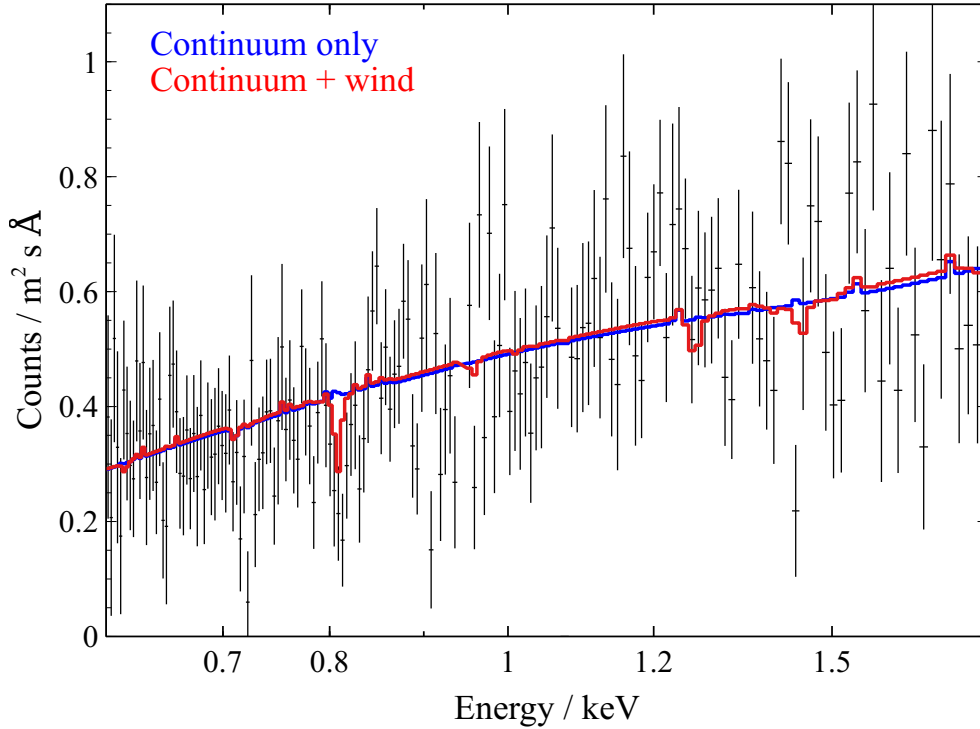


Fig. 4.5 RGS spectrum during the second *XMM-Newton* observation of the source. The Y-axis shows the source flux unfolded with a constant. The continuum only model is shown in blue colour, the continuum plus outflow model is in red. Data from RGS1 and RGS2 detectors are stacked and overbinned for plotting purposes.

#### 4.3.4 Significance of the wind detection

In the previous section, we show the possible detection of a relativistic outflow in the spectrum of NGC 300 ULX-1. However, it is not straightforward to rigorously assess its statistical significance. We obtained a relatively large  $\Delta C$ -stat value of 27.59, which by itself would give a very high  $\sigma$  significance, but it does not take into account the number of trials undertaken to find this solution. We will try to obtain the proper significance using 2 different approaches: with theory and with Monte Carlo simulations.

In theory, a search for spectral features of ionised absorption on a noisy continuum can be viewed as follows: we have a number of free parameters in addition to the broadband continuum, which we fit for in each step. In our case (section 4.3.3), there is just 1 variable: the column density of the absorber. The systematic velocity, the turbulent velocity and the ionisation parameter are all fixed in each fit, and then varied in a multi-parameter grid. Hence there is 1 additional degree of freedom compared to a continuum fit. Then we move the systematic velocity of the absorber and repeat the

fit, and similarly we repeat the whole procedure in the grid of turbulent velocities and ionisation parameters. Effectively, we perform  $N$  trials with 1 degree of freedom for the presence of an absorber in our spectrum, where  $N$  is the number of points in our multi-parameter grid. This increases the null hypothesis probability of receiving a fit improvement, i.e. interpreting Poisson noise as a real detection.

To assess the null hypothesis probability, we perform the  $\chi^2$  test. We group the RGS data by 20 counts per bin to achieve Gaussian-like statistics. For this part only, we stack the RGS detectors into a single spectrum to avoid overbinning any narrow spectral features. Data from the remaining instruments are already binned up so we can use  $\chi^2$  statistics instead of C-stat when fitting. Repeating the same direct fit to all data as in the previous section, we achieve a fit improvement of  $\Delta\chi^2 = 29.68$  upon adding the photoionised absorber to broadband continuum. Our single trial p-value for such  $\Delta\chi^2$  with 1 degree of freedom is about  $5.1 \times 10^{-8}$  (obtained by integrating the  $\chi^2$  probability density function). This is the probability of obtaining such fit improvement from spectral features introduced by noise only, if we performed just one measurement. We repeat the trial  $N = 401 \times 31 \times 3 = 37293$  times (the size of our multi-parameter grid - 120000 km/s velocity range divided into bins spaced by 300 km/s, ionisation parameters between 1.5 and 4.5 spaced by 0.1, and 3 different turbulent velocities), which brings up the null hypothesis probability to  $(5.1 \times 10^{-8}) \times 37293 = 0.19$  per cent. The significance of our detection is therefore around 99.81 per cent or  $3.1\sigma$ . We do stress, however, that this value needs to be taken cautiously. It rather serves as a lower limit on the statistical significance as it assumes that all the trials were completely independent of each other, i.e. for example it assumes the finite instrument spectral resolution has no effect. Monte Carlo simulations will give a more realistic estimate.

We also perform Monte Carlo simulations to assess the significance of the wind detection in a rigorous way. We simulate a fake continuum spectrum using the real source continuum model (accounting for uncertainties in continuum parameters when simulating the spectrum). Ideally, afterwards we would perform the same automated search on fake data and count the number of wind detections stronger than the one found in real data. Unfortunately, it is not possible to do several thousands of simulations (to test a  $3\sigma$  significance) with proper error search, neither with the wind parameters (ionisation, turbulent velocity) being left free nor fixing them but having to create a grid of these parameters (as done with real data). Either of these approaches would require well above 100000 CPU hours. Making the systematic velocity grid significantly coarser is not an option either, since we could possibly miss a detection driven by the RGS data which has the highest spectral resolution. We instead devise a new approach,

in which we separate the ionisation parameter space into 3 intervals, where  $\log(\xi/\text{erg cm s}^{-1})$  is left free to vary: 1.5 to 2.5, 2.5 to 3.5 and 3.5 to 4.5, and free the turbulent velocity (but limit it to between 250 and 5000 km/s). Then we perform the automated search on the same simulated dataset in the 3 different  $\xi$  intervals. Finally, the highest  $\Delta\text{C-stat}$  fit improvement is recovered out of these 3 scans at each systematic velocity. This way we speed up the search process considerably, as well as reasonably assure no sensible parameter space is left unexplored (such as the fit falling into a local C-stat minimum and not discovering the global one). We made sure that this procedure finds the same features in real data as the original automated search. In the end, the required computational time to run 5000 Monte Carlo simulations with the wind model XABS is of the order of 10000 CPU hours (using a recent quad core i7 Intel CPU).

Out of the 5000 performed MC simulations, only one has a  $\Delta\text{C-stat}$  fit improvement higher than 27.59, which was the highest  $\Delta\text{C-stat}$  value found in the real data XABS search using both the grid and the sped-up 3  $\xi$  interval approach. This means, taking into account the total number of simulations, that the significance of the detection is around 99.98 per cent ( $\sim 3.7\sigma$ ), much higher than  $3\sigma$ . For a  $3\sigma$  detection (corresponding to a false alarm probability of 0.27 per cent), the expected number of outliers equal or stronger than real data is 13. However, further simulations would be necessary to quantify the precise statistical significance. We note a good consistency between the result from the Monte Carlo simulations and our theoretical estimate which gives us a lower limit ( $3.1\sigma$ ) on the significance simply given by the total number of trials performed by the automated search for photoionised absorber. Fig. 4.6 contains a histogram comparing the  $\Delta\text{C-stat}$  values of the photoionisation grid search on real and simulated spectra. The histograms of the real data and simulated data scans strongly deviate, suggesting the significance of our detection of a fast ionised outflow in the spectrum of NGC 300 ULX-1.

### 4.3.5 The first *XMM-Newton* observation

We extracted a spectrum of the object using all instruments during the first observation of *XMM-Newton* (0791010101). A *NuSTAR* spectrum was also obtained for the same time interval. The flux of the source is very similar to its flux during the first observation, and the best-fit continuum spectral parameters are practically identical to those measured during the second observation (using the same continuum model). We perform the same Gaussian line scan (Fig 4.7) and a physical wind search as we did with the second observation but find no signs of the outflow at all. There is no evidence for outflow neither at the same systematic velocity, nor at any similar velocity

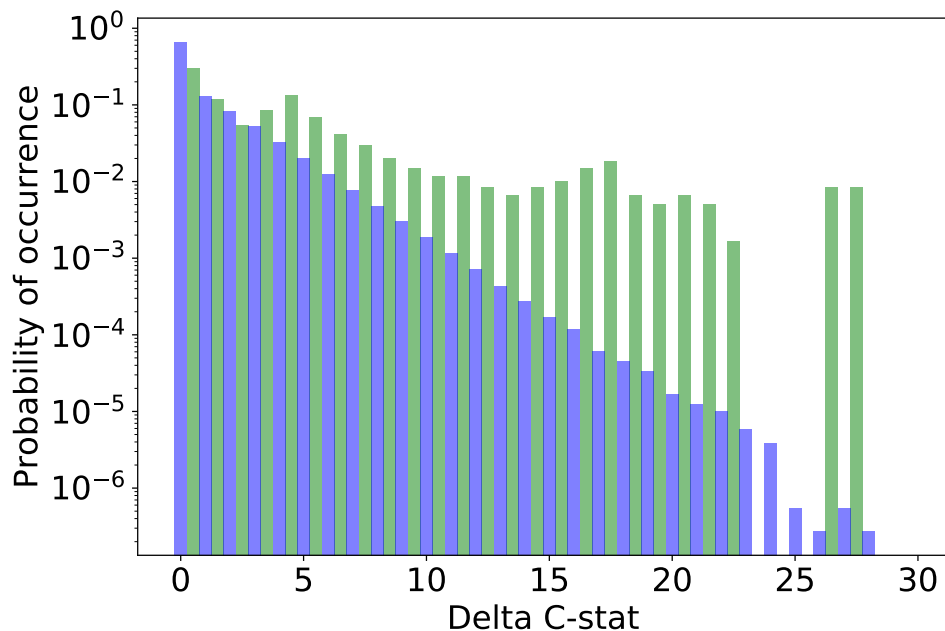


Fig. 4.6 Histogram of  $\Delta C$ -stat of the real XABS outflow scan of NGC 300 ULX-1 (green) and of XABS scans of 5000 Monte Carlo simulated datasets (blue). The Y axis is the probability density function, the integral of which is 1, and the X axis is the  $\Delta C$ -stat value.

for any reasonable ionisation parameter  $\xi$  and turbulent velocity  $v$ . The upper limit ( $1\sigma$ ) on the column density of an absorber with the same ionisation, systematic and turbulent velocity as in the other observation is  $0.2 \times 10^{23} \text{ cm}^{-2}$ .

## 4.4 Discussion

We performed an analysis of the simultaneous *XMM-Newton* and *NuSTAR* data of the pulsating ULX NGC 300 ULX-1, which was taken in December 2016. We detect an ultrafast outflow in the spectrum of this object with a significance of more than  $3\sigma$ . The fact that this significance is achieved by using 4 different instruments strengthens the credibility of the result. In addition, the statistical significance decreases upon removing any instrument from the analysis - which suggests that all the 4 different instruments individually prefer the wind solution. It is currently not possible to quantify the precise significance of the detection as this would require an extensive number of

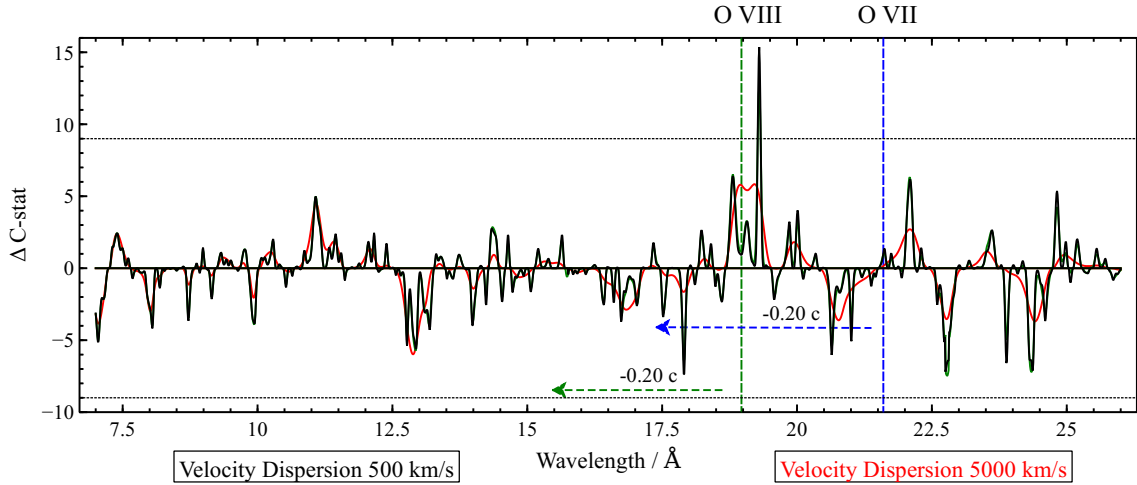


Fig. 4.7 Gaussian line search results of RGS data from the first *XMM-Newton* observation (0791010101). The Y axis is defined as  $\Delta C\text{-stat}$  times the sign of the line normalisation to show the difference between absorption and emission features. There are no strong ( $\Delta C\text{-stat} > 9$ ) absorption residuals at the same systematic shift ( $-0.2c$ ) of the O VII and O VIII lines (shown with green and blue arrows) as seen in the other observation, or at any other wavelengths.

MC simulations. However, the current number of simulations performed already gives a very tight limit on the p-value of our result.

This is the first direct evidence of an ultrafast wind in a pulsating ULX. Also it is the first time that the evidence is seen in a ULX spectrum in both soft and hard X-ray detectors simultaneously, and fitted using a single physical model of the outflow. Walton et al. [417] achieved a  $3\sigma$  detection of a possible iron K component to the wind in NGC 1313 X-1 [306], but did not show a consistent fit of both soft and hard features at once.

The presence of a strong wind is consistent with the existence of super-Eddington accretion flow beyond the magnetosphere of the neutron star. The wind might be launched from this optically and geometrically thick part of the disk. If this is the case, the fact that the absorption is seen in both low- and high-energy X-ray data likely suggests that the absorption from this wind is imprinted on the emission from both the disk and the central accretion column [414].

Comparing with other ULXs with known outflows, the speed of 65000 km/s (about  $0.22c$ ) does not stand out as other ULXs have winds at  $0.20\text{-}0.27c$ . A turbulent velocity of about 1000 km/s is also similar to what is observed in other objects. The ionisation parameter  $\xi$ , however, which is about  $\log(\xi/\text{erg cm s}^{-1}) = 3.9$ , is higher than most best-fit solutions for the wind ionisation in the 3 other ULXs. The only exception is

NGC 1313 X-1, where an outflow with  $\log(\xi/\text{erg cm s}^{-1}) = 4.5$  is allowed. In fact, the ionisation parameter of around  $\log(\xi/\text{erg cm s}^{-1}) = 4$  is more similar to values measured in AGN with known UFOs, e.g. IRAS 13224-3809 [297, 303].

The fact that we observe the wind in only one of the two observations suggests variability on relatively short timescales of tens of ks. *XMM-Newton* observed the source on 2016-12-17, followed by a second observation on 2016-12-19. The time interval between the end of the first and the beginning of the second exposure was less than 10 hours. Such fast variability suggests a clumpy wind, in agreement with recent simulations [385, 192]. Alternatively, the viewing angle of the system might have changed to introduce obscuring material into the line of sight, however the change must have been small enough not to affect the broadband continuum, which is very similar during both observations. This seems unlikely. Wind variability has also been observed in NGC 1313 X-1 [see Fig. 2 of 306].

A clumpy nature of the outflow could imply that the ionised outflow is only partially covering the X-ray source. However, given the current data quality, the covering factor is degenerate with the column density of the absorber and so it cannot be estimated.

Since we know the velocity and the ionisation parameter of the outflow, we can calculate its mechanical energy in comparison with the X-ray luminosity of the object, following the steps in Pinto et al. [304]. The wind power can be expressed as  $\dot{E}_{\text{kin}} = 0.5\dot{M}u^2$  where  $u$  is the wind velocity. The outflow rate  $\dot{M}$  can then be determined using the definition of the ionisation parameter  $\xi$ :  $\dot{M} = 4\pi\Omega C_V L_{\text{ion}} m_{\text{H}} \mu u / \xi$  where  $\Omega$  is the solid angle of the outflow as a fraction of  $4\pi$ ,  $L_{\text{ion}}$  is the ionising luminosity, and  $C_V$  is the volume filling factor of the wind defining how clumpy it is.  $m_{\text{H}}$  is the hydrogen (proton) mass and  $\mu$  the mean atomic weight ( $\sim 1.2$  if taking Solar abundances). We obtain the following expression for the mechanical power of the outflow:  $\dot{E}_{\text{kin}} = 2\pi\Omega C_V L_{\text{ion}} m_{\text{H}} \mu u^3 / \xi$ .

Substituting in the fitted and known variables, the kinetic power is  $\dot{E}_{\text{kin}} \sim 400 \Omega C_V L_{\text{ion}}$ . Assuming a fairly large solid angle fraction of  $\Omega \sim 0.5$  (wind at the inclination angles of between  $40^\circ$  and  $80^\circ$  from the rotation axis, as seen from the central object) and a volume filling factor of  $C_V \sim 0.3$  as found in simulations [385], we reach  $\dot{E}_{\text{kin}} \sim 60 L_{\text{ion}}$ . We can compare this value with the X-ray luminosity  $L_X$  of the PULX. For an order of magnitude estimate, we assume that half of the X-ray luminosity ionises the wind, ignoring any possible strong beaming. Most of the ULX flux is usually found in the X-ray band so we do not need to account for any other ionising radiation. That means  $L_{\text{ion}}/L_X \sim 0.5$ , which results in  $\dot{E}_{\text{kin}}/L_X \sim 30$ . Then taking  $L_X \sim 3 \times 10^{39} \text{ erg s}^{-1}$  (obtained by fitting the X-ray spectrum), means that the total kinetic power is  $\dot{E}_{\text{kin}} \sim 10^{41} \text{ erg s}^{-1}$ . This

is an extreme value if compared to outflows in any sub-Eddington systems of stellar mass. However, it is similar (although on the higher end) to the values necessary to inflate ionised superbubbles many ULXs and microquasars are often located in, which require a mechanical inflating power of  $10^{39}$  to several  $10^{40}$  erg s<sup>-1</sup> [292, 293, 61]. It is possible that in this case (a neutron star ULX), a larger fraction of the X-ray flux is beamed into the evacuated funnel and the ratio of the ionising luminosity  $L_{\text{ion}}$  to the X-ray luminosity  $L_X$  is much smaller, which would bring down the kinetic power  $\dot{E}_{\text{kin}}$  to  $10^{39}$  -  $10^{40}$  erg s<sup>-1</sup>. Some level of anisotropy is in fact required for the system to pulse at all. In comparison, the kinetic power needed to inflate the W50 bubble around the Galactic microquasar SS433 [possibly a misaligned ULX, 106] is a few times  $10^{39}$  erg s<sup>-1</sup> [233]. In this case, however, most of the kinetic energy is likely provided by its jets, observed in the optical band.

NGC 300 ULX-1 is one of two (the other one being NGC 7793 P13) currently known, easily observable neutron star ULXs. The two remaining PULXs are either too far or contaminated by nearby X-ray sources. The source is still active as of February 2018 at a luminosity of about  $2 \times 10^{39}$  erg s<sup>-1</sup>, and is a fascinating object, showing an ultrafast outflow appearing out of nothing on timescales of less than 100ks, in addition to pulsations with an extremely high pulsed fraction [45]. We therefore strongly encourage further observations of the source with both high-resolution and broadband X-ray instruments.

The high ionisation factor of the ultrafast wind  $\log(\xi/\text{erg cm s}^{-1}) = 3.9$  and its projected velocity of 0.22c means that most of its spectral features are in the >2 keV energy band. A majority of these features such as Mg, Si, S Ly $\alpha$  absorption lines is unresolvable with the current generation of X-ray instruments with the exception of *Chandra* gratings, which do not have sufficient collecting area (and therefore need long exposure times). The lines will however be easily resolved with the microcalorimeter onboard *XRISM* [*Hitomi* replacement, 383], thus making it a prime instrument for studies of highly ionised outflows in ULXs.

## 4.5 Conclusions

We performed a detailed, high spectral resolution and broadband search for an ultrafast outflow in the recently discovered ultraluminous pulsar NGC 300 ULX-1. Our findings can be summarised as follows:

- We found strong evidence for a UFO in this object with a significance of more than  $3\sigma$  during one of the two *XMM-Newton* observations of the source, including simultaneous *NuSTAR* data.
- Evidence for the UFO is seen in both soft X-ray data (driven by RGS gratings), and hard X-ray data (PN, MOS and FPM detectors). Removing any of the instruments from the simultaneous analysis reduces the total statistical significance.
- The projected velocity of the outflow is  $65100_{-2200}^{+1000}$  km/s ( $0.217_{-0.007}^{+0.004}$   $c$ ), with a turbulent velocity of  $800_{-500}^{+1100}$  km/s and a high ionisation factor of  $\log(\xi/\text{erg cm s}^{-1}) = 3.92_{-0.13}^{+0.19}$ . Its velocity is similar to outflows in other ULXs, but the ionisation parameter  $\xi$  is more alike the outflows observed in AGN.
- Curiously, we find no signs of the wind during the other observation of the source by *XMM-Newton* (with simultaneous *NuSTAR* coverage), which ended just 10 hours before the start of the second one. This could mean that either the wind is clumpy, or that the viewing angle of the system changed slightly, without affecting the overall broadband X-ray spectrum.
- Further observations of the source are necessary to determine the process that drives the variability of the wind, and to place tighter constraints on its physical parameters as well as its interaction with the rest of the accretion flow in the system.

## Chapter 5

**A variable ultra-fast outflow in the  
Narrow Line Seyfert 1 galaxy PG  
1448+273**



# Abstract

Relativistically blueshifted absorption features of highly ionised ions, the so-called ultra-fast outflows, have been detected in the X-ray spectra of a number of accreting supermassive black holes. If these features truly originate from accretion disc winds accelerated to more than 10 per cent of the speed of light, their energy budget is very significant and they can contribute to or even drive galaxy-scale feedback from AGN. However, the UFO spectral features are often weak due to high ionisation of the outflowing material, and the inference of the wind physical properties can be complicated by other spectral features in AGN such as relativistic reflection. To address these issues, we developed an automated, systematic routine for detecting outflows in accreting systems. In this chapter, the method is used to achieve an unambiguous detection of a UFO in a highly accreting Narrow Line Seyfert 1 galaxy PG 1448+273. The UFO absorption is observed in both soft and hard X-ray bands with the *XMM-Newton* observatory. The velocity of the outflow is  $(26900 \pm 600)$  km/s ( $\sim 0.09c$ ), with an ionisation parameter of  $\log(\xi/\text{erg cm s}^{-1}) = 4.03^{+0.10}_{-0.08}$  and a column density above  $10^{23}$  cm $^{-2}$ . At the same time, we detect weak warm absorption features in the spectrum of the object. Our systematic outflow search suggests the presence of further multi-phase wind structure, but we cannot claim a significant detection considering the present data quality. The UFO is not detected in a second, shorter observation with *XMM-Newton*, indicating variability in time, observed also in other similar AGN.

## 5.1 Introduction

Highly blueshifted absorption lines of ionised material have recently been detected in the X-ray spectra of a number of AGN, reaching velocities from  $\sim 0.1c$  to as high as  $0.5c$  [e.g. 316, 332, 393, 395, 394, 279, 297, 196, 420]. These absorption lines could originate from accretion disc winds, launched at high velocities from the accretion flow of AGN by radiation pressure [322] or magnetic forces [121]. The large velocity and

the consequent significant kinetic power makes these outflows strong candidates for being the drivers of AGN feedback in galaxies [97, 188]. Alternatively, these blueshifted absorption lines could originate from low-density material co-rotating with the inner accretion flow without the need for an outflow from the system [127, 102].

In most cases the signatures of these so-called ‘ultra-fast outflows’ were identified using the highly ionised features of Fe XXV and Fe XXVI [393] in the iron K band (7-10 keV). The iron K band, however, is often on the upper edge of the energy range of the current instruments like *XMM-Newton* (EPIC pn and MOS) and *Chandra*, where the collecting area of the instruments steeply drops off, resulting in poor counts and signal-to-noise ratios. Additionally, this band commonly contains strong features of relativistically blurred reflection of the AGN coronal emission from the accretion disc [386, 104]. Therefore the observed absorption features can be hard to interpret as outflow signatures and it is difficult to infer the wind properties such as the velocity and the ionisation level [438]. Furthermore, spurious low significance features or lines of instrumental origin can be interpreted as real UFO signatures.

Less frequently, fast ionised wind absorption lines are also observed in softer X-rays ( $< 5$  keV), for example using the Si XIV, S XVI and O VIII transitions [169, 303, 331]. The soft X-ray band (0.3-2.0 keV) can however be dominated by the commonly observed warm absorption from low ionisation material at larger distances from the AGN [e.g. 175, 183, 33, 73], which complicates line identification.

It is therefore important to study UFOs in different objects and across a broad X-ray band, comparing their properties to the source X-ray continuum properties in order to understand the true nature of UFOs and their relationship to AGN.

Here we present the detection of an ultrafast outflow with a velocity of  $0.09c$  in the spectrum of an NLS1 galaxy PG 1448+273 observed with the *XMM-Newton* observatory. The signatures of the outflow are observed in both hard X-rays (iron K band) and soft X-rays (0.3-2.0 keV), and we constrain its physical properties systematically using an automated multi-parameter search of the X-ray spectrum with photo-ionised absorption grids.

PG 1448+273 is an NLS1 [35, 143] located at a redshift of  $z=0.0645$  [5]. Its black hole mass is  $(9 \pm 2) \times 10^6 M_{\odot}$  [409, from single-epoch optical spectroscopy]. PG 1448+273 has an estimated bolometric luminosity of  $\sim 10^{45.5}$  erg/s [143], resulting in an Eddington ratio above unity ( $L/L_{Edd} \sim 3$ ). PG 1448+273 could therefore be a super-Eddington accretor [185]. At such a high Eddington fraction, radiation pressure is an important component of the accretion flow and is expected to drive powerful

outflows from the accretion disc [363]. PG 1448+273 is therefore a natural candidate for a spectroscopic search of UFO signatures.

Previous X-ray studies have remarked on the complex shape of the soft X-ray excess [161] of PG 1448+273, requiring more than the usual  $\sim 0.1$  keV blackbody component for an accurate description. The AGN is however not heavily absorbed by neutral absorption or a strong warm absorber. Its X-ray spectrum is also highly variable [311].

This chapter consists of 5 sections. The observation and data reduction is described in Section 5.2. The details of our analysis and the results are shown in Section 5.3, followed by a discussion of the findings in Section 5.4. Section 5.5 contains the conclusions of this study.

## 5.2 Observation and data reduction

The *XMM-Newton* [166] data were downloaded from the XSA<sup>1</sup> archive. The main dataset consists of a single observation taken on 24/01/2017 (ID: 0781430101, proposal PI: A. Zoghbi) with a total raw exposure of 126 ks. We reduced the data using standard pipelines with SAS v17. There were no high background periods of time during the observation and thus no time intervals needed to be filtered out.

The observation with the EPIC pn and MOS instruments was split into two exposures, a scheduled (‘S’) and an unscheduled (‘U’) part. Initially we extracted the spectra of the two exposures separately, but found no significant differences between them. We therefore combined the scheduled and unscheduled parts of the observation into a single exposure.

The EPIC pn [378] instrument was operated in Small Window mode during the observation to limit pile-up. The data are reduced following the standard procedure (section 2.1.2). An image of the pointing was made using standard routines. We noticed a strong non-uniformity of background counts across the image (Fig. 5.1), likely due to source counts from the wing of the source point spread function (PSF). To avoid including source counts in the background spectrum, we chose background regions to be two small polygons as far from the source as possible. Furthermore, we decreased the importance of background subtraction by choosing a small (20 arcsec) source region. This boosted the signal-to-noise ratio in the critical 6 – 10 keV energy band where the Doppler-shifted absorption features of highly ionised iron (Fe XXV/XXVI) are expected. The average EPIC pn count rate was 2.2 ct/s, but the source is strongly variable, varying between 1 ct/s and 4 ct/s over the course of the observation.

---

<sup>1</sup>[nxsa.esac.esa.int/nxsa-web/](http://nxsa.esac.esa.int/nxsa-web/)

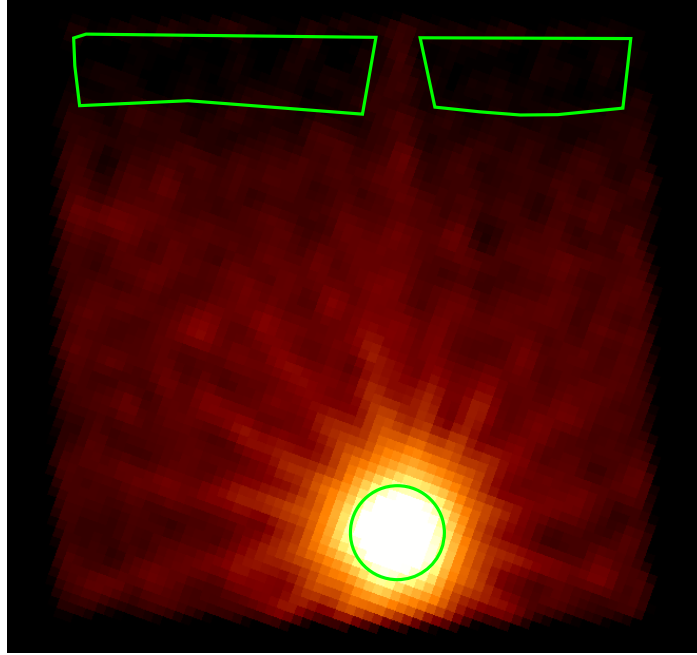


Fig. 5.1 Image of the EPIC pn Small Window Mode exposure. The source region used in the analysis is the green circle (20 arcsec radius), the 2 polygons are the regions used to extract the background spectrum. The non-uniform background count distribution (in the vertical direction) is evident and is likely caused by the wings of the source point spread function.

EPIC/MOS 1 and 2 [400] were operated in Large Window mode. The source region was chosen to be a circle with a radius of 20 arcsec, similar to pn data. The background covered the rest of the central chip area, at least 110 arcsec away from the source, avoiding other bright point sources. We did not notice any background non-uniformity as observed in EPIC pn data, confirming that the non-uniformity observed in the EPIC pn image is caused by the wings of the PSF. The average EPIC MOS 1 count rate was 0.44 ct/s and the average MOS 2 count rate was 0.43 ct/s. We stacked data from MOS 1 and MOS 2 into a single spectrum with the EPICSPECCOMBINE routine.

Data from both EPIC/pn and EPIC/MOS were grouped using the SPECGROUP procedure to at least 25 counts per bin, and to oversample the detector resolution by a factor of at most 3. The clean exposure time of the pn dataset is 76 ks, and the exposure of the combined MOS 1 and MOS 2 data is 108 ks (pn exposure is smaller due to a lower Live time in Small Window mode).

RGS [72] data were reduced using standard routines with default values and with standard observational background, following the description in section 2.1.1. Data

were binned by a factor of 3 directly within the SPEX fitting package. The clean exposure of RGS 1 and RGS 2 data is 115 ks.

After reduction, the data were converted into SPEX FITS format. All spectral models were fitted using Cash statistics [47] and the errors are stated at  $1\sigma$  level. We use 3 cross-calibration constants to account for calibration differences between the four spectral datasets (pn, MOS, RGS1 and RGS2). The differences are smaller than 10 per cent in all cases.

EPIC pn and MOS data were initially ignored below 0.3 keV and above 10 keV following standard guidelines. RGS data were used in the range between 7.5 Å (1.7 keV) and 28 Å (0.44 keV), limited by strong background on both ends of this interval. We found a 10-15 per cent discrepancy between EPIC and RGS data in the 0.3-1.0 keV range which could be caused by poor spectral resolution of the EPIC instruments in this range, or by calibration differences. At these energies EPIC lacks the resolution to resolve the fine structure of absorption lines but would drive the spectral fits due to much higher count rates than RGS (resulting in much smaller errorbars compared to RGS data). To avoid confusion between different unresolved spectral components, we ignored EPIC pn and MOS data below 1.7 keV altogether in the main part of our analysis.

## 5.3 Results

### 5.3.1 Broadband X-ray continuum

First we fit the broadband 0.3-10 keV spectrum with a phenomenological X-ray AGN spectral model. We fit the RGS, EPIC pn and MOS data simultaneously with the same spectral model except for the cross-calibration constant. The model consists of a powerlaw (POW in SPEX) model describing the Inverse Compton coronal emission, a blackbody (BB) model describing the soft excess below 2 keV, and a relativistically blurred iron K emission line. Blurred reflection is described with a LAOR model applied to a Gaussian line (GA) with the energy fixed to 6.4 keV to avoid too much model freedom with the available data quality. All of these models are subject to any interstellar absorption in the host galaxy of the AGN described by a HOT model within SPEX. We assume Solar abundances of this additional absorption component to avoid too much modelling freedom, although in principle the elemental abundances in the PG 1448+273 host could be different. The spectral model is then redshifted by  $z=0.0645$  of the host galaxy (found on the NED database) using the REDS model. Finally, Galactic

interstellar absorption is applied with a second HOT spectral model (assuming Solar abundances) with a fixed value of  $N_{\text{H}} = 2.5 \times 10^{20} \text{ cm}^{-2}$  [179]. The final spectral model has the following form:  $\text{HOT}(\text{REDS}(\text{HOT}(\text{POW}+\text{BB}+\text{LAOR} \times \text{GA})))$ .

We find that PG 1448+273 shows properties very similar to other Narrow Line Seyfert 1 AGN (for a summary of the continuum parameters, see Table 5.1). The powerlaw slope is measured to be  $2.07 \pm 0.03$ , and the soft excess can be described with a blackbody of temperature  $0.097 \pm 0.003 \text{ keV}$ . The black hole appears to have a high spin value with a minimum disc radius of just  $1.52_{-0.29}^{+0.19} R_{\text{G}}$ , but we draw no firm conclusions since the relativistic iron K reflection is described only with a simple phenomenological model. The emissivity slope is  $q = 4.6 \pm 0.5$  and the measured disc inclination  $44_{-3}^{+2}$  degrees. We also find a significant non-zero interstellar absorption in the host galaxy of PG 1448+273 with a column density of  $(9.8 \pm 2.1) \times 10^{20} \text{ cm}^{-2}$ . The fit statistics are C-stat=1594.43 for 1278 degrees of freedom (D.o.F.).

Table 5.1 Best-fitting X-ray continuum parameters of PG 1448+273.

Spectral model	Host $N_{\text{H}}$	$\Gamma$	$T_{\text{soft}}$	Fe K <sup>1</sup>	$R_{\text{in}}^1$	$q^1$	$i^1$	$L^2$
	$10^{20} \text{ cm}^{-2}$		keV	keV	$R_{\text{G}}$			$10^{43} \text{ erg/s}$
Continuum only	$9.8 \pm 2.1$	$2.07 \pm 0.03$	$0.097 \pm 0.003$	6.4 (fix)	$1.52^{+0.19}_{-0.29}$	$4.6 \pm 0.5$	$44^{+2}_{-3}$	$1.40 \pm 0.03$
Cont.+UFO+warm. abs.	$6.5^{+2.0}_{-2.2}$	$1.97 \pm 0.03$	$0.102 \pm 0.003$	6.4 (fix)	$1.7 \pm 0.5$	$3.5^{+2.1}_{-0.5}$	$38^{+16}_{-3}$	$1.81^{+0.17}_{-0.10}$

<sup>1</sup>The parameters of the blurred iron K line (modelled as a Laor shape): the line energy, the inner disc radius, the emissivity index and the disc inclination.

<sup>2</sup>Luminosity in the 2-10 keV band.

Upon visual inspection of the spectrum, strong residuals in EPIC pn and MOS data within the iron K band are obviously evident (Fig. 5.2), as are residuals in the RGS band (Fig. 5.3). The iron K band residuals suggest the presence of a highly ionised, high-velocity outflow, the flux drop above 7 keV is very similar to that of another NLS1 1H 0707-495 with a known high-velocity outflow [36, 196]. The RGS data point to a more complex situation. There is a prominent absorption residual at 18-19 Å (observed wavelength), which could correspond to O VIII absorption, blueshifted by  $\sim 0.1c$ . Further structures are also seen around 12 Å and 24 Å in observed wavelength.

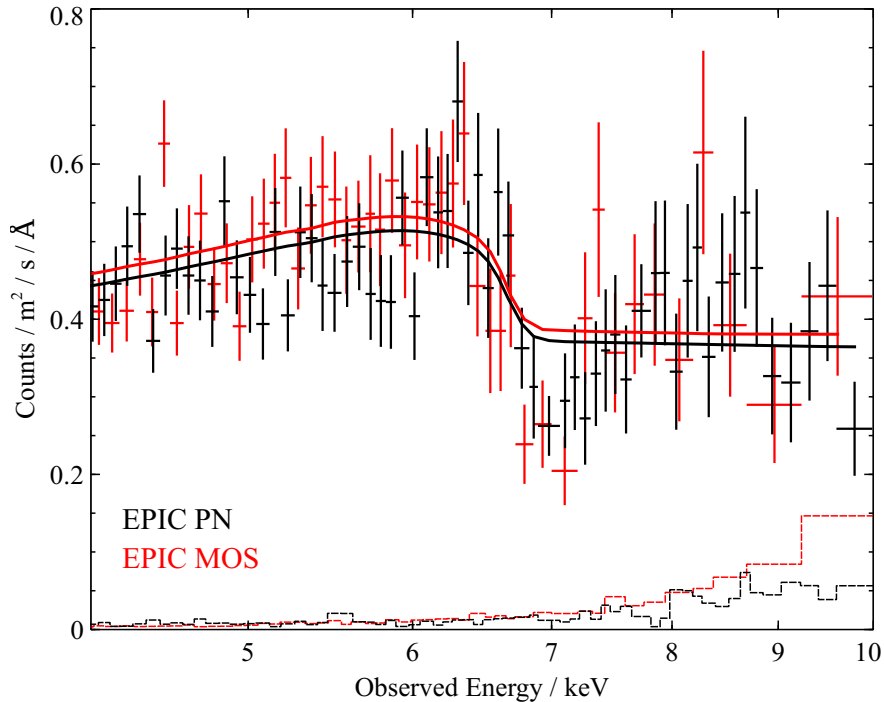


Fig. 5.2 EPIC pn (black) and MOS (red, MOS 1 and MOS 2 stacked) data (4.5 – 10 keV) of PG 1448+273 fitted with the phenomenological AGN continuum model from Section 5.3.1. Apparent is the strong absorption residual observed at  $\sim 7$  keV. Black (pn) and red (MOS) solid lines show the best-fitting continuum models, and the dashed lines show the subtracted background spectra.

### 5.3.2 Ionised wind search

#### Wind search set up and results

To determine the blueshift and physical parameters of any ionised outflow component as well as its significance in the present data, we systematically scan the X-ray spectrum

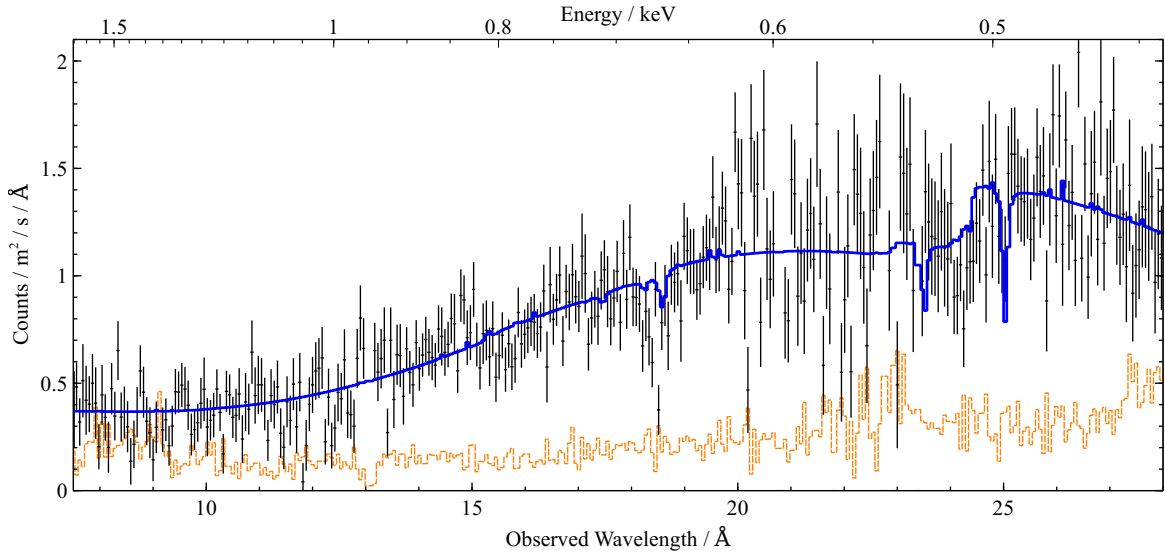


Fig. 5.3 Background-subtracted RGS data (7.5–28 Å) of PG 1448+273, stacked and overbinned for plotting purposes only, fitted with the phenomenological AGN continuum model from Section 5.3.1 (blue colour). The model particularly fails to reproduce the strong residuals around 18–19 Å, however further residuals are seen around 12, 15.5 and 24 Å. The edge at 24.5 Å and the strong absorption line at 25 Å suggest the presence of neutral absorption intrinsic to the AGN. The subtracted background is shown in orange.

of PG 1448+273 with an automated ionised absorber search. We follow the steps outlined in section 2.2.2. We use the best-fitting broadband spectral continuum from the previous section, and search the parameter space of ionisation parameters between  $\log(\xi/\text{erg cm s}^{-1}) = -1.0$  and  $\log(\xi/\text{erg cm s}^{-1}) = 4.8$ , systematic outflow velocities between +20000 km/s (to account for possible infalling gas) and -100000 km/s (blueshift of roughly  $0.4c$ , after relativistic correction), and turbulent velocities of 100 km/s, 1000 km/s and 10000 km/s.

The photoionisation model we use here to describe the spectral features (absorption lines) of an ionised outflow is XABS in the SPEX fitting package (see section 1.4.3 for more details about the model). The model calculates the ionising balance and absorption line strengths based on the Spectral Energy Distribution shape of the AGN NGC 5548 [373, 372]. The SED of NGC 5548 should be a reasonable approximation for the PG 1448+273 SED, although the black hole of the former is likely more massive at  $(9 \pm 3) \times 10^7 M_{\odot}$ , and has a smaller Eddington ratio [224]. The coronal powerlaw slope of NGC 5548 is  $\Gamma \approx 1.8$  versus  $\Gamma = 2.07 \pm 0.03$  in PG 1448+273, so PG 1448+273 has a softer spectrum but not as soft as the more extreme NLS1 AGN like IRAS 13224-3809 where  $\Gamma$  varies between 2.2 and 2.9 [303]. Nevertheless, the spectra of NGC 5548 and

PG 1448+273 should still be reasonably similar. We therefore use the XABS model to describe the ionised outflow absorption, which makes the outflow search computationally reasonable. At each step, we also check our results for consistency with the PION model in the SPEX fitting package. PION takes into account the actual continuum SED of the currently used spectral model, albeit at a much higher computational cost, which is the limiting factor in our analysis.

We search the large parameter space for signatures of an ionised outflow as described above, using the full dataset (RGS + pn + MOS) on PG 1448+273. The results of the search are shown in Fig. 5.4. The wind search achieves a strong detection of ionised plasma with a systematic outflow velocity of  $\sim 30000$  km/s, with a fit improvement of  $\Delta C\text{-stat} > 70$ . The plasma is highly ionised with  $\log \xi$  of 4.0–4.2 and the fit improvement is much higher in the scans with 1000 or 10000 km/s turbulent velocity compared to the one with 100 km/s velocity width. All the other  $\Delta C\text{-stat}$  peaks in the systematic scans are much smaller, reaching at most  $\Delta C\text{-stat} \sim 30\text{--}35$ , hence the ‘primary’ (strongest) solution is highly preferred.

### Monte Carlo simulations

The  $\Delta C\text{-stat}$  value corresponds to a specific false detection probability, but their exact relationship depends on the dataset used and the size of the parameter space. In principle, the formal statistical significance needs to be estimated by running simulations tailored to match the particular search performed. However, multiple recent wind searches deployed for outflow detection in other objects found that  $3\sigma$  detection significance corresponded to roughly  $\Delta C\text{-stat} \sim 20$  or  $\Delta\chi^2 \sim 20$  (depending on the fitting method used). The exact values found were  $\Delta\chi^2 = 18.5$  in the analysis of the IRAS 00521-7054 AGN [420],  $\Delta C\text{-stat} \sim 20$  when studying the ultra-fast outflow of the ULX NGC 1313 X-1 [307] and  $\Delta C\text{-stat} \sim 22$  in the ULX NGC 5204 X-1 spectrum search [198]. Similarly,  $\Delta C\text{-stat} \sim 30$  fit improvements corresponded to roughly  $4\sigma$  significances in ULX wind studies [199, 307]. The fact that our detection is above  $\Delta C\text{-stat} = 70$  already strongly suggests the significance of this outflow component, comparing with all previous similar analyses.

Nevertheless, we employ Monte Carlo simulations to verify the significance of the UFO detection. The simulations are performed on simulated data with the same exposure as the real observation, and should be performed in the same manner as the wind search on real data. However, it is prohibitively expensive to search the whole parameter space. Each MC simulation performed in the same manner as the previous wind search (Fig. 5.4) would take several days on a single (quad-core)

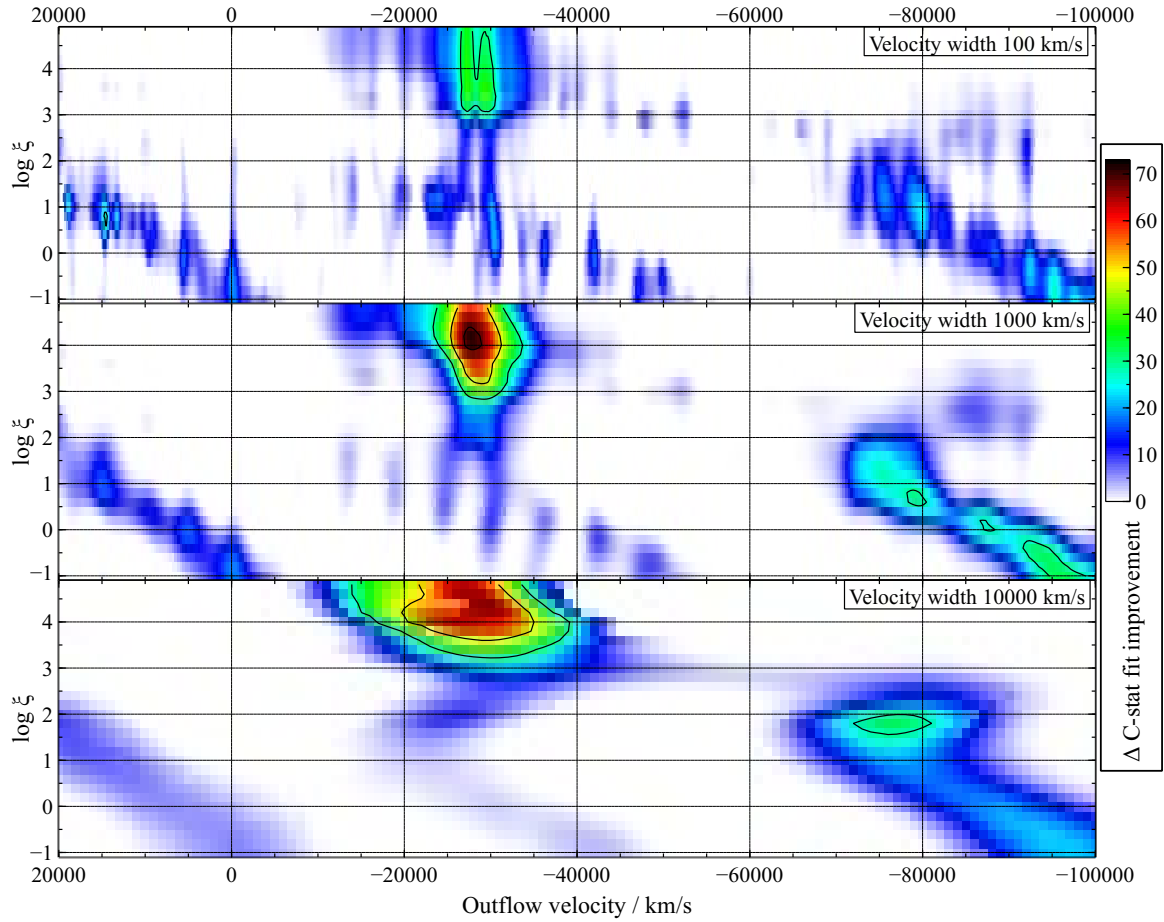


Fig. 5.4 Systematic scan for ionised outflow features in the spectrum of PG 1448+273. The spectrum is scanned with ionised absorption model grids with systematic velocities between +20000 km/s and -100000 km/s, ionisation parameters  $\log \xi$  between -1.0 and +4.8, with turbulent velocities of 100 km/s, 1000 km/s and 10000 km/s. The colour shows the  $\Delta C$ -stat fit improvement upon adding the absorption grid to the baseline continuum model, the black contours show  $\Delta C$ -stat fit improvements of 30, 50 and 70, respectively.

computer. We therefore slightly modify the wind search for the MC simulations. We only choose the parameter space between ionisation parameters  $\log(\xi/\text{erg cm s}^{-1}) = 3.5$  and  $\log(\xi/\text{erg cm s}^{-1}) = 4.5$ , to cover exactly the properties of the UFO found in the real data (this also covers roughly 1/6 of the full ionisation parameter space). This range of  $\log \xi$  is also the region in which most UFOs are detected. Choosing this limited parameter space, we can run a single wind scan for each simulated dataset where the ionisation parameter is allowed to vary in the permitted range, and the turbulent velocity can vary in the 250 km/s to 5000 km/s range, covering most of the velocity width parameter space. The ranges are chosen to be limited so that the routine

avoids missing the best-fitting solution at each systematic velocity. The systematic velocity range is the same as in the previous search (20000 km/s to -100000 km/s) with a spacing of 300 km/s. With this set up, each MC simulation takes about 7-8 hours on a single computer.

To test this modified wind search we first apply it on the real data, finding the primary peak with a fit improvement of  $\Delta C\text{-stat} \sim 83$ . We note that this is a stronger detection than in the first wind search (where the maximum was  $\Delta C\text{-stat} \sim 73$ ) as the turbulent velocity of the absorption grid is allowed to vary freely and is not bound to either 100 km/s, 1000 km/s or 10000 km/s. The search is therefore able to find a slightly better fitting solution. We performed 1000 Monte Carlo simulations in total, and found no simulated searches with  $\Delta C\text{-stat} > 22$ . Since this is much lower than the real data outflow detection, we cannot quantify the precise significance of the detection, only its lower limit, which is  $\sim 3\sigma$  (given the number of simulations performed). The difference between the strongest simulated search  $\Delta C\text{-stat}$  and the real data  $\Delta C\text{-stat}$  suggests that the actual significance is much higher than  $3\sigma$ .

The strongest fake detection is  $\Delta C\text{-stat} = 21.16$ , the  $3\sigma$  detection limit with the limited parameter space is hence at  $\Delta C\text{-stat} \sim 19.6$ . Even though the simulated search only covers 1/6 of the full ionisation parameter space, the simulations prove the significance of the UFO detected in the PG 1448+273 spectrum. Assuming the false alarm probability scales linearly with the parameter space (we stress that this is only a very rough assumption), the 95 per cent ( $2\sigma$ ) detection limit is at  $\Delta C\text{-stat} \sim 16$  from our MC simulations. Fig. 5.5 contains a comparison between the histograms  $\Delta C\text{-stat}$  values of the real data XABS search with XABS searches on 1000 simulated datasets. The histograms are completely different and their comparison shows that the detection of a UFO in the spectrum of PG 1448+273 is highly statistically significant.

### Secondary detections in the wind search

We also find a large number of secondary peaks with  $\Delta C\text{-stat}$  between 25-35 which by themselves could be considered significant detections, if they were detected alone. Their presence suggests that there could be further wind structure hiding in the spectrum of PG 1448+273. However, at this point it is not certain that the secondary peaks are independent of the primary peak. These secondary solutions could in fact be fitting some of the same spectral residuals to the baseline continuum as the primary peak, but with a different set of atomic lines, resulting in a shallower  $\Delta C\text{-stat}$  improvement.

Secondly, we notice a  $\Delta C\text{-stat}$  peak around the rest-frame of the AGN in the 100 km/s velocity width search. The peak is not particularly strong with  $\Delta C\text{-stat} \sim 20$  at the

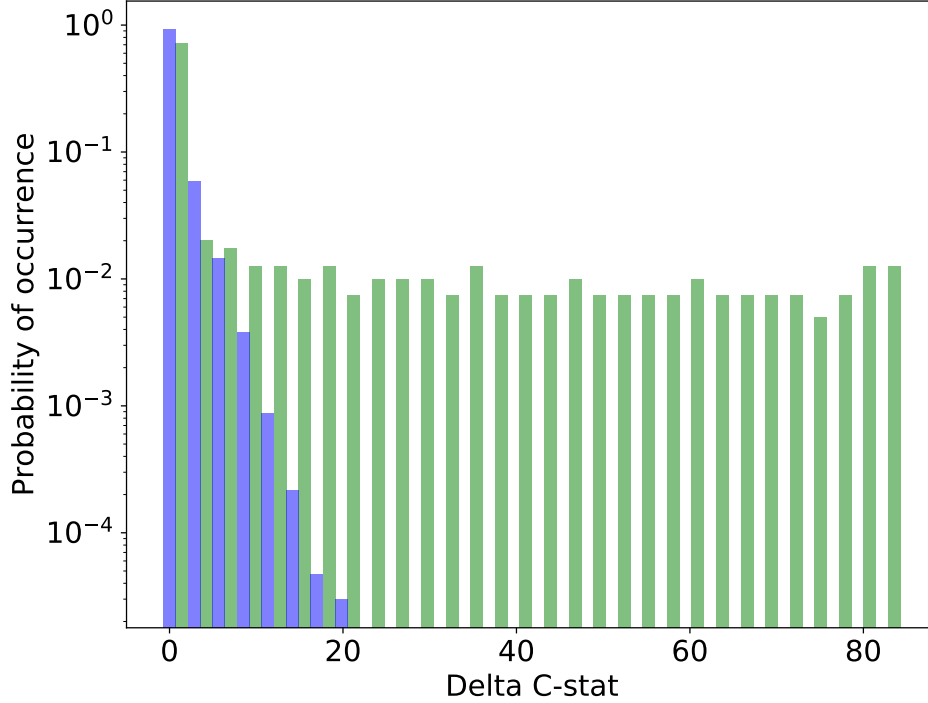


Fig. 5.5 Histogram of  $\Delta C$ -stat of the real XABS outflow scan of PG 1448+273 (green) and of XABS scans of 1000 Monte Carlo simulated datasets (blue). The Y axis is the probability density function, the integral of which is 1, and the X axis is the  $\Delta C$ -stat value.

ionisation parameter of  $\log(\xi/\text{erg cm s}^{-1}) = -0.6$ , but could mean the presence of a weak warm absorber. Absorbers with similar ionisation parameters are very commonly observed in other AGN [e.g. 33], it is thus not unlikely than one could also appear in the spectrum of PG 1448+273. If this is the case, the same look-elsewhere effect as for the UFO detection does not apply. Warm absorbers in particular only appear over a very small systematic velocity parameter space (velocities from hundreds of km/s to a few thousands of km/s at maximum). The same  $\Delta C$ -stat significance rules for UFO detections hence do not apply as the available parameter space is much smaller, and a significantly weaker warm absorber detection might still represent real absorption features. For this reason we fit both the features of the UFO primary peak as well those of the warm absorber in the next section.

Finally, we notice smaller diagonal peaks in the systematic wind search (Fig. 5.4). These streaks indicate some degeneracy between the velocity and ionisation parameters

of detections in the search. They appear to be moving to lower velocities at higher ionisations, e.g. from  $v = -50000$  km/s at  $\log(\xi/\text{erg cm s}^{-1}) = -0.5$  to  $v = -20000$  km/s at  $\log(\xi/\text{erg cm s}^{-1}) = 1.5$ . These likely originate in absorption residuals which are fitted with absorption lines moving to lower wavelengths (i.e. requiring lower blueshift) with increasing ionisation parameter. In particular the Fe UTA feature (at  $15 - 17 \text{ \AA}$ ) is a likely candidate for creating such degeneracy. Nevertheless, these degenerate peaks have much weaker  $\Delta\text{C-stat}$  fit improvements than the primary outflow detection.

### 5.3.3 Ultrafast outflow and warm absorption

To learn more about the properties of the ionised absorbers in PG 1448+273, we fit its spectrum directly with a model which includes the original baseline continuum (with all the parameters freed), plus two ionised absorbers described with the XABS model. The first XABS model is supposed to fit the primary peak in the systematic absorber search at around 30000 km/s, the second one should fit the possible features of a warm absorber in the rest-frame of the AGN. The best-fitting wind spectral model is shown in Fig. 5.6 (EPIC pn and MOS data only) and in Fig. 5.7 (RGS data only).

The primary ultrafast component is found with an outflow velocity of  $26900 \pm 600$  km/s (including the relativistic correction). Its column density is  $2.8_{-0.7}^{+1.2} \times 10^{23} \text{ cm}^{-2}$ , with an ionisation parameter of  $\log(\xi/\text{erg cm s}^{-1}) = 4.03_{-0.08}^{+0.10}$  and a velocity width of  $2100_{-500}^{+600}$  km/s. The final fit improvement of adding this component to the baseline model is very strong with  $\Delta\text{C-stat}=83.27$ , confirming the significance of the ultrafast outflow features in the spectrum of PG 1448+273. The strongest spectral features of the UFO absorption are the Fe XXV and Fe XXVI lines at  $\sim 7$  keV (in the EPIC band) and the O VIII line at  $18.5 \text{ \AA}$  ( $\sim 0.7$  keV, in the RGS band).

The warm absorber has a column density of  $(3.8 \pm 1.7) \times 10^{20} \text{ cm}^{-2}$  and an ionisation parameter of  $\log(\xi/\text{erg cm s}^{-1}) = -0.4_{-0.4}^{+0.3}$ . Its systematic velocity is  $-100 \pm 200$  km/s in the rest-frame of the AGN so it is consistent with being at rest, with a velocity width of  $50_{-30}^{+40}$  km/s. It is similar to warm absorbers found in other AGN [183, 372, 73], apart from the column density which is much lower in PG 1448+273, resulting in rather weak spectral features, and a lower  $\Delta\text{C-stat}$  fit improvement of 15.19. The  $\Delta\text{C-stat}$  is smaller than the original value found in the automated wind search ( $\sim 20$ ), suggesting that the ultra-fast and warm absorber models are partly fitting the same residuals to the original baseline continuum. The spectral features of the warm absorber are located at around  $24 \text{ \AA}$  (0.5 keV) in the RGS band.

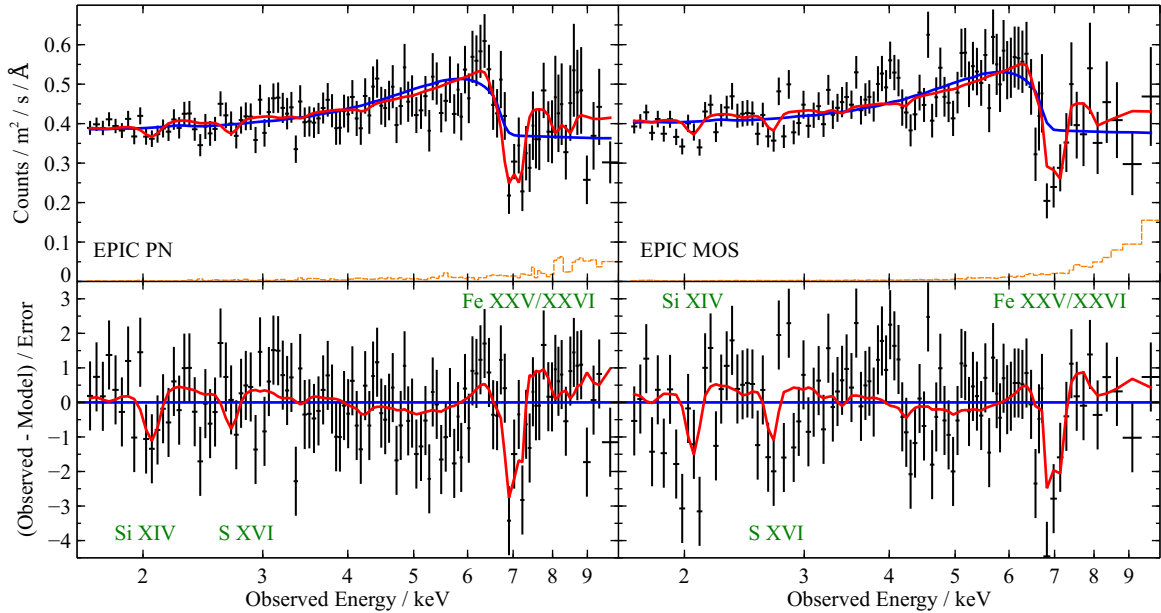


Fig. 5.6 EPIC pn (left subplots) and MOS (right subplots) data (1.7 – 10 keV) of PG 1448+273 fitted with the phenomenological AGN continuum model from Sect. 5.3.1, plus two wind components: one ultrafast, highly ionised component outflowing at  $\sim 27000$  km/s, and a warm absorber component in the rest-frame of the AGN. The top subplots show the spectra with the best-fitting baseline continuum (blue colour) and the continuum + wind models (red colour), the bottom subplots contain the residuals to the continuum model as well as the best-fitting wind solution (red). The orange dashed lines show the subtracted background spectra. Green labels name the strongest absorption lines of the UFO absorption.

Since the strongest absorption lines of the warm absorption lie in the  $24 \text{ \AA}$  range, they overlap with the N VII absorption of the 0.1c ultra-fast phase. It is therefore possible that these features instead could originate in N VII absorption of the ultra-fast phase. We attempt to describe the features by freeing the abundance of N in our final spectral model (with the warm absorber column density fixed to 0 and all other elemental abundances fixed to Solar), and reach fit statistic improvements at a  $\Delta C\text{-stat} \approx 10$  level (compared to a continuum + UFO with solar abundances spectral model), for a nitrogen over-abundance of  $7_{-2}^{+3}$ . We consider this to be a very high abundance value and prefer the warm absorption origin for the  $24 \text{ \AA}$  features. We find it unlikely that out of all elements only nitrogen would be over-abundant by such a large amount with the other elements remaining at Solar abundance.

The baseline continuum parameters slightly shift (for a summary of the continuum parameters, see Table 5.1), with the best-fitting powerlaw slope being  $1.97 \pm 0.03$  and the soft excess blackbody temperature of  $0.102 \pm 0.003$  keV, however they still agree

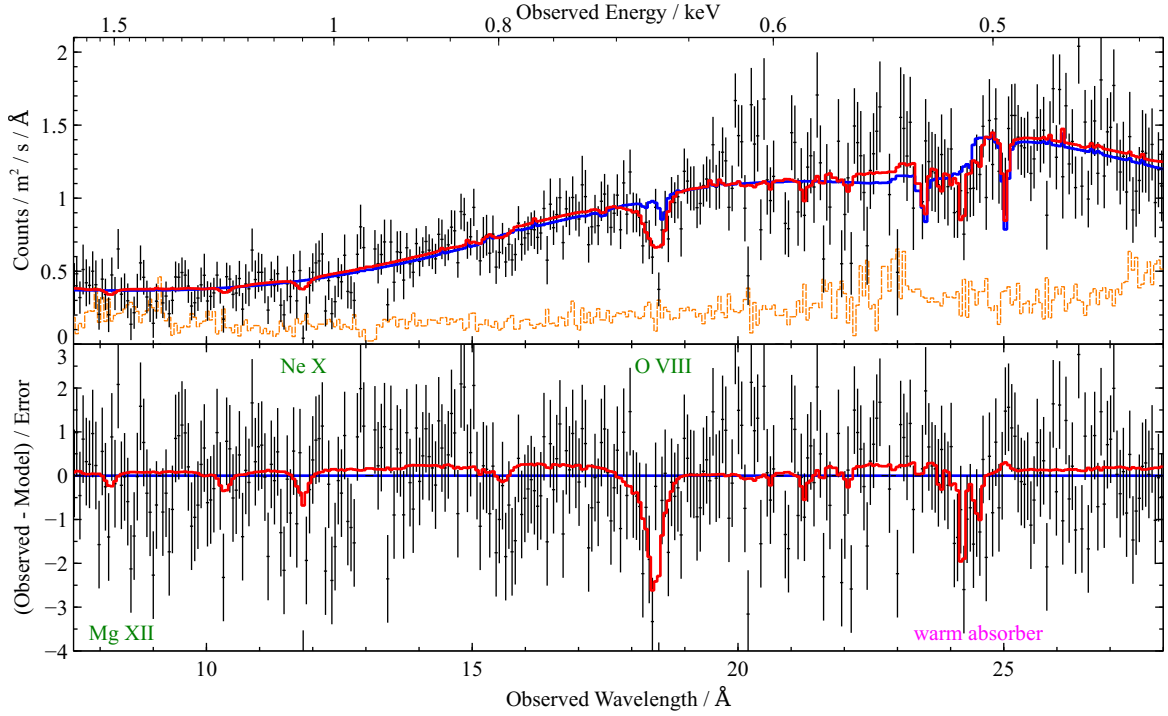


Fig. 5.7 RGS data between  $7.5 \text{ \AA}$  ( $1.7 \text{ keV}$ ) and  $28 \text{ \AA}$  ( $0.4 \text{ keV}$ ) of PG 1448+273, stacked and overbinned for plotting purposes only, fitted with the phenomenological AGN continuum model from Section 5.3.1, plus two ionised components: one ultrafast, highly ionised component moving at  $\sim 27000 \text{ km/s}$ , and a warm absorber component in the rest-frame of the AGN. The top subplot contains the RGS spectrum fitted with the baseline continuum (blue colour) and continuum + wind (red colour) models, the bottom subplot shows the residuals to the continuum model and the best-fitting wind solution (red). The subtracted background in orange colour. Green labels name the most notable absorption lines of the UFO absorption and the magenta label shows the spectral features of the warm absorber.

with the original continuum fit values within  $\sim 3\sigma$  errors. The inner disc radius (from the iron K line) is  $1.7 \pm 0.5 R_G$ , the emissivity slope is  $3.5^{+2.1}_{-0.5}$  and the disc inclination is found to be  $38^{+16}_{-3}$  degrees. Most notably, the best-fitting neutral absorber (in the rest-frame of PG 1448+273) is now weaker with a column density of  $6.5^{+2.0}_{-2.2} \times 10^{20} \text{ cm}^{-2}$ . This could be explained if the warm absorber (with a low ionisation parameter) is fitting similar spectral residuals as the neutral absorption. The final fit statistics are C-stat=1495.97 for 1270 D.o.F.

### 5.3.4 Residual structure in the spectrum - a multiphase outflow?

The large C-stat value of the best-fitting spectral model given the number of degrees of freedom, and the secondary peaks in the systematic wind search suggest the presence of further ionised outflow components in the spectrum of PG 1448+273, assuming our baseline continuum model is accurate. However, the secondary peaks might not be independent of the primary wind detection, i.e. their spectral signatures could be shared. For this reason, it does not make sense to directly fit the secondary peaks based on the existing automated wind search (Fig. 5.4).

We therefore perform a new set of wind searches which includes the two outflow components described above (in Sec. 5.3.3). We choose the best-fitting baseline continuum with 2 additional XABS components (ultra-fast outflow and warm absorber) to be the new baseline model. We then run the same wind search as described in Sec. 5.3.2, with all the baseline continuum parameters allowed to vary freely. The results are shown in Fig. 5.8.

There are no strong wind detections in the search with a turbulent velocity of 1000 km/s. On the other hand, there are roughly 5 peaks with fit improvements between  $\Delta C$ -stat of 15 and 22 in the search with 100 km/s turbulent velocity, suggesting tentative evidence of further ionised outflow components. Furthermore, there is a similarly strong peak ( $\Delta C$ -stat $\sim$ 20) in the 10000 km/s width search.

If only a single peak with a similar fit improvement ( $\Delta C$ -stat $\sim$ 20) was detected, it would be trivial to assign a false alarm probability to its detection based on our Monte Carlo simulation results from Sect. 5.3.2. However, the fact that there are 6 peaks with similar  $\Delta C$ -stat values means that we likely cannot statistically differentiate which of these solutions are real and which are false detections as they will all result in similar statistical significances/false alarm probabilities. The situation is further complicated because these peaks are probably not independent, i.e. multiple potential peaks are fitting the same residuals to the baseline continuum, but with different outflow models.

We individually fit each of the peaks with  $\Delta C$ -stat  $> 15$  but find no further fit improvement or any particularly strong outliers. The tentative solutions mostly fit residuals in the RGS band, in particular those at 12-13 Å, at 15-16 Å and in the 20-22 Å range (Fig. 5.7). At the current data quality these residuals can be fitted equally well with multiple wind models. Since multiple wind solutions fit the RGS residuals similarly well, we cannot identify a unique solution with the present data. We find that none of the tentative peaks fit the remaining residuals seen in the iron K band,

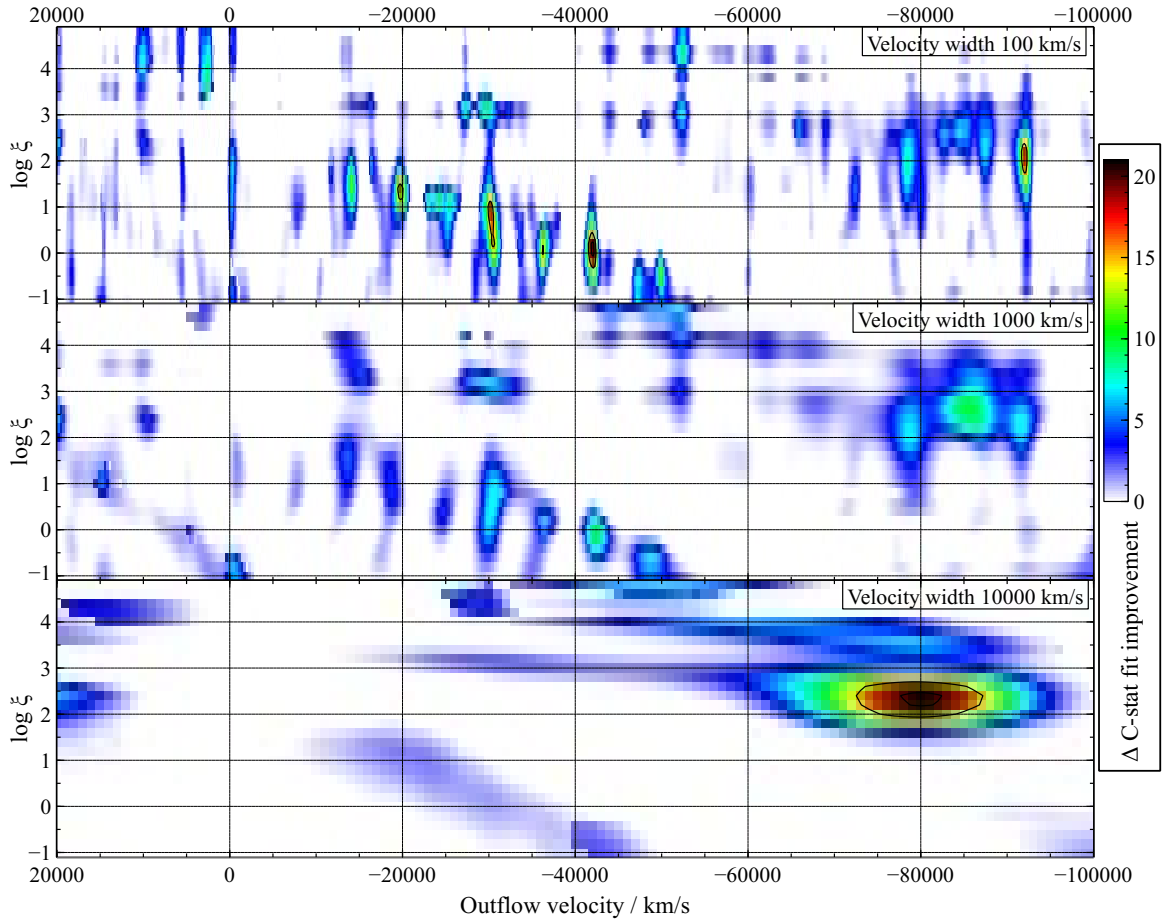


Fig. 5.8 Systematic scan for ionised outflow features in the spectrum of PG 1448+273, in addition to the primary ultrafast component outflowing at 27000 km/s and a warm absorber component in the AGN rest-frame. The spectrum is scanned with ionised absorption grids with systematic velocities between +20000 km/s and -100000 km/s (the X axis), ionisation parameters  $\log \xi$  between -1.0 and +4.8 (the Y axis), with turbulent velocity 100 km/s (top subplot), 1000 km/s (middle subplot) and 10000 km/s (bottom subplot). The colour shows the fit improvement  $\Delta C$ -stat upon adding the absorption grid to the continuum model (according to the colour bar on the right), the black contours show  $\Delta C$ -stat fit improvement of 15 and 20, respectively.

which could instead be interpreted as our imperfect fitting of the relativistic reflection with just the phenomenological Laor model (omitting the reflection continuum).

The large abundance of peaks with  $\Delta C$ -stat of around 15-20 however still suggests a very likely presence of a multi-phase outflow in PG 1448+273 because such strong false detections should occur rarely by chance. Based on our MC simulations, even accounting for their limited parameter space, we can very roughly assign a  $2\sigma$  statistical significance (including the look-elsewhere effect) to a  $\Delta C$ -stat=16 outflow detection. Such strong

fake detections should therefore only occur in 5 per cent of observations, suggesting that the secondary peaks are real. At this moment, unfortunately, identification of these potential components is just beyond the possibilities of the current data quality.

## 5.4 Discussion

We have performed a systematic search for an ionised outflow in the X-ray spectrum of the NLS1 AGN PG 1448+273. We significantly detect a highly ionised wind with a velocity of  $(0.090 \pm 0.002)c$ .

The absorption lines of the outflow are detected in both hard X-rays (iron K band) and soft X-rays (0.3-2.0 keV, particularly the O VIII line). This suggests the wind is not as extremely ionised as in other AGN and X-ray binaries where often only Fe XXV/XXVI features are observed [e.g. 393, 310]. This fact simplifies the inference of the wind parameters as it reduces the uncertainties in both the velocity and ionisation state of the outflow while simultaneously modelling the wind features as well as the iron K reflection.

The velocity of the outflow of  $\sim 0.1c$  is also not as high as seen in many other AGN [for a review of the recent UFO detections and their velocities see 295], where velocities as high as  $0.3c$ - $0.5c$  were detected [e.g. 330, 420, are the most extreme examples], although velocities in the range of  $0.05 - 0.1c$  have also been detected in some AGN [e.g. 313]. Similarly, the velocity width of the observed features is not large at  $2100_{-500}^{+600}$  km/s. This suggests that the AGN corona ionising the atoms within the outflow cannot be either too large or too close to where the wind absorption occurs as otherwise the toroidal motion within the wind (imprinted to the wind by the Keplerian rotation of the accretion disc) would broaden the absorption features [123].

We also note that the outflow velocity is lower than that of the UFO observed in IRAS 13224-3809 [ $0.25c$ , 297]. At the same time, the inclination of PG 1448+273 ( $\sim 40^\circ$ ) is lower than the inclination of IRAS 13224-3809 [about  $70^\circ$ , 169]. A lower UFO velocity in PG 1448+273 would be expected in the framework of a model where the UFO absorption is produced in an atmosphere co-rotating with the accretion disc [102] because the projected disc velocities are lower in PG 1448+273.

Curiously, the UFO is not detected in the short (20 ks) 2003 *XMM-Newton* observation of PG 1448+273 (Appendix B). The dataset is good enough to significantly reject a UFO of parameters similar to that observed in the main dataset. It is possible that the UFO is still present but at much higher ionisation or with a much lower column density. A change in the outflow velocity alone cannot explain the disappearance

of absorption lines from both EPIC and particularly RGS data. Interestingly, PG 1448+273 shows a higher flux during the shorter observation when the UFO is not seen. This is a similar behaviour to that of IRAS 13224-3809, which hosts a time-variable UFO, which anti-correlates in absorption strength with the AGN X-ray flux [297, 303]. Further long exposures with *XMM-Newton* will be required for a proper flux-resolved analysis to confirm the existence of this important trend in PG 1448+273.

We also detect a weak warm absorber in PG 1448+273. Warm absorbers were detected in multiple AGN with UFO detections, including PG 1211+143 [331], PG 1114+445 [360], IRAS 17020+4544 [217, 223] and IRAS 13349+2438 [350, 296]. Comparing their energetics and mass outflow rates can be helpful in explaining their (possibly common) origin [392] and their interaction with the surrounding environment. Unfortunately, the warm absorber in PG 1448+273 has a very small outflow velocity of  $100 \pm 200$  km/s, consistent with being at rest. The limits placed on its energetics are therefore not useful.

We search the X-ray spectrum of PG 1448+273 for further wind structure as multiphase ultra-fast outflows were previously detected in the X-ray spectra of other similar systems such as PG 1211+143 [two outflowing components at 0.06c and 0.13c, 313, 314, 204], 1H 0707-495 [0.03c and 0.13c, 196] and PDS 456 [ $\sim 0.25c$  and  $\sim 0.5c$ , 34]. Evidence for even more complex wind structure was found in PG 1114+445 [360] and in IRAS 17020+4544 [223]. The energetics of the different outflow phases can be used to infer the mode of interaction of the outflow with the surroundings of the AGN. Tombesi et al. [394] found that the kinetic powers of the X-ray and the molecular phases of the outflow in IRAS F11119+3257 are similar, suggesting an energy-conserving feedback. Kosec et al. [196] found that three individual outflowing components (including one observed in the UV band) likely have comparable kinetic powers in 1H 0707-495. On the other hand, Reeves and Braitto [329] detected a momentum-conserving outflow in the NLS1 I Zwicky 1.

Our second automated wind search locates a number of tentative outflow phases with a broad range of physical parameters, which would be difficult to identify with manual approach. However, the current data quality prevents us from claiming a significant detection of a multi-phase outflow in the present spectra. Future dedicated campaigns with *XMM-Newton* or with future X-ray observatories, doubling or tripling the total count statistics on PG 1448+273, would be able to constrain these features or rule them out as false detections.

Assuming our measurement of the ionisation parameter of the outflowing material is accurate, we can calculate the kinetic power of the detected accretion disc wind. Following the derivation in section 4.4, the kinetic power of an outflow is:

$$\dot{E}_K = \frac{1}{2} C_V \Omega \mu m_p v^3 \frac{L_{\text{ion}}}{\xi} \quad (5.1)$$

where  $\Omega$  the solid angle into which the wind is launched (in steradians). Using the results from the best-fitting two absorber model in Sect. 5.3.3 ( $v = 26900 \pm 600$  km/s,  $\log(\xi/\text{erg cm s}^{-1}) = 4.03_{-0.08}^{+0.10}$ ), we find:

$$\dot{E}_K = (1.8 \pm 0.5) C_V \Omega L_{\text{ion}} \quad (5.2)$$

Even if the clumping factor and the outflow solid angle are relatively small (unlikely as PG 1448+273 is not an edge-on AGN and yet we observe the wind), the kinetic power of the outflow can be comparable to its ionising (13.6 eV – 13.6 keV) luminosity. The wind is thus likely more than capable to drive AGN feedback in the host galaxy of PG 1448+273 [77, 190, 57]. Its energy budget is as large as the UFOs detected in similar NLS1s such as 1H 0707-495 [196] and IRAS 13224-3809 [297].

## 5.5 Conclusions

Here we summarize our results:

- We systematically searched the X-ray spectrum of the Narrow Line Seyfert 1 galaxy PG 1448+273 for signatures of ionised outflows. We unambiguously detect an ultra-fast outflow with a velocity of  $26900 \pm 600$  km/s ( $0.090_{-0.002}^{+0.002}c$ ). Our Monte Carlo simulations of the systematic wind search on simulated data show that the UFO detection is highly statistically significant.
- The wind material has an ionisation parameter of  $\log(\xi/\text{erg cm s}^{-1}) = 4.03_{-0.08}^{+0.10}$  and a column density  $2.8_{-0.7}^{+1.2} \times 10^{23}$  cm<sup>-2</sup>. The ionisation of the material is similar to that of the outflows found in other AGN. The projected wind velocity is on the lower end of the range of the extreme outflows observed in other AGN.
- The spectral features of the ionised outflow are observed in both hard X-rays (iron K band) with EPIC pn and MOS detectors, and in the soft X-ray band with RGS gratings onboard the *XMM-Newton* observatory.

- Our results underline the importance of the soft X-ray band in detecting high-velocity highly ionised outflows. Inferring the outflow properties from just the iron K band (7-8 keV) is often problematic due to the common presence of the blue wing of the relativistically blurred iron K reflection at similar energies [438], as well as due to confusion between the Fe XXV and Fe XXVI absorption lines of the ionised outflow.
- A UFO of similar parameters is not detected in a second, shorter (20ks) observation of PG 1448+273 during which the AGN was in a higher X-ray flux state. The outflow could still be present in the X-ray spectrum, but at a much higher ionisation or with a significantly lower column density. The UFO disappearance at higher fluxes suggests similarities between PG 1448+273 and another NLS1 IRAS 13224-3809, where the wind absorption anti-correlates with the X-ray flux [297].
- We also detect a low ionisation warm absorber in the soft X-ray band. It is consistent with being at rest and has a column density of  $(3.8 \pm 1.7) \times 10^{20} \text{ cm}^{-2}$  and an ionisation parameter of  $\log(\xi/\text{erg cm s}^{-1}) = -0.4^{+0.3}_{-0.4}$ .
- We perform a systematic search for further ionisation and velocity phases of the outflow and tentatively detect one or more phases with potential outflow velocities in the range between 20000 and 90000 km/s. However, with the present data quality we are unable to significantly confirm or reject their presence in the spectrum of PG 1448+273.

## Chapter 6

A stratified ultrafast outflow in the  
active galactic nucleus

1H 0707-495?



# Abstract

UFOs have been found in the spectra of a number of AGN and are strong candidates for driving AGN feedback. 1H 0707-495 is a highly accreting Narrow Line Seyfert 1 and the second most X-ray variable bright AGN. Previous studies found evidence of blueshifted absorption at 0.1-0.2c in its spectrum. We perform a flux-resolved analysis of the full *XMM-Newton* dataset on this AGN using both CCD and grating data, focusing on the low flux spectrum. We find strong evidence for an ultrafast outflow in absorption at  $\sim 0.13c$ , with an ionisation parameter  $\log(\xi/\text{erg cm s}^{-1}) = 4.3$ . Surprisingly, we also detect blueshifted photoionised emission, with the velocity increasing at higher ionisation states, consistent with a trend that has been observed in the UV spectrum of this object. The bulk of the X-ray emitting material is moving at a velocity of 8000 km/s, with an ionisation parameter of  $\log(\xi/\text{erg cm s}^{-1}) = 2.4$ . The wind kinetic power inferred from the UFO absorption is comparable to that of the UV and X-ray emission features despite their different velocities and ionisation states, suggesting that we are viewing an energy-conserving wind slowing down and cooling at larger distances from the AGN.

## 6.1 Introduction

UFOs are thought to be powerful winds from AGN with outflow velocities greater than 10000 km/s. They are most commonly identified through high-energy absorption features from Fe XXV/XXVI in the 7-10 keV energy band [e.g. 393], consistent with highly ionized gas blueshifted at significant fractions of the speed of light. These features are generally thought to originate in winds magnetically or radiatively driven off the AGN accretion disc at high Eddington rates [316, 332, 124]. If this scenario is correct, these winds are of great interest because they are very strong candidates for driving AGN feedback, as they couple with galactic gas much more efficiently than jets.

NLS1s are a subclass of highly variable AGN that usually host lower-mass super-massive black holes ( $10^6 - 10^7 M_{\odot}$ ). They are thought to accrete at high Eddington

fractions [possibly super-Eddington, 172]. IRAS 13224-3809 (hereafter IRAS 13224) and 1H 0707-495 (hereafter 1H0707) are the most X-ray variable objects from this class, varying by factors of tens within hours. These two objects share many similarities, including their broadband X-ray spectra, timing behaviour [437, 182] and UV emission features [218].

Parker et al. [297, 294] recently found a variable  $\sim 0.2c$  UFO in the spectrum of IRAS 13224. It is observed most clearly in the 7-10 keV band, but is also visible in the 0.4-2 keV RGS data [303]. The UFO absorption is strongest when the flux of the AGN is low, and almost disappears in high flux states, varying on time-scales of ks. Given all the similarities between IRAS 13224 and 1H0707, it is reasonable to expect 1H0707 to also possess powerful winds.

Early studies of 1H0707 with *XMM-Newton* already noticed a sharp drop in flux at 7 keV, which was interpreted as the blue wing of relativistically broadened iron K emission, or alternatively as blueshifted ionised iron absorption or the blue wing of a P Cygni wind profile [36, 98, 85]. With larger datasets, it was possible to show that a major component of the continuum emission is indeed iron K and L reflection [104, 437]. Dauser et al. [63] found absorption features, on top of smeared reflection, consistent with the Si, S, Ar and Ca Ly $\alpha$  lines in the long 2008 and 2010 *XMM-Newton* observing campaigns, with outflow velocities of 0.11c and 0.18c, respectively. Blustin and Fabian [32] found double-peaked emission lines consistent with a broad-line region origin, but no signs of a UFO in the high-spectral resolution RGS data using the full 2008 campaign dataset. More recently, Hagino et al. [145] re-analysed the archival *XMM-Newton* data, finding clear evidence of an absorption feature at 8 keV, likely from blueshifted ionised iron.

Here we perform a flux-resolved analysis of the full *XMM-Newton* dataset including the high spectral-resolution RGS data aiming to confirm the presence of absorption features from a UFO in 1H0707. We focus only on the low flux periods of time, following the approach of [297] in analysing IRAS 13224 *XMM-Newton* data. We find strong evidence for an ultrafast outflow at 0.14c in the low flux spectrum of 1H0707. We also report the detection of blueshifted photoionised gas in emission with velocity increasing with ionisation state (in agreement with earlier UV data) in the same dataset.

## 6.2 Observations and data reduction

There is a wealth of data from multiple campaigns on this source. Here we use the full *XMM-Newton* dataset [166], spanning a time period from 2000 to 2010, excluding only observations shorter than 10 ks.

The data were reduced using a standard pipeline with SAS v16, CalDB as of April 2018. We use data from pn [378] and RGS [72] instruments only and process them as described in section 2.1. The high-background periods are filtered with a threshold of 0.4 counts/sec for pn and 0.15 counts/sec for RGS data. The source regions for pn were circles centred on the object with a radius of 20 arcsec (to maximise the signal-to-noise ratio in the 7-10 keV band), and the background regions were circles with a radius of 60 arcsec on the same chip as the source while avoiding the copper ring.

All spectra were converted into SPEX format. The pn data were grouped to at least 25 counts per bin and also binned by at least a factor 3. RGS data were binned by a factor of 3 directly in SPEX. The RGS spectral range used was 7 Å (1.77 keV) to 31 Å (0.4 keV), limited by the background; pn data were used between 1 and 10 keV to provide some overlap with the RGS energy band where the RGS count rate is low ( $<12$  Å).

We performed a flux-resolved reduction to analyse the source spectrum in the low flux state, which is the state in which the UFO absorption is strongest in IRAS 13224 [297]. We extracted 3 spectra of the source in different flux states so that each has comparable statistics (Fig. 6.1). This was done by taking a full lightcurve (bin size of 100 s) of the source during all the 15 *XMM-Newton* observations and identifying the flux cut limits. Afterwards, the flux-resolved pn and RGS spectra were extracted for each observation, making sure that the extracted intervals for RGS and pn instruments are identical. Finally, all the individual observation spectra were stacked into 3 RGS and 3 pn spectra. The low-flux spectra are shown in Fig. 6.2. The total exposure (RGS1/RGS2) is around 500 ks, with a 0.3-10 keV average flux of  $4.0 \times 10^{-12}$  erg s<sup>-1</sup> cm<sup>-2</sup>.

We obtained the object redshift of  $z = 0.0405$  from the NASA/IPAC Extragalactic Database. The Galactic column density at the source position is around  $N_H = 4.6 \times 10^{20}$  cm<sup>-2</sup> [Leiden/Argentine/Bonn Survey of Galactic HI, 179]. All the fits are performed in the SPEX fitting package using Cash statistics [47]. All uncertainties are stated at the  $1\sigma$  level. Throughout the study we assume solar abundances [220].

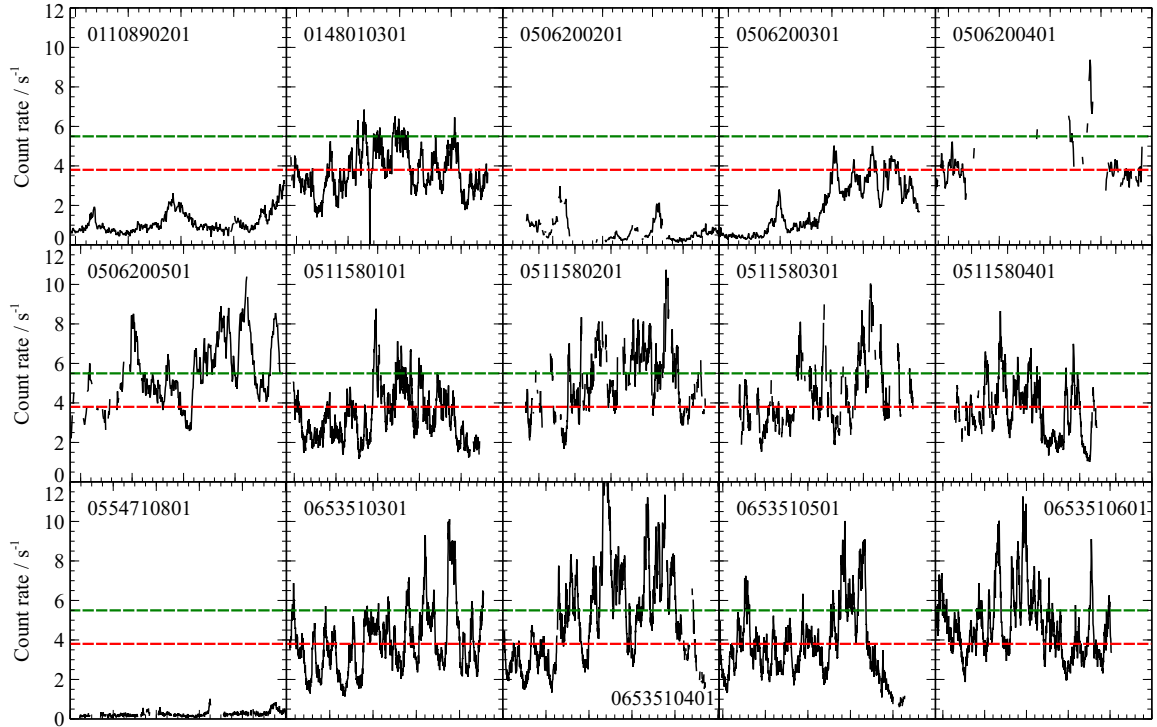


Fig. 6.1 The lightcurve of 1H0707 using all the *XMM-Newton* observations. The EPIC pn count rate (on the Y axis) is extracted only in the 0.4 – 1.77 keV RGS band. The green and red horizontal dashed lines split the whole dataset into three data groups, each with similar total counts in the RGS band. In this chapter we only analyse the lowest flux periods (below the red dashed line). The missing lightcurve intervals were filtered out due to strong background flaring.

## 6.3 Methods and results

### 6.3.1 Broadband fitting

The broadband (0.4-10 keV) spectrum was fitted with a phenomenological model composed of a powerlaw (POW), a soft ( $\sim 0.1$  keV) blackbody (BB) and 2 relativistic disc lines (LAOR  $\times$  GAUSS), similar to the model used in Fabian et al. [104]. The first Laor line describes smeared iron K reflection at 6 keV, the second one represents broadened iron L reflection around 1 keV and the blackbody models the soft excess of the source. The redshift of the source is represented with a REDS model. All of the components are obscured by Galactic (mostly) neutral gas using the HOT model in SPEX. An identical spectral model was used by Pinto et al. [303] to describe the spectrum of IRAS 13224-3809 and results in an acceptable fit.

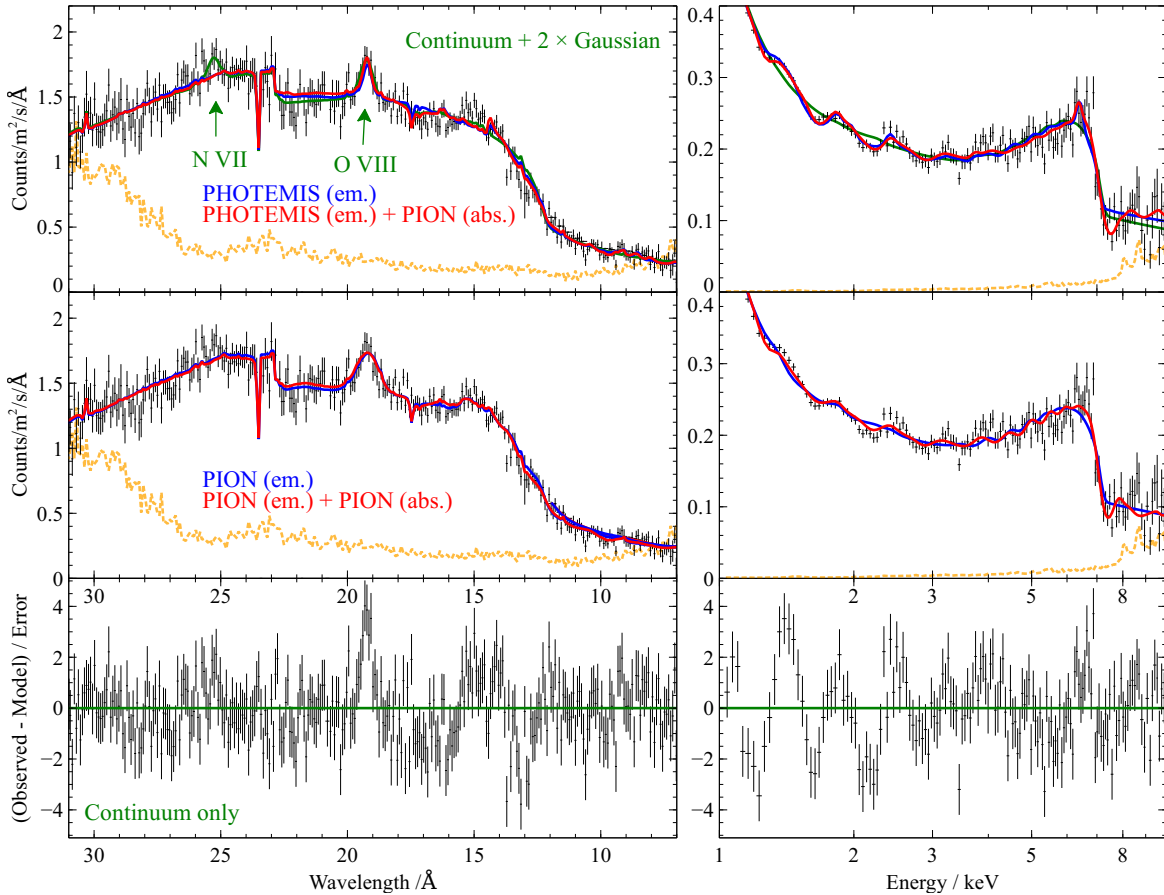


Fig. 6.2 Low flux X-ray spectrum of 1H 0707-495 using all *XMM-Newton* data and both RGS (left subplots) and pn (right subplots) instruments. The top 2 rows of sub-plots contain the same data but fitted with different spectral models (Section 6.3). The top plots show a broadband continuum model plus 2 additional Gaussians (green), continuum plus PHOTEMIS (blue), and continuum plus PHOTEMIS + PION (red). The two middle plots contain fits with the continuum model plus PION (emission, blue), and PION+PION (both emission and absorption, in red). The bottom plots show the residuals to the broadband continuum fit (from section 6.3.1) without any blueshifted emission or absorption included. We note that the left plots are in Angstrom and the X-axis is linear, while the right plots are in keV with a logarithmic X-axis, both axes show the observed quantities (not rest-frame). The Y-axis shows flux, unfolded with the instrument response only, and is linear in all plots (but note the different units in the left and right plots). Background is shown in orange colour. The RGS spectrum has been rebinned for plotting purposes.

We describe the low flux spectrum of 1H 0707-495 with this model, which results in a relatively poor fit (C-stat of 1554.60 for 935 D.o.F.), mostly because of a very strong emission feature around  $19 \text{ \AA}$  (0.65 keV), but also due to an emission residual around  $25 \text{ \AA}$  (0.5 keV) and multiple unresolved residuals in the pn spectrum. The best-fitting parameters are: powerlaw slope  $\Gamma = 2.61 \pm 0.02$ , blackbody temperature  $0.107 \pm 0.001$  keV, Laor line rest-frame energies  $0.795_{-0.002}^{+0.007}$  keV and  $5.64_{-0.03}^{+0.05}$  keV. We note that the best-fitting iron K line energy is impossibly low, which suggests probable absorption of its blue wing, as expected if a UFO is present. The inner disc radius given by the laor model is  $1.29_{-0.06}^{+0.04} R_G$ , the emissivity of the disc is  $7.3_{-0.2}^{+0.4}$  and its inclination  $70.7_{-0.2}^{+0.3}$  degrees, in rough agreement with previous work. The fitted neutral column density is  $7.3_{-0.5}^{+0.4} \times 10^{20} \text{ cm}^{-2}$ , significantly higher than Galactic [in agreement with 63].

### 6.3.2 Emission lines fitted with Gaussians

From the fit statistics and the apparent residuals, it is evident that the simple broadband spectral model is insufficient. The strongest emission residuals are located at around  $19 \text{ \AA}$  (0.65 keV) and  $25 \text{ \AA}$  (0.50 keV) – very close to the rest-frame positions of O VIII and N VII transitions. There is no excess around  $22 \text{ \AA}$  (0.56 keV), where the O VII transition is located. However, this part of the spectrum could be affected by neutral absorption in our and the host galaxy; also our exposure in the O VII energy band is halved (due to a missing chip in RGS2).

First, we fit these emission features with Gaussians (in addition to the broadband spectral model) to determine whether they are indeed rest-frame to the AGN host galaxy. We choose to couple the velocity widths of both lines, otherwise the N VII line runs away to unreasonably large linewidths. The best-fitting line centroids (in the host galaxy rest-frame) are:  $18.49 \pm 0.04 \text{ \AA}$  compared to O VIII rest-frame wavelength of  $18.97 \text{ \AA}$  and  $24.30 \pm 0.08 \text{ \AA}$  compared to N VII rest-frame wavelength  $24.78 \text{ \AA}$ . The velocity width is  $4200_{-800}^{+900} \text{ km/s}$ . The line positions are neither rest-frame to the host nor our Galaxy and the lines are broad, therefore they must come from blueshifted gas near the AGN. The systematic velocity of the gas emitting O VIII is  $7600_{-600}^{+500} \text{ km/s}$ , and that of N VII is  $5800 \pm 1000 \text{ km/s}$ . Both Gaussians are highly statistically significant, O VIII improving the fit statistics by  $\Delta\text{C-stat} \sim 88$  and N VII by  $\Delta\text{C-stat} \sim 23$ .

We note that both these emission features were already described by Blustin and Fabian [32] in the 2008 campaign dataset, who also suggested the presence of redshifted components (both components interpreted to originate in the accretion disc at  $\sim 1600 R_G$ ). Using the full low-flux dataset, we do not see evidence for any redshifted emission

with flux comparable to the blueshifted features, and instead interpret the blueshifted emission as a photoionised wind.

### 6.3.3 Physical models of photoionised emission

The different blueshifts of the emission lines and the lack of O VII mean that it is not possible to fit them with a single spectral model with just one ionisation parameter. In the following part, we mainly focus on the stronger of the two features, the O VIII emission line. We fit the spectrum with two spectral models describing photoionised emission physically: PHOTEMIS and PION. We have also attempted to fit the spectrum with collisional ionisation models (emission originating in shocks) but they generally provide a significantly worse description of the features, i.e. they offer poor  $\Delta C$ -stat fit improvements compared to the fit improvements obtained with photoionisation models.

First we use the PHOTEMIS model, which describes recombination and collisional excitation emission from a photoionised slab of plasma. It is implemented in the XSPEC package, and can be exported into SPEX as a table. We achieve the best fit for the ionisation parameter of  $\log \xi = 2.3$  ( $\text{erg cm s}^{-1}$ ) and the velocity width of 3000 km/s. Adding the photoionised emission component is highly statistically significant and improves the fit to C-stat=1354 for 933 D.o.F. ( $\Delta C$ -stat= 200 for 4 additional D.o.F.). While this is still a formally unacceptable fit, the fit improvement is very large and hence the addition of the photoionised emission component is highly statistically significant. We note that this fit not only describes the O VIII feature, but also reproduces residuals in pn spectrum between 2 and 5 keV very well. The systematic velocity of the outflowing photoionised emitter is  $8400_{-500}^{+400}$  km/s.

Secondly, we use a native SPEX model PION (see section 1.4.3 for more details about PION). PION self-consistently calculates the photoionisation balance directly from the continuum fit and can reproduce both emission and absorption features. The disadvantage in using the model is a much higher computational cost. In this section we use the model to reproduce the emission residuals only (by setting the covering fraction  $F_{\text{COV}} = 0$  and the opening angle  $\Omega = 1$ ). We achieve the best-fitting solution for an ionisation parameter of  $\log(\xi/\text{erg cm s}^{-1}) = 2.35_{-0.03}^{+0.05}$  and a velocity width of  $6300_{-500}^{+700}$  km/s, with a systematic velocity of  $8700_{-700}^{+400}$  km/s with respect to the host rest-frame. The column density of emitting gas is  $3.5 \pm 0.3 \times 10^{21} \text{ cm}^{-2}$  and the fit improvement is  $\Delta C$ -stat = 164 for 4 additional D.o.F.

### 6.3.4 UFO absorption signatures

The very low energy of the iron K line (broadened with a LAOR shape) suggests that its blue wing might be obscured - potentially by a UFO. To test for this possibility, we add another component to our continuum + photoionised emission fit. We use a second PION component to describe the potential blueshifted absorption only (setting  $F_{\text{COV}} = 1$  and  $\Omega = 0$  to just model absorption features). Both absorption and emission cannot be described by a single PION component because the velocities of the emitting and absorbing gas are likely different (absorption is usually much faster,  $\sim 0.1c$ ). The blueshifted emission is in this case modelled by PION ( $F_{\text{COV}} = 0$  and  $\Omega = 1$  as in the previous section).

Adding the blueshifted absorber results in a significant fit improvement of  $\Delta C$ -stat = 117 for 4 additional degrees of freedom (column density, ionisation parameter, systematic and turbulent velocity), with C-stat = 1273 for 927 D.o.F. The result is shown in Fig. 6.2 and in Table 6.1. The best-fitting outflow velocity (relativistically-corrected) is  $38400_{-1000}^{+700}$  km/s (0.13c) and the ionisation parameter is  $\log(\xi/\text{erg cm s}^{-1}) = 4.32_{-0.02}^{+0.03}$ . The column density of the absorber is  $2.4 \pm 0.2 \times 10^{23}$  cm $^{-2}$  and its turbulent velocity is  $9600_{-800}^{+900}$  km/s. The parameters of the slow emitter are similar to those in the previous section: column density  $3.9_{-0.3}^{+0.5} \times 10^{21}$  cm $^{-2}$ , ionisation parameter  $\log(\xi/\text{erg cm s}^{-1}) = 2.44 \pm 0.03$ , turbulent velocity  $6100_{-700}^{+600}$  km/s and systematic velocity  $8400_{-700}^{+400}$  km/s. We note that the energy of the iron K line is now  $6.61 \pm 0.05$  keV - which seems plausible if the line is produced by a mix of neutral (6.4 keV) and ionised (6.7 keV) iron.

We verified that using a PHOTEMIS component to describe the emission lines produces comparable results. The best-fitting solution has a speed of  $\sim 0.14c$  with the fit statistics of 1268 for 929 d.o.f., a  $\Delta C$ -stat = 86 improvement over the model with PHOTEMIS emission only. The UFO absorption velocity is  $41900 \pm 800$  km/s, column density  $3.9 \pm 0.1 \times 10^{23}$  cm $^{-2}$ , ionisation parameter  $\log(\xi/\text{erg cm s}^{-1}) = 4.16 \pm 0.02$  and turbulent velocity  $12200_{-700}^{+800}$  km/s. The continuum and emission parameters remain almost unchanged except for the best-fitting emitter ionisation parameter, which is  $\log(\xi/\text{erg cm s}^{-1})_i = 2.1$ .

Table 6.1 The best-fitting parameters of the models of photoionised emission and absorption (see Sect. 6.3.4).

Model	Emission			Absorption			
	$V_{\text{syst}}$ km s <sup>-1</sup>	$N_{\text{H}}$ cm <sup>-2</sup>	$\log(\xi)$ erg cm s <sup>-1</sup>	$V_{\text{turb}}$ km s <sup>-1</sup>	$N_{\text{H}}$ cm <sup>-2</sup>	$\log(\xi)$ erg cm s <sup>-1</sup>	$V_{\text{turb}}$ km s <sup>-1</sup>
PION+PION	$8400^{+400}_{-700}$	$10^{21}$	$2.44 \pm 0.03$	$6100^{+600}_{-700}$	$10^{23}$	$4.32^{+0.03}_{-0.02}$	$9600^{+900}_{-800}$
PHOTEMIS+PION	$8100^{+300}_{-400}$	*	2.1	3000	$(3.9 \pm 0.1)$	$4.16 \pm 0.02$	$12200^{+800}_{-700}$

\* It is not possible to extract an accurate value of the gas column density with PHOTEMIS.

A large fraction of the statistical significance upon adding the UFO absorption comes from the Fe XXV/XXVI absorption (Fig. 6.2). In addition, the absorption lines of Mg XII, Si XIV and S XVI are clearly fitted between 1.5 and 3 keV. Smaller absorption features are located at  $\sim 10 \text{ \AA}$  (Ne X) and  $\sim 17 \text{ \AA}$  (O VIII). We note that the features between 2 and 3 keV can also be fitted with S XV emission instead of absorption (PHOTEMIS emission fit only), although the first option is more plausible [the features are also seen in IRAS 13224 where no strong photoionised emission is present, 294]. Additionally, the PHOTEMIS fit also adds an iron emission feature at  $\sim 6.4 \text{ keV}$ , likely a blend of Fe XIX-XXI lines.

To place the UFO solution on a firmer footing, we quantify the statistical fit improvement for the strongest individual UFO absorption lines: Fe XXV/XXVI, S XVI, Si XIV, Mg XII, Ne X and O VIII. We take the original broadband continuum and add a Gaussian at the energy where an absorption line is expected for the best-fitting UFO velocity, fit for its parameters, recovering the fit improvement  $\Delta C$ -stat, its blueshift and turbulent velocity. The results are shown in Table 6.2. We note that a fit improvement of more than  $\Delta C$ -stat = 25 is very high for an individual line [including the look-elsewhere effect, 198] but Monte Carlo simulations would have to be performed to quantify the exact statistical significance. There are 2 likely explanations for the 7.6 keV residual - Fe XXV or Fe XXVI. At the ionisation level of  $\log(\xi/\text{erg cm s}^{-1}) = 4.0 - 4.3$ , the feature will most likely be a blend of both Fe XXV and Fe XXVI, but the majority of absorption will still originate from Fe XXV. In conclusion, most of the absorption residuals are highly significant and support a coherent picture of a UFO moving at a velocity of  $\sim 40000 \text{ km/s}$ . We note that the velocity width of the Mg XII residual is significantly lower than the widths of the other residuals. It is possible that the residual is affected by nearby slow emission transitions. This could also be the case for the 2 lowest energy transitions, Ne X and O VIII, where the blueshifted emission features are strongest and the simple broadband continuum does a poor job of reproducing the spectrum. Specifically, upon accounting for the emission features with a physical model, the underlying continuum changes slightly which can affect the true absorption line position and its depth (and hence the  $\Delta C$ -stat fit improvement). Most notably, the absorption residual associated with O VIII is located between 2 strong emission lines at  $19 \text{ \AA}$  (O VIII) and  $15 \text{ \AA}$  (Fe XVII) in observed frame (see Fig. 6.2). Therefore the best-fitting energies of these low energy ( $< 2 \text{ keV}$ ) absorption lines should be taken with caution.

Table 6.2 The strongest absorption residuals fitted with a Gaussian. The first two transitions detail different interpretations for the same Fe K feature.

Transition	$\Delta C$ -stat <sup>1</sup>	Rest-frame energy keV	Best-fitting energy keV	Blueshift km s <sup>-1</sup>	Turbulent width km s <sup>-1</sup>
Fe XXV	44.68	6.70	$7.63 \pm 0.03$	$38900 \pm 1100$	$12800^{+1000}_{-1100}$
Fe XXVI	44.68	6.96	$7.63 \pm 0.03$	$27600 \pm 1100$	$12800^{+1000}_{-1100}$
S XVI	6.76	2.62	$2.97 \pm 0.06$	$38000 \pm 6000$	$21000 \pm 11000$
Si XIV	41.01	2.01	$2.23 \pm 0.02$	$32000 \pm 3000$	$25000^{+6000}_{-7000}$
Mg XII	25.72	1.472	$1.702 \pm 0.005$	$43200 \pm 800$	$< 2100$
Ne X	62.58	1.022	$1.188^{+0.019}_{-0.014}$	$45000^{+4000}_{-5000}$	$27000^{+4000}_{-6000}$
O VIII	49.99	0.654	$0.765 \pm 0.006$	$47000 \pm 2000$	$17700^{+2200}_{-1900}$

<sup>1</sup>Fit improvement in  $\Delta C$ -stat upon fitting the feature with a Gaussian.

### 6.3.5 Time and flux variability of the emission and absorption features

A possible caveat of using 10 years worth of data to perform a flux-resolved analysis is potential time variability of the emission and absorption features. Such variability could for example wash out the features or broaden them. Indeed, Dauser et al. [63] find evidence for a shift in the UFO absorption velocity when comparing the datasets from two long *XMM-Newton* campaigns on the source, in 2008 and 2010. On the other hand, the emission features are expected to be less variable (if they originate at larger distances from the central engine). To check that this is the case, we extract low-flux spectra from the 2008 and 2010 campaigns separately using the same flux limits obtained in the full dataset reduction.

We fit the 2 spectra with the photoionisation emission code PHOTEMIS+PION in addition to the standard broadband continuum, which is computationally less expensive than using the PION+PION model. The best-fitting blueshifted emission parameters for the 2008 campaign data are: the systematic velocity of  $7100 \pm 700$  km/s,  $\log(\xi/\text{erg cm s}^{-1}) = 2.2$  and a turbulent velocity of 2000 km/s. The systematic velocity of the emitter during the 2010 campaign was  $8500^{+500}_{-300}$  km/s,  $\log(\xi/\text{erg cm s}^{-1}) = 2.0$  and a turbulent velocity of 2500 km/s. The strongest feature of the photoionised emission is O VIII - the spectra of the O VIII spectral band during 2008 and 2010 are shown in Fig. 6.3 as a visual check.

We do therefore observe some variability between the two epochs, with approximately a  $2\sigma$  change in the outflow velocity. The ionisation parameter values need to be taken with caution as the data quality is much lower than using the full dataset. It does seem likely that co-adding the two epochs causes some broadening of the features. Nevertheless, the effects of stacking do not seem to be too severe and do not change the main conclusions of this analysis.

Assuming the photoionised gas has a transverse velocity comparable with the projected outflow velocity, and at the same time its total velocity is approximately the escape velocity, we can estimate the likely timescales of variability of the outflowing structure in case it is not axisymmetric. Taking the 1H0707 mass to be  $2 \times 10^6 M_{\odot}$  [83], the rotational period of the whole structure is  $P \sim \frac{2\pi R}{v} = \frac{2\pi GM}{v^3} \approx 1$  month. This timescale is completely averaged over during our full multi-year observational campaign. Nevertheless, the small change between the wind properties in 2008 and 2010 (both of these intensive campaigns lasted roughly 1 week) argues against strong intrinsic time variability or a highly non-axisymmetric structure of the photoionised emitter.

A full analysis of the medium and the high flux spectrum of 1H0707 is outside the scope of this work. However, upon inspection of these spectra, it is evident that with increasing flux, the emission residuals decrease in relative strength compared to the broadband continuum. It is possible to fit them approximately with the same PHOTEMIS model of photoionised emission used for the low flux spectrum (including its normalisation) which suggests that the emitting wind is independent of the AGN flux changes, as expected if it is located further from the AGN. The UFO absorption can be much more variable as seen in IRAS 13224 [297]. In the case of 1H0707, with increasing flux the absorption residuals get weaker but are still present in the spectrum. Therefore it seems that the UFO does not disappear completely as might be the case for IRAS 13224.

## 6.4 Discussion and conclusions

Our results show that using flux-resolved high-resolution X-ray spectroscopy to obtain a low-flux spectrum of the NLS1 1H 0707-495 reveals blueshifted emission as a UFO in absorption.

We find reasonable agreement between the different spectral models used to describe the emission features. It is especially reassuring that the models agree on the velocity of about 8000 km/s and the ionisation parameter of  $\log(\xi/\text{erg cm s}^{-1}) \sim 2.1 - 2.4$ ,

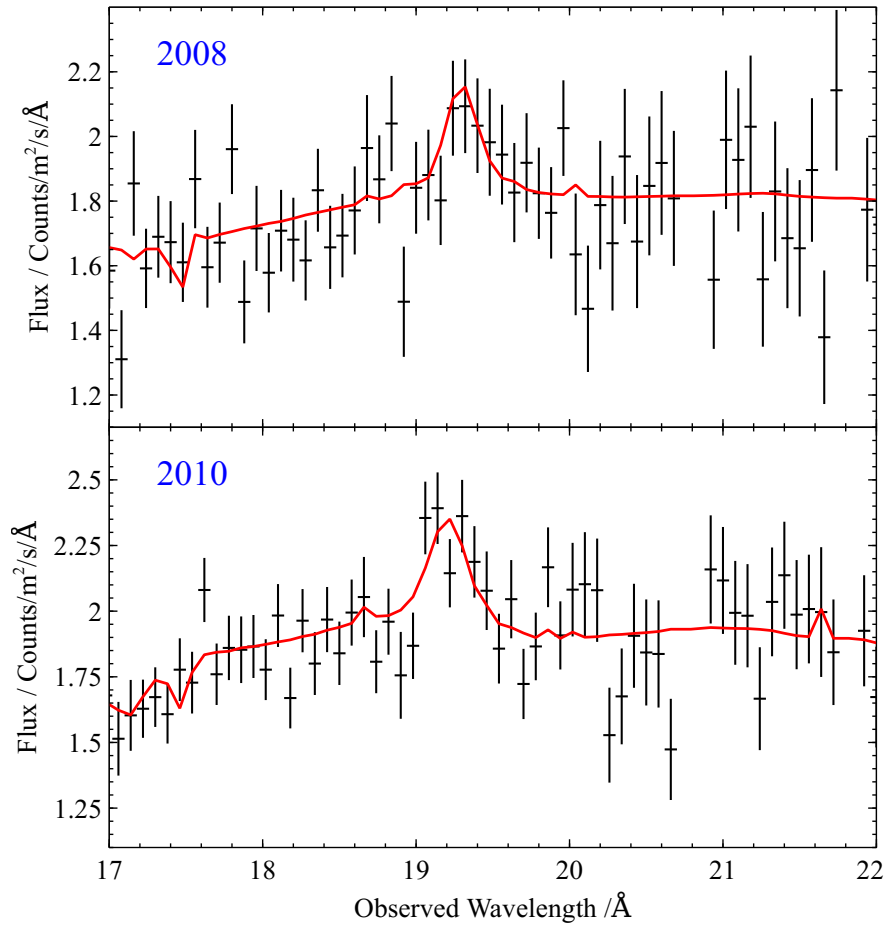


Fig. 6.3 The O VIII region of the 2008 (top) and 2010 (bottom) campaign low flux spectra extracted using the same flux limits used for the full dataset reduction. The X-axis shows the observed (not rest-frame) wavelength in Å, and the Y-axis shows flux, unfolded with the instrument response only.

from which the physical properties of the wind can be inferred. The turbulent velocity of gas is 3000-6000 km/s, and the column density is several times  $10^{21} \text{ cm}^{-2}$ .

Since the outflowing gas is observed in emission, we would also expect to observe the receding (redshifted) part of the outflow. However, no redshifted emission lines are detected. This material therefore has to be absorbed. Given that most of the photoionised emission is observed in the soft X-ray band, the neutral column density required for the absorption is not extreme, but has to be around  $3 \times 10^{21} \text{ cm}^{-2}$  or higher. If the outflow is close to its escape velocity, it is located at a distance of 1000s of  $R_G$  from the black hole. The extent of the neutral absorber would have to be comparable. Alternatively, the outflow could have a bi-conical structure and its

receding part could be obscured by the accretion disc itself. Given that the velocity width of the observed photoionised emission is almost comparable to the systematic velocity, it is possible that we are only viewing the approaching side of the wind. If this is the case, considering the relatively high inclination of 1H0707 of around  $60^\circ$  [104] and the non-detection of any redshifted emission, this material should be moving at angles smaller than  $30^\circ$  to the axis of the accretion disc. Fig. 6.5 shows this scenario in a schematic containing both outflow components: the blueshifted emission, and the UFO.

The UFO material is much more ionised than the blueshifted emitter with  $\log(\xi/\text{erg cm s}^{-1}) \sim 4.3$ , column density of  $3 \times 10^{23} \text{ cm}^{-2}$ , turbulent velocity of 10000-12000 km/s and systematic speed of 39000-42000 km/s (0.13-0.14c). The parameters of the UFO do not stand out if compared to other AGN, where velocities between 0.1 and 0.3c are commonly observed [393, 295]. The ionisation parameter and column density are very similar to the UFO observed in IRAS 13224, although the velocity is smaller [0.2-0.25c in IRAS 13224, see 294]. Dauser et al. [63] analysed the 2010 and 2012 campaigns on 1H0707 separately and found evidence for a UFO velocity shift from 0.11c to 0.18c. Our result of 0.14c using the low flux state of the full dataset (2000 to 2011) therefore averages over this possible shift (however the full dataset is necessary to analyse the emission features). This is likely captured in the rather high velocity width of the UFO lines ( $\sim 10000 \text{ km/s}$ ). A velocity shift would also decrease the UFO detection significance, which is nevertheless still very high with  $\Delta C\text{-stat} = 85 - 115$  for 4 D.o.F. [see 198, 199, to see how Monte Carlo simulations can be used to determine the precise statistical significance]. In each case, it is encouraging that including the absorber raises the rest-frame energy of the smeared iron K emission line from an unphysically low value of  $\sim 5.6 \text{ keV}$  to  $\sim 6.6 \text{ keV}$ , regardless of the absorption model used.

With this discovery, we are adding 1H0707 to a list of known AGN with strong evidence for multiphase outflows. Detection of two UFOs in absorption at 0.06c and 0.13c was reported using hard X-ray, soft X-ray and also UV data in the spectrum of another NLS1 PG 1211+143 [313, 314, 204]. Similarly, the spectrum of PDS 456 shows evidence for two very fast UFOs at 0.25c and at 0.46c [279, 330]. Other examples are IRAS 17020+4544, with evidence for up to 5 UFO phases [223], and IRAS F11119+3257, where X-ray UFO absorption as well as a kpc-scale molecular outflow (with comparable energetics) is observed [394]. However, we note two important differences between these objects and 1H0707. First, all the aforementioned outflows were detected in absorption only. To our knowledge, 1H0707 is currently the only known object to

show significantly blueshifted X-ray absorption and emission at the same time. NGC 4051 shows evidence for some blueshifted X-ray emission [317], but much slower at  $\sim 750$  km/s. The second difference is in the outflow velocities - while most UFOs in absorption achieve sub-relativistic speeds of 0.05-0.5c, here the blueshifted emission is significantly slower at  $< 10000$  km/s.

It is useful to estimate the total kinetic power of the outflowing gas. Here we estimate the power separately for both absorbing and emitting gas and compare them. Following the derivation in section 4.4, the mechanical power of an outflow is  $\dot{E}_{\text{kin}} = 2\pi\Omega C_V L_{\text{ion}} m_H \mu u^3 / \xi$ . For the ultrafast absorber, using the best-fitting values from the PION + PION fit, we obtain  $\dot{E}_{\text{kin}} = 34_{-5}^{+4} \Omega C_V L_{\text{ion}}$ . Repeating the same calculation for the photoionised emitter (from the same spectral fit) gives  $\dot{E}_{\text{kin}} = 27_{-7}^{+6} \Omega C_V L_{\text{ion}}$ . If the ionising luminosity, solid angle and filling factor of the outflows are comparable, these are two strikingly similar estimates despite completely different velocities and ionisation parameters. However, we note that the volume filling factor,  $C_V$ , of both gas phases is highly uncertain. If for instance the lower ionisation wind component is in the form of compact clumps, its  $C_V$  could be much smaller than the one of the UFO absorbing gas. Then the kinetic power of the soft X-ray emitting material could be significantly lower than estimated above.

Leighly and Moore [218] performed a UV spectral study of 1H0707 and IRAS 13224 and found that while the low ionisation lines such as Mg II and C III appear to be rest-frame and of disc origin, the higher ionisation lines [Si IV, O IV] and C IV are blueshifted at up to  $\sim 2000$  km/s. Here we have discovered an extension of the same trend in X-rays with 2 high ionisation transitions, N VII and O VIII, at much higher velocities (see Fig. 6.4). If we fit the ions with non-zero velocity with a function in form  $v = b \times \xi^a$ , where  $v$  is velocity,  $\xi$  is the ionisation parameter and  $a$  and  $b$  are constants, the best-fitting powerlaw slope is  $a = 0.36 \pm 0.04$  [we note that we choose arbitrary 500 km/s errorbars on UV ion velocities due to a lack of uncertainties in 218]. This suggests that  $\frac{v^3}{\xi}$  is consistent with being constant and hence that energy is being conserved if the ion emission comes from the same wind which produces the UFO absorption and the soft X-ray emission.

Curiously, no blueshifted O VII emission is seen. This suggests a lack of moderately ionised gas with ionisation parameters lower than that of the O VIII emitting gas (described in section 6.3.3) but higher than that of the UV emitting gas. A similar lack of moderate ionisation gas has also been observed in some AGN exhibiting warm absorbers [e.g. Fig. 5 of 155] and was attributed to a thermal instability at these ionisation parameters. Such effect could be at play in 1H0707 too. Nevertheless, the

absence of the O VII line must be treated cautiously. First, the dataset exposure around the wavelength of O VII is effectively halved as one of the RGS detectors is not functional in this band. Secondly, due to the redshift of 1H0707, its O VII band is also affected by absorption in our Galaxy (low ionisation O lines around  $\sim 23 \text{ \AA}$ ).

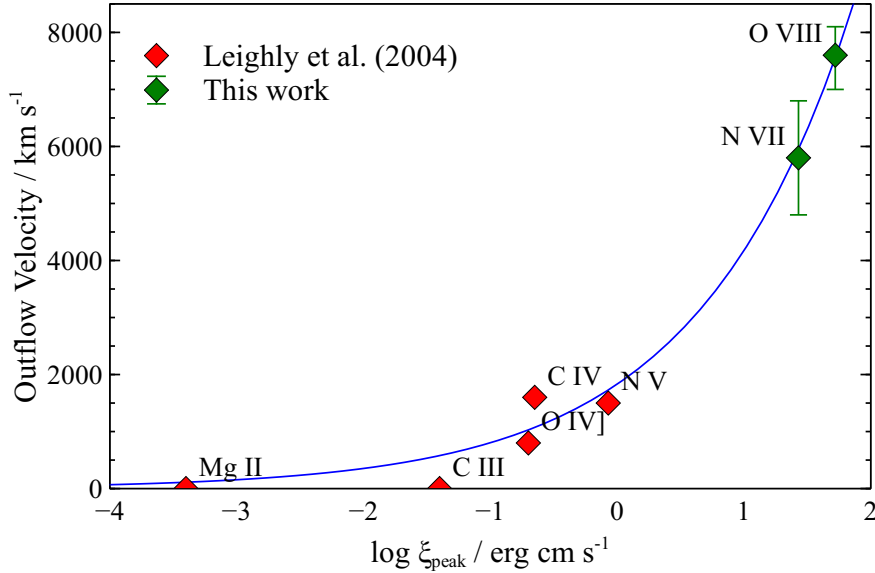


Fig. 6.4 The outflow velocity of different ions versus the ionisation parameter at which the abundance of each partially ionised ion in a photoionised plasma peaks [the SPEX value from 240]. Values for the low-ionisation transitions were taken from Leighly and Moore [218], Leighly [216]. The blue curve is the best fit function to ions with non-zero velocity, in form  $v = b \times (\xi / \text{erg cm s}^{-1})^a$ , where  $a = 0.36 \pm 0.04$  and  $b = (1800 \pm 300) \text{ km s}^{-1}$ .

In conclusion, we present strong evidence of ultrafast absorption as well as slower blueshifted emission in the X-ray spectrum of 1H0707. The trend of increasing velocities of higher ionised ions and the possible similar kinetic powers of UV, soft X-ray emitters and UFO absorbers suggest that we are witnessing the evolution of a stratified, kinetic energy-conserving wind (Fig. 6.5 schematic A). It would likely be launched close to the central accretor by radiation pressure, especially if the mass accretion rate is around or above the Eddington limit [which is probably the case for 1H0707, 172], and leave an imprint in the form of UFO absorption. During the expansion, the wind would cool and slow down upon interaction with surrounding material, imprint the soft X-ray and UV spectra, and eventually deposit its kinetic energy at much larger (kpc) scales to produce AGN feedback. We note that this is not to be confused with the energy

conserving feedback, which occurs on much larger (kpc) scales when the outflowing gas is no longer Compton-cooled by the AGN radiation and it expands adiabatically.

An alternative solution is that the blueshifted soft X-ray emission lines are the extension of an accelerating line-driven wind, proposed by [216] based on the UV features only (Fig. 6.5 schematic B). The UFO absorption could then be completely unrelated, its kinetic power only coincidentally similar to that of the remaining features. It is also possible that the observed UFO absorption is not in fact a signature of a real outflow, but rather it is blueshifted absorption of the relativistic reflection spectrum by an extended co-rotating atmosphere of small clouds above the disk [102].

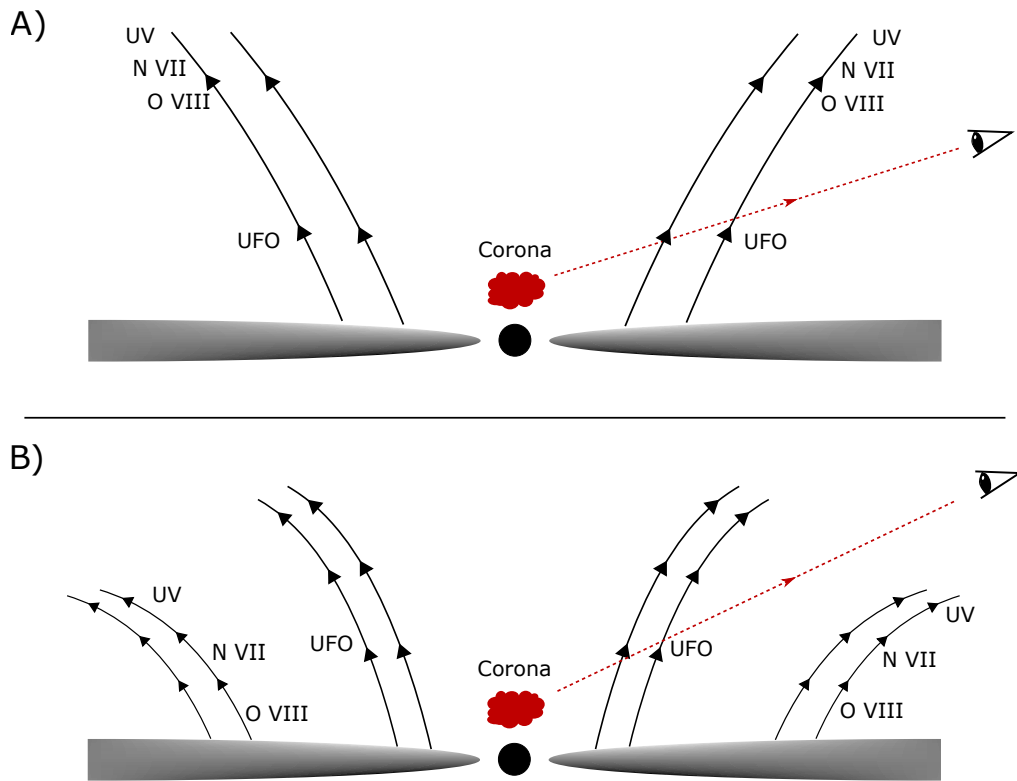


Fig. 6.5 Schematics showing two possible interpretations of the outflows detected in the spectrum of 1H0707. The top schematic contains the stratified wind interpretation, i.e. all outflow components originate in the same wind but at different points along the streamline. The UFO features are produced close to the wind launching site and are seen in absorption. The soft X-ray and UV features originate much further from the disc and are observed in emission. The variant B instead assumes a separate origin for the UFO and soft X-ray/UV features. The features originate from two different wind components but coincidentally they appear to have comparable energetics.



## Chapter 7

# An ionised accretion disc wind in Hercules X-1



# Abstract

Hercules X-1 is one of the best studied highly magnetised neutron star X-ray binaries with a wealth of archival data. In this chapter, I present the discovery of an ionised wind in its X-ray spectrum when the source is in the Main High state, accreting matter with an Eddington fraction of  $0.1 - 0.2$ . The wind detection is statistically significant in most of the *XMM-Newton* observations, with velocities ranging from 200 to 1000 km/s. Observed features in the iron K band can be explained by both wind absorption or by a forest of iron emission lines. However, nitrogen, oxygen and neon absorption lines are also detected at the same systematic velocity in the high-resolution RGS grating spectra. The wind must be launched from the accretion disc, and could be the progenitor of the UV absorption features observed at comparable velocities, but the latter likely originate at significantly larger distances from the compact object. There are strong correlations between the ionisation level of the outflowing material and the ionising luminosity as well as the super-orbital phase. If the luminosity is driving the correlation, the wind could be launched by a combination of Compton heating and radiation pressure. If instead the super-orbital phase is the driver for the variations, the observations are likely scanning the wind at different heights above the warped accretion disc. If this is the case, we can estimate the wind mass outflow rate, corrected for the limited launching solid angle, to be roughly 70% of the mass accretion rate.

## 7.1 Introduction

If a system is accreting significantly below the Eddington limit, radiation pressure cannot be the dominant launching force of a disc wind. Nevertheless, highly ionised winds have been well established in the X-ray spectra of a number of sub-Eddington stellar mass accretors such as black hole [e.g. 259, 280] and neutron star binaries [e.g. 404, 258], with velocities of 100s to 1000s km/s. Such winds might in fact be a universal phenomenon during the bright (Eddington fraction of  $\sim 0.1$ ) soft state of black hole binaries [310]. The high ionisation state of these winds necessarily means that they are

best observed in the Fe K energy band ( $\sim 7$  keV) located within the X-ray part of the electromagnetic spectrum.

The origin of these outflows is the accretion disc of the compact object, but their driving mechanism and energy budget are currently still in question. As the wind material is highly ionised (usually  $\xi > 10^3$ ), line driving is unlikely to provide enough driving force [322], and since the objects in question are accreting below the Eddington limit, the radiation pressure on electrons is likely not sufficient to launch significant winds [although see 281]. If the base of the wind is illuminated by hard X-ray radiation from the inner accretion flow, the material could be Compton heated and launched in the form of a thermally-driven wind [21]. This effect was invoked to explain the winds in a number of X-ray binaries [280, 79]. Alternatively, the wind could be driven by magnetic forces [259, 261, 122].

Evidence of even faster winds ( $\sim 0.2c$ ) has been found in ULXs [306, 304, 417], which are thought to be powered by super-Eddington stellar mass accretors, including one ULX harbouring a neutron star [199]. In these objects, radiation pressure might be the natural driving mechanism of the outflowing material. How the winds in stellar-mass accretors relate to the ultrafast outflows [e.g. 316, 332, 297] and warm absorbers [e.g. 338, 215] observed in AGN and tidal disruption events [257, 181] and whether they are driven by the same phenomenon, is currently not understood. It is, however, certain that accretion disc winds play a major role in the phenomenon of accretion and thus need to be studied in detail.

Here we present the discovery of highly ionised blueshifted absorption in the X-ray spectrum of the neutron star X-ray binary Hercules X-1 in the High state. Previous work found blueshifted UV absorption lines attributed to a circumbinary wind launched from the irradiated surface of the secondary [37], but only weak signatures ( $\sim 2\sigma$ ) of an X-ray counterpart were found so far [213]. We significantly detect the outflowing material in most of the Main High state observations made with *XMM-Newton* (using RGS and pn instruments), at a velocity of 200-1000 km/s. We find that the wind is launched from within the accretion disc of the primary, and that the mass outflow rate is of the same order as the mass accretion rate onto the neutron star. We conclude that the wind is most likely driven by magnetic fields or by Compton heating, but at the moment we cannot pinpoint the exact mechanism.

### 7.1.1 Hercules X-1

Hercules X-1 [hereafter Her X-1, 138] is one of the most famous, brightest and most studied neutron star X-ray binaries. The system consists of a highly magnetised

neutron star and a  $2 M_{\odot}$  secondary HZ Herculis [246] and is therefore considered an intermediate mass X-ray binary. Her X-1 is especially well known for the three different timescales of its multi-wavelength variability.

The shortest is the 1.24 s rotation period [136] of the neutron star. The neutron star is known to harbour a strong magnetic field of the order of  $10^{12}$  G, which manifests through a cyclotron scattering feature with an energy of 35-40 keV [398, 370].

The second important timescale is the 1.7-day orbital period of the binary, accompanied by X-ray eclipses [14], suggesting that the system is observed almost edge-on. The longest timescale is the 35-day super-orbital cycle of High, Low and Short-on X-ray flux states [387]. Each cycle begins with a 10 day High state with a brightness of  $\sim 4 \times 10^{37}$  erg/s, followed by a Low state during which the flux drops by a factor of 10. This is followed by a Short-on state [100] with a flux of  $\sim 1/3$  of the maximum flux for a few days and then again by a Low state.

Such behaviour can be explained by a model according to which the accretion disc of the neutron star (seen almost edge-on) is warped [286] and precesses with a 35-day period [134]. Although accretion onto the compact object continues at a steady rate [since the X-ray irradiation and heating of the secondary star is still observed during the whole 35-day cycle, 134], the inner parts of the disc and the object itself are obscured from our view for extended parts of the cycle. The hard X-ray radiation originates in the accretion column [135] near the surface of the neutron star and is beamed [359]. The size of the magnetosphere [206] of  $\sim 2 \times 10^8$  cm  $\approx 1000 R_G$  defines the inner edge of the accretion disc. The outer edge of the disc is at about  $2 \times 10^{11}$  cm ( $10^6 R_G$ ) and the binary separation is around  $3 \times 10^{11}$  cm [53]. A schematic of the Her X-1 system is shown in Fig. 7.14.

Throughout the manuscript, we adopt a distance of Her X-1 of 6.1 kpc [with upper and lower limits of 5.7 kpc and 7.0 kpc, 212]. All the uncertainties are stated at  $1\sigma$  level.

## 7.2 Observations and data reduction

*XMM-Newton* [166] data were used in this study as the observatory offers a combination of good collecting area as well as very good spectral resolution. Furthermore, its archive contains a wealth of data on Her X-1. Most of the *XMM-Newton* observations were performed in two intensive campaigns in 2011/2012 and in 2016. However, these observations, despite the exquisite data quality, have not yet been published at all.

Table 7.1 Log of the observations used in this work.

Obs. ID	Obs. date	Clean exposures (s)			Mean count rates ( $s^{-1}$ )			Notes
		RGS1	RGS2	pn	RGS1	RGS2	pn	
0134120101	2001-01-26	11296	—	5659	11.5	—	389.3	1
0153950301	2002-03-17	—	7258	2774	—	19.2	591.8	2
0673510501	2011-07-31	8376	8362	6803	11.5	12.6	456.0	3
0673510601	2011-09-07	32242	32130	19320	16.5	17.8	706.6	
0673510801	2012-02-28	12801	12741	4815	19.4	20.9	794.1	
0673510901	2012-04-01	13122	13029	9426	11.6	12.7	491.8	
0783770501	2016-08-17	4598	4550	4588	4.03	4.37	206.8	3
0783770601	2016-08-17	5234	5223	4492	9.38	10.3	399.4	3
0783770701	2016-08-18	12331	12277	6886	12.9	14.2	554.7	

<sup>1</sup> RGS 2 instrument was not operational during this observation.

<sup>2</sup> RGS 1 instrument was not operational during this observation.

<sup>3</sup> obvious dips were visible in the lightcurve during the observation, only high flux periods were extracted for this analysis.

Initially, we utilise all *XMM-Newton* observations with good enough statistics for analysis of absorption lines in the RGS grating data. Considering the current archive of Her X-1, this effectively limits us to observations of the object in the High state. Low and Short-on state grating observations are individually sufficient for emission line studies [170], however the continuum flux is too low for absorption line searches. All of the High state observations of Her X-1 used in this study are listed in Table 7.1 along with their clean exposures and count rate information. Whenever possible, we use simultaneously RGS [72] data which offer best spectral resolution, as well as EPIC pn [378] data to capture the broadband continuum outside the RGS band. All the available archival *XMM-Newton* data were downloaded from the XSA archive and reduced using a standard pipeline with SAS v16, CalDB as of July 2017.

RGS data were extracted following the description in section 2.1.1 with default source and background selection regions. High-background periods were filtered with a threshold of 0.25 counts/sec. Both first- and second-order data were extracted but as the count rate in the second order is much lower, it was only used in selected instances. The second order RGS 1 spectrum was used during the analysis of observation 0134120101 where RGS 2 detector was not working, and conversely the second order RGS 2 spectrum was used in observation 0153950301 where RGS 1 was not operational. The first-order data were binned by a factor of 3 directly in the SPEX fitting package. The second order data were binned by a factor of 6 to achieve similar spectral binning

as the first order data. The data were used in the spectral range between  $7 \text{ \AA}$  (1.8 keV) and  $35 \text{ \AA}$  (0.35 keV).

The EPIC pn detector was in Timing mode during all observations due to very high Her X-1 flux. The calibration accuracy of Timing mode can be found in the following *XMM-Newton* Calibration Technical Note<sup>1</sup>. High-background periods were filtered on a case-by-case basis as the standard routine thresholds were often below the actual Her X-1 fluxes in the High state. The background regions were very small rectangles as far from the source position as possible. However, the background was very weak (usually  $< 3\%$  of source flux) compared to the source flux in all of the observations used in this study. The data were grouped to at least 25 counts per bin and also binned by at least a factor 3. pn data were used in the spectral range of 3 keV to 10 keV. Data below 2 keV were not necessary as this range was covered by the RGS instrument with superior spectral resolution. The range between 2 and 3 keV contained in multiple instances strong residuals and was ignored in this study. These residuals were also present in lower flux observations and therefore were not likely caused only by pile-up. They could be a result of incorrect calibration around the Au edge at 2.3 keV [308].

All the reduced data were converted from the OGIP format to SPEX format for fitting in the SPEX package. All the data were fitted with Cash statistic [47].

### 7.2.1 Orbital and super-orbital phases

We determine the exact orbital and super-orbital phase of the system for each of the *XMM-Newton* observations. The phases are listed in Table 7.2.

The orbital phase of each observation was determined using *XMM-Newton* GTI files. The starting and ending time of the exposure (in *XMM-Newton* seconds) was extracted and converted to the Modified Julian Date (MJD). We then used the Her X-1 orbital solution from Staubert et al. [369] to determine the current orbital phase. The error on the MJD and the orbital phase value listed in Table 7.2 is defined as half the clean exposure time of the observation. All the *XMM-Newton* exposures are much shorter than the binary orbital period and therefore the orbital phase change during a single observation is relatively small.

The super-orbital phase of each observation was calculated by determining the High state turn-on point for the current and the next super-orbital cycle. We used the *Swift*/BAT Hard X-ray Transient Monitor [203] to produce a 15-50 keV lightcurve of Her X-1 between 2007 and 2019. The BAT lightcurve samples the flux of Her

<sup>1</sup><http://xmm2.esac.esa.int/docs/documents/CAL-TN-0083.pdf>

Table 7.2 Modified Julian dates, orbital and super-orbital phases of Her X-1 for each of the High state *XMM-Newton* observations.

Obs. ID	Midpoint MJD <sup>1</sup>	Orbital phase <sup>1</sup>	Super-orbital phase <sup>2</sup>
0134120101	51935.078 ± 0.042	0.210 ± 0.025	0.170 ± 0.015
0153950301	52350.068 ± 0.050	0.297 ± 0.029	0.036 ± 0.014
0673510501	55773.362 ± 0.055	0.802 ± 0.032	0.028 ± 0.015
0673510601	55811.511 ± 0.185	0.240 ± 0.108	0.123 ± 0.015
0673510801	55985.142 ± 0.073	0.366 ± 0.043	0.104 ± 0.015
0673510901	56018.912 ± 0.075	0.229 ± 0.044	0.090 ± 0.015
0783770501	57617.323 ± 0.043	0.379 ± 0.025	0.003 ± 0.014
0783770601	57617.853 ± 0.031	0.690 ± 0.018	0.018 ± 0.014
0783770701	57618.803 ± 0.070	0.249 ± 0.041	0.045 ± 0.014

<sup>1</sup>The errorbar on the MJD and orbital phase denotes half the length of each observation.

<sup>2</sup>The errorbar on the super-orbital phase is given by the accuracy of the High state turn-on time determination.

X-1 approximately every 2 hours for the whole period between 2007 and 2019. The 35-day super-orbital cycle turn-on can therefore be determined when the source rises from the Low state. The *XMM-Newton* observation times were determined and then the neighbouring turn-on times were estimated from the lightcurve. The phase was calculated as the time elapsed from the previous turn-on divided by the time difference between the neighbouring turn-on times. The super-orbital period is relatively stable with a period of 35 days on average [201], but with a longterm variation of ±2 days [214]. We assume an uncertainty of 0.5 day for the turn-on point determination, which gives the errorbar on the super-orbital phase for each observation. Finally, the super-orbital phases of observations 0134120101 and 0153950301 (which happened before *Swift* was launched) were taken from Leahy and Igna [214].

We use the orbital phase information of each observation to correct the measured wind velocity for the orbital motion of the neutron star and its accretion disc. The projected orbital velocity of the neutron star is  $v \sin i = 169.049 \pm 0.004 \text{ km s}^{-1}$  [70] and the systemic velocity of the system was measured to be  $(-65 \pm 2) \text{ km s}^{-1}$  [335]. The eccentricity of the binary is very small:  $(4.2 \pm 0.8) \times 10^{-4}$  [369]. We can therefore correct the outflow velocity by assuming a sinusoid shape of the orbital velocity evolution with time, such as:

$$v_{\text{corr}} = v_0 + 65 \text{ km s}^{-1} + 169 \text{ km s}^{-1} \times \sin(2\pi\phi_{\text{orb}}) \quad (7.1)$$

where  $v_0$  is negative (spectral lines are blueshifted) and  $\phi_{\text{orb}}$  is the midpoint orbital phase for each observation ( $\phi_{\text{orb}} = 0$  defines the center of the neutron star eclipse). All the wind velocity values in this manuscript including those in Table 7.3 are already corrected for the binary motion.

## 7.3 Results

### 7.3.1 Continuum modelling

First we fit the broadband X-ray spectrum of Her X-1 with an appropriate spectral model. Most of the observations are fitted with the same continuum model, and it will be indicated later where this is not the case. Both RGS and pn data are fitted simultaneously and with the same spectral model within the appropriate energy bands.

A sample pn (3-10 keV) spectrum is shown in Fig. 7.1. The high-energy ( $>3$  keV) continuum of the object can be very well reproduced by a Comptonisation model or a powerlaw with an exponential cut-off of about 25 keV [62]. At an even harder band, a cyclotron scattering feature is observed with an energy of about 35-40 keV [120] but this occurs out of the *XMM-Newton* energy band and thus does not need to be taken into account in this study. We describe the broadband continuum with the COMT model within SPEX, obtaining a seeding temperature of about 0.05 – 0.1 keV, an electron temperature of  $\sim 3 - 4$  keV and an opacity of around 10 for all the High state observations.

The Fe K band of the spectrum also contains a strong emission line whose energy and width changes based on the state of Her X-1. In the Low state, its energy is  $\sim 6.4$  keV, with a low ( $\sim 0.1$  keV) width, whereas in the High state, the line energy is closer to 6.6-6.7 keV with a width of 0.3-0.8 keV. At least in the High state, the emission line is pulsed [436]. In this study, for simplicity we fit this region with a Gaussian. One exception is observation 0134120101, where we detect both a narrow (0.1 keV) 6.4 keV emission line and also a broad ( $\sim 1$  keV) 6.5 keV emission feature - we fit each with a Gaussian.

The physical origin of the broad Fe K line is not understood. The width (up to 1 keV), if produced by orbital motion, corresponds to velocities of emitting material of  $\sim 0.1c$ . Such velocities are unlikely to occur in this system given that the accretion disc of Her X-1 is likely truncated by the magnetic field of the neutron star at  $\sim 1000 R_G$ . Asami et al. [9] consider different possible origins of the width of the line including line blending, comptonisation from an accretion disc corona or Doppler broadening

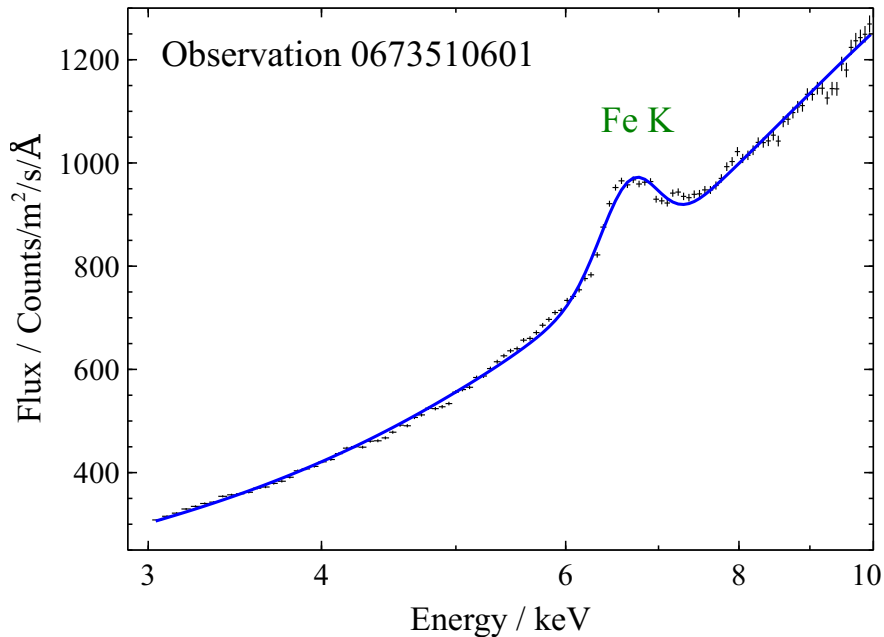


Fig. 7.1 Example 3-10 keV spectrum of Her X-1 with the *XMM-Newton* pn instrument (Obs ID 0673510601). The broadband shape is reasonably well fitted with a Comptonisation model plus a broad iron line at  $\sim 6.6$  keV.

but do not find a plausible explanation. An alternative possibility is that the feature originates in the accretion column of the pulsar.

The Fe K region in most observations also contains strong residuals which will be well reproduced by highly ionised absorption. Alternatively, they can be fitted with an array of emission lines of iron at various ionisation states [e.g. Figs. 4-6 of 9].

The soft X-ray (RGS) spectrum is much more complicated. An example observation is shown in Fig. 7.2. A soft ( $\sim 0.1$  keV) blackbody fits reasonably well the low-energy end of this energy band. However, this is not a signature of the inner accretion disc itself because the spectral component pulses at the pulsar frequency but out of phase compared to the main beam [94, 326, 436]. It is likely that the origin of this component is reprocessed accretion column beam radiation [151].

Secondly, a strong and broad ( $\sim 0.4$  keV) Gaussian-like feature is observed at 0.95 keV, also pulsing with the pulsar period. Its origin is currently unknown, but it is suggested to be iron L reflection [94, 120]. We note that the feature is fully resolved in the RGS data and yet its best-fitting spectral model is a simple Gaussian. The feature therefore does not look like an array of unresolved lines, but instead like a single broad feature. Here we describe it with a Gaussian for simplicity.

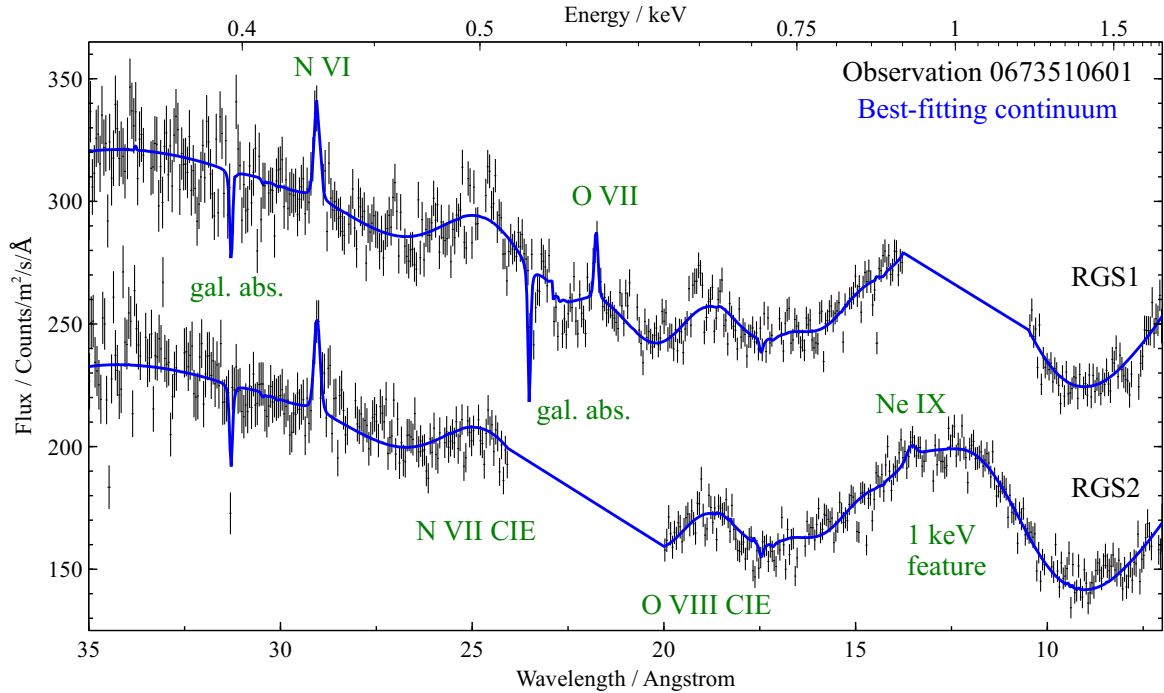


Fig. 7.2 Example 35 Å (0.35 keV) to 7 Å (1.8 keV) spectrum of Her X-1 using RGS 1 and RGS 2 (Obs ID 0673510601). RGS1 data are shifted by a constant amount for plotting purposes and data from both detectors are heavily overbinned for clarity. Individual spectral components are named with green labels. Data between 11 and 14 Å in RGS 1 and between 20 and 24 Å in RGS 2 are missing because of chip gaps.

Additionally, narrow emission lines can be observed at rest-frame energies of N VI, O VII and Ne IX intercombination lines which suggest the presence of a high density environment. These are especially prominent in the Low state of Her X-1 [170, 171, 167] but still noticeable in the High state.

Adding all of the above components into a continuum spectral fit results in a relatively good fit, however we noticed broad emission residuals at around 19 and 25 Å (Fig. 7.2). Their wavelengths correspond to the rest-frame positions of O VIII and N VII ions. If the residuals were real, they could correspond to photo- or collisionally ionised plasma with large (10000-20000 km/s) velocity widths. Alternatively, these lines could be a signature of blurred reflection. As we do not see residuals of similar strength centred on the rest-frame energies of other N or O lines and/or lines of other elements, it is not possible to distinguish between the first two potential origins of the residuals. Attempting to fit these features with a physical reflection model is beyond the scope of this work. We thus fit the two broad residuals phenomenologically to describe the overall continuum as well as possible. We choose the collisional ionisation

emission model CIE in SPEX which is not computationally expensive to fit. We free the normalisation, temperature, velocity width and nitrogen abundance in the model to obtain a simple model with enough freedom, which results in significant fit improvements ( $\Delta C\text{-stat} > 100$ ) in each High state observation.

The temperature of this plasma is  $\sim 0.25$  keV in all observations, with a velocity width of  $\sim 15000$  km/s and an over-abundance of N/O of about 8-10. Both the velocity width and the N/O ratio seem very high to explain within a system like Her X-1. However, we note that previous studies suggest a N/O over-abundance of at least 4 [171] and that velocities of  $10^4$  km/s should not be impossible to achieve at the inner accretion disk/magnetosphere boundary of Her X-1. The orbital velocity at the  $r=2 \times 10^8$  cm magnetosphere boundary ( $\approx$  co-rotation radius as the neutron star is likely rotating close to equilibrium) of a canonical  $1.4 M_{\odot}$  neutron star is exactly  $\sim 10000$  km/s. In Fig. 7.2 it also appears that the velocity width for both N VII and O VIII ions is at least slightly overestimated by our simple model. It is also possible that the N line strength is overestimated compared to the continuum in the  $25 \text{ \AA}$  region. This is the case for multiple High state observations, and could be caused if another spectral component, such as the disc blackbody from the inner accretion disc, is present in the soft X-ray continuum, but is not accounted for by the current spectral model. If the disc blackbody temperature is only  $\sim 0.05$  keV, it would be hard to distinguish and constrain given the current energy band and the number of other spectral components present in the soft X-ray spectrum.

The broad emission line component, if real, could therefore originate on the boundary between the inner accretion disk and the magnetosphere of the neutron star. Further studies with future high-spectral resolution instruments like *Arcus* [367] should offer sufficient data quality to confirm or reject the presence of these lines and show their origin.

The continuum components mentioned above are shown in a schematic in Fig. 7.3. All of the spectral components are further obscured by interstellar absorption, which we describe with a HOT model in SPEX. We set a lower limit of  $1.7 \times 10^{20} \text{ cm}^{-2}$  to the column density of interstellar gas, fix its temperature to 0.5 eV (neutral gas) and assume Solar abundances. The column density value was obtained from Kalberla et al. [179]. Finally, we add normalisation constants to RGS 2 and pn datasets to account for calibration differences between the three detectors. Their values are usually very close to 1 (in the 0.95-1.05 range). The final spectral continuum model in SPEX is thus in the form of  $\text{HOT} \times (\text{COMT} + \text{BB} + 5 \times \text{GAUSS} + \text{CIE})$ .

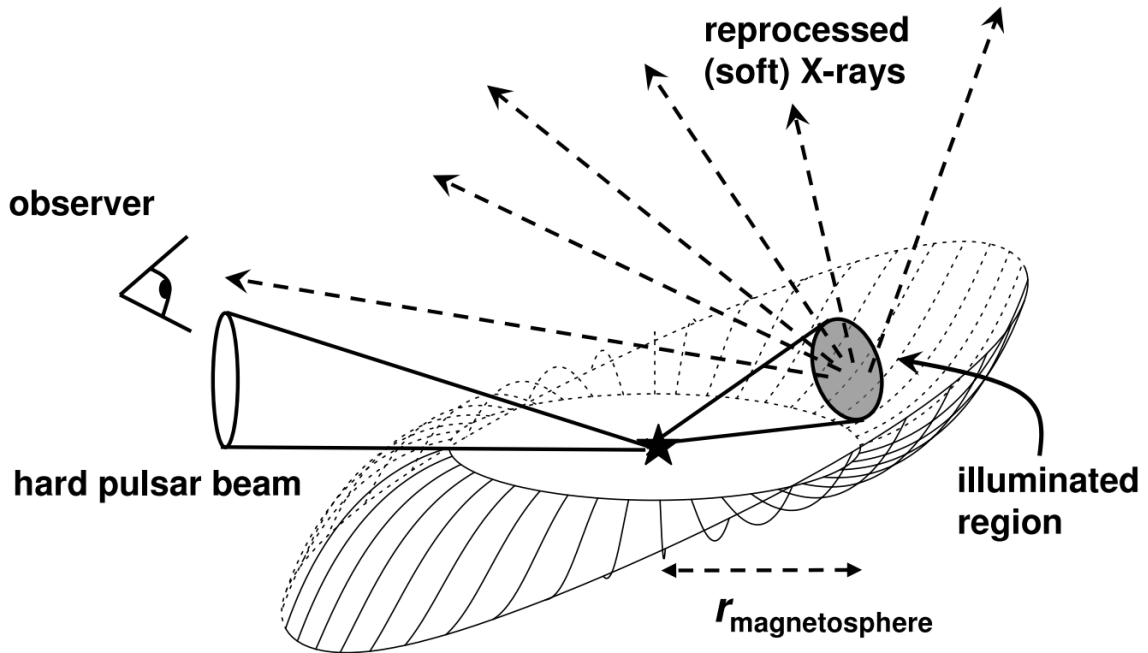


Fig. 7.3 A schematic of the spectral components of Her X-1. The primary, Comptonised emission originates in the accretion column very close to the neutron star. A part of the primary emission is reprocessed in the inner disc and produces the pulsed soft blackbody. The broad iron K emission and the 1 keV line are likely produced in this region as well. This is where the broad soft X-ray lines could also originate. Alternatively, they could originate in a shock at the magnetosphere boundary. This figure was taken from Hickox et al. [151].

### 7.3.2 Photoionised wind modelling

In this subsection we model the wind absorption features, measure its physical properties and describe how significant is the wind detection in the X-ray spectrum of Her X-1.

The spectral model used to describe the blueshifted absorption in this section is called PION (see section 1.4.3 for more details about PION). We repeat the same process for each observation. Initially, the spectra are fitted with the continuum model described in Section 7.3.1. The model parameters as well as the final C-stat value defining the ‘goodness’ of the fit are recovered. Then the PION component is added to the spectral model with appropriate initial parameters. We fit for column density  $N_{\text{H}}$ , ionisation parameter  $\log \xi$ , turbulent velocity  $v$  and systematic (outflow) velocity  $z$  of the photoionised absorber. In this section we assume Solar abundances for simplicity. Afterwards, the best-fitting wind parameters as well as the fit improvement  $\Delta\text{C-stat}$  over the original continuum spectral model are recovered.

The best-fitting wind parameters for each observation in our study are listed in Table 7.3. Our results show that the wind velocity varies significantly between the individual observations in the range of 200-1000 km/s. We also find that the ionisation level of the outflowing gas is high with ionisation parameters,  $\log \xi$ , of 3.0 to almost 5.0. The column density also varies alongside with the ionisation parameter.

The velocity width of the ionised absorber (from the absorption line widths) is of the order of 100 km/s in most observations, with the exception of 0783770701, where if freed, it runs away to thousands of km/s (likely due to lack of statistics). The width could be introduced by internal turbulent motion within the flow. Alternatively, it could originate if our line of sight intercepts multiple layers of the wind with a gradient in the line of sight velocity over a range of radii. In each case, the velocity width ( $\sim 100$  km/s) is generally small compared to the line of sight velocity (median value of  $\sim 450$  km/s), suggesting that the turbulence within the wind is not very strong and that the velocity gradient of all wind layers along the line of sight is not large either.

Table 7.3 Best-fitting wind parameters for each observation of Her X-1.

Obs. ID	Luminosity 0.3-10 keV erg s <sup>-1</sup>	Luminosity 1-1000 Ryd erg s <sup>-1</sup>	Luminosity 0.0136-80 keV erg s <sup>-1</sup>	Column density 10 <sup>24</sup> cm <sup>-2</sup>	log $\xi$ erg cm s <sup>-1</sup>	Turb. velocity km s <sup>-1</sup>	Outflow velocity km s <sup>-1</sup>	$\Delta C^1$
0134120101	1.61 <sup>+0.07</sup> <sub>-0.13</sub> × 10 <sup>37</sup>	2.39 <sup>+0.10</sup> <sub>-0.20</sub> × 10 <sup>37</sup>	3.17 <sup>+0.13</sup> <sub>-0.26</sub> × 10 <sup>37</sup>	0.950 <sup>+0.016</sup> <sub>-0.126</sub>	4.71 <sup>+0.21</sup> <sub>-0.16</sub>	31 <sup>+26</sup> <sub>-13</sub>	-270 <sup>+80</sup> <sub>-180</sub>	10.96
0153950301	1.25 <sup>+0.28</sup> <sub>-0.11</sub> × 10 <sup>37</sup>	1.87 <sup>+0.42</sup> <sub>-0.16</sub> × 10 <sup>37</sup>	2.50 <sup>+0.56</sup> <sub>-0.22</sub> × 10 <sup>37</sup>	0.17 <sup>+0.03</sup> <sub>-0.09</sub>	3.96 <sup>+0.18</sup> <sub>-0.12</sub>	60 <sup>+50</sup> <sub>-30</sub>	-230 <sup>+150</sup> <sub>-170</sub>	26.00
0673510501	9.87 <sup>+0.68</sup> <sub>-0.54</sub> × 10 <sup>36</sup>	1.51 <sup>+0.10</sup> <sub>-0.08</sub> × 10 <sup>37</sup>	2.08 <sup>+0.14</sup> <sub>-0.12</sub> × 10 <sup>37</sup>	0.15 <sup>+0.07</sup> <sub>-0.07</sub>	3.81 <sup>+0.08</sup> <sub>-0.08</sub>	140 <sup>+50</sup> <sub>-30</sub>	-1000 <sup>+110</sup> <sub>-120</sub>	88.20
0673510601	1.58 <sup>+0.07</sup> <sub>-0.14</sub> × 10 <sup>37</sup>	2.43 <sup>+0.10</sup> <sub>-0.21</sub> × 10 <sup>37</sup>	3.61 <sup>+0.15</sup> <sub>-0.31</sub> × 10 <sup>37</sup>	0.35 <sup>+0.03</sup> <sub>-0.02</sub>	4.60 <sup>+0.07</sup> <sub>-0.06</sub>	130 <sup>+100</sup> <sub>-60</sub>	-360 <sup>+110</sup> <sub>-110</sub>	34.69
0673510801	1.41 <sup>+0.01</sup> <sub>-0.01</sub> × 10 <sup>37</sup>	2.16 <sup>+0.01</sup> <sub>-0.01</sub> × 10 <sup>37</sup>	3.34 <sup>+0.01</sup> <sub>-0.01</sub> × 10 <sup>37</sup>	0.006 <sup>+0.118</sup> <sub>-0.005</sub>	3.60 <sup>+0.28</sup> <sub>-0.17</sub>	80 <sup>+510</sup> <sub>-80</sub>	-700 <sup>+400</sup> <sub>-320</sub>	2.72
0673510901	9.89 <sup>+0.11</sup> <sub>-0.07</sub> × 10 <sup>36</sup>	1.50 <sup>+0.02</sup> <sub>-0.01</sub> × 10 <sup>37</sup>	2.18 <sup>+0.03</sup> <sub>-0.02</sub> × 10 <sup>37</sup>	0.032 <sup>+0.006</sup> <sub>-0.010</sub>	3.56 <sup>+0.07</sup> <sub>-0.08</sub>	120 <sup>+90</sup> <sub>-40</sub>	-600 <sup>+120</sup> <sub>-100</sub>	37.20
0783770501	5.15 <sup>+0.09</sup> <sub>-0.09</sub> × 10 <sup>36</sup>	7.45 <sup>+0.13</sup> <sub>-0.13</sub> × 10 <sup>36</sup>	9.95 <sup>+0.17</sup> <sub>-0.17</sub> × 10 <sup>36</sup>	0.084 <sup>+0.024</sup> <sub>-0.021</sub>	2.97 <sup>+0.05</sup> <sub>-0.05</sub>	75 <sup>+14</sup> <sub>-19</sub>	-550 <sup>+100</sup> <sub>-180</sub>	49.86
0783770601	8.43 <sup>+0.18</sup> <sub>-0.17</sub> × 10 <sup>36</sup>	1.30 <sup>+0.03</sup> <sub>-0.03</sub> × 10 <sup>37</sup>	1.89 <sup>+0.04</sup> <sub>-0.04</sub> × 10 <sup>37</sup>	0.13 <sup>+0.04</sup> <sub>-0.05</sub>	3.25 <sup>+0.09</sup> <sub>-0.07</sub>	70 <sup>+20</sup> <sub>-12</sub>	-450 <sup>+110</sup> <sub>-60</sub>	81.67
0783770701	1.03 <sup>+0.03</sup> <sub>-0.01</sub> × 10 <sup>37</sup>	1.55 <sup>+0.04</sup> <sub>-0.02</sub> × 10 <sup>37</sup>	2.28 <sup>+0.06</sup> <sub>-0.03</sub> × 10 <sup>37</sup>	0.023 <sup>+0.074</sup> <sub>-0.015</sub>	3.67 <sup>+0.10</sup> <sub>-0.14</sub>	150*	-460 <sup>+190</sup> <sub>-230</sub>	15.13

<sup>1</sup> The statistical fit improvement of the final model compared to the baseline continuum spectral model.

\* In observation 0783770701, we fixed the turbulent velocity of ionised gas to 150 km/s as otherwise it runs away to values much larger than observed in other observations.

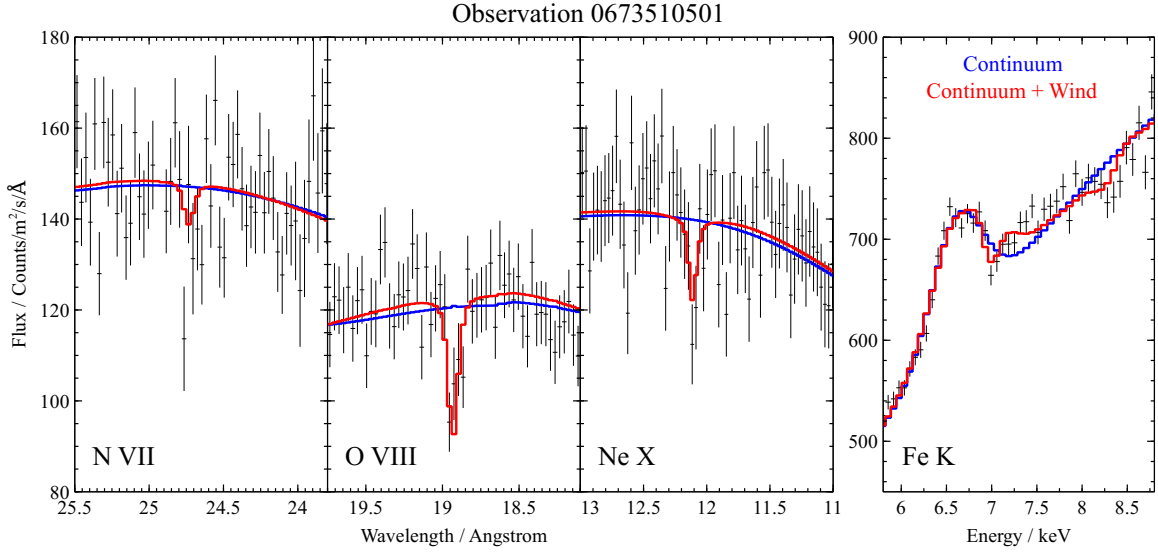


Fig. 7.4 Energy bands around the rest-frame energies of N VII, O VIII, Ne X and Fe XXV/XXVI ions from observation 0673510501. The first three bands only contain RGS1 and RGS2 data, stacked for plotting purposes only, the fourth band only contains EPIC-pn data. The best-fitting baseline continuum is shown in blue, the final wind solution in red.

The five observations with the strongest wind features are shown in figures 7.4 to 7.8. At such high ionisation level of the material, the observable features of this wind in our energy band (and considering the CCD resolution of the pn instrument) are only a few high ionisation lines, hence we only show plots containing narrow energy bands around N VII, O VIII, Ne X and Fe XXV/XXVI line energies. Other strong features of plasma at these ionisation levels are the absorption lines of Mg XII, Si XIV and S XVI, which are occasionally observed in other neutron star [GX 13+1, 404] and black hole [GRO 1655-40, 259] binaries with similar ionised winds. However, Si XIV and S XVI are located in the 2-3 keV energy band which is ignored in this study due to instrumental features in pn data (RGS band only reaches to  $7\text{\AA} \sim 1.8\text{ keV}$ ). Mg XII (at  $8.4\text{\AA} \sim 1.5\text{ keV}$ ) is within the RGS band, but at a wavelength where both the spectral resolution and the effective area of the instrument begin to drop. Consequently, the Mg XII line is not strongly detected.

Unless the abundances of these elements are significantly lower than expected [which has been observed in GRO J1655-40, 180], Mg XII, Si XIV and S XVI absorption lines should be detectable with the *Chandra* HETG gratings, offering a broader (0.3-10 keV) energy bandpass than RGS. Analysis of archival *Chandra* observations of the High state of Her X-1 will be addressed in our future work.

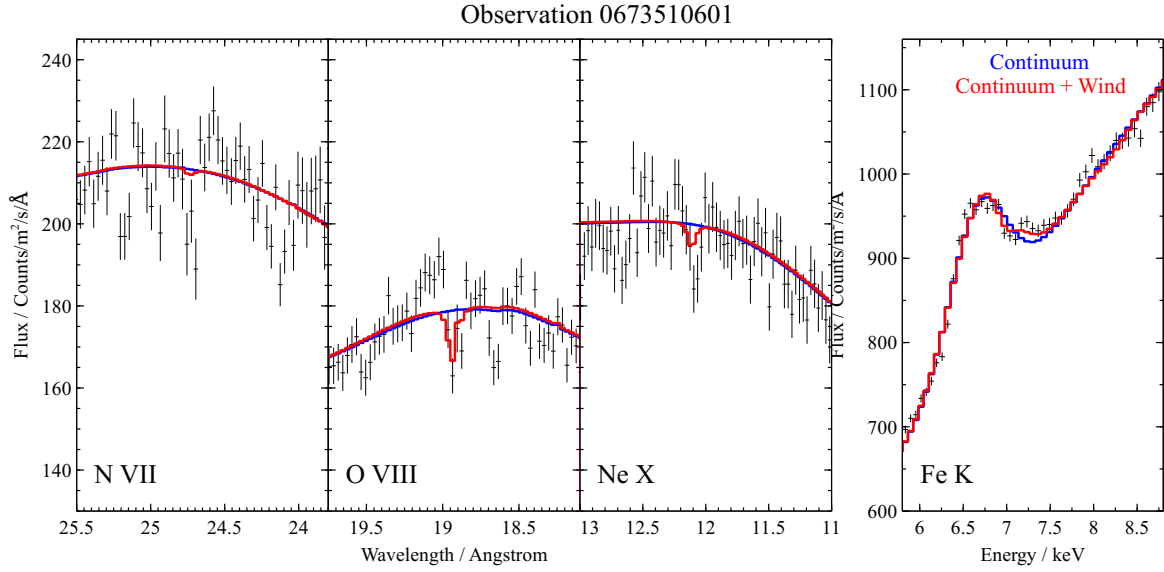


Fig. 7.5 Same plot as Fig. 7.4 but for observation 0673510601.

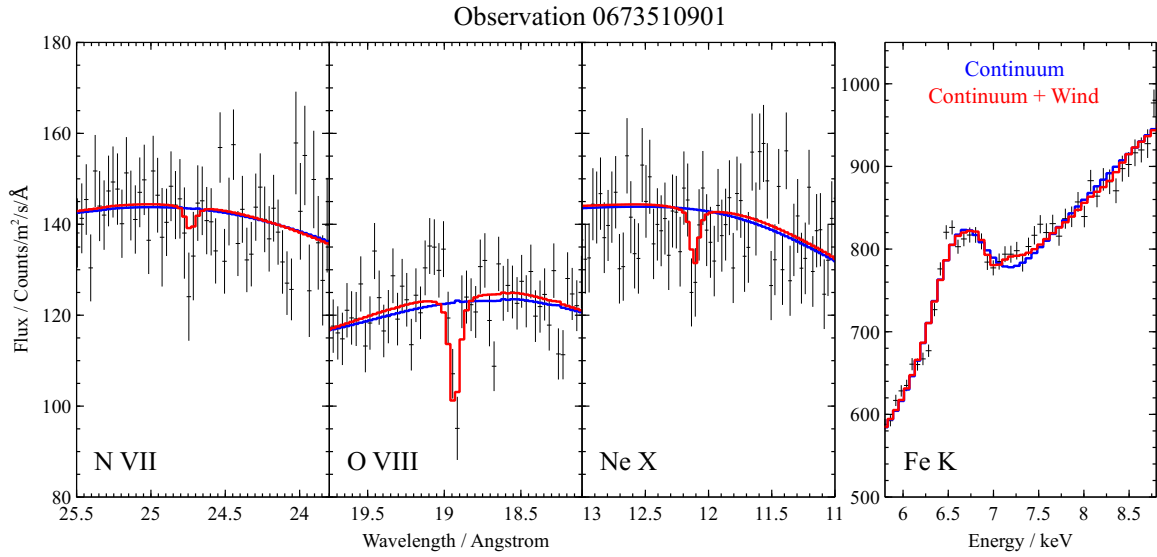


Fig. 7.6 Same plot as Fig. 7.4 but for observation 0673510901.

The statistical fit improvements  $\Delta C$ -stat vary by a large amount between the individual observations but we consider most detections statistically significant. The strongest detections were achieved in observations 0673510501 and 0783770601, in both cases the  $\Delta C$ -stat values are  $\sim 80$ . On the other end, the wind was practically undetected in 0673510801 with  $\Delta C$ -stat=2.7. Other observations with weak detections were 0134120101 and 0783770701.

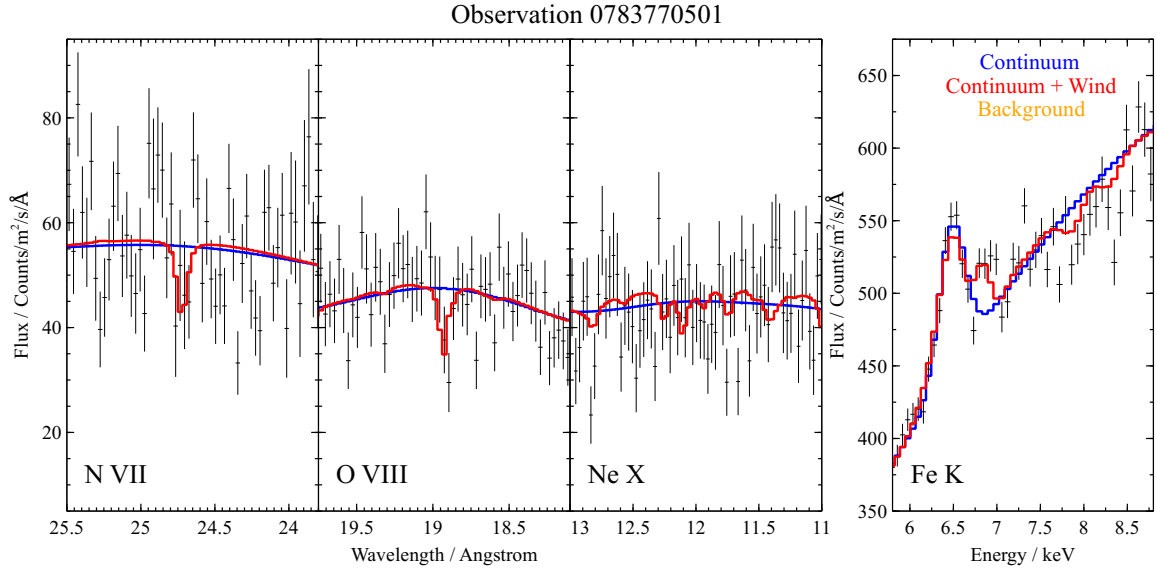


Fig. 7.7 Same plot as Fig. 7.4 but for observation 0783770501.

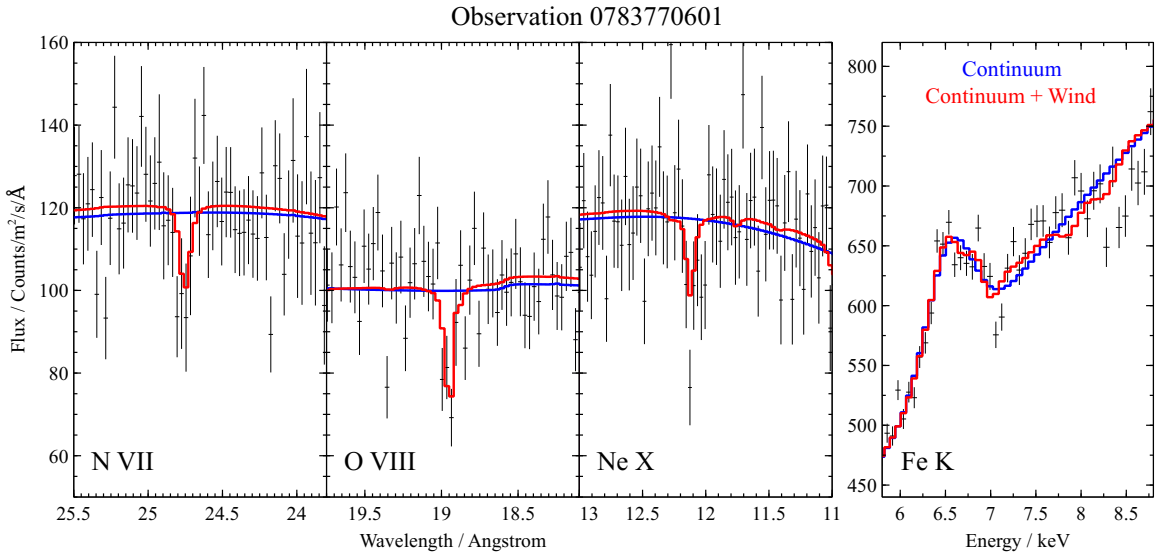


Fig. 7.8 Same plot as Fig. 7.4 but for observation 0783770601.

The statistical significance of the detection of an additional spectral component, in this case of blueshifted absorption can be inferred from the fit improvement  $\Delta C$ -stat between the two fits (continuum vs continuum + wind). The crucial parameter here is the number of additional free parameters that the wind spectral models adds (in our case this is 4 - column density, ionisation parameter, turbulent and systematic velocity of the absorber). However, since the continuum model is effectively on the edge of the parameter space of the more complicated, continuum+wind model (where the

column density of the ionised absorber is simply 0), it is not possible to determine the significance rigorously by a theoretical approach like an F-test [323]. The solution is to perform Monte Carlo simulations - first a blind search is ran over the wind parameters using the real data. Then a similar dataset containing only the continuum model spectrum is simulated, and the same wind search is ran on the simulated data. The statistical significance of the detection of a wind in the real dataset is then 1 minus the fraction of occurrences of detections in fake data stronger (with larger  $\Delta C$ -stat values) than the  $\Delta C$ -stat value of the real detection.

It is not computationally feasible to perform such a search in this situation and assess the detection significance completely rigorously. This is because the underlying spectral continuum of Her X-1 is too complex, causing the simulated blind search to become very computationally expensive. However, we would like to compare the fit improvements seen in this study with the results from Kosec et al. [199], where a full Monte Carlo simulation suite was performed. In that study a wind with  $\Delta C$ -stat of  $\sim 27$  was detected using 4 additional free wind parameters (the same number as here). However, they used a much wider parameter space - systematic velocity space of 0 km/s to 120000 km/s, whereas in this study we only assess wind velocities from 0 to a few thousands km/s. The statistical significance of wind detection in Kosec et al. [199] was about  $3.5\sigma$ . We therefore argue that the wind detection in most of the observations of Her X-1 is statistically significant.

Photon pile-up could affect some of our datasets, especially pn and RGS2. We address this issue in Appendix C. However, it is unlikely that it could introduce absorption features which line up in the velocity space. We conclude that our detection of an ionised wind in the spectrum of Her X-1 is robust.

We also consider a possibility that the outflowing plasma is multiphase, i.e. it has multiple ionisation and velocity components. This seems to be the case for other X-ray binaries with wind detections [e. g. 253]. We can exclude significant absorption by low ionisation ( $\log \xi < 2$ ) material, which would have a strong signature in the soft X-ray (RGS) band. Unfortunately, most of our observations do not offer high enough data quality (statistics) to address this hypothesis for the higher ionisation levels. This is due to low column densities of the wind given the ionisation state and consequently low optical depths of absorption features (e. g. Fig. 7.6). Additionally, at such high ionisation levels ( $\log \xi = 3 - 5$ ), there is only a small number of strong lines left in the absorption spectrum. In most observations we thus do not have enough photon counts to distinguish multiple wind components, despite the high flux of Her X-1. Future longer exposure observations may address this problem.

We attempt to test the multiphase hypothesis at least in the observations where the wind absorption is the strongest. Choosing the two observations with the highest  $\Delta C$ -stat fit improvement upon adding the ionised absorption component (0673510501 and 0783770601), we fit the spectra with a double ionised absorption model. We use the PION spectral model to describe the two absorption zones, with all relevant physical parameters decoupled. In the case of observation 0673510501, we find a very small fit improvement of  $\Delta C$ -stat $\sim 6$  compared to the single zone absorption model. In the case of observation 0783770601, the fit improvement is  $\Delta C$ -stat $\sim 14$ , larger but still not statistically significant to warrant the addition of a second absorption zone. In conclusion, with the current data quality there is no strong evidence for a multiphase nature of the wind in Her X-1.

### 7.3.3 Short-on and Low state observations

We checked the Low and Short-on state observations of Her X-1 for any obvious signatures of blueshifted absorption lines. Naturally, the flux and hence the count rate during these epochs are much lower than in the High state. None of the observations individually can be used to constrain the presence of the wind - the continuum is too weak in the RGS band and only photoionised line emission is detected significantly. We omit the Fe K band as it is more complicated than in the High state, with a 6.4 keV narrow line (Fe I), a possible 6.97 keV line (Fe XXVI) plus an edge at 7.1 keV due to a partial covering absorber [167].

To improve the statistics, we stack all the available Low state RGS data for observations which are not affected too strongly by background flares, for a clean exposure of roughly 45 ks per detector. This allows us to get a significant detection of the X-ray continuum, nevertheless we do not observe any obvious absorption features at similar systematic velocities (0 – 1000 km/s) compared to the ones seen in the High state. The search is naturally complicated by the fact that the stack comes from averaging over several years of observations. If the wind velocity is time variable, even if the absorption is present in the Low state, its features would be smeared and difficult to detect using the stacked dataset. The analysis is further complicated by the strong Low state line emission, which is challenging to model physically. Any possible absorption features will be difficult to disentangle from the emission lines which are at similar energies (outflow velocity of 1000 km/s corresponds to a wavelength shift of just  $3 \times 10^{-3}$ ). A rigorous search of the Low state data is beyond the scope of this work.

## 7.4 Elemental abundances in the wind

So far we have assumed solar abundances while fitting the wind parameters. However, the outflowing material can serve as a powerful probe to independently determine the composition of the matter accreted onto Her X-1. Previous studies based on line emission in the Low state suggested an over-abundance of N and Ne compared to O [171].

The measurement of abundances from blueshifted absorption lines is in principle a much easier task, however given the high ionisation level of the wind, the absorption spectrum only contains a few metallic lines and there is very little continuum absorption. This has two important consequences given the current data quality.

First, we choose to perform a simultaneous fit of multiple observations at once to increase the signal-to-noise. We free all of the individual observation model parameters with the exception of wind material abundances (within the PION model) and simultaneously fit 5 observations with the strongest wind detection - 0673510501, 0673510601, 0673510901, 0783770501 and 0783770601. We could in principle fit all of the available observations simultaneously, but this would be too computationally expensive.

The second important consequence is that this analysis is unable to measure absolute abundances. It can only constrain relative abundances of elements compared to one selected element whose absorption line is strong enough to anchor the spectral fit. The only elements with strong enough lines present in photoionised spectra at this ionisation level and in our energy band are N, O, Ne and Fe (O and Fe being the strongest). We therefore follow two avenues: first, we fix the iron abundance and measure relative abundances of N, O and Ne compared to Fe; afterwards we fix the oxygen abundance and fit for N, Ne and Fe. Ideally, these two approaches should result in similar elemental ratios and serve as an independent check. We further note that all the abundances stated below denote relative abundances to Solar values, not the absolute numerical abundances.

It is not obvious how to treat the abundances of the remaining elements such as Mg, Si, S, Ni and others. At Solar abundances, their absorption lines are weak. However, once we free the abundances of the main elements, they might become important. Initially, we freeze their abundance to 1. This effectively means that the abundances of these elements are equal to that of the comparison element (Fe or O).

First, we freeze the abundance of Fe. We recover an over-abundance of N, Ne and Fe of 2 to 4 compared to O, for a modest fit improvement of  $\Delta C\text{-stat} \approx 20$  (1st row of Table 7.4). Secondly, we freeze the abundance of O. In this case we find a much larger fit improvement of  $\Delta C\text{-stat} \approx 120$  and also much higher elemental ratios

(3rd row of Table 7.4). The Fe/O ratio is the highest at  $17.1_{-1.2}^{+1.5}$ . We interpret this significant difference between the fit quality in these two approaches to be caused by the remaining elements whose abundances are frozen. When O is freed, its abundance begins to decrease compared to Fe. However, the O VIII line is the strongest wind absorption line, so to remain fitted correctly, the column density of the wind material must be increased, thus strengthening the absorption lines of all the frozen elements (whose lines are weak in the actual spectrum). We conclude that this suggests that the abundance O is not under-abundant compared to these elements, and hence this approach to fitting the abundances is not trustworthy.

We also experiment with setting the abundances of the ‘weak’ elements to 0. While this is an unphysical scenario, it approximates a situation in which the abundance of the comparison element (which is frozen to 1) is much larger than the abundance of the ‘weak’ elements (without adding too much computational cost). We find similar results regardless of whether Fe or O is the comparison element (2nd and 4th rows of Table 7.4), as is expected. N and Ne appear to be over-abundant compared to O by a factor of 2 to 4, and the Fe/O ratio is as high as 10.

Table 7.4 Best-fitting abundances of elements and elemental ratios for each of the four approaches to the chemical analysis. The last column contains the fit improvement in  $\Delta C$ -stat for each approach.

N	O	Ne	Fe	Other elements	N/O	Ne/O	Fe/O	$\Delta C$ -stat
$1.6^{+0.7}_{-0.6}$	$0.44^{+0.06}_{-0.08}$	$0.96^{+0.22}_{-0.17}$	1*	1*	$3.6^{+1.7}_{-1.4}$	$2.2^{+0.7}_{-0.5}$	$2.3^{+0.4}_{-0.3}$	19.74
$0.21^{+0.08}_{-0.07}$	$0.086^{+0.024}_{-0.018}$	$0.36^{+0.09}_{-0.13}$	1*	0*	$2.4^{+1.1}_{-1.1}$	$4.2^{+1.4}_{-1.9}$	$11.6^{+2.4}_{-3.3}$	121.16
$3.9^{+1.6}_{-1.3}$	1*	$5.6^{+2.0}_{-1.7}$	$17.1^{+1.5}_{-1.2}$	1*	$3.9^{+1.6}_{-1.3}$	$5.6^{+2.0}_{-1.7}$	$17.1^{+1.5}_{-1.2}$	118.40
$1.9^{+1.0}_{-0.6}$	1*	$2.5^{+1.2}_{-0.7}$	$9.1^{+1.3}_{-0.9}$	0*	$1.9^{+1.0}_{-0.6}$	$2.5^{+1.2}_{-0.7}$	$9.1^{+1.3}_{-0.9}$	134.03

\* The elemental abundance is fixed to the corresponding value during the fit.

In conclusion, our results confirm the previous findings of Jimenez-Garate et al. [170, 171] regarding the elemental ratios of N/O and Ne/O. We find that the N/O ratio is between 2 and 4 for different approaches to the fitting analysis. Ne is also over-abundant compared to O, we find that  $\text{Ne/O} \approx 2 - 6$ , in line with previous results.

Unexpectedly, we also find very high Fe/O ratios. The exact ratio heavily depends on the approach chosen - we obtain  $\text{Fe/O} \approx 2$  for Fe fixed to 1 (but do not trust this result because of the reasons given above),  $\text{Fe/O} \approx 10$  for both approaches with the remaining elements fixed to 0, and  $\text{Fe/O} \approx 17$  for O fixed to 1. We suspect that the last value is a strong overestimate, possibly driven by the abundance of the ‘weak’ frozen elements. We prefer the results from the approaches where the ‘weak’ elements are set to 0 and argue that the Fe/O ratio might be as high as 8 – 10. This is still very high but probably more realistic than  $> 15$ . We find that these two approaches result in very similar elemental ratios and  $\Delta\text{C-stat}$  fit improvements, as expected because they should be almost equivalent.

We however stress one important point - the Fe abundance measurements at these ionisation levels are all based on the Fe K energy band. Our spectral resolution in this band is modest ( $\sim 100$  eV resolution of the pn instrument) and its modelling is quite simplistic. If the true underlying spectral model is significantly more complicated than assumed in this work (i.e. if there is a range of Fe emission lines at 6.4 keV, 6.7 keV and 6.97 keV compared to one broad Gaussian line), the Fe/O elemental ratios obtained here must be taken with caution. Finally, we note that we have assumed that the gas is in equilibrium, which might not be entirely true (for example if the wind is driven along magnetic lines).

We conclude that the abundances in Her X-1 are strongly non-Solar. This is evidenced by the large fit improvements ( $\Delta\text{C-stat} > 100$ ) upon freeing the abundance parameters.

The abundance of elements should in principle match the composition of the surface of the donor star. Unfortunately, not much is known about the donor composition due to observational difficulties - the donor is strongly affected by the X-ray irradiation from Her X-1, and the measurement of its abundances is not straightforward. Its metallicity is likely sub-Solar [212] but the exact elemental abundances have not been measured to our knowledge. The very high elemental ratios of N and Ne to O measured in this and previous studies [170, 171] are unlikely to be found in an isolated star. Jimenez-Garate et al. [170] suggest the enhanced N/O ratio and the low O/Ne ratio are the result of H burning by the CNO cycle in the core of a massive star. This implies mass transfer from the progenitor of Her X-1, either during its evolved phase or during the supernova

that created the neutron star, and the pollution of the outer layers of the donor star HZ Her.

## 7.5 Discussion

We have shown that the X-ray spectrum of Her X-1 during the High state contains strong evidence of blueshifted wind absorption. The Fe K band of the spectrum by itself could be explained by an array of Fe emission lines (at 6.4, 6.7, 6.97 keV) rather than by absorption features [9]. However, the N VII, O VIII and Ne X regions unambiguously show blueshifted absorption lines at the same systematic velocity, thus confirming that we are observing an ionised wind. The wind detection is statistically significant in most of the *XMM-Newton* observations with the exception of 0673510801 and 0134120101, where the evidence for absorption features is weaker. At this moment we do not find evidence for similar blueshifted absorption in the Short-on and Low states of Her X-1, but the data quality of these observations is much lower. Stacking multiple datasets likely smears the absorption signatures as the wind appears to be variable in time.

We will now investigate how the wind parameters vary across different High state observations. Afterwards, we will estimate the launching radius of the wind as well as the mass outflow rate. Finally, we will attempt to pinpoint its launching mechanism and try to explain the variation of wind parameters in time.

### 7.5.1 Wind evolution with luminosity, orbital and super-orbital phase

For these calculations, it is necessary to obtain the luminosity of the ionising radiation of the object. The wind naturally sees the full energy band of radiation and not just the luminosity in the RGS and pn band (0.3-10 keV, listed in the 2<sup>nd</sup> column of Table 7.3). By definition the 1-1000 Ryd energy band is taken when considering the ionising flux. For this reason we calculate the extrapolated 0.0136 – 13.6 keV luminosity of Her X-1 for each observation. The errors introduced by this extrapolation on the upper energy end are not going to be large (< 5 per cent) as our pn data coverage reaches to 10 keV. At the low energy end, we neglect the EUV radiation from the accretion disc whose spectrum does not reach into the X-ray band and thus cannot be constrained by *XMM-Newton*. However, given that the disc is truncated at  $\sim 1000 R_G$ , its luminosity is negligible compared to the X-ray luminosity of Her X-1 and thus the systematic error introduced by neglecting the disc radiation is small (< 5 per cent). The ionising

luminosity estimates are shown in Table 7.3 (3<sup>rd</sup> column). Finally, we also calculate the total luminosity of Her X-1 for each observation by extrapolating between 0.0136 – 80 keV (4<sup>th</sup> column of Table 7.3). These estimates should be taken with some amount of caution.

We plot the ionising luminosity with respect to the super-orbital phase for each observation in Fig. 7.9. The range of luminosities sampled by *XMM-Newton* observations nicely reproduces the High state part of the super-orbital flux lightcurve of Her X-1 [e.g. Fig. 2 from 214]. The only outlier is observation 0673510901, during which the luminosity is around 50% lower than would be predicted by fitting all the other data points. To investigate this outlier we checked the pn lightcurve of observation 0673510901 but found no evidence for discrete obscuration events.

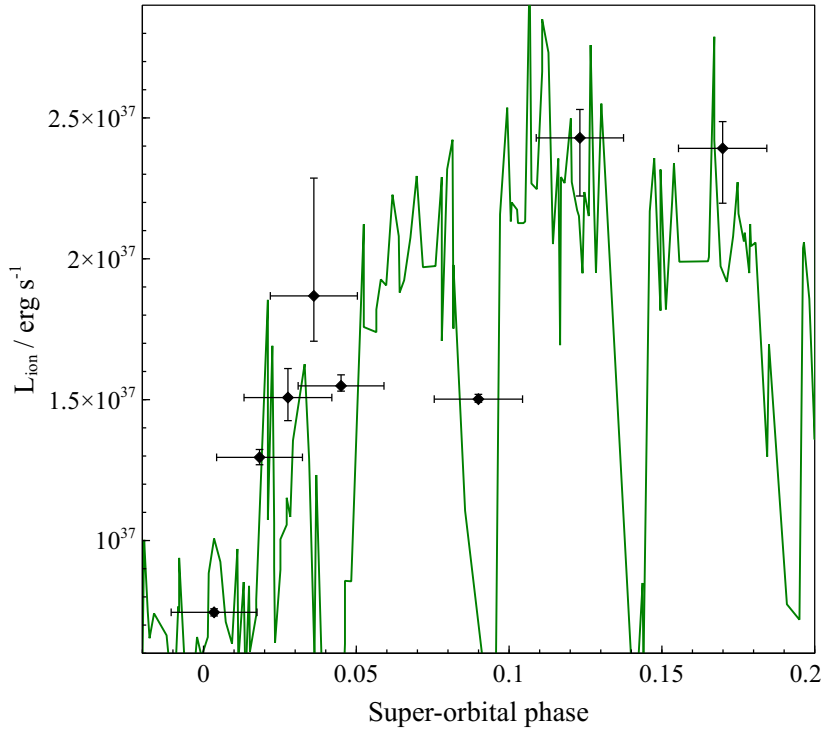


Fig. 7.9 The extrapolated 1-1000 Ryd ionising luminosity for each of the High state observations versus the super-orbital phase. An example High state *Swift* BAT lightcurve is shown in green. The lightcurve corresponds to the cycle starting on the 8th July 2018. The large flux drops are the eclipses of Her X-1 by the secondary.

We note that in the next part of the study we omit observation 0673510801 results as the wind detection is insignificant and its uncertainties are too large for any informative conclusions.

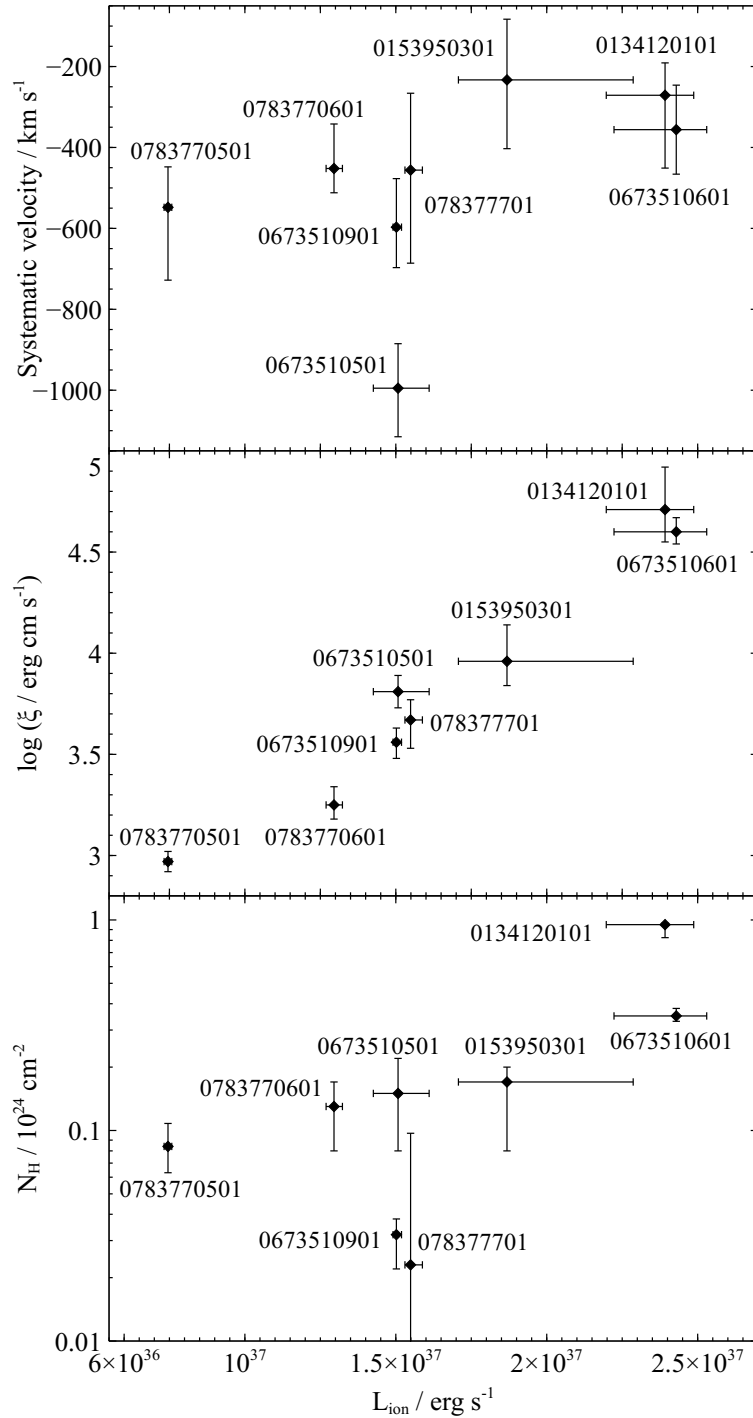


Fig. 7.10 *Top plot*: Systematic velocity of the ionised absorber with respect to the extrapolated 1-1000 Ryd ionising luminosity of Her X-1 for each observation in the High state. *Middle plot*: Ionisation parameter of the absorber versus the extrapolated 1-1000 Ryd luminosity for each observation in the High state. *Bottom plot*: Column density of the absorber versus the 1-1000 Ryd luminosity for each observation.

The projected wind velocity spans a range of velocities between 200 and 1000 km/s and is inconsistent with being constant across all the observations. Fig. 7.10 (top plot) shows that there does not seem to be a clear correlation between the outflow velocity and the 1-1000 Ryd luminosity. Observation 0673510501 appears to be an outlier during which the wind was apparently much faster.

On the other hand, there is a clear positive correlation between the ionisation parameter and the luminosity of Her X-1, shown in Fig. 7.10 (middle plot). Such correlation suggests that the wind responds to the change in luminosity of the object and thus sees similar if not the same luminosity as we observe. This was not a given because the change in Her X-1 luminosity is likely only an obscuration or projection effect and the accretion onto the primary continues at a nearly constant pace.

There is a tentative correlation between the wind column density and the ionising luminosity (Fig. 7.10, bottom plot), but with clear outliers - observations 0673510901 and 0134120101.

We do not observe any significant correlations between the wind parameters and the orbital phase of each observation. This finding suggests that the wind is not tied in any way to the secondary of the binary system or the motion of the primary and is only related to the accretion disc of the neutron star. The wind parameters with respect to the orbital phase are shown in Fig. 7.11.

Fig. 7.12 shows the wind parameters versus the super-orbital phase of each exposure. As with the ionising luminosity, we do not find any correlation between the outflow velocity and the super-orbital phase. We notice a strong correlation between the ionisation parameter and the super-orbital phase, with one obvious outlier - observation 0673510901. This correlation comes naturally since the ionising luminosity is correlated with the super-orbital phase and the ionisation parameter is correlated with the 1-1000 Ryd ionising luminosity. However, the fact that observation 0673510901 is an outlier in the super-orbital plot and not in the luminosity plot could suggest that the ionisation parameter depends on the luminosity and not on the super-orbital phase. This could mean that we are not only probing different lines of sight from the neutron star (as the super-orbital phase progresses), but that the ionising flux on the wind gas must also change in time. Alternatively, observation 0673510901 could be an outlier in the super-orbital cycle, an anomalous state. Finally, there is a tentative correlation between the column density of the outflowing material and the super-orbital phase, with two outliers being observations 0673510901 and 078377701.

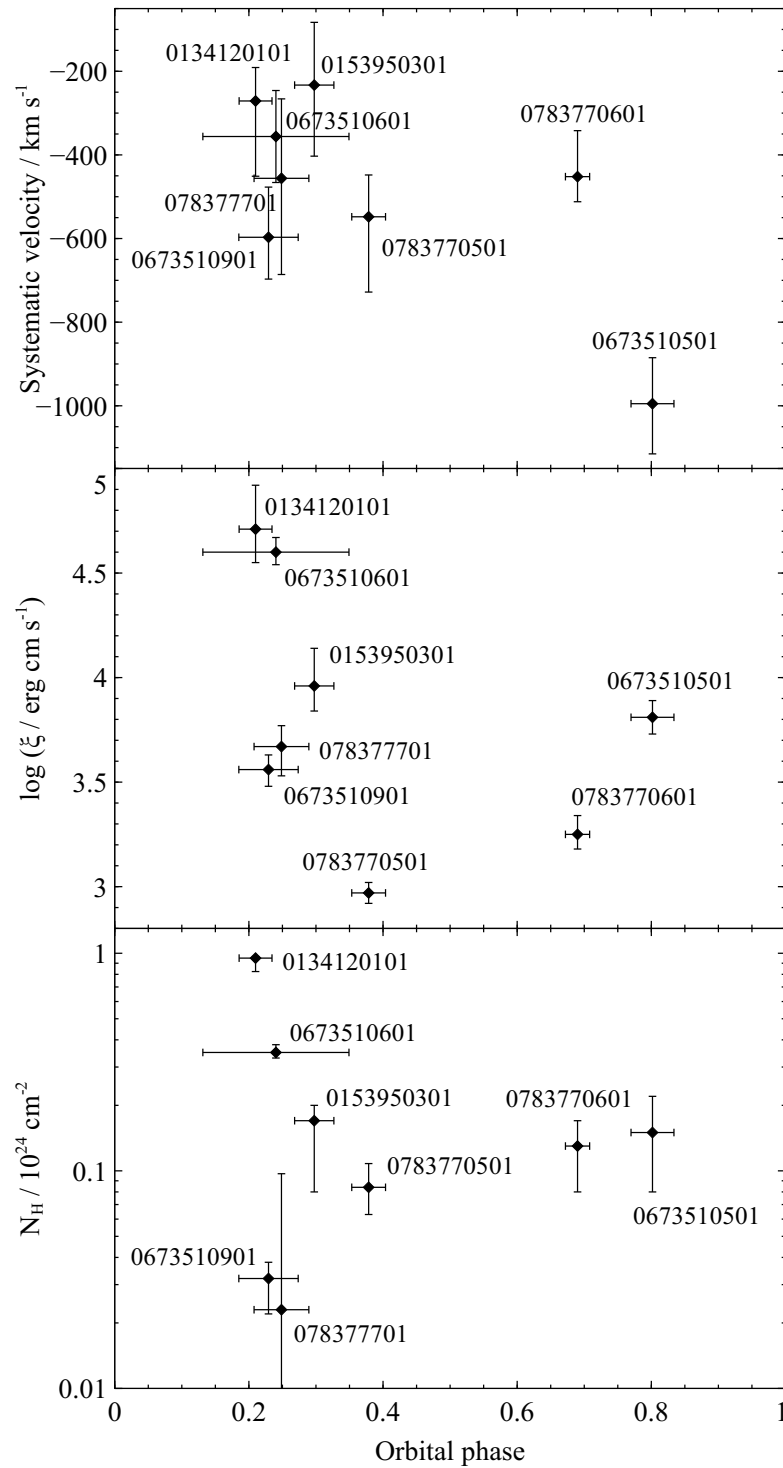


Fig. 7.11 *Top plot*: Systematic velocity of the ionised absorber with respect to the orbital phase during each observation. *Middle plot*: Ionisation parameter of the absorber versus the orbital phase during each observation. *Bottom plot*: Column density of the absorber versus the orbital phase during each observation.

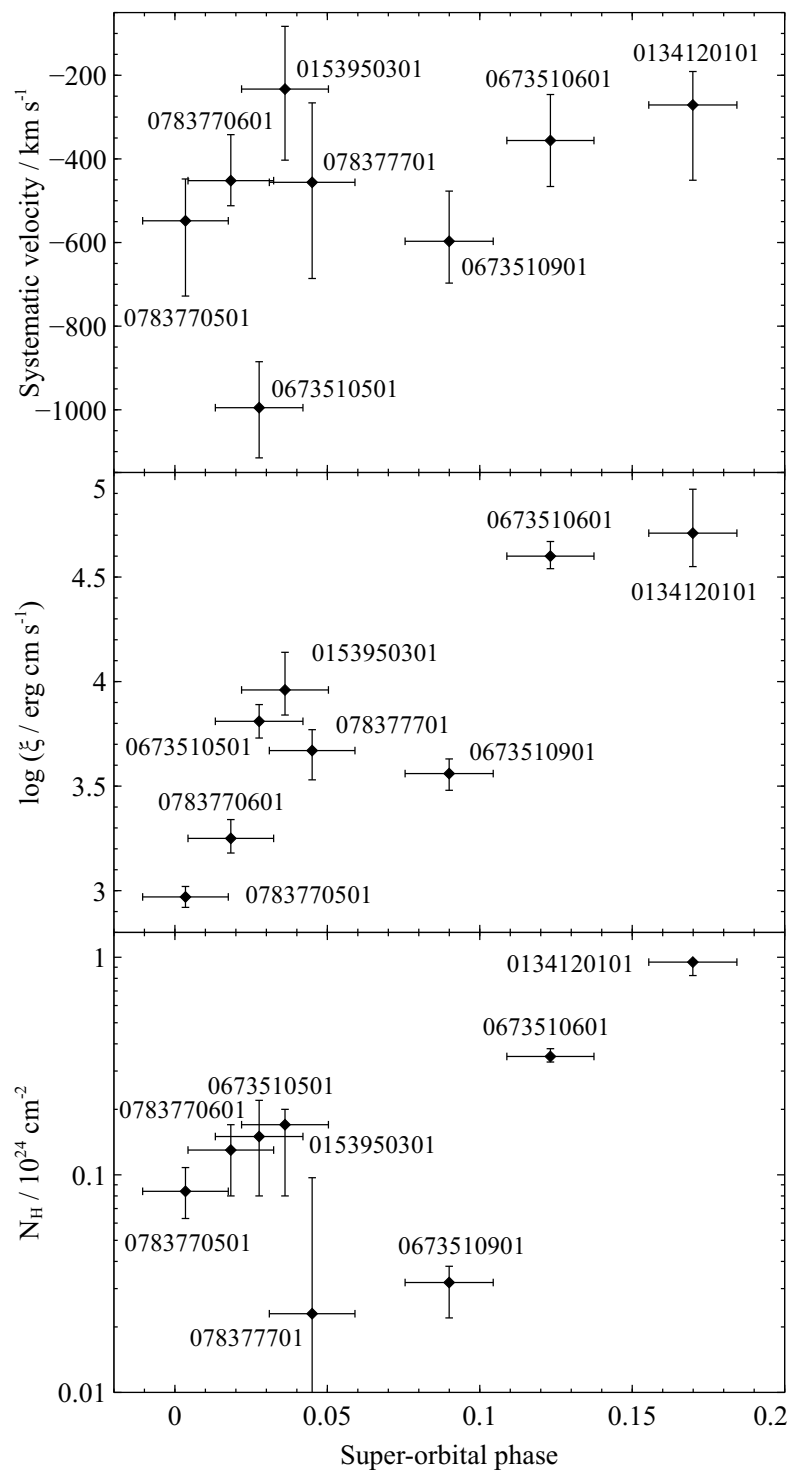


Fig. 7.12 *Top plot*: Systematic velocity of the ionised absorber with respect to the super-orbital phase during each observation. *Middle plot*: Ionisation parameter of the absorber versus the super-orbital phase during each observation. *Bottom plot*: Column density of the absorber versus the super-orbital phase during each observation.

### 7.5.2 Location of the wind absorption

Boroson et al. [37] found blueshifted absorption UV lines in Her X-1 with a velocity of several hundred km/s using the FOS and STIS spectrographs onboard the Hubble Space Telescope. They concluded that the wind is likely launched from the X-ray irradiated side of the secondary, and it is observed at larger, circumbinary distances from the system. The conclusion was motivated by the stability of the wind systematic velocity over the orbital cycle of the binary.

We similarly attempt to pinpoint the location of the X-ray absorber and its relation to the UV absorber, as well as the likely launching mechanism. The high ionisation level of the gas by itself suggests the proximity of absorption to the ionising (X-ray emitting) source. We can put an upper limit on the distance of the wind absorption from the neutron star by using the ionisation parameter and the column density of the absorber.

We will assume that the wind is in equilibrium with the ionising radiation. The unabsorbed 1-1000 Ryd luminosity is used as the ionising luminosity as opposed to a constant  $4 \times 10^{37}$  erg/s luminosity because the ionisation parameter is seen to respond to the luminosity change.

The ionisation parameter of the absorber is then defined as:

$$\xi = \frac{L_{\text{ion}}}{nR^2} \quad (7.2)$$

where  $L_{\text{ion}}$  is the ionising luminosity,  $n$  is the ion number density and  $R$  is the distance from the ionising source [388]. The column density can be expressed as:

$$N_{\text{H}} = n\Delta R = nR\delta R. \quad (7.3)$$

where  $\Delta R$  is the thickness of the absorbing layer and  $\delta R = \Delta R/R$  is its relative thickness ( $\delta R < 1$ ). We can hence express  $R$  as:

$$R = \frac{L_{\text{ion}}}{N_{\text{H}}\xi} \delta R \quad (7.4)$$

This is naturally a very simple calculation assuming that the absorbing layer is uniform and gives an approximate upper limit on the distance of the absorber from the neutron star. If the absorption occurs over a layer that is not very thin, the fractional distance  $\delta R = 0.1 - 1$  and thus the  $\delta R$  correction factor is not going to be too important. The maximum distance for each Her X-1 observation is shown in Fig. 7.13 with other relevant scales of the system and is also listed in Table 7.5.

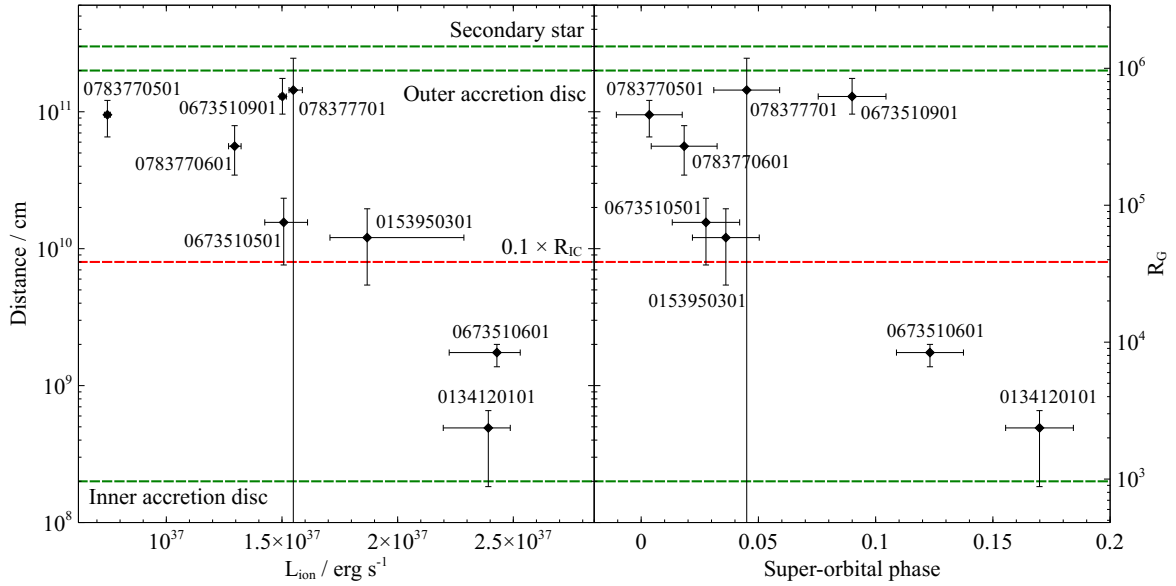


Fig. 7.13 The estimate of the maximum distance of photoionised absorption from the ionising source versus the ionising luminosity (left subplot) and the super-orbital phase (right subplot). The green horizontal lines show the positions of the inner and outer edges of the accretion disc, and the distance of the secondary star from the primary (see Fig. 7.14 for a schematic of the Her X-1 system). The red dashed line shows the approximate position of the minimum wind launching radius if the wind is powered by Compton heating of the accretion disc.

All of the results clearly lie within the accretion disc of the primary, and they do not seem to cluster on the inner edge of the disc. A few results (0783770701, 0673510901) are consistent with the outer disc boundary or the secondary star surface, but most are completely inconsistent with this interpretation. We note that even if the correction factor  $\delta R$  is mild (0.1-0.5), it will push most of the outlying results down inside the accretion disk. We therefore argue that the absorption occurs within the size of the accretion disk of the primary. The wind must hence be launched from the accretion disc (or even closer to the neutron star) and cannot originate on the irradiated side of the secondary. Fig. 7.14 contains a schematic of the Her X-1 system with the disc wind. Our interpretation is that the wind originates from the accretion disc with a speed higher than the escape velocity and is thus able to leave the system. At larger (circumbinary) distances, as its ionisation state drops, the wind creates the absorption features observed by Boroson et al. [37] in the UV spectrum of Her X-1.

On the other hand, unless the thickness of the wind launching region is quite small ( $\delta R \ll 0.1$ ) which does not seem likely (unless the launching region is highly localised such as the top point of the warp in the accretion disc), it is difficult to explain all

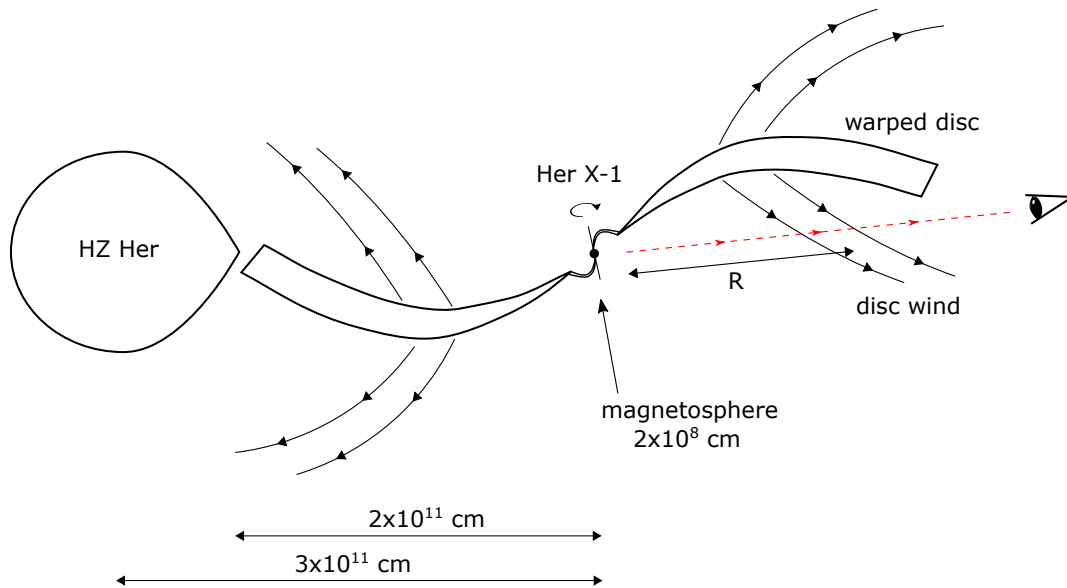


Fig. 7.14 A schematic of the Her X-1 system showing the outflow originating from the accretion disc of the neutron star. The scheme contains the most important scales of the system: the magnetosphere size, the accretion disc outer radius and the binary separation.  $R$  is the distance between the ionising source and the disc wind along our line of sight, calculated from Eq. (7.4) and shown in Fig. 7.13.

of the results in the context of a wind being launched from close to the inner edge of the disc. We will attempt to pinpoint the launching mechanism of the wind in section 7.5.4.

Fig. 7.13 also shows how the inferred distance depends on the ionising luminosity (left sub-plot) and the super-orbital phase (right sub-plot). The distance is strongly anti-correlated with both of these parameters, with one outlier: observation 0673510901. Observation 0783770701 is consistent with a broad range of distances due to the large uncertainty on the wind column density. The fact that observation 0673510901 is an outlier in both plots suggests that the distance does not only depend on the luminosity of the source but also on the super-orbital phase, i.e. we are likely probing different lines of sight from the neutron star (different inclinations and vertical heights from the accretion disc).

We also explore the dependence of the inferred absorption distance on the orbital phase but do not find any noteworthy correlation.

Eq. (7.4) can be turned around to extract the minimum density of the outflowing material:

$$n = \frac{N_{\text{H}}^2 \xi}{L_{\text{ion}} \delta R^2} \quad (7.5)$$

Minimum densities required are between  $10^{11}$  and  $10^{15} \text{ cm}^{-3}$  (with most of the measurements falling in the range of  $10^{12} - 10^{13} \text{ cm}^{-3}$ ), and we observe a positive correlation between the density and both the ionising luminosity and the super-orbital phase (an opposite trend as the absorption distance, in Fig. 7.13). However, the uncertainties in the density measurement are considerably larger than those of the absorption distance due to both  $N_{\text{H}}$  and  $\delta R$  appearing in the second power in Eq. 7.5. Finally, we do not observe any significant correlation between the plasma density and the orbital phase of the binary.

### 7.5.3 Mass outflow rate

Table 7.5 Estimates of the maximum distance of absorption and the mass outflow rate of the wind for each observation. The first mass outflow rate estimate (third column) was made using the ionising luminosity, systematic velocity and the ionisation parameter of the material, and the second estimate (fourth column) was calculated using the column density of the material and its systematic velocity. We stress that these calculations assume a full ( $4\pi$ ) solid angle of the wind. If the launch solid angle is much smaller (which is likely the case), the mass outflow rates will correspondingly decrease.

Obs. ID	Maximum distance cm	Mass outflow rate	
		$L_{\text{ion}}, \xi, v$ $M_{\odot} \text{ yr}^{-1}$	$N_{\text{H}}, v$ $M_{\odot} \text{ yr}^{-1}$
0134120101	$4.9_{-3.1}^{+1.7} \times 10^8$	$5.0_{-3.5}^{+3.7} \times 10^{-9}$	$3.5_{-2.4}^{+1.1} \times 10^{-6}$
0153950301	$1.2_{-0.7}^{+0.8} \times 10^{10}$	$1.9_{-1.6}^{+1.5} \times 10^{-8}$	$7.3_{-6.6}^{+4.9} \times 10^{-7}$
0673510501	$1.6_{-0.8}^{+0.8} \times 10^{10}$	$9.3_{-2.2}^{+2.0} \times 10^{-8}$	$1.5_{-0.8}^{+0.7} \times 10^{-7}$
0673510601	$1.7_{-0.4}^{+0.3} \times 10^9$	$8.6_{-3.2}^{+2.9} \times 10^{-9}$	$9.9_{-3.1}^{+3.2} \times 10^{-7}$
0673510901	$1.3_{-0.4}^{+0.5} \times 10^{11}$	$9.8_{-2.6}^{+2.4} \times 10^{-8}$	$5.4_{-1.9}^{+1.5} \times 10^{-8}$
0783770501	$9.5_{-0.3}^{+0.3} \times 10^{10}$	$1.7_{-0.4}^{+0.6} \times 10^{-7}$	$1.5_{-0.7}^{+0.5} \times 10^{-7}$
0783770601	$5.6_{-2.2}^{+2.3} \times 10^{10}$	$1.3_{-0.5}^{+0.3} \times 10^{-7}$	$2.9_{-1.2}^{+1.2} \times 10^{-7}$
0783770701	$1.4_{-1.4}^{+1.0} \times 10^{11}$	$6.0_{-3.0}^{+3.5} \times 10^{-8}$	$5.1_{-4.2}^{+16.5} \times 10^{-8}$

The ionisation level, column density and velocity of the wind can also be used to estimate the mass outflow rate in the wind and compare it with the mass accretion rate.

We will use two independent approaches, one making use of the ionisation parameter, the velocity of the outflowing material and the ionising luminosity of Her X-1, and the second one making use of the systematic velocity and the column density of the wind. In both cases we assume that the wind structure is axisymmetric. Again we assume Solar abundances in this section.

First we use the ionisation parameter of gas. The mass outflow rate can be written as:

$$\dot{M}_{\text{out}} = \rho A v = (C_V \mu m_p n) \left( \frac{\Omega}{4\pi} 4\pi R^2 \right) v \quad (7.6)$$

where  $\rho$  is the density of outflowing gas,  $A$  is the surface area into which it is launched,  $v$  the outflow velocity,  $C_V$  is the volume filling factor (assumed to be constant across different observations),  $\mu$  defines the mean atomic mass ( $\approx 1.2$  for solar abundances),  $m_p$  the hydrogen ( $\approx$  proton) mass,  $n$  the ion concentration in the wind,  $\frac{\Omega}{4\pi}$  is the solid angle into which the wind is launched as a fraction of  $4\pi$  and  $R$  is the distance from the ionising source at which the ionised absorption occurs.

Here we use  $v$  as the observed projected velocity, measured from the line blueshift. In principle, if the wind is launched from the disc and is observed close to its launching point (which is probably the case here because Her X-1 is a high inclination system), it will also likely carry a toroidal velocity component from the Keplerian rotation within the accretion disc. Such a velocity component is impossible to measure from the absorption line shifts alone. From the absorption distance calculations in Section 7.5.2 (also shown in Fig. 7.13), the wind originates at distances of around  $10^5 R_G$  in the disc, with two exceptions (observations 0134120101 and 0673510601) where it could originate as close as  $10^3 - 10^4 R_G$ . The corresponding Keplerian velocities at these radii are  $\sim 1000$  km/s and  $\sim 5000$  km/s (taking  $3 \times 10^3 R_G$ ), hence the total wind velocity could be significantly larger.

Nevertheless, unless the wind also carries a considerable vertical speed component (which we will argue against later in this work), the toroidal motion will not affect our calculation of the mass outflow rate because the velocity perpendicular to the surface of integration remains the same as the projected component which is observed.

We can now use the definition of the ionising parameter (7.2) to show that:

$$\dot{M}_{\text{out}} = 4\pi \mu m_p v \frac{L_{\text{ion}}}{\xi} C_V \frac{\Omega}{4\pi} \quad (7.7)$$

The volume filling factor  $C_V$  and the solid angle  $\Omega$  are unknown, but we can make an estimate of the mass outflow rate using the remaining parameters (assuming  $C_V$  and  $\Omega$

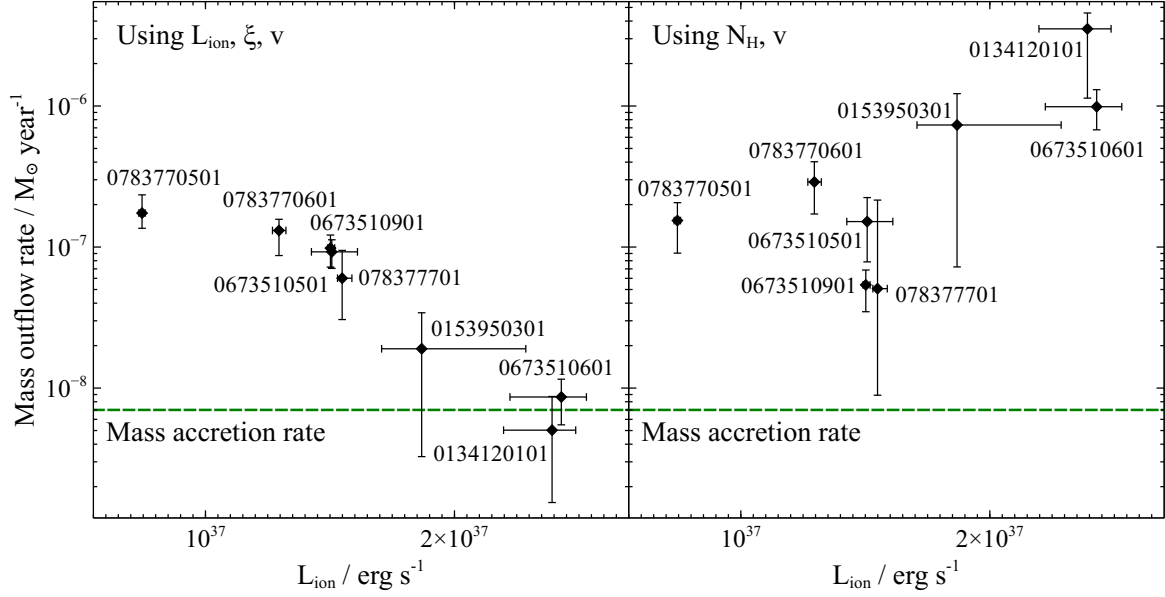


Fig. 7.15 The mass outflow rate of the wind for each observation. The estimate in the left plot was made using the ionising luminosity of the source, the ionisation parameter and the velocity of the material. The estimate in the right plot was made using the column density and the velocity of the wind. The green horizontal lines show the mass accretion rate through the accretion disc [38].

are equal to unity). The results for each observation are shown in Table 7.5 and Fig. 7.15 (left subplot). In reality, both  $C_V$  and  $\Omega$  must be smaller than unity and thus all of the mass outflow rate estimates are upper limits on their real values.

Alternatively, we can estimate the mass outflow rate by assuming that the systematic velocity of the absorber is approximately equal to the escape velocity at the location of wind absorption. Under this assumption, we can write

$$v^2 = \frac{2GM}{R} \quad (7.8)$$

where  $G$  is the gravitational constant and  $M$  is the mass of the neutron star. Then, using (7.3), we can express (7.6) as

$$\dot{M}_{\text{out}} = 4\pi\mu m_p v \frac{N_H}{R\delta R} R^2 C_V \frac{\Omega}{4\pi} = 4\pi\mu m_p v \frac{N_H}{\delta R} \frac{2GM}{v^2} C_V \frac{\Omega}{4\pi} \quad (7.9)$$

Therefore we find that

$$\dot{M}_{\text{out}} = 4\pi\mu m_p \frac{N_H}{\delta R} \frac{2GM}{v} C_V \frac{\Omega}{4\pi} = 8\pi\mu m_p GM \frac{N_H}{v} \frac{1}{\delta R} C_V \frac{\Omega}{4\pi} \quad (7.10)$$

This assumption necessarily also ignores the projection effect on the actual outflow velocity. The estimated mass outflow rate for each observation is shown again in Table 7.5 and Fig. 7.15 (right subplot), taking the mass of the central neutron star to be  $1.4 M_{\odot}$ , and assuming the  $C_V$ ,  $\Omega$  and  $\delta R$  parameters are equal to unity.

We find that most of the mass outflow rate estimates are significantly higher than the mass accretion rate, on average more than an order of magnitude larger. Fig. 7.15 also shows that the two different mass outflow estimates diverge with luminosity. This suggests that the assumption of the outflow velocity being parabolic is most likely incorrect. This fact is also underlined by the apparent lack of correlations between the outflow velocity and the ionising luminosity, orbital or super-orbital phase. Therefore the mass outflow rates estimated by the second method should be taken cautiously.

There is a strong correlation between the mass outflow rates inferred from the ionisation parameter and the ionising luminosity of the neutron star. This correlation is necessarily driven by the strong dependence of the ionisation parameter on the luminosity.

On the first look, the mass outflow rate estimates appear too high. However, these values do not account for the limited solid angle and volume filling correction factors. I.e., using a modest opening angle of  $5^\circ$  (above and below the accretion disc) into which the wind is outflowing, we obtain  $\frac{\Omega}{4\pi} \approx 0.1$ , bringing down the mass outflow rates by an order of magnitude. Nevertheless, even if the volume filling factor is very small as well ( $C_V \sim 0.1$ ), the mass outflow rates are still of the same order as the mass accretion rates onto the primary and hence the wind is an important component of the accretion flow.

Very high wind mass outflow rates, of the same order as the mass accretion rate or higher, were previously found in other X-ray binaries [e. g. 259, 280]. Similar results were also found in the studies of warm absorbers [33] and ultrafast outflows [279] in AGN. Blustin et al. [33] find almost one order of magnitude higher median mass outflow rates than the median mass accretion rates using a sample of 23 AGN with detected warm absorbers.

#### 7.5.4 Possible wind launching mechanisms

Her X-1 is thought to be consistently in a sub-Eddington mass accretion state with an Eddington ratio of  $\sim 0.1 - 0.2$ . The hard X-ray radiation from the accretion column is beamed, but not by an extreme factor hence the beamed flux should not reach Eddington levels. Radiation pressure on electrons therefore should not be sufficient to drive the wind from the accretion disc to  $\sim 1000$  km/s velocities.

Line driving could enhance the pressure on outflowing material, however the material cannot be over-ionised as it is being accelerated away from the disc [322]. The high inclination of Her X-1 suggests that we might be viewing the wind close to the launching site. The very high ionisation degree ( $\log \xi > 3$ ) therefore implies that the wind is most likely not driven by line pressure.

The wind could originate in the part of the accretion disc periodically irradiated by the beam of the neutron star. This might be the same region that produces the soft blackbody in the X-ray spectrum of Her X-1, which pulses with the same period but with a variable phase delay compared to the neutron star accretion column [the phase delay is likely due to reprocessing effects, 326]. The temperature of this component, found in previous studies and also here is approximately 0.1 keV. The sound speed at this temperature is:  $c_s = \sqrt{\frac{kT}{m_p}}$ , where  $k$  is the Boltzmann constant,  $T$  the temperature of the plasma and  $m_p$  is the hydrogen (proton) mass. For  $T = 0.1$  keV  $\approx 1.2 \times 10^6$  K, we find  $c_s \approx 100$  km/s, much lower than the outflow velocities observed in this study.

Alternatively, if the hard X-ray radiation illuminates the outer part of the accretion disc (not unlikely as the accretion column radiation is beamed and the disc is warped), these regions could be Compton heated to a high enough velocity to escape the local gravity [21]. The ‘inverse Compton temperature’  $T_{IC}$  to which the outer disc regions can be heated to is defined as

$$kT_{IC} = \frac{1}{4} \langle \epsilon \rangle = \frac{1}{4} L^{-1} \int_0^\infty E L_E dE \quad (7.11)$$

where  $L$  is the total luminosity and  $L_E$  is the luminosity at energy  $E$ .  $T_{IC}$  for each of our observations of Her X-1 vary, and also depend on whether the full X-ray SED is taken or only the accretion column radiation (the COMT component, producing harder radiation than the full SED). However, all the estimates are in the range between 2.5 and 3.5 keV, and on the upper end of this interval if only the accretion column radiation is taken as the heat source. The  $T_{IC}$  values for each observation are listed in Table 7.6.

Thus a Compton-heated thermal wind will occur for accretion disc radii greater than [using equations 2.7 and 2.8 from 21]

$$R/R_{IC} \gtrsim 0.1 \quad (7.12)$$

where  $R_{IC}$  is:

$$R_{IC} = \frac{GM\mu m_p}{kT_{IC}} \quad (7.13)$$

Table 7.6 Inverse Compton temperatures and approximate wind launching radii for each observation.

Obs. ID	Full SED		Accretion column SED	
	$T_{\text{IC}}$	$0.1 \times R_{\text{IC}}$	$T_{\text{IC}}$	$0.1 \times R_{\text{IC}}$
	keV	cm	keV	cm
0134120101	2.21	$1.05 \times 10^{10}$	2.67	$8.72 \times 10^9$
0153950301	2.24	$1.04 \times 10^{10}$	2.76	$8.44 \times 10^9$
0673510501	2.36	$9.87 \times 10^9$	2.88	$8.09 \times 10^9$
0673510601	2.64	$8.82 \times 10^9$	3.18	$7.33 \times 10^9$
0673510801	2.79	$8.35 \times 10^9$	3.26	$7.15 \times 10^9$
0673510901	2.58	$9.03 \times 10^9$	3.01	$7.74 \times 10^9$
0783770501	2.39	$9.75 \times 10^9$	2.65	$8.79 \times 10^9$
0783770601	2.58	$9.03 \times 10^9$	3.04	$7.66 \times 10^9$
0783770701	2.62	$8.89 \times 10^9$	3.05	$7.64 \times 10^9$

If we take  $kT_{\text{IC}} \sim 3 \text{ keV} \sim 3.5 \times 10^7 \text{ K}$ , the wind should be launched at distances larger than  $R \sim 8 \times 10^9 \text{ cm}$  ( $4 \times 10^4 R_{\text{G}}$ ) from the neutron star (precise values for each observation are tabulated in Table 7.6). This corresponds to the outer half of the accretion disc, and matches very well with most of our estimates of the absorption distance from the ionising source (Section 7.5.2). At the same time, the critical luminosity required for a significant mass flux within the wind is [eq. 2.12b from 21]

$$L_{\text{cr}} = 0.030 (T_{\text{IC}}/10^8 \text{ K})^{-1/2} L_{\mathcal{E}} \quad (7.14)$$

where  $L_{\mathcal{E}}$  is the Eddington luminosity:

$$L_{\mathcal{E}} = 1.5 \times 10^{38} (M/M_{\odot}) \text{ erg/s} \quad (7.15)$$

For  $T_{\text{IC}} \sim 3.5 \times 10^7 \text{ K}$ , we obtain  $L_{\text{cr}} \sim 1.1 \times 10^{37} \text{ erg/s}$ . This is just about the luminosity of the lowest flux observation (0783770501, Table 7.3) and much lower than the average flux during remaining observations. Thus the luminosity of Her X-1 is above the critical luminosity and a Compton-heated thermal wind should occur in the High state of Her X-1 with a significant mass outflow rate if the outer part of the accretion disc is illuminated by the accretion column beam. Unfortunately, we cannot estimate the mass

outflow rate from theory as the value depends on the pressure of gas in the launching point of the wind.

On the other hand, we can roughly estimate the outflow velocity. The rms velocity of a Compton-heated particle of the wind ( $T_{\text{IC}} \sim 3$  keV) is:

$$v = \sqrt{\frac{3kT}{\mu m_p}} \sim 850 \text{ km/s} \quad (7.16)$$

The outflow velocity estimate compares very well to the values we are measuring in most observations. Compton heating is therefore a very plausible candidate for driving the wind.

Lastly, magnetic driving is also a possible launching mechanism for the wind [30]. Magnetic field of the neutron star [ $B_0 \approx 4 \times 10^{12}$  G on the star surface, 371] could potentially provide the driving force. If the neutron star field is a dipole, at distance  $R$  it will decay such as  $B = B_0(R/R_0)^{-3}$  where  $R_0$  is the neutron star radius (the strength will decay faster if the field is higher order than a dipole). Thus the field strength at the inner accretion disc radius ( $\sim 10^9$  cm) is roughly  $10^3 - 10^4$  G, which could be sufficient to drive the wind [406, 80, 260]. If the outflow however originates beyond  $R \sim 10^{10}$  cm, which is likely the case for most of our *XMM-Newton* observations, the field will be of the order of  $\sim 10$  Gauss or less, insufficient to launch the material. Alternatively, additional magnetic field could originate in the accretion disc itself. However, as we cannot readily estimate this field, it is difficult to judge whether it can or cannot contribute to or drive the wind in this object.

Winds with similar properties (velocities, ionisation parameters) have been discovered in other neutron star binary systems such as GX 13+1 [404], IGR J17480-2446 [258] and IGR J17591-2342 [285]. The difference between these three and Her X-1 is that the column density observed in Her X-1 is significantly lower during most observations and thus the absorption strength is correspondingly lower. The outflow properties are also comparable to the ionised winds observed in Galactic black hole binaries such as GRO J1655-40 [259, 122], GRS 1915+105 [280] and other objects where both Compton thermal and magnetic driving were invoked to explain the wind origin.

On the other hand, one important difference between all of the aforementioned examples is that Her X-1 is known to be a highly magnetised ( $10^{12}$  G) neutron star. To our current knowledge, Her X-1 is the first highly magnetised neutron star to harbour such a wind. The magnetic field effectively puts an absolute lower limit of  $\sim 1000 R_G$

on the wind launching radius as it truncates the inner accretion disc. This can be used as an effective constraint in theoretical models explaining the appearance of the wind.

### 7.5.5 Are observations over the super-orbital period probing different lines of sight?

We observe an inverse correlation between the distance at which the wind absorption occurs and the ionising luminosity of Her X-1 (Fig. 7.13). The relation could suggest that the wind launching radius decreases with increasing luminosity. Such a correlation would be expected for example if the radiation pressure on the outflowing material played a role. This explanation would come naturally within the framework of a wind driven by a combination of Compton heating and radiative force.

At the same time, the correlation between the distance and luminosity necessarily implies that the absorption distance is correlated with the super-orbital phase too (since luminosity and super-orbital phase are connected, from Fig. 7.9). If the super-orbital phase is the driver for the correlation instead of the ionising luminosity, an alternative explanation for the variations is possible. The super-orbital period is likely introduced by the precession of a warped accretion disc, which at times obscures our view into the innermost accretion disc and onto the neutron star. But even in the High state, when our view of the inner regions is unobstructed, the disc continues precessing and the angle between different annuli of the disc and our line of sight keeps changing [Fig. 3 of 211]. It is thus possible, that by observing the wind at different super-orbital phases, we are probing different heights of the wind above the accretion disc.

If this is the case, we are presented with a rare opportunity to study the vertical structure of a disc wind. We might be able to determine the opening angle of the outflow (except for any wind component which is fully ionised) and consequently obtain an accurate estimate of the wind mass outflow rate. Fig. 7.16 shows that at the highest ionising luminosities during the Her X-1 High state (i.e. at super-orbital phases of 0.1-0.2), the mass outflow rate estimates are an order of magnitude smaller than those at super-orbital phase equal to 0 (the turn-on point).

At this point we can make a zeroth-order effort to calculate the real mass outflow rate which accounts for the limited wind launching solid angle. We can use the fact that the mass outflow rate decreases very steeply with the increasing super-orbital phase. We assume that each super-orbital phase corresponds ('maps to') to a specific angle between our line of sight and the accretion disc plane. We also assume that the dependence between this angle and the phase is linear. This is naturally a gross

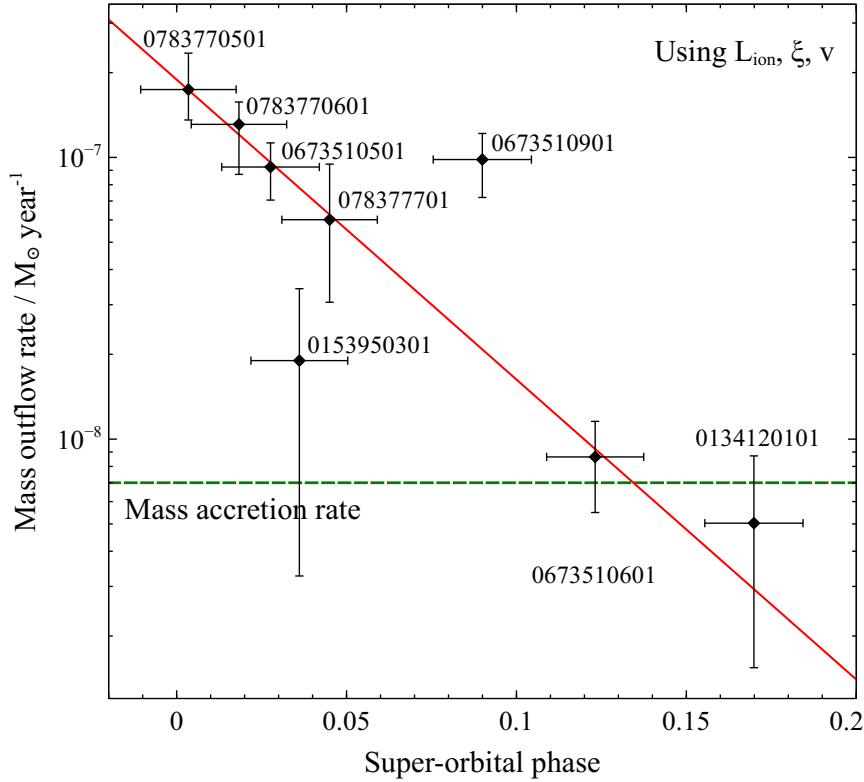


Fig. 7.16 Wind mass outflow rate versus the super-orbital phase of each observation. The red line shows the best log-linear fit to the data, excluding observations 0153950301 and 0673510901 and treating them as outliers.

oversimplification, and in reality the function might resemble a sinusoid [but not necessarily, we again refer to Fig. 3 from 211]. At phase equal to 0, the angle is also zero - the surface of the accretion disc is just about grazing our line of sight towards the neutron star. At the highest luminosity of Her X-1, which occurs roughly around phase equal to 0.12 [368], the angle will then also reach a maximum.

We will further assume that this inclination is the maximum angle between our line of sight towards the neutron star and the accretion disc. The maximum angle is likely around  $\theta \approx 5^\circ \approx 0.087$  rad [211]. Then the mass outflow rate per solid angle can be obtained from eq. 7.7 as:

$$\frac{d\dot{M}_{\text{out}}}{d\Omega} = \frac{\dot{M}_{\text{exp}}}{4\pi} \quad (7.17)$$

where  $\dot{M}_{\text{exp}}$  is the experimentally measured mass outflow rate value which assumes a full solid angle and full volume filling factor (this is the value listed in Fig. 7.15 and

Table 7.5). We can relate the solid angle to an inclination angle  $\theta$  from the disc such as:

$$d\Omega = \frac{dA}{R^2} = \frac{2 \times 2\pi R^2 \cos \theta d\theta}{R^2} \approx 4\pi d\theta \quad (7.18)$$

for very small angles  $\theta$  (satisfied here). The first factor 2 in the numerator of the fraction is introduced because the disc wind is launched from both sides of the accretion disc. Then the total mass outflow rate can be integrated as:

$$\dot{M}_{\text{out}} = \int \frac{\dot{M}_{\text{exp}}}{4\pi} d\Omega = \int \frac{\dot{M}_{\text{exp}}}{4\pi} 4\pi d\theta = \frac{d\theta}{d\phi} \int \frac{\dot{M}_{\text{exp}}}{d\Omega} d\phi \quad (7.19)$$

where  $\phi$  is the super-orbital phase. Now taking  $\phi_{\text{max}} \approx 0.12$ ,  $\theta_{\text{max}} \approx 0.087$  rad, if  $\phi$  and  $\theta$  are linearly related (as assumed) we obtain  $\frac{d\theta}{d\phi} = 0.73$ . It remains to integrate  $\int \frac{d\dot{M}_{\text{out}}}{d\Omega} d\phi$ . Fig. 7.16 shows the best log-linear fit to the measured mass outflow rates versus the super-orbital phase, excluding observations 0153950301 and 0673510901 which appear to be outliers. The best-fitting relation is in form

$$\log(\dot{M}_{\text{out}}/M_{\odot} \text{ year}^{-1}) = -15.48 - 24.51 \times \phi \quad (7.20)$$

We integrate from phase  $\phi_{\text{min}} = 0$  to  $\phi_{\text{max}} = 0.12$ , obtaining  $7.3 \times 10^{-9} M_{\odot} \text{ year}^{-1}$ . If we use all of the observations in the calculation (including the apparent outliers), we instead get  $5.8 \times 10^{-9} M_{\odot} \text{ year}^{-1}$ . With this approach we are ignoring any wind at inclination angles higher than  $\theta_{\text{max}} \sim 5^\circ$ , which never crosses our line of sight. However, the mass outflow rate seems to be a strongly decreasing function with super-orbital phase (and consequently the inclination angle) and therefore the error on the total mass outflow rate introduced this way should be small. The total mass outflow rate is:

$$\dot{M}_{\text{out}} \approx \frac{d\theta}{d\phi} \int \frac{d\dot{M}_{\text{out}}}{d\Omega} d\phi \approx 5 \times 10^{-9} M_{\odot} \text{ year}^{-1} \quad (7.21)$$

Alternatively, if all of the observations are included in the calculation, we obtain  $\sim 4 \times 10^{-9} M_{\odot} \text{ year}^{-1}$ . Both of these estimates are very comparable to the mass accretion rate which is around  $7 \times 10^{-9} M_{\odot} \text{ year}^{-1}$  [measured from the UV spectrum of the accretion disc, 38]. Finally, we note that this estimate still does not account for the volume filling factor of the wind. To summarize, approximately half of the originally accreting mass is likely expelled by the wind. Such large fraction of outflowing matter is not unexpected and has been found in other binary systems exhibiting both jet and wide angle outflows [e.g. 25, 280].

If the super-orbital disc precession drives the wind variation, the outflow must have a small solid launching angle with an opening angle of  $\sim 5^\circ$ . It is possible that fully ionised material, undetectable with X-ray spectroscopy, is launched to larger solid angles. However, at high ionisation levels this material contributes little to the overall mass outflow rate budget, unless it is launched at much larger velocities. A small wind opening angle is also supported by the fact that any P-Cygni profiles from the outflowing material not along our line of sight are weak or non-existent [as opposed to other X-ray binaries where evidence of P-Cygni features has been seen, 253]. This is especially the case for the highest quality observations (0673510501 and 0783770601). Furthermore, at higher super-orbital phases, we do not observe any signatures of winds from phases close to 0, which suggests that the wind is launched directly at us, i.e. its vertical velocity component is likely not large.

At the moment it is not clear which of the above possibilities is correct - whether the evolution of the wind is dictated by the ionising luminosity, by the super-orbital phase or in fact by some combination of both. Future studies, which will sample wind evolution during the super-orbital phase more densely, might be able to answer this question. To conclude, Hercules X-1 is a fascinating system that potentially offers us a unique opportunity to sample the vertical structure of an equatorial accretion disc wind.

## 7.6 Conclusions

We have performed an in-depth X-ray spectral analysis of Hercules X-1 with *XMM-Newton* combining both broadband and high-spectral resolution instruments and focusing mainly on the High flux state of this famous object. The conclusions of our study are follow:

- We detect a highly ionised blueshifted wind in the High state of Her X-1. The detection is statistically significant in most of the *XMM-Newton* observations. The wind has a projected outflow velocity of 200 to 1000 km/s, varying between different observations, and an ionisation parameter in the range of  $\log \xi$  of 3.0 to 5.0. Her X-1 can thus be added to a list of known neutron star binaries with detected ionised outflows, such as GX 13+1, IGR J17480-2446 and IGR J17591-2342.

- While photon pile-up due to very high X-ray fluxes might affect a fraction of our datasets, especially pn and RGS 2 data, we conclude that the wind detection is robust and the absorption features are not induced by this instrumental effect.
- We find a clear correlation between the luminosity of Her X-1 and the ionisation parameter of the wind, suggesting that the material in the outflow observes a similar X-ray flux as we do. We also observe a correlation between the super-orbital phase and the ionisation parameter. We do not observe any significant correlations between the outflow velocity and these two parameters.
- The best-fitting wind properties suggest that the absorption takes place within the accretion disc of the primary. It is plausible that the X-ray outflow, launched from the accretion disc, is the progenitor of the UV blueshifted absorption observed in Her X-1, but the latter only occurs at larger, circumbinary distances from the system.
- We find that the mass outflow rate in the wind can easily be of the same order as the mass accretion onto Her X-1. It is thus an important component of the accretion process. We conclude that it is driven either by Compton heating of the outer accretion disc or by magnetic fields.
- If the super-orbital phase is the driver for the wind variability instead of the ionising luminosity, the individual observations are likely observing different lines of sight above the accretion disc and sampling the vertical structure of the wind. If this is the case, we can estimate the mass outflow rate corrected by the limited launching solid angle to be  $5 \times 10^{-9} M_{\odot} \text{ year}^{-1}$ , approximately 70% of the mass accretion rate.
- Our chemical analysis of elemental abundances in the ionised wind finds a strong over-abundance of iron compared to oxygen. We also confirm the results of previous studies which found an over-abundance of nitrogen and neon compared to oxygen. At the same time, there is evidence that oxygen is not in fact under-abundant compared to the remaining chemical elements.
- None of the Low state or Short-on *XMM-Newton* observations of Her X-1 are of high enough quality to detect a similarly ionised wind. We stack all of the available Low state data but do not find obvious evidence of blueshifted absorption. Future long exposure observations, or observations with instruments with higher

collecting area [such as *ATHENA*, 273] might be able to detect a wind if present in the Low state.

# Chapter 8

## Conclusions and future research

In the first section of this concluding chapter I discuss the conclusions of the research chapters of this thesis. The second section lists a number of further research directions in this field which I would like to address in the near future. The third section describes the relevant upcoming X-ray observatories which will transform the field of accretion physics in the next 10 – 15 years.

### 8.1 Conclusions

Accretion disc winds appear to be a ubiquitous component of the accretion flow in most types of accretors including active galactic nuclei (studied in chapters 5 and 6), classical X-ray binaries (chapter 7) and likely also ultraluminous X-ray sources (chapters 3 and 4). In this thesis, I have studied various accreting systems to detect the presence of disc winds in their spectra, and to understand the outflow energetics, structure and their impact on the accretion flow and the accretor surroundings. I have shown that high-resolution X-ray spectroscopy holds great potential for studying the physics of outflows in accretors.

#### 8.1.1 Ultraluminous X-ray sources

The systematic analysis of ULX high-resolution grating data (chapter 3) shows that the vast majority of ULXs do not have deep and high enough quality X-ray spectra, preventing us from achieving further detections of ultra-fast outflows, in addition to the first three UFO detections [306, 304]. Further long exposure campaigns with current or future X-ray missions are necessary to detect and study winds in other ULXs.

NGC 5204 X-1 is among the ULXs with high quality high-resolution data. I achieved a  $3\sigma$  detection of an outflow with a projected velocity of  $0.34c$  in its spectrum. NGC 5204 X-1 is thus the fourth ULX with a fast outflow, however the outflow observational signatures are very different to those of the first 3 ULXs. With blueshifted emission signatures rather than absorption signatures, the outflow might not be a wide angle disc wind but instead a collimated jet, such as the one observed in the only known persistent Galactic super-Eddington accretor SS 433 [235].

The detection of an ultra-fast outflow in the newly discovered neutron star ULX NGC 300 ULX-1 (chapter 4, the first ever detection of a UFO in a neutron star ULX) suggests that at least a part of the accretion flow of these objects is a standard supercritical disc [363]. This is where the outflows are most likely being launched, although it is still possible that they originate directly from the accretion column. If the pulsating ULX has a supercritical part of the accretion flow, the magnetosphere of the neutron star cannot be too large otherwise the magnetosphere would directly transition into a thin, sub-Eddington disc.

In other words, the UFO discovery argues against the possibility of these objects having huge magnetospheres and thus magnetar-like surface magnetic fields [ $10^{14} - 10^{15}$  G, 91, 271, 399]. Currently, NGC 300 ULX-1 is the only pulsating ULX to show winds, however future long exposure observations, particularly with the upcoming instruments such as *XRISM* and *ATHENA* have the potential to detect outflows in many more (at least an order of magnitude more) objects.

Secondly, the energetics of the UFO in NGC 300 ULX-1 are extreme. Its kinetic power is easily comparable to the radiative output of the source, and is sufficient to inflate the ionised super-bubbles in which many ULXs are embedded [291]. The wind is therefore a possible source of power for these ionised bubbles.

### 8.1.2 Active galactic nuclei

In chapters 5 and 6 I detect UFOs in two extreme Narrow Line Seyfert 1 galaxies with supermassive black holes likely accreting close to or around the Eddington limit. Both of the detections are unambiguous with very high data quality. With velocities of around  $0.1c$ , the kinetic powers of the UFOs are sufficient to drive AGN feedback in their host galaxies, similar to what has been measured in other AGN [e.g. 394, 279, 297].

Multiple *XMM-Newton* observations of PG 1448+273 allow me to show that the UFO properties must be time variable (chapter 5). Such variability has been observed in other AGN, and in particular in IRAS 13224-3809 where the UFO absorption strength

anti-correlates with the AGN X-ray flux [297, 303]. A similar trend is observed in PG 1448+273, where the UFO is not detected in a higher flux observation.

The outflow of 1H 0707-495 is clearly multi-phase (chapter 6). Multi-wavelength coverage across the UV and X-ray bands allowed me to separate at least three components (two of which are observed in X-rays). The kinetic powers of all the wind phases are consistent with being equal, suggesting the outflow is energy-conserving at the observed scales. Energy conservation between the wind phases has been observed in at least one other source by Tombesi et al. [394]. On the other hand, a momentum-conserving outflow has been detected in another AGN [329]. The means of outflow propagation through the accretor surroundings (energy versus momentum conservation) is important as it governs the impact of the outflow on the AGN host galaxy [57].

### 8.1.3 Classical X-ray binaries

In the last part of this thesis, I focused on a sub-Eddington accretor, the neutron star X-ray binary Hercules X-1. With a re-analysis of archival *XMM-Newton* datasets, I achieved the first detection of a disc wind in this object, and in general in an accreting X-ray pulsar. The wind with a typical projected velocity of 200 – 1000 km/s is detected in 8 individual observations of Hercules X-1 and its properties such as the ionisation state and column density are strongly variable. The variation, knowing that the system has a warped accretion disc which periodically precesses, can be explained in terms of a changing line of sight rather than actual time variability. We are therefore likely sampling the vertical distribution of the wind. I used the measurements of the wind vertical structure to estimate the total mass outflow rate, which is as high as 70% of the mass accretion rate through the accretion disc.

Her X-1 is currently the only accreting object where we can directly study the vertical disc wind structure via absorption lines. Accurately sampling the structure would be a very powerful step towards pinpointing the exact wind launching mechanism and measuring precisely its mass outflow rate as well as the kinetic power, thus understanding the impact the disc wind has on the binary system.

The wind structure can be studied with other methods, for example through statistical studies of winds in binaries at various inclinations [310] and by studying the emission signatures of the wind [253, 260]. However, the statistical methods can be plagued by physical variations between different objects. Similarly, the emission line signatures are difficult to interpret as their studies are complicated by other spectral features in accreting systems such as relativistic reflection. To sum up, Hercules X-1 offers a unique opportunity to understand the properties of accretion disc winds.

## 8.2 Future research

### 8.2.1 Efficient ionised outflow search

Together with C. Pinto, we developed automated routines to search accretor spectra for ionised wind signatures and successfully used them to detect outflows in ULXs for the first time. The first, simple search routine scans the spectral energy range with a Gaussian line [Chapter 3, also 306]. I developed a more advanced method, which scans over a multi-dimensional parameter grid of self-consistent physical plasma models (Chapters 3 and 4). The detection statistical significance is determined by Monte Carlo simulations. These methods are powerful but computationally expensive - a single scan can take 10000 seconds on a 4-core CPU, depending on the instrument's spectral resolution. Particularly difficult is the detection significance assessment which involves running 1000s of simulated searches to test a  $3 - 4\sigma$  significance of an outflow detection. This kind of analysis will become untenable in the era of future X-ray observatories like *XRISM* and *ATHENA*, which will offer excellent spectral resolution ( $R \sim 200 - 2000$ ) over a broad X-ray band ( $0.5 - 10$  keV).

A new technique for automated search of emission lines in high-spectral resolution data was recently developed by Mao et al. [231] and is based on wavelet transform (Fig. 8.1). Its main advantage is the search speed, over 1000 times higher in comparison with current methods. I will improve and expand this method significantly - instead of a Gaussian-like shape, a physical plasma model (effectively an assortment of Gaussians at specific energies) can be simulated. Creating a multi-dimensional grid of these models for a broad range of absorber parameters will allow me to scan the X-ray spectra of accretors and detect ionised winds with much lower computational costs.

I will develop and optimise this efficient outflow detection method. To test the method I will apply the method to the full high-spectral resolution X-ray dataset on ULXs, creating a catalogue of emission/absorption line detections as well as wind detections in these objects. Later I will also apply the routine to the X-ray Imaging and Spectroscopy Mission (*XRISM*) dataset simulations. It will be finished before the launch of *XRISM* (early 2022), which will produce a wealth of high quality high-spectral resolution data on accreting systems of all masses. The wind search efficiency will allow large numbers of datasets to be analysed and thus I will be able to carry out a large population study of accretion disc winds.

I will in particular search the *XMM-Newton* and *Chandra* archives of AGN for multi-phase outflows. Such outflows have been detected in several AGN [394, 313, 314, 196, 34]. Comparing the energetics, structure and location (i.e. the distance from the ionising

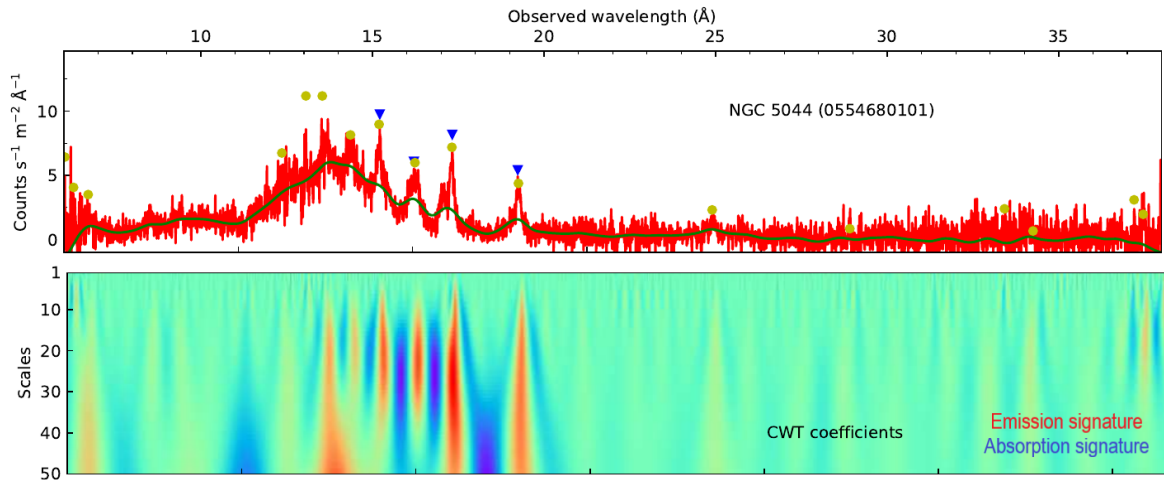


Fig. 8.1 Example of a wavelet-based emission line spectral search (figure adapted from Mao et al. [231]). Continuous Wavelet Transform (CWT) coefficients define the strength of spectral features, the ‘scale’ parameter defines the line spectral width.

source) of the different phases can potentially allow us to infer the wind driving mechanism as well as the impact of the wind on the AGN surroundings.

I will carry out a population study to understand specifically how the wind speed and ionisation evolve with distance from the black hole. I will compare the resulting correlations with the theoretical predictions of different launching mechanisms (radiative/magnetic/thermal driving) and with the models of wind propagation through the surrounding medium [momentum versus energy conservation, 57] to relate disc winds to AGN feedback models. Later, I will extend this study to include the new high quality data from the *XRISM* observatory, to be launched in early 2022.

### 8.2.2 Understanding the vertical structure of accretion disc winds

I have identified a unique object to study the vertical structure of accretion disc winds in classical X-ray binaries - Hercules X-1 [Chapter 7, 197]. I have leveraged the warped accretion disc precession to sample the vertical properties of Her X-1 disc wind using 8 individual *XMM-Newton* observations. However, these observations were taken over multiple years and over many precession cycles, with unequal sampling over the super-orbital precession period. Our results are therefore likely plagued by poor sampling, and possible long-term variations in the accretion flow and wind structure.

We can do much better with a single, focused follow-up campaign on Hercules X-1. I am the PI of the 400 ks Large *XMM-Newton* proposal (awarded in *XMM-Newton*

AO-19) to observe a large fraction of a single precession cycle of Her X-1 (phases 0 to 0.12, about half of the Main High state). My main aim is to study the wind variability within the cycle, free of any long-term variation in the mass accretion rate and the accretion flow and wind geometry. The campaign will allow us to fully understand the Her X-1 wind structure, mapping it in 3D, as well as accurately calculate its mass outflow rate and kinetic power, and constrain the wind launching mechanism.

The *XMM-Newton* campaign will mostly focus on the nitrogen, oxygen and neon lines of the disc wind as they are within the RGS grating energy band, and thus the campaign will mostly cover the less ionised part of the outflowing material. The higher energy transitions of the more ionised part will not be covered in detail due to the poorer spectral resolution of the wide energy band CCD cameras onboard *XMM-Newton*. These transitions, which include the highly abundant silicon, sulphur and iron ions, could however be studied with the upcoming X-ray observatory *XRISM*, offering very high spectral resolution in the 2-10 keV energy band. I will write proposals to follow-up the *XMM-Newton* campaign with a similar *XRISM* observation, to understand the structure of the highly ionised part of Her X-1 disc wind, and to understand accretion disc winds in X-ray binaries in general. *XRISM* will also be able to determine the wind velocity distribution much more accurately than *XMM-Newton*.

Additionally, I will write further proposals to observe similar objects to Her X-1. The neutron star binary LMC X-4 could resemble Her X-1 but is at a much larger distance and currently has no disc wind detections. The detection of a possible wind in this object will therefore be significantly more challenging.

## 8.3 Future X-ray observatories

The future of X-ray astronomy is bright. A number of future X-ray observatories are currently being built or planned, each of which have potential to revolutionise this field, and in particular the studies of disc winds. Below I describe a few of these missions and mission concepts.

### 8.3.1 X-ray Imaging and Spectroscopy Mission (*XRISM*)

*XRISM* (see Fig. 8.2 for artist's impression), expected to launch in early 2022 [433] is the replacement for the *Hitomi* X-ray mission (lost in 2016). Its main instrument will be an X-ray micro-calorimeter, with a very high spectral resolution of 5-7 eV, approximately constant in energy across the energy band. This results in a moderate

$R \sim 200$  resolution at 1 keV (comparable or worse than RGS at this energy) but very high,  $R \gtrsim 1000$  resolution in the iron K band (around 7 keV). *XRISM* will therefore be an ideal instrument for studies of highly ionised plasma in the iron K band, where most UFO absorption features are observed. Additionally, the micro-calorimeter will not be a dispersive instrument and hence will not suffer from contamination by other sources along the roll angle of the spacecraft.

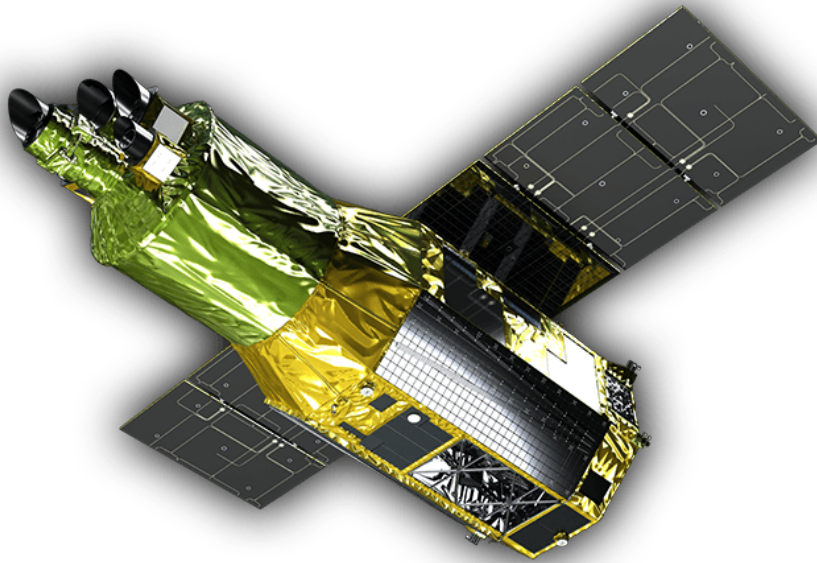


Fig. 8.2 Artist's impression of the *XRISM* X-ray observatory (credit: JAXA).

The effective area of the mirrors onboard *XRISM* will be 150-300 cm<sup>2</sup> across the energy band (slightly better than RGS). It will offer a relatively poor 1-2 arcmin spatial resolution and a field of view of  $3 \times 3$  arcmin separated into 36 pixels, each acting as an individual micro-calorimeter. The high spectral resolution but limited collecting area and spatial resolution means that *XRISM* will be most useful for observations of sources such as X-ray binaries, and bright (nearby) AGN and ULXs (see Fig. 8.4 for an example simulation). *XRISM* will be able to separate the broad iron K reflection features from the narrow wind absorption lines, resulting in much more confident detection of winds in AGN and X-ray binaries. Furthermore, *XRISM* will bring a revolution beyond the field of disc winds, particularly to the studies of extended X-ray sources such as galaxy clusters and supernova remnants [433].

### 8.3.2 Advanced Telescope for High Energy Astrophysics (*ATHENA*)

*ATHENA* [Fig. 8.3, 273] is one of the European Space Agency flagship observatories, to be launched in early 2030s. It will carry two main instruments: the Wide Field Imager [WFI, 327], and the X-ray Integral Field Unit [XIFU, 20]. WFI is a wide field (40 arcmin) CCD camera with moderate spectral resolution (50 – 100 eV), benefiting from the  $\sim 5$  arcsec spatial resolution of the telescope. XIFU is a micro-calorimeter similar to the one onboard *XRISM*, but with a better spectral resolution of 2 – 3 eV and with significantly more (4000) active pixels (vs 36 on *XRISM*).

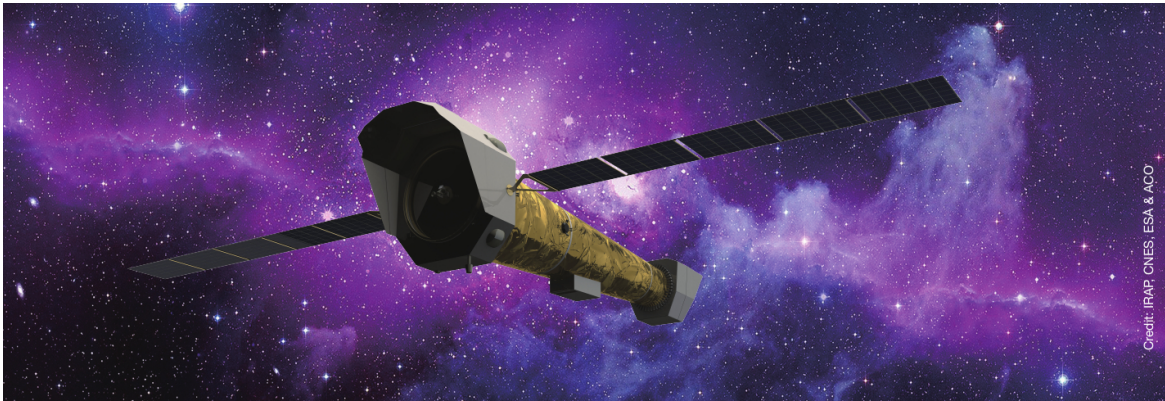


Fig. 8.3 Artist's impression of the *ATHENA* X-ray observatory (credit: IRAP, CNES, ESA & ACO).

Both instruments will benefit from a large mirror with the total collecting area of  $1.4 \text{ m}^2$ . The large collecting area will be the main driver for the science of accretion disc winds with *ATHENA*, allowing objects  $50\times$  fainter to be studied with a similar level of detail as the objects observed with *XRISM* (see Fig. 8.4 for an example simulation of a nearby ULX). For point X-ray sources, XIFU will be able to carry out similar science as the micro-calorimeter onboard *XRISM*, but with much shorter exposures, or for much more distant objects. It will therefore be able to perform a large population study of accretion disc winds to great detail, as well as detect disc winds in high-redshift AGN. For the bright X-ray sources, XIFU will be able to perform time-resolved spectral studies on the dynamical timescales of the wind. Beyond the disc wind science, *ATHENA* will bring another revolution in the studies of extended sources due to very good spatial resolution and a large number of XIFU active pixels.

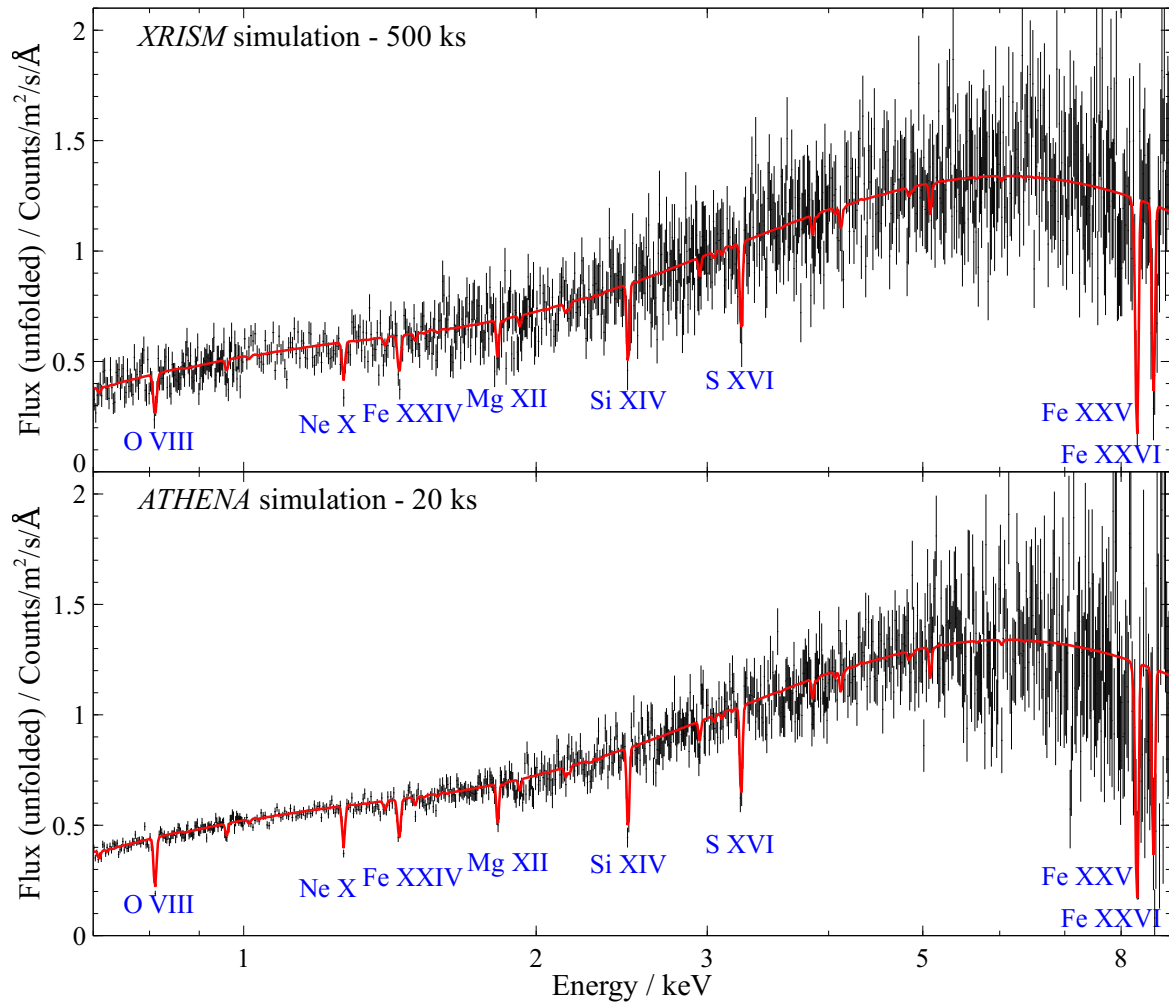


Fig. 8.4 A 500 ks simulation of NGC 300 ULX-1 with *XRISM* (top sub-plot). The bottom subplot contains a 20 ks *ATHENA* simulation of the same object. The ultrafast outflow of NGC 300 ULX-1 (the best-fitting spectral model is in red colour and is taken from chapter 4) is unambiguously constrained in both simulations through several strongly detected absorption lines (annotated in blue). The spectral resolution is very high with both telescopes. In addition, *ATHENA* benefits from the huge collecting area allowing it to achieve the required results within a very short exposure time.

### 8.3.3 *Arcus*

*Arcus* [367] is a proposed X-ray mission concept which (if approved) could be launched in the late 2020s. The main instrument of *Arcus* is a high resolution X-ray grating spectrometer with a soft X-ray bandpass (0.25 – 1.0 keV) similar to RGS onboard *XMM-Newton*, but with a significantly better spectral resolution ( $R \sim 3000$ ) and a higher collecting area ( $\sim 300 \text{ cm}^2$ ). The instrument will offer very high data quality

around the wavelength of O VII and O VIII transitions, allowing for detailed studies of less ionised outflows (which are often observed in AGN) in an energy band where *XRISM* and *ATHENA* will offer relatively poor spectral resolutions ( $R < 400$ ).

# References

- [1] Abramowicz, M. A., Czerny, B., Lasota, J. P., and Szuszkiewicz, E. (1988). Slim Accretion Disks. *ApJ*, 332:646.
- [2] Abt, H. A. and Levy, S. G. (1976). Multiplicity among solar-type stars. *ApJS*, 30:273–306.
- [3] Agrawal, V. K. and Misra, R. (2006). The Unusual Spectrum of the Ultraluminous X-Ray Source M82 X-1. *ApJ*, 638(2):L83–L86.
- [4] Aird, J., Coil, A. L., and Georgakakis, A. (2018). X-rays across the galaxy population - II. The distribution of AGN accretion rates as a function of stellar mass and redshift. *MNRAS*, 474:1225–1249.
- [5] Alam, S., Albareti, F. D., Allende Prieto, C., Anders, F., Anderson, S. F., Anderton, T., Andrews, B. H., Armengaud, E., Aubourg, É., Bailey, S., Basu, S., Bautista, J. E., Beaton, R. L., Beers, T. C., Bender, C. F., Berlind, A. A., Beutler, F., Bhardwaj, V., Bird, J. C., Bizyaev, D., Blake, C. H., Blanton, M. R., Blomqvist, M., Bochanski, J. J., Bolton, A. S., Bovy, J., Shelden Bradley, A., Brandt, W. N., Brauer, D. E., Brinkmann, J., Brown, P. J., Brownstein, J. R., Burden, A., Burtin, E., Busca, N. G., Cai, Z., Capozzi, D., Carnero Rosell, A., Carr, M. A., Carrera, R., Chambers, K. C., Chaplin, W. J., Chen, Y.-C., Chiappini, C., Chojnowski, S. D., Chuang, C.-H., Clerc, N., Comparat, J., Covey, K., Croft, R. A. C., Cuesta, A. J., Cunha, K., da Costa, L. N., Da Rio, N., Davenport, J. R. A., Dawson, K. S., De Lee, N., Delubac, T., Deshpande, R., Dhital, S., Dutra-Ferreira, L., Dwelly, T., Ealet, A., Ebelke, G. L., Edmondson, E. M., Eisenstein, D. J., Ellsworth, T., Elsworth, Y., Epstein, C. R., Eracleous, M., Escoffier, S., Esposito, M., Evans, M. L., Fan, X., Fernández-Alvar, E., Feuillet, D., Filiz Ak, N., Finley, H., Finoguenov, A., Flaherty, K., Fleming, S. W., Font-Ribera, A., Foster, J., Frinchaboy, P. M., Galbraith-Frew, J. G., García, R. A., García-Hernández, D. A., García Pérez, A. E., Gaulme, P., Ge, J., Génova-Santos, R., Georgakakis, A., Ghezzi, L., Gillespie, B. A., Girardi, L., Goddard, D., Gontcho, S. G. A., González Hernández, J. I., Grebel, E. K., Green, P. J., Grieb, J. N., Grieves, N., Gunn, J. E., Guo, H., Harding, P., Hasselquist, S., Hawley, S. L., Hayden, M., Hearty, F. R., Hekker, S., Ho, S., Hogg, D. W., Holley-Bockelmann, K., Holtzman, J. A., Honscheid, K., Huber, D., Huehnerhoff, J., Ivans, I. I., Jiang, L., Johnson, J. A., Kinemuchi, K., Kirkby, D., Kitaura, F., Klaene, M. A., Knapp, G. R., Kneib, J.-P., Koenig, X. P., Lam, C. R., Lan, T.-W., Lang, D., Laurent, P., Le Goff, J.-M., Leauthaud, A., Lee, K.-G., Lee, Y. S., Licquia, T. C., Liu, J., Long, D. C., López-Corredoira, M., Lorenzo-Oliveira, D., Lucatello, S., Lundgren, B., Lupton, R. H., Mack, Claude E., I., Mahadevan, S., Maia, M. A. G.,

- Majewski, S. R., Malanushenko, E., Malanushenko, V., Manchado, A., Manera, M., Mao, Q., Maraston, C., Marchwinski, R. C., Margala, D., Martell, S. L., Martig, M., Masters, K. L., Mathur, S., McBride, C. K., McGehee, P. M., McGreer, I. D., McMahon, R. G., Ménard, B., Menzel, M.-L., Merloni, A., Mészáros, S., Miller, A. A., Miralda-Escudé, J., Miyatake, H., Montero-Dorta, A. D., More, S., Morganson, E., Morice-Atkinson, X., Morrison, H. L., Mosser, B., Muna, D., Myers, A. D., Nandra, K., Newman, J. A., Neyrinck, M., Nguyen, D. C., Nichol, R. C., Nidever, D. L., Noterdaeme, P., Nuza, S. E., O’Connell, J. E., O’Connell, R. W., O’Connell, R., Ogando, R. L. C., Olmstead, M. D., Oravetz, A. E., Oravetz, D. J., Osumi, K., Owen, R., Padgett, D. L., Padmanabhan, N., Paegert, M., Palanque-Delabrouille, N., Pan, K., Parejko, J. K., Pâris, I., Park, C., Pattarakijwanich, P., Pellejero-Ibanez, M., Pepper, J., Percival, W. J., Pérez-Fournon, I., Prez-Ra’fols, I., Petitjean, P., Pieri, M. M., Pinsonneault, M. H., Porto de Mello, G. F., Prada, F., Prakash, A., Price-Whelan, A. M., Protopapas, P., Raddick, M. J., Rahman, M., Reid, B. A., Rich, J., Rix, H.-W., Robin, A. C., Rockosi, C. M., Rodrigues, T. S., Rodríguez-Torres, S., Roe, N. A., Ross, A. J., Ross, N. P., Rossi, G., Ruan, J. J., Rubiño-Martín, J. A., Rykoff, E. S., Salazar-Albornoz, S., Salvato, M., Samushia, L., Sánchez, A. G., Santiago, B., Sayres, C., Schiavon, R. P., Schlegel, D. J., Schmidt, S. J., Schneider, D. P., Schultheis, M., Schwobe, A. D., Scóccola, C. G., Scott, C., Sellgren, K., Seo, H.-J., Serenelli, A., Shane, N., Shen, Y., Shetrone, M., Shu, Y., Silva Aguirre, V., Sivarani, T., Skrutskie, M. F., Slosar, A., Smith, V. V., Sobreira, F., Souto, D., Stassun, K. G., Steinmetz, M., Stello, D., Strauss, M. A., Streblyanska, A., Suzuki, N., Swanson, M. E. C., Tan, J. C., Tayar, J., Terrien, R. C., Thakar, A. R., Thomas, D., Thomas, N., Thompson, B. A., Tinker, J. L., Tojeiro, R., Troup, N. W., Vargas-Magaña, M., Vazquez, J. A., Verde, L., Viel, M., Vogt, N. P., Wake, D. A., Wang, J., Weaver, B. A., Weinberg, D. H., Weiner, B. J., White, M., Wilson, J. C., Wisniewski, J. P (2015). The Eleventh and Twelfth Data Releases of the Sloan Digital Sky Survey: Final Data from SDSS-III. *ApJS*, 219(1):12.
- [6] Antonucci, R. (1993). Unified models for active galactic nuclei and quasars. *ARA&A*, 31:473–521.
- [7] Arnaud, K. A. (1996). XSPEC: The First Ten Years. In Jacoby, G. H. and Barnes, J., editors, *Astronomical Data Analysis Software and Systems V*, volume 101 of *Astronomical Society of the Pacific Conference Series*, page 17.
- [8] Arnaud, K. A., Branduardi-Raymont, G., Culhane, J. L., Fabian, A. C., Hazard, C., McGlynn, T. A., Shafer, R. A., Tennant, A. F., and Ward, M. J. (1985). EXOSAT observations of a strong soft X-ray excess in MKN 841. *MNRAS*, 217:105–113.
- [9] Asami, F., Enoto, T., Iwakiri, W., Yamada, S., Tamagawa, T., Mihara, T., and Nagase, F. (2014). Broad-band spectroscopy of Hercules X-1 with Suzaku. *PASJ*, 66:44.
- [10] Aschenbach, B., Briel, U. G., Haberl, F., Braeuninger, H. W., Burkert, W., Oppitz, A., Gondoin, P., and Lumb, D. H. (2000). *Imaging performance of the XMM-Newton x-ray telescopes*, volume 4012 of *Society of Photo-Optical Instrumentation Engineers (SPIE) Conference Series*, pages 731–739.

- [11] Bañados, E., Venemans, B. P., Mazzucchelli, C., Farina, E. P., Walter, F., Wang, F., Decarli, R., Stern, D., Fan, X., Davies, F. B., Hennawi, J. F., Simcoe, R. A., Turner, M. L., Rix, H.-W., Yang, J., Kelson, D. D., Rudie, G. C., and Winters, J. M. (2018). An 800-million-solar-mass black hole in a significantly neutral Universe at a redshift of 7.5. *Nature*, 553(7689):473–476.
- [12] Bachetti, M., Harrison, F. A., Walton, D. J., Grefenstette, B. W., Chakrabarty, D., Fürst, F., Barret, D., Beloborodov, A., Boggs, S. E., Christensen, F. E., Craig, W. W., Fabian, A. C., Hailey, C. J., Hornschemeier, A., Kaspi, V., Kulkarni, S. R., Maccarone, T., Miller, J. M., Rana, V., Stern, D., Tendulkar, S. P., Tomsick, J., Webb, N. A., and Zhang, W. W. (2014). An ultraluminous X-ray source powered by an accreting neutron star. *Nature*, 514:202–204.
- [13] Bachetti, M., Rana, V., Walton, D. J., Barret, D., Harrison, F. A., Boggs, S. E., Christensen, F. E., Craig, W. W., Fabian, A. C., Fürst, F., Grefenstette, B. W., Hailey, C. J., Hornschemeier, A., Madsen, K. K., Miller, J. M., Ptak, A. F., Stern, D., Webb, N. A., and Zhang, W. W. (2013). The Ultraluminous X-Ray Sources NGC 1313 X-1 and X-2: A Broadband Study with NuSTAR and XMM-Newton. *ApJ*, 778:163.
- [14] Bahcall, J. N. and Bahcall, N. A. (1972). The Period and Light Curve of HZ Herculis. *ApJ*, 178:L1.
- [15] Balbus, S. A. and Hawley, J. F. (1991). A Powerful Local Shear Instability in Weakly Magnetized Disks. I. Linear Analysis. *ApJ*, 376:214.
- [16] Balbus, S. A. and Hawley, J. F. (1998). Instability, turbulence, and enhanced transport in accretion disks. *Reviews of Modern Physics*, 70(1):1–53.
- [17] Baldry, I. K., Glazebrook, K., Brinkmann, J., Ivezić, Ž., Lupton, R. H., Nichol, R. C., and Szalay, A. S. (2004). Quantifying the Bimodal Color-Magnitude Distribution of Galaxies. *ApJ*, 600(2):681–694.
- [18] Ballantyne, D. R. (2020). Examining the physical conditions of a warm corona in active galactic nuclei accretion discs. *MNRAS*, 491(3):3553–3561.
- [19] Bardeen, J. M., Press, W. H., and Teukolsky, S. A. (1972). Rotating Black Holes: Locally Nonrotating Frames, Energy Extraction, and Scalar Synchrotron Radiation. *ApJ*, 178:347–370.
- [20] Barret, D., Lam Trong, T., den Herder, J.-W., Piro, L., Cappi, M., Houvelin, J., Kelley, R., Mas-Hesse, J. M., Mitsuda, K., Paltani, S., Rauw, G., Rozanska, A., Wilms, J., Bandler, S., Barbera, M., Barcons, X., Bozzo, E., Ceballos, M. T., Charles, I., Costantini, E., Decourchelle, A., den Hartog, R., Duband, L., Duval, J.-M., Fiore, F., Gatti, F., Goldwurm, A., Jackson, B., Jonker, P., Kilbourne, C., Macculi, C., Mendez, M., Molendi, S., Orleanski, P., Pajot, F., Pointecouteau, E., Porter, F., Pratt, G. W., Prêle, D., Ravera, L., Sato, K., Schaye, J., Shinozaki, K., Thibert, T., Valenziano, L., Valette, V., Vink, J., Webb, N., Wise, M., Yamasaki, N., Douchin, F., Mesnager, J.-M., Pontet, B., Pradines, A., Branduardi-Raymont, G., Bulbul, E., Dadina, M., Etti, S., Finoguenov, A., Fukazawa, Y., Janiuk, A.,

- Kaastra, J., Mazzotta, P., Miller, J., Miniutti, G., Naze, Y., Nicastro, F., Scioritino, S., Simionescu, A., Torrejon, J. M., Frezouls, B., Geoffray, H., Peille, P., Aicardi, C., André, J., Daniel, C., Clénet, A., Etcheverry, C., Gloaguen, E., Hervet, G., Jolly, A., Ledot, A., Paillet, I., Schmitter, R., Vella, B., Damery, J.-C., Boyce, K., Dipirro, M., Lotti, S., Schwander, D., Smith, S., Van Leeuwen, B.-J., van Weers, H., Clerc, N., Cobo, B., Dauser, T., Kirsch, C., Cucchetti, E., Eckart, M., Ferrando, P., and Natalucci, L. (2018). The ATHENA X-ray Integral Field Unit (X-IFU). In *Proc. SPIE*, volume 10699 of *Society of Photo-Optical Instrumentation Engineers (SPIE) Conference Series*, page 106991G.
- [21] Begelman, M. C., McKee, C. F., and Shields, G. A. (1983). Compton heated winds and coronae above accretion disks. I Dynamics. *ApJ*, 271:70–88.
- [22] Begelman, M. C., Sarazin, C. L., Hatchett, S. P., McKee, C. F., and Arons, J. (1980). Beam models for SS 433. *ApJ*, 238:722–730.
- [23] Begelman, M. C., Volonteri, M., and Rees, M. J. (2006). Formation of supermassive black holes by direct collapse in pre-galactic haloes. *MNRAS*, 370(1):289–298.
- [24] Bell, E. F., McIntosh, D. H., Katz, N., and Weinberg, M. D. (2003). The Optical and Near-Infrared Properties of Galaxies. I. Luminosity and Stellar Mass Functions. *ApJS*, 149(2):289–312.
- [25] Belloni, T., Migliari, S., and Fender, R. P. (2000). Disk mass accretion rate and infrared flares in GRS 1915+105. *A&A*, 358:L29–L32.
- [26] Benson, A. J., Bower, R. G., Frenk, C. S., Lacey, C. G., Baugh, C. M., and Cole, S. (2003). What Shapes the Luminosity Function of Galaxies? *ApJ*, 599(1):38–49.
- [27] Bildsten, L., Chakrabarty, D., Chiu, J., Finger, M. H., Koh, D. T., Nelson, R. W., Prince, T. A., Rubin, B. C., Scott, D. M., Stollberg, M., Vaughan, B. A., Wilson, C. A., and Wilson, R. B. (1997). Observations of Accreting Pulsars. *ApJS*, 113(2):367–408.
- [28] Binder, B., Williams, B. F., Kong, A. K. H., Gaetz, T. J., Plucinsky, P. P., Dalcanton, J. J., and Weisz, D. R. (2011). Chandra Detection of SN 2010da Four Months After Outburst: Evidence for a High-mass X-Ray Binary in NGC 300. *ApJ*, 739:L51.
- [29] Blandford, R. D. and Königl, A. (1979). Relativistic jets as compact radio sources. *ApJ*, 232:34–48.
- [30] Blandford, R. D. and Payne, D. G. (1982). Hydromagnetic flows from accretion discs and the production of radio jets. *MNRAS*, 199:883–903.
- [31] Blandford, R. D. and Znajek, R. L. (1977). Electromagnetic extraction of energy from Kerr black holes. *MNRAS*, 179:433–456.
- [32] Blustin, A. J. and Fabian, A. C. (2009). An accretion disc origin for the ‘X-ray broad-line region’ in 1H0707-495. *MNRAS*, 399:L169–L173.

- [33] Blustin, A. J., Page, M. J., Fuerst, S. V., Branduardi-Raymont, G., and Ashton, C. E. (2005). The nature and origin of Seyfert warm absorbers. *A&A*, 431:111–125.
- [34] Boissay-Malaquin, R., Danehkar, A., Marshall, H. L., and Nowak, M. A. (2019). Relativistic Components of the Ultra-fast Outflow in the Quasar PDS 456 from Chandra/HETGS, NuSTAR, and XMM-Newton Observations. *ApJ*, 873(1):29.
- [35] Boller, T., Brandt, W. N., and Fink, H. (1996). Soft X-ray properties of narrow-line Seyfert 1 galaxies. *A&A*, 305:53.
- [36] Boller, T., Fabian, A. C., Sunyaev, R., Trümper, J., Vaughan, S., Ballantyne, D. R., Brandt, W. N., Keil, R., and Iwasawa, K. (2002). XMM-Newton discovery of a sharp spectral feature at  $\sim 7$  keV in the narrow-line Seyfert 1 galaxy 1H 0707 - 49. *MNRAS*, 329:L1–L5.
- [37] Boroson, B., Kallman, T., and Vrtilik, S. D. (2001). Hot Outflowing Gas from the X-Ray Binary Hercules X-1. *ApJ*, 562:925–935.
- [38] Boroson, B. S., Vrtilik, S. D., Raymond, J. C., and Still, M. (2007). FUSE Observations of a Full Orbit of Hercules X-1: Signatures of Disk, Star, and Wind. *ApJ*, 667:1087–1110.
- [39] Bowler, R. A. A., Hewett, P. C., Allen, J. T., and Ferland, G. J. (2014). Line-driven radiative outflows in luminous quasars. *MNRAS*, 445(1):359–377.
- [40] Brandt, W. N. and Schulz, N. S. (2000). The Discovery of Broad P Cygni X-Ray Lines from Circinus X-1 with the Chandra High-Energy Transmission Grating Spectrometer. *ApJ*, 544(2):L123–L127.
- [41] Brusa, M., Bongiorno, A., Cresci, G., Perna, M., Marconi, A., Mainieri, V., Maiolino, R., Salvato, M., Lusso, E., Santini, P., Comastri, A., Fiore, F., Gilli, R., La Franca, F., Lanzuisi, G., Lutz, D., Merloni, A., Mignoli, M., Onori, F., Piconcelli, E., Rosario, D., Vignali, C., and Zamorani, G. (2015). X-shooter reveals powerful outflows in  $z \sim 1.5$  X-ray selected obscured quasi-stellar objects. *MNRAS*, 446(3):2394–2417.
- [42] Cackett, E. M., Miller, J. M., Ballantyne, D. R., Barret, D., Bhattacharyya, S., Boutelier, M., Miller, M. C., Strohmayer, T. E., and Wijnands, R. (2010). Relativistic Lines and Reflection from the Inner Accretion Disks Around Neutron Stars. *ApJ*, 720(1):205–225.
- [43] Carniani, S., Marconi, A., Maiolino, R., Balmaverde, B., Brusa, M., Cano-Díaz, M., Ciccone, C., Comastri, A., Cresci, G., Fiore, F., Feruglio, C., La Franca, F., Mainieri, V., Mannucci, F., Nagao, T., Netzer, H., Piconcelli, E., Risaliti, G., Schneider, R., and Shemmer, O. (2015). Ionised outflows in  $z \sim 2.4$  quasar host galaxies. *A&A*, 580:A102.
- [44] Carpano, S., Haberl, F., and Maitra, C. (2018a). Title: Detection of a 31.6 s pulse period for the supernova impostor SN 2010da in NGC 300, observed in ULX state. *The Astronomer's Telegram*, 11158.

- [45] Carpano, S., Haberl, F., Maitra, C., and Vasilopoulos, G. (2018b). Discovery of pulsations from NGC 300 ULX1 and its fast period evolution. *ArXiv e-prints*.
- [46] Casella, P., Ponti, G., Patruno, A., Belloni, T., Miniutti, G., and Zampieri, L. (2008). Weighing the black holes in ultraluminous X-ray sources through timing. *MNRAS*, 387(4):1707–1711.
- [47] Cash, W. (1979). Parameter estimation in astronomy through application of the likelihood ratio. *ApJ*, 228:939–947.
- [48] Castor, J. I., Abbott, D. C., and Klein, R. I. (1975). Radiation-driven winds in Of stars. *ApJ*, 195:157–174.
- [49] Chandrasekhar, S. (1931). The Maximum Mass of Ideal White Dwarfs. *ApJ*, 74:81.
- [50] Chartas, G., Brandt, W. N., and Gallagher, S. C. (2003). XMM-Newton Reveals the Quasar Outflow in PG 1115+080. *ApJ*, 595(1):85–93.
- [51] Chartas, G., Brandt, W. N., Gallagher, S. C., and Garmire, G. P. (2002). CHANDRA Detects Relativistic Broad Absorption Lines from APM 08279+5255. *ApJ*, 579(1):169–175.
- [52] Chartas, G., Saez, C., Brandt, W. N., Giustini, M., and Garmire, G. P. (2009). Confirmation of and Variable Energy Injection by a Near-Relativistic Outflow in APM 08279+5255. *ApJ*, 706(1):644–656.
- [53] Cheng, F. H., Vrtilik, S. D., and Raymond, J. C. (1995). An Archival Study of Hubble Space Telescope Observations of Hercules X-1/HZ Herculis. *ApJ*, 452:825.
- [54] Churazov, E., Gilfanov, M., and Revnivtsev, M. (2001). Soft state of Cygnus X-1: stable disc and unstable corona. *MNRAS*, 321(4):759–766.
- [55] Cicone, C., Maiolino, R., Sturm, E., Graciá-Carpio, J., Feruglio, C., Neri, R., Aalto, S., Davies, R., Fiore, F., Fischer, J., García-Burillo, S., González-Alfonso, E., Hailey-Dunsheath, S., Piconcelli, E., and Veilleux, S. (2014). Massive molecular outflows and evidence for AGN feedback from CO observations. *A&A*, 562:A21.
- [56] Corbel, S., Kaaret, P., Jain, R. K., Bailyn, C. D., Fender, R. P., Tomsick, J. A., Kalemci, E., McIntyre, V., Campbell-Wilson, D., Miller, J. M., and McCollough, M. L. (2001). X-Ray States and Radio Emission in the Black Hole Candidate XTE J1550-564. *ApJ*, 554(1):43–48.
- [57] Costa, T., Sijacki, D., and Haehnelt, M. G. (2014). Feedback from active galactic nuclei: energy- versus momentum-driving. *MNRAS*, 444(3):2355–2376.
- [58] Crenshaw, D. M., Kraemer, S. B., and George, I. M. (2003). Mass Loss from the Nuclei of Active Galaxies. *ARA&A*, 41:117–167.
- [59] Croton, D. J., Springel, V., White, S. D. M., De Lucia, G., Frenk, C. S., Gao, L., Jenkins, A., Kauffmann, G., Navarro, J. F., and Yoshida, N. (2006). The many lives of active galactic nuclei: cooling flows, black holes and the luminosities and colours of galaxies. *MNRAS*, 365(1):11–28.

- [60] Crummy, J., Fabian, A. C., Gallo, L., and Ross, R. R. (2006). An explanation for the soft X-ray excess in active galactic nuclei. *MNRAS*, 365(4):1067–1081.
- [61] Cseh, D., Corbel, S., Kaaret, P., Lang, C., Grisé, F., Paragi, Z., Tzioumis, A., Tudose, V., and Feng, H. (2012). Black Hole Powered Nebulae and a Case Study of the Ultraluminous X-Ray Source IC 342 X-1. *ApJ*, 749:17.
- [62] dal Fiume, D., Orlandini, M., Cusumano, G., del Sordo, S., Feroci, M., Frontera, F., Oosterbroek, T., Palazzi, E., Parmar, A. N., Santangelo, A., and Segreto, A. (1998). The broad-band (0.1-200 keV) spectrum of HER X-1 observed with BeppoSAX. *A&A*, 329:L41–L44.
- [63] Dauser, T., Svoboda, J., Schartel, N., Wilms, J., Dovčiak, M., Ehle, M., Karas, V., Santos-Lleó, M., and Marshall, H. L. (2012). Spectral analysis of 1H 0707-495 with XMM-Newton. *MNRAS*, 422:1914–1921.
- [64] Davidson, K. (1973). Accretion at a Magnetic Pole of a Neutron Star. *Nature Physical Science*, 246(149):1–4.
- [65] Davidson, K. and Ostriker, J. P. (1973). Neutron-Star Accretion in a Stellar Wind: Model for a Pulsed X-Ray Source. *ApJ*, 179:585–598.
- [66] Davis, S. W., Narayan, R., Zhu, Y., Barret, D., Farrell, S. A., Godet, O., Servillat, M., and Webb, N. A. (2011). The Cool Accretion Disk in ESO 243-49 HLX-1: Further Evidence of an Intermediate-mass Black Hole. *ApJ*, 734(2):111.
- [67] de Kool, M. and Begelman, M. C. (1995). Radiation Pressure-driven Magnetic Disk Winds in Broad Absorption Line Quasi-stellar Objects. *ApJ*, 455:448.
- [68] De Marco, B., Ponti, G., Miniutti, G., Belloni, T., Cappi, M., Dadina, M., and Muñoz-Darias, T. (2013). Time lags in the ultraluminous X-ray source NGC 5408 X-1: implications for the black hole mass. *MNRAS*, 436(4):3782–3791.
- [69] de Plaa, J., Werner, N., Bleeker, J. A. M., Vink, J., Kaastra, J. S., and Méndez, M. (2007). Constraining supernova models using the hot gas in clusters of galaxies. *A&A*, 465:345–355.
- [70] Deeter, J. E., Boynton, P. E., and Pravdo, S. H. (1981). Pulse-timing observations of Hercules X-1. *ApJ*, 247:1003–1012.
- [71] Dekel, A. and Birnboim, Y. (2006). Galaxy bimodality due to cold flows and shock heating. *MNRAS*, 368(1):2–20.
- [72] den Herder, J. W., Brinkman, A. C., Kahn, S. M., Branduardi-Raymont, G., Thomsen, K., Aarts, H., Audard, M., Bixler, J. V., den Boggende, A. J., Cottam, J., Decker, T., Dubbeldam, L., Erd, C., Goulooze, H., Güdel, M., Guttridge, P., Hailey, C. J., Janabi, K. A., Kaastra, J. S., de Korte, P. A. J., van Leeuwen, B. J., Mauche, C., McCalden, A. J., Mewe, R., Naber, A., Paerels, F. B., Peterson, J. R., Rasmussen, A. P., Rees, K., Sakelliou, I., Sako, M., Spodek, J., Stern, M., Tamura, T., Tandy, J., de Vries, C. P., Welch, S., and Zehnder, A. (2001). The Reflection Grating Spectrometer on board XMM-Newton. *A&A*, 365:L7–L17.

- [73] Detmers, R. G., Kaastra, J. S., Steenbrugge, K. C., Ebrero, J., Kriss, G. A., Arav, N., Behar, E., Costantini, E., Branduardi-Raymont, G., Mehdipour, M., Bianchi, S., Cappi, M., Petrucci, P., Ponti, G., Pinto, C., Ratti, E. M., and Holczer, T. (2011). Multiwavelength campaign on Mrk 509. III. The 600 ks RGS spectrum: unravelling the inner region of an AGN. *A&A*, 534:A38.
- [74] Dewangan, G. C., Griffiths, R. E., and Rao, A. R. (2006a). Quasi-periodic Oscillations and Strongly Comptonized X-Ray Emission from Holmberg IX X-1. *ApJ*, 641(2):L125–L128.
- [75] Dewangan, G. C., Jithesh, V., Misra, R., and Ravikumar, C. D. (2013). X-Ray Spectral Cutoff and the Lack of Hard X-Ray Emission from Two Ultraluminous X-Ray Sources M81 X-6 and Holmberg IX X-1. *ApJ*, 771(2):L37.
- [76] Dewangan, G. C., Titarchuk, L., and Griffiths, R. E. (2006b). Black Hole Mass of the Ultraluminous X-Ray Source M82 X-1. *ApJ*, 637(1):L21–L24.
- [77] Di Matteo, T., Springel, V., and Hernquist, L. (2005). Energy input from quasars regulates the growth and activity of black holes and their host galaxies. *Nature*, 433(7026):604–607.
- [78] Díaz Trigo, M. and Boirin, L. (2016). Accretion disc atmospheres and winds in low-mass X-ray binaries. *Astronomische Nachrichten*, 337(4-5):368.
- [79] Díaz Trigo, M., Sidoli, L., Boirin, L., and Parmar, A. N. (2012). XMM-Newton observations of GX 13 + 1: correlation between photoionised absorption and broad line emission. *A&A*, 543:A50.
- [80] Donati, J.-F., Jardine, M. M., Gregory, S. G., Petit, P., Bouvier, J., Dougados, C., Ménard, F., Collier Cameron, A., Harries, T. J., Jeffers, S. V., and Paletou, F. (2007). Magnetic fields and accretion flows on the classical T Tauri star V2129 Oph. *MNRAS*, 380:1297–1312.
- [81] Done, C., Davis, S. W., Jin, C., Blaes, O., and Ward, M. (2012). Intrinsic disc emission and the soft X-ray excess in active galactic nuclei. *MNRAS*, 420(3):1848–1860.
- [82] Done, C., Gierliński, M., and Kubota, A. (2007a). Modelling the behaviour of accretion flows in X-ray binaries. Everything you always wanted to know about accretion but were afraid to ask. *A&ARv*, 15(1):1–66.
- [83] Done, C. and Jin, C. (2016). The mass and spin of the extreme Narrow Line Seyfert 1 Galaxy 1H 0707-495 and its implications for the trigger for relativistic jets. *MNRAS*, 460(2):1716–1724.
- [84] Done, C. and Kubota, A. (2006). Disc-corona energetics in the very high state of Galactic black holes. *MNRAS*, 371(3):1216–1230.
- [85] Done, C., Sobolewska, M. A., Gierliński, M., and Schurch, N. J. (2007b). The iron K feature in narrow line Seyfert 1 galaxies: evidence for a P Cygni profile? *MNRAS*, 374:L15–L19.

- [86] Dubus, G., Long, K. S., and Charles, P. A. (1999). The Compact UV Nucleus of M33. *ApJ*, 519(2):L135–L138.
- [87] Duquennoy, A. and Mayor, M. (1991). Multiplicity among solar-type stars in the solar neighbourhood. II - Distribution of the orbital elements in an unbiased sample. *A&A*, 500:337–376.
- [88] Eddington, A. S. (1926). *The Internal Constitution of the Stars*.
- [89] Eggleton, P. P. (1983). Approximations to the radii of Roche lobes. *ApJ*, 268:368–369.
- [90] Einstein, A. (1916). Die Grundlage der allgemeinen Relativitätstheorie. *Annalen der Physik*, 354(7):769–822.
- [91] Eksi, K. Y., Andac, I. C., Cikintoglu, S., Gencali, A. A., Gungor, C., and Oztekin, F. (2015). The ultraluminous X-ray source NuSTAR J095551+6940.8: a magnetar in a high-mass X-ray binary. *MNRAS*, 448:L40–L42.
- [92] Elias-Rosa, N., Mauerhan, J. C., and van Dyk, S. D. (2010). SN 2010da is a SN “impostor“. *The Astronomer’s Telegram*, 2636.
- [93] Elitzur, M. and Shlosman, I. (2006). The AGN-obscuring Torus: The End of the “Doughnut” Paradigm? *ApJ*, 648(2):L101–L104.
- [94] Endo, T., Nagase, F., and Mihara, T. (2000). Pulse-Phase Resolved Spectroscopy of Hercules X-1 with ASCA. *PASJ*, 52:223.
- [95] Esin, A. A., McClintock, J. E., and Narayan, R. (1997). Advection-Dominated Accretion and the Spectral States of Black Hole X-Ray Binaries: Application to Nova Muscae 1991. *ApJ*, 489(2):865–889.
- [96] Fabbiano, G. (1988). The X-Ray Emission of M81 and Its Nucleus. *ApJ*, 325:544.
- [97] Fabian, A. C. (2012). Observational Evidence of Active Galactic Nuclei Feedback. *ARA&A*, 50:455–489.
- [98] Fabian, A. C., Ballantyne, D. R., Merloni, A., Vaughan, S., Iwasawa, K., and Boller, T. (2002). How the X-ray spectrum of a narrow-line Seyfert 1 galaxy may be reflection-dominated. *MNRAS*, 331:L35–L39.
- [99] Fabian, A. C., Lohfink, A., Kara, E., Parker, M. L., Vasudevan, R., and Reynolds, C. S. (2015). Properties of AGN coronae in the NuSTAR era. *MNRAS*, 451(4):4375–4383.
- [100] Fabian, A. C., Pringle, J., and Rees, M. (1973). Long-term Behaviour of Hercules X-1. *Nature*, 244:212–213.
- [101] Fabian, A. C., Rees, M. J., Stella, L., and White, N. E. (1989). X-ray fluorescence from the inner disc in Cygnus X-1. *MNRAS*, 238:729–736.

- [102] Fabian, A. C., Reynolds, C. S., Jiang, J., Pinto, C., Gallo, L. C., Parker, M. L., Lasenby, A. N., Alston, W. N., Buisson, D. J. K., Cackett, E. M., De Marco, B., Garcia, J., Kara, E., Kosec, P., Middleton, M. J., Miller, J. M., Miniutti, G., Walton, D. J., Wilkins, D. R., and Young, A. J. (2020). Blueshifted absorption lines from X-ray reflection in IRAS 13224-3809. *MNRAS*.
- [103] Fabian, A. C., Sanders, J. S., Allen, S. W., Crawford, C. S., Iwasawa, K., Johnstone, R. M., Schmidt, R. W., and Taylor, G. B. (2003). A deep Chandra observation of the Perseus cluster: shocks and ripples. *MNRAS*, 344(3):L43–L47.
- [104] Fabian, A. C., Zoghbi, A., Ross, R. R., Uttley, P., Gallo, L. C., Brandt, W. N., Blustin, A. J., Boller, T., Caballero-Garcia, M. D., Larsson, J., Miller, J. M., Miniutti, G., Ponti, G., Reis, R. C., Reynolds, C. S., Tanaka, Y., and Young, A. J. (2009). Broad line emission from iron K- and L-shell transitions in the active galaxy 1H0707-495. *Nature*, 459:540–542.
- [105] Fabrika, S. (2004). The jets and supercritical accretion disk in SS433. *Astrophysics and Space Physics Reviews*, 12:1–152.
- [106] Fabrika, S., Ueda, Y., Vinokurov, A., Sholukhova, O., and Shidatsu, M. (2015). Supercritical accretion disks in ultraluminous X-ray sources and SS 433. *Nature Physics*, 11:551–553.
- [107] Farrell, S. A., Webb, N. A., Barret, D., Godet, O., and Rodrigues, J. M. (2009). An intermediate-mass black hole of over 500 solar masses in the galaxy ESO243-49. *Nature*, 460:73–75.
- [108] Fender, R. and Belloni, T. (2012). Stellar-Mass Black Holes and Ultraluminous X-ray Sources. *Science*, 337(6094):540.
- [109] Fender, R., Corbel, S., Tzioumis, T., McIntyre, V., Campbell-Wilson, D., Nowak, M., Sood, R., Hunstead, R., Harmon, A., Durouchoux, P., and Heindl, W. (1999). Quenching of the Radio Jet during the X-Ray High State of GX 339-4. *ApJ*, 519(2):L165–L168.
- [110] Feng, H., Rao, F., and Kaaret, P. (2010). Discovery of Millihertz X-Ray Oscillations in a Transient Ultraluminous X-Ray Source in M82. *ApJ*, 710(2):L137–L141.
- [111] Feng, H., Tao, L., Kaaret, P., and Grisé, F. (2016). Nature of the Soft ULX in NGC 247: Super-Eddington Outflow and Transition between the Supersoft and Soft Ultraluminous Regimes. *ApJ*, 831:117.
- [112] Ferrarese, L. and Ford, H. (2005). Supermassive Black Holes in Galactic Nuclei: Past, Present and Future Research. *Space Sci. Rev.*, 116(3-4):523–624.
- [113] Ferrarese, L. and Merritt, D. (2000). A Fundamental Relation between Supermassive Black Holes and Their Host Galaxies. *ApJ*, 539(1):L9–L12.
- [114] Ferreira, J., Petrucci, P. O., Henri, G., Saugé, L., and Pelletier, G. (2006). A unified accretion-ejection paradigm for black hole X-ray binaries. I. The dynamical constituents. *A&A*, 447(3):813–825.

- [115] Feruglio, C., Maiolino, R., Piconcelli, E., Menci, N., Aussel, H., Lamastra, A., and Fiore, F. (2010). Quasar feedback revealed by giant molecular outflows. *A&A*, 518:L155.
- [116] Fiacconi, D., Pinto, C., Walton, D. J., and Fabian, A. C. (2017). Constraining the mass of accreting black holes in ultraluminous X-ray sources with ultrafast outflows. *MNRAS*, 469:L99–L103.
- [117] Fluetsch, A., Maiolino, R., Carniani, S., Marconi, A., Cicone, C., Bourne, M. A., Costa, T., Fabian, A. C., Ishibashi, W., and Venturi, G. (2019). Cold molecular outflows in the local Universe and their feedback effect on galaxies. *MNRAS*, 483(4):4586–4614.
- [118] Foltz, C. B., Chaffee, F. H., Hewett, P. C., Weymann, R. J., and Morris, S. L. (1990). On the Fraction of Optically-Selected QSOs with Broad Absorption Lines in Their Spectra. In *BAAS*, volume 22, page 806.
- [119] Foltz, C. B., Weymann, R. J., Morris, S. L., and Turnshek, D. A. (1987). The Complex Absorption Spectrum of the Broad Absorption Line QSO 1303+308. *ApJ*, 317:450.
- [120] Fuerst, F., Grefenstette, B. W., Staubert, R., Tomsick, J. A., Bachetti, M., Barret, D., Bellm, E. C., Boggs, S. E., Chenevez, J., Christensen, F. E., Craig, W. W., Hailey, C. J., Harrison, F., Klochkov, D., Madsen, K. K., Pottschmidt, K., Stern, D., Walton, D. J., Wilms, J., and Zhang, W. (2013). The smooth cyclotron line in Her X-1 as seen with NuSTAR. *arXiv e-prints*, page arXiv:1309.5361.
- [121] Fukumura, K., Kazanas, D., Contopoulos, I., and Behar, E. (2010). Magnetohydrodynamic Accretion Disk Winds as X-ray Absorbers in Active Galactic Nuclei. *ApJ*, 715(1):636–650.
- [122] Fukumura, K., Kazanas, D., Shrader, C., Behar, E., Tombesi, F., and Contopoulos, I. (2017). Magnetic origin of black hole winds across the mass scale. *Nature Astronomy*, 1:0062.
- [123] Fukumura, K. and Tombesi, F. (2019). Constraining X-Ray Coronal Size with Transverse Motion of AGN Ultra-fast Outflows. *ApJ*, 885(2):L38.
- [124] Fukumura, K., Tombesi, F., Kazanas, D., Shrader, C., Behar, E., and Contopoulos, I. (2015). Magnetically Driven Accretion Disk Winds and Ultra-fast Outflows in PG 1211+143. *ApJ*, 805:17.
- [125] Fürst, F., Walton, D. J., Harrison, F. A., Stern, D., Barret, D., Brightman, M., Fabian, A. C., Grefenstette, B., Madsen, K. K., Middleton, M. J., Miller, J. M., Pottschmidt, K., Ptak, A., Rana, V., and Webb, N. (2016). Discovery of Coherent Pulsations from the Ultraluminous X-Ray Source NGC 7793 P13. *ApJ*, 831:L14.
- [126] Gallo, E., Fender, R. P., and Pooley, G. G. (2003). A universal radio-X-ray correlation in low/hard state black hole binaries. *MNRAS*, 344(1):60–72.
- [127] Gallo, L. C. and Fabian, A. C. (2013). The origin of blueshifted absorption features in the X-ray spectrum of PG 1211+143: outflow or disc. *MNRAS*, 434:L66–L69.

- [128] García, J., Dauser, T., Lohfink, A., Kallman, T. R., Steiner, J. F., McClintock, J. E., Brenneman, L., Wilms, J., Eikmann, W., Reynolds, C. S., and Tombesi, F. (2014). Improved Reflection Models of Black Hole Accretion Disks: Treating the Angular Distribution of X-Rays. *ApJ*, 782(2):76.
- [129] García, J. A., Fabian, A. C., Kallman, T. R., Dauser, T., Parker, M. L., McClintock, J. E., Steiner, J. F., and Wilms, J. (2016). The effects of high density on the X-ray spectrum reflected from accretion discs around black holes. *MNRAS*, 462(1):751–760.
- [130] Gebhardt, K., Bender, R., Bower, G., Dressler, A., Faber, S. M., Filippenko, A. V., Green, R., Grillmair, C., Ho, L. C., Kormendy, J., Lauer, T. R., Magorrian, J., Pinkney, J., Richstone, D., and Tremaine, S. (2000). A Relationship between Nuclear Black Hole Mass and Galaxy Velocity Dispersion. *ApJ*, 539(1):L13–L16.
- [131] Gebhardt, K., Lauer, T. R., Kormendy, J., Pinkney, J., Bower, G. A., Green, R., Gull, T., Hutchings, J. B., Kaiser, M. E., Nelson, C. H., Richstone, D., and Weistrop, D. (2001). M33: A Galaxy with No Supermassive Black Hole. *AJ*, 122(5):2469–2476.
- [132] George, I. M. and Fabian, A. C. (1991). X-ray reflection from cold matter in Active Galactic Nuclei and X-ray binaries. *MNRAS*, 249:352.
- [133] George, I. M., Turner, T. J., Netzer, H., Nandra, K., Mushotzky, R. F., and Yaqoob, T. (1998). ASCA Observations of Seyfert 1 Galaxies. III. The Evidence for Absorption and Emission Due to Photoionized Gas. *ApJS*, 114(1):73–120.
- [134] Gerend, D. and Boynton, P. E. (1976). Optical clues to the nature of Hercules X-1/HZ Herculis. *ApJ*, 209:562–573.
- [135] Ghosh, P. and Lamb, F. K. (1979). Accretion by rotating magnetic neutron stars. III - Accretion torques and period changes in pulsating X-ray sources. *ApJ*, 234:296–316.
- [136] Giacconi, R., Gursky, H., Kellogg, E., Levinson, R., Schreier, E., and Tananbaum, H. (1973). Further X-ray observations of Hercules X-1 from Uhuru. *ApJ*, 184:227–236.
- [137] Giacconi, R., Gursky, H., Kellogg, E., Schreier, E., and Tananbaum, H. (1971). Discovery of Periodic X-Ray Pulsations in Centaurus X-3 from UHURU. *ApJ*, 167:L67.
- [138] Giacconi, R., Murray, S., Gursky, H., Kellogg, E., Schreier, E., and Tananbaum, H. (1972). The Uhuru catalog of X-ray sources. *ApJ*, 178:281–308.
- [139] Gierliński, M., Zdziarski, A. A., Poutanen, J., Coppi, P. S., Ebisawa, K., and Johnson, W. N. (1999). Radiation mechanisms and geometry of Cygnus X-1 in the soft state. *MNRAS*, 309(2):496–512.
- [140] Gladstone, J. C., Roberts, T. P., and Done, C. (2009). The ultraluminous state. *MNRAS*, 397:1836–1851.

- [141] Granato, G. L. and Danese, L. (1994). Thick tori around active galactic nuclei: a comparison of model predictions with observations of the infrared continuum and silicate features. *MNRAS*, 268:235–252.
- [142] Grisé, F., Kaaret, P., Pakull, M. W., and Motch, C. (2011). Optical Properties of the Ultraluminous X-Ray Source Holmberg IX X-1 and Its Stellar Environment. *ApJ*, 734(1):23.
- [143] Grupe, D., Wills, B. J., Leighly, K. M., and Meusinger, H. (2004). A Complete Sample of Soft X-Ray-Selected AGNs. I. The Data. *AJ*, 127(1):156–179.
- [144] Gültekin, K., Richstone, D. O., Gebhardt, K., Lauer, T. R., Tremaine, S., Aller, M. C., Bender, R., Dressler, A., Faber, S. M., Filippenko, A. V., Green, R., Ho, L. C., Kormendy, J., Magorrian, J., Pinkney, J., and Siopis, C. (2009). The M- $\sigma$  and M-L Relations in Galactic Bulges, and Determinations of Their Intrinsic Scatter. *ApJ*, 698(1):198–221.
- [145] Hagino, K., Odaka, H., Done, C., Tomaru, R., Watanabe, S., and Takahashi, T. (2016). A disc wind interpretation of the strong Fe K $\alpha$  features in 1H 0707-495. *MNRAS*, 461:3954–3963.
- [146] Häring, N. and Rix, H.-W. (2004). On the Black Hole Mass-Bulge Mass Relation. *ApJ*, 604(2):L89–L92.
- [147] Harrison, C. M., Alexander, D. M., Mullaney, J. R., and Swinbank, A. M. (2014). Kiloparsec-scale outflows are prevalent among luminous AGN: outflows and feedback in the context of the overall AGN population. *MNRAS*, 441(4):3306–3347.
- [148] Harrison, F. A., Craig, W. W., Christensen, F. E., Hailey, C. J., Zhang, W. W., Boggs, S. E., Stern, D., Cook, W. R., Forster, K., Giommi, P., Grefenstette, B. W., Kim, Y., Kitaguchi, T., Koglin, J. E., Madsen, K. K., Mao, P. H., Miyasaka, H., Mori, K., Perri, M., Pivovarov, M. J., Puccetti, S., Rana, V. R., Westergaard, N. J., Willis, J., Zoglauer, A., An, H., Bachetti, M., Barrière, N. M., Bellm, E. C., Bhalerao, V., Brejnholt, N. F., Fuerst, F., Liebe, C. C., Markwardt, C. B., Nynka, M., Vogel, J. K., Walton, D. J., Wik, D. R., Alexander, D. M., Cominsky, L. R., Hornschemeier, A. E., Hornstrup, A., Kaspi, V. M., Madejski, G. M., Matt, G., Molendi, S., Smith, D. M., Tomsick, J. A., Ajello, M., Ballantyne, D. R., Baloković, M., Barret, D., Bauer, F. E., Blandford, R. D., Brandt, W. N., Brenneman, L. W., Chiang, J., Chakrabarty, D., Chenevez, J., Comastri, A., Dufour, F., Elvis, M., Fabian, A. C., Farrah, D., Fryer, C. L., Gotthelf, E. V., Grindlay, J. E., Helfand, D. J., Krivonos, R., Meier, D. L., Miller, J. M., Natalucci, L., Ogle, P., Ofek, E. O., Ptak, A., Reynolds, S. P., Rigby, J. R., Tagliaferri, G., Thorsett, S. E., Treister, E., and Urry, C. M. (2013). The Nuclear Spectroscopic Telescope Array (NuSTAR) High-energy X-Ray Mission. *ApJ*, 770:103.
- [149] Hasinger, G. and van der Klis, M. (1989). Two patterns of correlated X-ray timing and spectral behaviour in low-mass X-ray binaries. *A&A*, 225:79–96.
- [150] Heger, A., Fryer, C. L., Woosley, S. E., Langer, N., and Hartmann, D. H. (2003). How Massive Single Stars End Their Life. *ApJ*, 591(1):288–300.

- [151] Hickox, R. C., Narayan, R., and Kallman, T. R. (2004). Origin of the Soft Excess in X-Ray Pulsars. *ApJ*, 614:881–896.
- [152] Hitomi Collaboration, Aharonian, F., Akamatsu, H., Akimoto, F., Allen, S. W., Anabuki, N., Angelini, L., Arnaud, K., Audard, M., Awaki, H., Axelsson, M., Bamba, A., Bautz, M., Blandford, R., Brenneman, L., Brown, G. V., Bulbul, E., Cackett, E., Chernyakova, M., Chiao, M., Coppi, P., Costantini, E., de Plaa, J., den Herder, J.-W., Done, C., Dotani, T., Ebisawa, K., Eckart, M., Enoto, T., Ezoe, Y., Fabian, A. C., Ferrigno, C., Foster, A., Fujimoto, R., Fukazawa, Y., Furuzawa, A., Galeazzi, M., Gallo, L., Gandhi, P., Giustini, M., Goldwurm, A., Gu, L., Guainazzi, M., Haba, Y., Hagino, K., Hamaguchi, K., Harrus, I., Hatsukade, I., Hayashi, K., Hayashi, T., Hayashida, K., Hiraga, J., Hornschemeier, A., Hoshino, A., Hughes, J., Iizuka, R., Inoue, H., Inoue, Y., Ishibashi, K., Ishida, M., Ishikawa, K., Ishisaki, Y., Itoh, M., Iyomoto, N., Kaastra, J., Kallman, T., Kamae, T., Kara, E., Kataoka, J., Katsuda, S., Katsuta, J., Kawaharada, M., Kawai, N., Kelley, R., Khangulyan, D., Kilbourne, C., King, A., Kitaguchi, T., Kitamoto, S., Kitayama, T., Kohmura, T., Kokubun, M., Koyama, S., Koyama, K., Kretschmar, P., Krimm, H., Kubota, A., Kunieda, H., Laurent, P., Lebrun, F., Lee, S.-H., Leutenegger, M., Limousin, O., Loewenstein, M., Long, K. S., Lumb, D., Madejski, G., Maeda, Y., Maier, D., Makishima, K., Markevitch, M., Matsumoto, H., Matsushita, K., McCammon, D., McNamara, B., Mehdipour, M., Miller, E., Miller, J., Mineshige, S., Mitsuda, K., Mitsuishi, I., Miyazawa, T., Mizuno, T., Mori, H., Mori, K., Moseley, H., Mukai, K., Murakami, H., Murakami, T., Mushotzky, R., Nagino, R., Nakagawa, T., Nakajima, H., Nakamori, T., Nakano, T., Nakashima, S., Nakazawa, K., Nobukawa, M., Noda, H., Nomachi, M., O’Dell, S., Odaka, H., Ohashi, T., Ohno, M., Okajima, T., Ota, N., Ozaki, M., Paerels, F., Paltani, S., Parmar, A., Petre, R., Pinto, C., Pohl, M., Porter, F. S., Pottschmidt, K., Ramsey, B., Reynolds, C., Russell, H., Safi-Harb, S., Saito, S., Sakai, K., Sameshima, H., Sato, G., Sato, K., Sato, R., Sawada, M., Schartel, N., Serlemitsos, P., Seta, H., Shidatsu, M., Simionescu, A., Smith, R., Soong, Y., Stawarz, L., Sugawara, Y., Sugita, S., Szymkowiak, A., Tajima, H., Takahashi, H., Takahashi, T., Takeda, S., Takei, Y., Tamagawa, T., Tamura, K., Tamura, T., Tanaka, T., Tanaka, Y., Tanaka, Y., Tashiro, M., Tawara, Y., Terada, Y., Terashima, Y., Tombesi, F., Tomida, H., Tsuboi, Y., Tsujimoto, M., Tsunemi, H., Tsuru, T., Uchida, H., Uchiyama, H., Uchiyama, Y., Ueda, S., Ueda, Y., Ueno, S., Uno, S., Urry, M., Ursino, E., de Vries, C., Watanabe, S., Werner, N., Wik, D., Wilkins, D., Williams, B., Yamada, S., Yamaguchi, H., Yamaoka, K., Yamasaki, N. Y., Yamauchi, M., Yamauchi, S., Yaqoob, T., Yatsu, Y., Yonetoku, D., Yoshida, A., Yuasa, T., Zhuravleva, I., and Zoghbi, A. (2016). The quiescent intracluster medium in the core of the Perseus cluster. *Nature*, 535:117–121.
- [153] Hjellming, R. M. and Johnston, K. J. (1981). An analysis of the proper motions of SS 433 radio jets. *ApJ*, 246:L141–L145.
- [154] Ho, L. C. (2008). Nuclear activity in nearby galaxies. *ARA&A*, 46:475–539.
- [155] Holczer, T., Behar, E., and Kaspi, S. (2007). Absorption Measure Distribution of the Outflow in IRAS 13349+2438: Direct Observation of Thermal Instability? *ApJ*, 663(2):799–807.

- [156] Homan, J. and Belloni, T. (2005). The Evolution of Black Hole States. *Ap&SS*, 300(1-3):107–117.
- [157] Houck, J. C. and Denicola, L. A. (2000). *ISIS: An Interactive Spectral Interpretation System for High Resolution X-Ray Spectroscopy*, volume 216 of *Astronomical Society of the Pacific Conference Series*, page 591.
- [158] Hurley, J. R., Tout, C. A., and Pols, O. R. (2002). Evolution of binary stars and the effect of tides on binary populations. *MNRAS*, 329(4):897–928.
- [159] Hut, P. (1981). Tidal evolution in close binary systems. *A&A*, 99:126–140.
- [160] Iben, I., J. and Renzini, A. (1983). Asymptotic giant branch evolution and beyond. *ARA&A*, 21:271–342.
- [161] Inoue, H., Terashima, Y., and Ho, L. C. (2007). Fe K Line Profile in Low-Redshift Quasars: Average Shape and Eddington Ratio Dependence. *ApJ*, 662(2):860–871.
- [162] Ishibashi, W. and Fabian, A. C. (2015). AGN feedback: galactic-scale outflows driven by radiation pressure on dust. *MNRAS*, 451(1):93–102.
- [163] Ishibashi, W., Fabian, A. C., Ricci, C., and Celotti, A. (2018). Revisiting the ‘forbidden’ region: AGN radiative feedback with radiation trapping. *MNRAS*, 479(3):3335–3342.
- [164] Israel, G. L., Belfiore, A., Stella, L., Esposito, P., Casella, P., De Luca, A., Marelli, M., Papitto, A., Perri, M., Puccetti, S., Castillo, G. A. R., Salvetti, D., Tiengo, A., Zampieri, L., D’Agostino, D., Greiner, J., Haberl, F., Novara, G., Salvaterra, R., Turolla, R., Watson, M., Wilms, J., and Wolter, A. (2017). An accreting pulsar with extreme properties drives an ultraluminous x-ray source in NGC 5907. *Science*, 355:817–819.
- [165] Jaffe, W., Meisenheimer, K., Röttgering, H. J. A., Leinert, C., Richichi, A., Chesneau, O., Fraix-Burnet, D., Glazenberg-Kluttig, A., Granato, G. L., Graser, U., Heijligers, B., Köhler, R., Malbet, F., Miley, G. K., Paresce, F., Pel, J. W., Perrin, G., Przygodda, F., Schoeller, M., Sol, H., Waters, L. B. F. M., Weigelt, G., Woillez, J., and de Zeeuw, P. T. (2004). The central dusty torus in the active nucleus of NGC 1068. *Nature*, 429(6987):47–49.
- [166] Jansen, F., Lumb, D., Altieri, B., Clavel, J., Ehle, M., Erd, C., Gabriel, C., Guainazzi, M., Gondoin, P., Much, R., Munoz, R., Santos, M., Schartel, N., Texier, D., and Vacanti, G. (2001). XMM-Newton observatory. I. The spacecraft and operations. *A&A*, 365:L1–L6.
- [167] Ji, L., Schulz, N., Nowak, M., Marshall, H. L., and Kallman, T. (2009). The Photoionized Accretion Disk in Her X-1. *ApJ*, 700:977–988.
- [168] Jiang, J., Fabian, A. C., Wang, J., Walton, D. J., García, J. A., Parker, M. L., Steiner, J. F., and Tomsick, J. A. (2019). High-density reflection spectroscopy: I. A case study of GX 339-4. *MNRAS*, 484(2):1972–1982.

- [169] Jiang, J., Parker, M. L., Fabian, A. C., Alston, W. N., Buisson, D. J. K., Cackett, E. M., Chiang, C. Y., Dauser, T., Gallo, L. C., García, J. A., Harrison, F. A., Lohfink, A. M., De Marco, B., Kara, E., Miller, J. M., Miniutti, G., Pinto, C., Walton, D. J., and Wilkins, D. R. (2018). The 1.5 Ms observing campaign on IRAS 13224-3809 - I. X-ray spectral analysis. *MNRAS*, 477(3):3711–3726.
- [170] Jimenez-Garate, M. A., Hailey, C. J., den Herder, J. W., Zane, S., and Ramsay, G. (2002). High-Resolution X-Ray Spectroscopy of Hercules X-1 with the XMM-Newton Reflection Grating Spectrometer: CNO Element Abundance Measurements and Density Diagnostics of a Photoionized Plasma. *ApJ*, 578:391–404.
- [171] Jimenez-Garate, M. A., Raymond, J. C., Liedahl, D. A., and Hailey, C. J. (2005). Identification of an Extended Accretion Disk Corona in the Hercules X-1 Low State: Moderate Optical Depth, Precise Density Determination, and Verification of CNO Abundances. *ApJ*, 625:931–950.
- [172] Jin, C., Ward, M., Done, C., and Gelbord, J. (2012). A combined optical and X-ray study of unobscured type 1 active galactic nuclei - I. Optical spectra and spectral energy distribution modelling. *MNRAS*, 420:1825–1847.
- [173] Jones, M. L., Hickox, R. C., Black, C. S., Hainline, K. N., DiPompeo, M. A., and Goulding, A. D. (2016). The Intrinsic Eddington Ratio Distribution of Active Galactic Nuclei in Star-forming Galaxies from the Sloan Digital Sky Survey. *ApJ*, 826(1):12.
- [174] Kaaret, P., Feng, H., and Roberts, T. P. (2017). Ultraluminous X-Ray Sources. *ArXiv e-prints*.
- [175] Kaastra, J. S., Mewe, R., Liedahl, D. A., Komossa, S., and Brinkman, A. C. (2000). X-ray absorption lines in the Seyfert 1 galaxy NGC 5548 discovered with Chandra-LETGS. *A&A*, 354:L83–L86.
- [176] Kaastra, J. S., Mewe, R., Liedahl, D. A., Singh, K. P., White, N. E., and Drake, S. A. (1996a). Emission measure analysis methods: the corona of AR Lacertae revisited. *A&A*, 314:547–557.
- [177] Kaastra, J. S., Mewe, R., and Nieuwenhuijzen, H. (1996b). SPEX: a new code for spectral analysis of X & UV spectra. In Yamashita, K. and Watanabe, T., editors, *UV and X-ray Spectroscopy of Astrophysical and Laboratory Plasmas*, pages 411–414.
- [178] Kaastra, J. S., Werner, N., Herder, J. W. A. d., Paerels, F. B. S., de Plaa, J., Rasmussen, A. P., and de Vries, C. P. (2006). The O VII X-Ray Forest toward Markarian 421: Consistency between XMM-Newton and Chandra. *ApJ*, 652:189–197.
- [179] Kalberla, P. M. W., Burton, W. B., Hartmann, D., Arnal, E. M., Bajaja, E., Morras, R., and Pöppel, W. G. L. (2005). The Leiden/Argentine/Bonn (LAB) Survey of Galactic HI. Final data release of the combined LDS and IAR surveys with improved stray-radiation corrections. *A&A*, 440:775–782.
- [180] Kallman, T. R., Bautista, M. A., Goriely, S., Mendoza, C., Miller, J. M., Palmeri, P., Quinet, P., and Raymond, J. (2009). Spectrum Synthesis Modeling of the X-Ray Spectrum of GRO J1655-40 Taken During the 2005 Outburst. *ApJ*, 701(2):865–884.

- [181] Kara, E., Dai, L., Reynolds, C. S., and Kallman, T. (2018). Ultrafast outflow in tidal disruption event ASASSN-14li. *MNRAS*, 474(3):3593–3598.
- [182] Kara, E., Fabian, A. C., Cackett, E. M., Miniutti, G., and Uttley, P. (2013). Revealing the X-ray source in IRAS 13224-3809 through flux-dependent reverberation lags. *MNRAS*, 430:1408–1413.
- [183] Kaspi, S., Brandt, W. N., George, I. M., Netzer, H., Crenshaw, D. M., Gabel, J. R., Hamann, F. W., Kaiser, M. E., Koratkar, A., Kraemer, S. B., Kriss, G. A., Mathur, S., Mushotzky, R. F., Nandra, K., Peterson, B. M., Shields, J. C., Turner, T. J., and Zheng, W. (2002). The Ionized Gas and Nuclear Environment in NGC 3783. I. Time-averaged 900 Kilosecond Chandra Grating Spectroscopy. *ApJ*, 574(2):643–662.
- [184] Kauffmann, G., Heckman, T. M., White, S. D. M., Charlot, S., Tremonti, C., Peng, E. W., Seibert, M., Brinkmann, J., Nichol, R. C., SubbaRao, M., and York, D. (2003). The dependence of star formation history and internal structure on stellar mass for  $10^5$  low-redshift galaxies. *MNRAS*, 341(1):54–69.
- [185] Kawaguchi, T. (2003). Comptonization in Super-Eddington Accretion Flow and Growth Timescale of Supermassive Black Holes. *ApJ*, 593(1):69–84.
- [186] Kennea, J. A. (2018). NGC 300 ULX-1 / SN 2010da: Early Swift period measurement and modeling of spin-up. *The Astronomer’s Telegram*, 11229.
- [187] King, A. (2003). Black Holes, Galaxy Formation, and the  $M_{BH}-\sigma$  Relation. *ApJ*, 596(1):L27–L29.
- [188] King, A. and Pounds, K. (2015). Powerful Outflows and Feedback from Active Galactic Nuclei. *ARA&A*, 53:115–154.
- [189] King, A. R. (2009). Masses, beaming and Eddington ratios in ultraluminous X-ray sources. *MNRAS*, 393:L41–L44.
- [190] King, A. R. (2010). Black hole outflows. *MNRAS*, 402(3):1516–1522.
- [191] King, A. R., Davies, M. B., Ward, M. J., Fabbiano, G., and Elvis, M. (2001). Ultraluminous X-Ray Sources in External Galaxies. *ApJ*, 552:L109–L112.
- [192] Kobayashi, H., Ohsuga, K., Takahashi, H. R., Kawashima, T., Asahina, Y., Takeuchi, S., and Mineshige, S. (2018). Three-dimensional structure of clumpy outflow from supercritical accretion flow onto black holes. *ArXiv e-prints*.
- [193] Korista, K. T., Voit, G. M., Morris, S. L., and Weymann, R. J. (1993). Double Troughs in Broad Absorption Line Quasars and LY alpha –N V Line Locking. *ApJS*, 88:357.
- [194] Kormendy, J. and Ho, L. C. (2013). Coevolution (Or Not) of Supermassive Black Holes and Host Galaxies. *ARA&A*, 51(1):511–653.
- [195] Kormendy, J. and Richstone, D. (1995). Inward Bound—The Search For Supermassive Black Holes In Galactic Nuclei. *ARA&A*, 33:581.

- [196] Kosec, P., Buisson, D. J. K., Parker, M. L., Pinto, C., Fabian, A. C., and Walton, D. J. (2018a). A stratified ultrafast outflow in 1H0707-495? *MNRAS*, 481:947–953.
- [197] Kosec, P., Fabian, A. C., Pinto, C., Walton, D. J., Dyda, S., and Reynolds, C. S. (2020). An ionized accretion disc wind in Hercules X-1. *MNRAS*, 491(3):3730–3750.
- [198] Kosec, P., Pinto, C., Fabian, A. C., and Walton, D. J. (2018b). Searching for outflows in ultraluminous X-ray sources through high-resolution X-ray spectroscopy. *MNRAS*, 473:5680–5697.
- [199] Kosec, P., Pinto, C., Walton, D. J., Fabian, A. C., Bachetti, M., Brightman, M., Fürst, F., and Grefenstette, B. W. (2018c). Evidence for a variable Ultrafast Outflow in the newly discovered Ultraluminous Pulsar NGC 300 ULX-1. *MNRAS*, 479:3978–3986.
- [200] Kotani, T., Ebisawa, K., Dotani, T., Inoue, H., Nagase, F., Tanaka, Y., and Ueda, Y. (2000). ASCA Observations of the Absorption Line Features from the Superluminal Jet Source GRS 1915+105. *ApJ*, 539(1):413–423.
- [201] Kotze, M. M. and Charles, P. A. (2012). Characterizing X-ray binary long-term variability. *MNRAS*, 420(2):1575–1589.
- [202] Kouveliotou, C., Dieters, S., Strohmayer, T., van Paradijs, J., Fishman, G. J., Meegan, C. A., Hurley, K., Kommers, J., Smith, I., Frail, D., and Murakami, T. (1998). An X-ray pulsar with a superstrong magnetic field in the soft  $\gamma$ -ray repeater SGR1806 - 20. *Nature*, 393(6682):235–237.
- [203] Krimm, H. A., Holland, S. T., Corbet, R. H. D., Pearlman, A. B., Romano, P., Kennea, J. A., Bloom, J. S., Barthelmy, S. D., Baumgartner, W. H., Cummings, J. R., Gehrels, N., Lien, A. Y., Markwardt, C. B., Palmer, D. M., Sakamoto, T., Stamatikos, M., and Ukwatta, T. N. (2013). The Swift/BAT Hard X-Ray Transient Monitor. *ApJS*, 209(1):14.
- [204] Kriss, G. A., Lee, J. C., Danehkar, A., Nowak, M. A., Fang, T., Hardcastle, M. J., Neilsen, J., and Young, A. (2018). Discovery of an Ultraviolet Counterpart to an Ultrafast X-Ray Outflow in the Quasar PG 1211+143. *ApJ*, 853:166.
- [205] Krolik, J. H., McKee, C. F., and Tarter, C. B. (1981). Two-phase models of quasar emission line regions. *ApJ*, 249:422–442.
- [206] Lamb, F. K., Pethick, C. J., and Pines, D. (1973). A Model for Compact X-Ray Sources: Accretion by Rotating Magnetic Stars. *ApJ*, 184:271–290.
- [207] Lamers, H. J. G. L. M., Haser, S., de Koter, A., and Leitherer, C. (1999). The Ionization in the Winds of O Stars and the Determination of Mass-Loss Rates from Ultraviolet Lines. *ApJ*, 516(2):872–886.
- [208] Laor, A. (1991). Line Profiles from a Disk around a Rotating Black Hole. *ApJ*, 376:90.
- [209] Laor, A. and Netzer, H. (1989). Massive thin accretion discs. - I. Calculated spectra. *MNRAS*, 238:897–916.

- [210] Lau, R. M., Kasliwal, M. M., Bond, H. E., Smith, N., Fox, O. D., Carlon, R., Cody, A. M., Contreras, C., Dykhoff, D., Gehrz, R., Hsiao, E., Jencson, J., Khan, R., Masci, F., Monard, L. A. G., Monson, A. J., Morrell, N., Phillips, M., and Ressler, M. E. (2016). Rising from the Ashes: Mid-infrared Re-brightening of the Impostor SN 2010da in NGC 300. *ApJ*, 830:142.
- [211] Leahy, D. A. (2002). Modelling RXTE/ASM observations of the 35-d cycle in Her X-1. *MNRAS*, 334(4):847–854.
- [212] Leahy, D. A. and Abdallah, M. H. (2014). HZ Her: Stellar Radius from X-Ray Eclipse Observations, Evolutionary State, and a New Distance. *ApJ*, 793(2):79.
- [213] Leahy, D. A. and Chen, Y. (2019). AstroSat SXT Observations of Her X-1. *ApJ*, 871:152.
- [214] Leahy, D. A. and Igna, C. D. (2010). RXTE-based 35 Day Cycle Turn-on Times for Hercules X-1. *ApJ*, 713(1):318–324.
- [215] Lee, J. C., Ogle, P. M., Canizares, C. R., Marshall, H. L., Schulz, N. S., Morales, R., Fabian, A. C., and Iwasawa, K. (2001). Revealing the Dusty Warm Absorber in MCG -6-30-15 with the Chandra High-Energy Transmission Grating. *ApJ*, 554(1):L13–L17.
- [216] Leighly, K. M. (2004). Hubble Space Telescope STIS Ultraviolet Spectral Evidence of Outflow in Extreme Narrow-Line Seyfert 1 Galaxies. II. Modeling and Interpretation. *ApJ*, 611:125–152.
- [217] Leighly, K. M., Kay, L. E., Wills, B. J., Wills, D., and Grupe, D. (1997). The Optical Polarization and Warm Absorber in IRAS 17020+4544. *ApJ*, 489:L137.
- [218] Leighly, K. M. and Moore, J. R. (2004). Hubble Space Telescope STIS Ultraviolet Spectral Evidence of Outflow in Extreme Narrow-Line Seyfert 1 Galaxies. I. Data and Analysis. *ApJ*, 611:107–124.
- [219] Li, L.-X., Zimmerman, E. R., Narayan, R., and McClintock, J. E. (2005). Multi-temperature Blackbody Spectrum of a Thin Accretion Disk around a Kerr Black Hole: Model Computations and Comparison with Observations. *ApJS*, 157(2):335–370.
- [220] Lodders, K., Palme, H., and Gail, H.-P. (2009). Abundances of the Elements in the Solar System. *Landolt Börnstein*.
- [221] Long, K. S., Charles, P. A., Blair, W. P., and Gordon, S. M. (1996). A Deep X-Ray Image of M33. *ApJ*, 466:750.
- [222] Long, K. S., Dodorico, S., Charles, P. A., and Dopita, M. A. (1981). Observations of the X-ray sources in the nearby SC galaxy M 33. *ApJ*, 246:L61–L64.
- [223] Longinotti, A. L., Krongold, Y., Guainazzi, M., Giroletti, M., Panessa, F., Costantini, E., Santos-Lleo, M., and Rodriguez-Pascual, P. (2015). X-Ray High-resolution Spectroscopy Reveals Feedback in a Seyfert Galaxy from an Ultra-fast Wind with Complex Ionization and Velocity Structure. *ApJ*, 813(2):L39.

- [224] Lu, K.-X., Du, P., Hu, C., Li, Y.-R., Zhang, Z.-X., Wang, K., Huang, Y.-K., Bi, S.-L., Bai, J.-M., Ho, L. C., and Wang, J.-M. (2016). Reverberation Mapping of the Broad-line Region in NGC 5548: Evidence for Radiation Pressure? *ApJ*, 827(2):118.
- [225] Lynden-Bell, D. (1969). Galactic Nuclei as Collapsed Old Quasars. *Nature*, 223(5207):690–694.
- [226] Lynds, C. R. (1967). A Quasi-Stellar Source with a Rapidly Expanding Envelope. *ApJ*, 147:396.
- [227] Maccarone, T. J. and Coppi, P. S. (2003). Hysteresis in the light curves of soft X-ray transients. *MNRAS*, 338(1):189–196.
- [228] Madau, P., Haardt, F., and Dotti, M. (2014). Super-critical Growth of Massive Black Holes from Stellar-mass Seeds. *ApJ*, 784(2):L38.
- [229] Magdziarz, P. and Zdziarski, A. A. (1995). Angle-dependent Compton reflection of X-rays and gamma-rays. *MNRAS*, 273(3):837–848.
- [230] Maiolino, R., Gallerani, S., Neri, R., Cicone, C., Ferrara, A., Genzel, R., Lutz, D., Sturm, E., Tacconi, L. J., Walter, F., Feruglio, C., Fiore, F., and Piconcelli, E. (2012). Evidence of strong quasar feedback in the early Universe. *MNRAS*, 425(1):L66–L70.
- [231] Mao, J., Kaastra, J. S., Guainazzi, M., González-Riestra, R., Santos-Lleó, M., Kretschmar, P., Grinberg, V., Kalfountzou, E., Ibarra, A., Matzeu, G., Parker, M., and Rodríguez-Pascual, P. (2019). CIELO-RGS: a catalog of soft X-ray ionized emission lines. *A&A*, 625:A122.
- [232] Mapelli, M., Colpi, M., and Zampieri, L. (2009). Low metallicity and ultra-luminous X-ray sources in the Cartwheel galaxy. *MNRAS*, 395(1):L71–L75.
- [233] Margon, B. (1984). Observations of SS 433. *ARA&A*, 22:507–536.
- [234] Markoff, S., Nowak, M. A., and Wilms, J. (2005). Going with the Flow: Can the Base of Jets Subsume the Role of Compact Accretion Disk Coronae? *ApJ*, 635(2):1203–1216.
- [235] Marshall, H. L., Canizares, C. R., and Schulz, N. S. (2002). The High-Resolution X-Ray Spectrum of SS 433 Using the Chandra HETGS. *ApJ*, 564:941–952.
- [236] Mathur, S. (2000). Narrow-line Seyfert 1 galaxies and the evolution of galaxies and active galaxies. *MNRAS*, 314(4):L17–L20.
- [237] McClintock, J. E. and Remillard, R. A. (1986). The Black Hole Binary A0620-00. *ApJ*, 308:110.
- [238] McNamara, B. R., Nulsen, P. E. J., Wise, M. W., Rafferty, D. A., Carilli, C., Sarazin, C. L., and Blanton, E. L. (2005). The heating of gas in a galaxy cluster by X-ray cavities and large-scale shock fronts. *Nature*, 433(7021):45–47.

- [239] McNamara, B. R., Wise, M., Nulsen, P. E. J., David, L. P., Sarazin, C. L., Bautz, M., Markevitch, M., Vikhlinin, A., Forman, W. R., Jones, C., and Harris, D. E. (2000). Chandra X-Ray Observations of the Hydra A Cluster: An Interaction between the Radio Source and the X-Ray-emitting Gas. *ApJ*, 534(2):L135–L138.
- [240] Mehdipour, M., Kaastra, J. S., and Kallman, T. (2016). Systematic comparison of photoionised plasma codes with application to spectroscopic studies of AGN in X-rays. *A&A*, 596:A65.
- [241] Menou, K., Esin, A. A., Narayan, R., Garcia, M. R., Lasota, J.-P., and McClintock, J. E. (1999). Black Hole and Neutron Star Transients in Quiescence. *ApJ*, 520(1):276–291.
- [242] Mereghetti, S. (2008). The strongest cosmic magnets: soft gamma-ray repeaters and anomalous X-ray pulsars. *A&ARv*, 15(4):225–287.
- [243] Merritt, D., Ferrarese, L., and Joseph, C. L. (2001). No Supermassive Black Hole in M33? *Science*, 293(5532):1116–1119.
- [244] Michel, F. C. (1982). Theory of pulsar magnetospheres. *Reviews of Modern Physics*, 54(1):1–66.
- [245] Michell, J. (1784). On the Means of Discovering the Distance, Magnitude, &c. of the Fixed Stars, in Consequence of the Diminution of the Velocity of Their Light, in Case Such a Diminution Should be Found to Take Place in any of Them, and Such Other Data Should be Procured from Observations, as Would be Farther Necessary for That Purpose. By the Rev. John Michell, B. D. F. R. S. In a Letter to Henry Cavendish, Esq. F. R. S. and A. S. *Philosophical Transactions of the Royal Society of London Series I*, 74:35–57.
- [246] Middleditch, J. and Nelson, J. (1976). Studies of optical pulsations from HZ Herculis/Hercules X-1: a determination of the mass of the neutron star. *ApJ*, 208:567–586.
- [247] Middleton, M. J., Heil, L., Pintore, F., Walton, D. J., and Roberts, T. P. (2015a). A spectral-timing model for ULXs in the supercritical regime. *MNRAS*, 447:3243–3263.
- [248] Middleton, M. J., Roberts, T. P., Done, C., and Jackson, F. E. (2011). Challenging times: a re-analysis of NGC 5408 X-1. *MNRAS*, 411:644–652.
- [249] Middleton, M. J., Walton, D. J., Fabian, A., Roberts, T. P., Heil, L., Pinto, C., Anderson, G., and Sutton, A. (2015b). Diagnosing the accretion flow in ultraluminous X-ray sources using soft X-ray atomic features. *MNRAS*, 454:3134–3142.
- [250] Middleton, M. J., Walton, D. J., Roberts, T. P., and Heil, L. (2014). Broad absorption features in wind-dominated ultraluminous X-ray sources? *MNRAS*, 438:L51–L55.
- [251] Miller, J. M. (2007). Relativistic X-Ray Lines from the Inner Accretion Disks Around Black Holes. *ARA&A*, 45(1):441–479.

- [252] Miller, J. M., Fabbiano, G., Miller, M. C., and Fabian, A. C. (2003). X-Ray Spectroscopic Evidence for Intermediate-Mass Black Holes: Cool Accretion Disks in Two Ultraluminous X-Ray Sources. *ApJ*, 585(1):L37–L40.
- [253] Miller, J. M., Fabian, A. C., Kaastra, J., Kallman, T., King, A. L., Proga, D., Raymond, J., and Reynolds, C. S. (2015a). Powerful, Rotating Disk Winds from Stellar-mass Black Holes. *ApJ*, 814(2):87.
- [254] Miller, J. M., Fabian, A. C., and Miller, M. C. (2004a). A Comparison of Intermediate-Mass Black Hole Candidate Ultraluminous X-Ray Sources and Stellar-Mass Black Holes. *ApJ*, 614(2):L117–L120.
- [255] Miller, J. M., Fabian, A. C., and Miller, M. C. (2004b). Revealing a Cool Accretion Disk in the Ultraluminous X-Ray Source M81 X-9 (Holmberg IX X-1): Evidence for an Intermediate-Mass Black Hole. *ApJ*, 607(2):931–938.
- [256] Miller, J. M., Kaastra, J. S., Miller, M. C., Reynolds, M. T., Brown, G., Cenko, S. B., Drake, J. J., Gezari, S., Guillochon, J., Gultekin, K., Irwin, J., Levan, A., Maitra, D., Maksym, W. P., Mushotzky, R., O’Brien, P., Paerels, F., de Plaa, J., Ramirez-Ruiz, E., Strohmayer, T., and Tanvir, N. (2015b). Flows of X-ray gas reveal the disruption of a star by a massive black hole. *Nature*, 526:542–545.
- [257] Miller, J. M., Kaastra, J. S., Miller, M. C., Reynolds, M. T., Brown, G., Cenko, S. B., Drake, J. J., Gezari, S., Guillochon, J., Gultekin, K., Irwin, J., Levan, A., Maitra, D., Maksym, W. P., Mushotzky, R., O’Brien, P., Paerels, F., de Plaa, J., Ramirez-Ruiz, E., Strohmayer, T., and Tanvir, N. (2015c). Flows of X-ray gas reveal the disruption of a star by a massive black hole. *Nature*, 526:542–545.
- [258] Miller, J. M., Maitra, D., Cackett, E. M., Bhattacharyya, S., and Strohmayer, T. E. (2011). A Fast X-ray Disk Wind in the Transient Pulsar IGR J17480-2446 in Terzan 5. *ApJ*, 731:L7.
- [259] Miller, J. M., Raymond, J., Fabian, A., Steeghs, D., Homan, J., Reynolds, C., van der Klis, M., and Wijnands, R. (2006). The magnetic nature of disk accretion onto black holes. *Nature*, 441:953–955.
- [260] Miller, J. M., Raymond, J., Fabian, A. C., Gallo, E., Kaastra, J., Kallman, T., King, A. L., Proga, D., Reynolds, C. S., and Zoghbi, A. (2016). The Accretion Disk Wind in the Black Hole GRS 1915+105. *ApJ*, 821(1):L9.
- [261] Miller, J. M., Raymond, J., Reynolds, C. S., Fabian, A. C., Kallman, T. R., and Homan, J. (2008). The Accretion Disk Wind in the Black Hole GRO J1655-40. *ApJ*, 680:1359–1377.
- [262] Miller, M. C. and Colbert, E. J. M. (2004). Intermediate-Mass Black Holes. *International Journal of Modern Physics D*, 13(1):1–64.
- [263] Miller, M. C., Lamb, F. K., Dittmann, A. J., Bogdanov, S., Arzoumanian, Z., Gendreau, K. C., Guillot, S., Harding, A. K., Ho, W. C. G., Lattimer, J. M., Ludlam, R. M., Mahmoodifar, S., Morsink, S. M., Ray, P. S., Strohmayer, T. E., Wood, K. S., Enoto, T., Foster, R., Okajima, T., Prigozhin, G., and Soong, Y. (2019). PSR

- J0030+0451 Mass and Radius from NICER Data and Implications for the Properties of Neutron Star Matter. *ApJ*, 887(1):L24.
- [264] Milosavljević, M. and Merritt, D. (2001). Formation of Galactic Nuclei. *ApJ*, 563(1):34–62.
- [265] Mineo, S., Gilfanov, M., and Sunyaev, R. (2012). X-ray emission from star-forming galaxies - I. High-mass X-ray binaries. *MNRAS*, 419(3):2095–2115.
- [266] Mitsuda, K., Inoue, H., Koyama, K., Makishima, K., Matsuoka, M., Ogawara, Y., Shibasaki, N., Suzuki, K., Tanaka, Y., and Hirano, T. (1984). Energy spectra of low-mass binary X-ray sources observed from Tenma. *PASJ*, 36:741–759.
- [267] Monard, L. A. G. (2010). Supernova 2010da in NGC 300. *Central Bureau Electronic Telegrams*, 2289.
- [268] Morganti, R., Tadhunter, C. N., and Oosterloo, T. A. (2005). Fast neutral outflows in powerful radio galaxies: a major source of feedback in massive galaxies. *A&A*, 444(1):L9–L13.
- [269] Mortlock, D. J., Warren, S. J., Venemans, B. P., Patel, M., Hewett, P. C., McMahon, R. G., Simpson, C., Theuns, T., González-Solares, E. A., Adamson, A., Dye, S., Hambly, N. C., Hirst, P., Irwin, M. J., Kuiper, E., Lawrence, A., and Röttgering, H. J. A. (2011). A luminous quasar at a redshift of  $z = 7.085$ . *Nature*, 474(7353):616–619.
- [270] Munro, M. P., Remillard, R. A., and Chakrabarty, D. (2002). How Do Z and Atoll X-Ray Binaries Differ? *ApJ*, 568(1):L35–L39.
- [271] Mushtukov, A. A., Suleimanov, V. F., Tsygankov, S. S., and Poutanen, J. (2015). On the maximum accretion luminosity of magnetized neutron stars: connecting X-ray pulsars and ultraluminous X-ray sources. *MNRAS*, 454(3):2539–2548.
- [272] Nagase, F. (1989). Accretion-powered X-ray pulsars. *PASJ*, 41:1.
- [273] Nandra, K., Barret, D., Barcons, X., Fabian, A., den Herder, J.-W., Piro, L., Watson, M., Adami, C., Aird, J., Afonso, J. M., and et al. (2013). The Hot and Energetic Universe: A White Paper presenting the science theme motivating the Athena+ mission. *arXiv e-prints*, page arXiv:1306.2307.
- [274] Nandra, K., O’Neill, P. M., George, I. M., and Reeves, J. N. (2007). An XMM-Newton survey of broad iron lines in Seyfert galaxies. *MNRAS*, 382(1):194–228.
- [275] Narayan, R., McClintock, J. E., and Yi, I. (1996). A New Model for Black Hole Soft X-Ray Transients in Quiescence. *ApJ*, 457:821.
- [276] Narayan, R., Sadowski, A., and Soria, R. (2017). Spectra of Black Hole Accretion Models of Ultra-Luminous X-ray Sources. *ArXiv e-prints*.
- [277] Narayan, R. and Yi, I. (1994). Advection-dominated Accretion: A Self-similar Solution. *ApJ*, 428:L13.

- [278] Narayan, R. and Yi, I. (1995). Advection-dominated Accretion: Underfed Black Holes and Neutron Stars. *ApJ*, 452:710.
- [279] Nardini, E., Reeves, J. N., Gofford, J., Harrison, F. A., Risaliti, G., Braitto, V., Costa, M. T., Matzeu, G. A., Walton, D. J., Behar, E., Boggs, S. E., Christensen, F. E., Craig, W. W., Hailey, C. J., Matt, G., Miller, J. M., O'Brien, P. T., Stern, D., Turner, T. J., and Ward, M. J. (2015). Black hole feedback in the luminous quasar PDS 456. *Science*, 347(6224):860–863.
- [280] Neilsen, J. and Lee, J. C. (2009). Accretion disk winds as the jet suppression mechanism in the microquasar GRS 1915+105. *Nature*, 458:481–484.
- [281] Neilsen, J., Rahoui, F., Homan, J., and Buxton, M. (2016). A Super-Eddington, Compton-thick Wind in GRO J1655-40? *ApJ*, 822:20.
- [282] Nenkova, M., Ivezić, Ž., and Elitzur, M. (2002). Dust Emission from Active Galactic Nuclei. *ApJ*, 570(1):L9–L12.
- [283] Nixon, C. J. and Pringle, J. E. (2020). Strong surface outflows on accretion discs. *arXiv e-prints*, page arXiv:2003.01726.
- [284] Novikov, I. D. and Thorne, K. S. (1973). Astrophysics of black holes. In *Black Holes (Les Astres Occlus)*, pages 343–450.
- [285] Nowak, M. A., Paizis, A., Jaisawal, G. K., Chenevez, J., Chaty, S., Fortin, F., Rodriguez, J., and Wilms, J. (2019). Chandra-HETGS Characterization of an Outflowing Wind in the Accreting Millisecond Pulsar IGR J17591-2342. *ApJ*, 874(1):69.
- [286] Ogilvie, G. I. and Dubus, G. (2001). Precessing warped accretion discs in X-ray binaries. *MNRAS*, 320:485–503.
- [287] Oppenheimer, J. R. and Volkoff, G. M. (1939). On Massive Neutron Cores. *Physical Review*, 55(4):374–381.
- [288] Orosz, J. A. and Bailyn, C. D. (1997). Optical Observations of GRO J1655-40 in Quiescence. I. A Precise Mass for the Black Hole Primary. *ApJ*, 477(2):876–896.
- [289] Osterbrock, D. E. and Pogge, R. W. (1985). The spectra of narrow-line Seyfert 1 galaxies. *ApJ*, 297:166–176.
- [290] Owocki, S. P., Castor, J. I., and Rybicki, G. B. (1988). Time-dependent Models of Radiatively Driven Stellar Winds. I. Nonlinear Evolution of Instabilities for a Pure Absorption Model. *ApJ*, 335:914.
- [291] Pakull, M. W., Grisé, F., and Motch, C. (2006). Ultraluminous X-ray Sources: Bubbles and Optical Counterparts. In Meurs, E. J. A. and Fabbiano, G., editors, *Populations of High Energy Sources in Galaxies*, volume 230 of *IAU Symposium*, pages 293–297.
- [292] Pakull, M. W. and Mirioni, L. (2002). Optical Counterparts of Ultraluminous X-Ray Sources. *ArXiv Astrophysics e-prints*.

- [293] Pakull, M. W., Soria, R., and Motch, C. (2010). A 300-parsec-long jet-inflated bubble around a powerful microquasar in the galaxy NGC 7793. *Nature*, 466:209–212.
- [294] Parker, M. L., Alston, W. N., Buisson, D. J. K., Fabian, A. C., Jiang, J., Kara, E., Lohfink, A., Pinto, C., and Reynolds, C. S. (2017a). Revealing the ultrafast outflow in IRAS 13224-3809 through spectral variability. *MNRAS*, 469:1553–1558.
- [295] Parker, M. L., Buisson, D. J. K., Jiang, J., Gallo, L. C., Kara, E., Matzeu, G. A., and Walton, D. J. (2018a). Constraining the geometry of AGN outflows with reflection spectroscopy. *MNRAS*.
- [296] Parker, M. L., Matzeu, G. A., Guainazzi, M., Kalfountzou, E., Miniutti, G., Santos-Lleó, M., and Schartel, N. (2018b). A high-velocity component to the complex absorption in IRAS 13349+2438. *MNRAS*, 480(2):2365–2376.
- [297] Parker, M. L., Pinto, C., Fabian, A. C., Lohfink, A., Buisson, D. J. K., Alston, W. N., Kara, E., Cackett, E. M., Chiang, C.-Y., Dauser, T., De Marco, B., Gallo, L. C., Garcia, J., Harrison, F. A., King, A. L., Middleton, M. J., Miller, J. M., Miniutti, G., Reynolds, C. S., Uttley, P., Vasudevan, R., Walton, D. J., Wilkins, D. R., and Zoghbi, A. (2017b). The response of relativistic outflowing gas to the inner accretion disk of a black hole. *Nature*, 543:83–86.
- [298] Parmar, A. N., Oosterbroek, T., Boirin, L., and Lumb, D. (2002). Discovery of narrow X-ray absorption features from the dipping low-mass X-ray binary X 1624-490 with XMM-Newton. *A&A*, 386:910–915.
- [299] Patterson, J. (1984). The evolution of cataclysmic and low-mass X-ray binaries. *ApJS*, 54:443–493.
- [300] Peterson, J. R., Paerels, F. B. S., Kaastra, J. S., Arnaud, M., Reiprich, T. H., Fabian, A. C., Mushotzky, R. F., Jernigan, J. G., and Sakelliou, I. (2001). X-ray imaging-spectroscopy of Abell 1835. *A&A*, 365:L104–L109.
- [301] Petrucci, P. O., Ursini, F., De Rosa, A., Bianchi, S., Cappi, M., Matt, G., Dadina, M., and Malzac, J. (2018). Testing warm Comptonization models for the origin of the soft X-ray excess in AGNs. *A&A*, 611:A59.
- [302] Piconcelli, E., Jimenez-Bailón, E., Guainazzi, M., Schartel, N., Rodríguez-Pascual, P. M., and Santos-Lleó, M. (2005). The XMM-Newton view of PG quasars. I. X-ray continuum and absorption. *A&A*, 432(1):15–30.
- [303] Pinto, C., Alston, W., Parker, M. L., Fabian, A. C., Gallo, L. C., Buisson, D. J. K., Walton, D. J., Kara, E., Jiang, J., Lohfink, A., and Reynolds, C. S. (2018). Ultrafast outflows disappear in high-radiation fields. *MNRAS*, 476:1021–1035.
- [304] Pinto, C., Alston, W., Soria, R., Middleton, M. J., Walton, D. J., Sutton, A. D., Fabian, A. C., Earnshaw, H., Urquhart, R., Kara, E., and Roberts, T. P. (2017). From ultraluminous X-ray sources to ultraluminous supersoft sources: NGC 55 ULX, the missing link. *MNRAS*, 468:2865–2883.

- [305] Pinto, C., Mehdipour, M., Walton, D. J., Middleton, M. J., Roberts, T. P., Fabian, A. C., Guainazzi, M., Soria, R., Kosec, P., and Ness, J. U. (2020a). Thermal stability of winds driven by radiation pressure in super-Eddington accretion discs. *MNRAS*, 491(4):5702–5716.
- [306] Pinto, C., Middleton, M. J., and Fabian, A. C. (2016). Resolved atomic lines reveal outflows in two ultraluminous X-ray sources. *Nature*, 533:64–67.
- [307] Pinto, C., Walton, D. J., Kara, E., Parker, M. L., Soria, R., Kosec, P., Middleton, M. J., Alston, W. N., Fabian, A. C., Guainazzi, M., Roberts, T. P., Fuerst, F., Earnshaw, H. P., Sathyaprakash, R., and Barret, D. (2020b). XMM-Newton campaign on ultraluminous X-ray source NGC 1313 X-1: wind versus state variability. *MNRAS*, 492(4):4646–4665.
- [308] Pintore, F., Sanna, A., Di Salvo, T., Guainazzi, M., D’Aì, A., Riggio, A., Burderi, L., Iaria, R., and Robba, N. R. (2014). Testing rate-dependent corrections on timing mode EPIC-pn spectra of the accreting neutron star GX 13+1. *MNRAS*, 445:3745–3754.
- [309] Pollock, A. M. T., Corcoran, M. F., Stevens, I. R., and Williams, P. M. (2005). Bulk Velocities, Chemical Composition, and Ionization Structure of the X-Ray Shocks in WR 140 near Periastron as Revealed by the Chandra Gratings. *ApJ*, 629(1):482–498.
- [310] Ponti, G., Fender, R. P., Begelman, M. C., Dunn, R. J. H., Neilsen, J., and Coriat, M. (2012a). Ubiquitous equatorial accretion disc winds in black hole soft states. *MNRAS*, 422:L11–L15.
- [311] Ponti, G., Papadakis, I., Bianchi, S., Guainazzi, M., Matt, G., Uttley, P., and Bonilla, N. F. (2012b). CAIXA: a catalogue of AGN in the XMM-Newton archive. III. Excess variance analysis. *A&A*, 542:A83.
- [312] Portegies Zwart, S. F., Baumgardt, H., Hut, P., Makino, J., and McMillan, S. L. W. (2004). Formation of massive black holes through runaway collisions in dense young star clusters. *Nature*, 428(6984):724–726.
- [313] Pounds, K., Lobban, A., Reeves, J., and Vaughan, S. (2016a). Detection of a second high-velocity component in the highly ionized wind from PG 1211+143. *MNRAS*, 457:2951–2957.
- [314] Pounds, K. A., Lobban, A., Reeves, J. N., Vaughan, S., and Costa, M. (2016b). Imprints of a high-velocity wind on the soft X-ray spectrum of PG1211+143. *MNRAS*, 459:4389–4396.
- [315] Pounds, K. A., Nandra, K., Stewart, G. C., George, I. M., and Fabian, A. C. (1990). X-ray reflection from cold matter in the nuclei of active galaxies. *Nature*, 344(6262):132–133.
- [316] Pounds, K. A., Reeves, J. N., King, A. R., Page, K. L., O’Brien, P. T., and Turner, M. J. L. (2003). A high-velocity ionized outflow and XUV photosphere in the narrow emission line quasar PG1211+143. *MNRAS*, 345:705–713.

- [317] Pounds, K. A. and Vaughan, S. (2011). An extended XMM-Newton observation of the Seyfert galaxy NGC 4051 - II. Soft X-ray emission from a limb-brightened shell of post-shock gas. *MNRAS*, 415:2379–2387.
- [318] Poutanen, J., Lipunova, G., Fabrika, S., Butkevich, A. G., and Abolmasov, P. (2007). Supercritically accreting stellar mass black holes as ultraluminous X-ray sources. *MNRAS*, 377:1187–1194.
- [319] Press, W. H. and Schechter, P. (1974). Formation of Galaxies and Clusters of Galaxies by Self-Similar Gravitational Condensation. *ApJ*, 187:425–438.
- [320] Pringle, J. E. (1981). Accretion discs in astrophysics. *ARA&A*, 19:137–162.
- [321] Proga, D. and Kallman, T. R. (2002). On the Role of the Ultraviolet and X-Ray Radiation in Driving a Disk Wind in X-Ray Binaries. *ApJ*, 565(1):455–470.
- [322] Proga, D., Stone, J. M., and Kallman, T. R. (2000). Dynamics of Line-driven Disk Winds in Active Galactic Nuclei. *ApJ*, 543:686–696.
- [323] Protassov, R., van Dyk, D. A., Connors, A., Kashyap, V. L., and Siemiginowska, A. (2002). Statistics, Handle with Care: Detecting Multiple Model Components with the Likelihood Ratio Test. *ApJ*, 571:545–559.
- [324] Psaradaki, I., Costantini, E., Mehdipour, M., and Díaz Trigo, M. (2018). Modelling the disc atmosphere of the low mass X-ray binary EXO 0748-676. *A&A*, 620:A129.
- [325] Puchnarewicz, E. M., Mason, K. O., Siemiginowska, A., Fruscione, A., Comastri, A., Fiore, F., and Cagnoni, I. (2001). Constraining the Black Hole Mass and Accretion Rate in the Narrow-Line Seyfert 1 Galaxy RE J1034+396. *ApJ*, 550(2):644–654.
- [326] Ramsay, G., Zane, S., Jimenez-Garate, M. A., den Herder, J.-W., and Hailey, C. J. (2002). XMM-Newton EPIC observations of Her X-1. *MNRAS*, 337:1185–1192.
- [327] Rau, A., Meidinger, N., Nandra, K., Porro, M., Barret, D., Santangelo, A., Schmid, C., Struder, L., Tenzer, C., Wilms, J., Amoros, C., Andritschke, R., Aschauer, F., Bahr, A., Gunther, B., Furmetz, M., Ott, B., Perinati, E., Rambaud, D., Reiffers, J., Treis, J., von Kienlin, A., and Weidenspointner, G. (2013). The Hot and Energetic Universe: The Wide Field Imager (WFI) for Athena+. *arXiv e-prints*, page arXiv:1308.6785.
- [328] Rees, M. J. (1984). Black Hole Models for Active Galactic Nuclei. *ARA&A*, 22:471–506.
- [329] Reeves, J. N. and Braitto, V. (2019). A Momentum-conserving Accretion Disk Wind in the Narrow-line Seyfert 1 I Zwicky 1. *ApJ*, 884(1):80.
- [330] Reeves, J. N., Braitto, V., Nardini, E., Lobban, A. P., Matzeu, G. A., and Costa, M. T. (2018a). A New Relativistic Component of the Accretion Disk Wind in PDS 456. *ApJ*, 854(1):L8.

- [331] Reeves, J. N., Lobban, A., and Pounds, K. A. (2018b). The Variable Fast Soft X-Ray Wind in PG 1211+143. *ApJ*, 854(1):28.
- [332] Reeves, J. N., O’Brien, P. T., and Ward, M. J. (2003). A Massive X-Ray Outflow from the Quasar PDS 456. *ApJ*, 593:L65–L68.
- [333] Reeves, J. N. and Turner, M. J. L. (2000). X-ray spectra of a large sample of quasars with ASCA. *MNRAS*, 316(2):234–248.
- [334] Remillard, R. A. and McClintock, J. E. (2006). X-Ray Properties of Black-Hole Binaries. *ARA&A*, 44(1):49–92.
- [335] Reynolds, A. P., Quaintrell, H., Still, M. D., Roche, P., Chakrabarty, D., and Levine, S. E. (1997). A new mass estimate for Hercules X-1. *MNRAS*, 288:43–52.
- [336] Reynolds, C. S. (2019). Observing black holes spin. *Nature Astronomy*, 3:41–47.
- [337] Reynolds, C. S., Brenneman, L. W., Lohfink, A. M., Trippe, M. L., Miller, J. M., Fabian, A. C., and Nowak, M. A. (2012). A Monte Carlo Markov Chain Based Investigation of Black Hole Spin in the Active Galaxy NGC 3783. *ApJ*, 755(2):88.
- [338] Reynolds, C. S. and Fabian, A. C. (1995). Warm absorbers in active galactic nuclei. *MNRAS*, 273(4):1167–1176.
- [339] Reynolds, C. S. and Nowak, M. A. (2003). Fluorescent iron lines as a probe of astrophysical black hole systems. *Phys. Rep.*, 377(6):389–466.
- [340] Ricci, C., Trakhtenbrot, B., Koss, M. J., Ueda, Y., Schawinski, K., Oh, K., Lamperti, I., Mushotzky, R., Treister, E., Ho, L. C., Weigel, A., Bauer, F. E., Paltani, S., Fabian, A. C., Xie, Y., and Gehrels, N. (2017). The close environments of accreting massive black holes are shaped by radiative feedback. *Nature*, 549(7673):488–491.
- [341] Richstone, D., Ajhar, E. A., Bender, R., Bower, G., Dressler, A., Faber, S. M., Filippenko, A. V., Gebhardt, K., Green, R., Ho, L. C., Kormendy, J., Lauer, T. R., Magorrian, J., and Tremaine, S. (1998). Supermassive black holes and the evolution of galaxies. *Nature*, 385(6701):A14.
- [342] Riley, T. E., Watts, A. L., Bogdanov, S., Ray, P. S., Ludlam, R. M., Guillot, S., Arzoumanian, Z., Baker, C. L., Bilous, A. V., Chakrabarty, D., Gendreau, K. C., Harding, A. K., Ho, W. C. G., Lattimer, J. M., Morsink, S. M., and Strohmayer, T. E. (2019). A NICER View of PSR J0030+0451: Millisecond Pulsar Parameter Estimation. *ApJ*, 887(1):L21.
- [343] Roberts, T. P. (2007). X-ray observations of ultraluminous X-ray sources. *Ap&SS*, 311(1-3):203–212.
- [344] Roberts, T. P., Kilgard, R. E., Warwick, R. S., Goad, M. R., and Ward, M. J. (2006). Chandra monitoring observations of the ultraluminous X-ray source NGC 5204 X-1. *MNRAS*, 371:1877–1890.

- [345] Roberts, T. P., Warwick, R. S., Ward, M. J., and Goad, M. R. (2004). Chandra observations of five ultraluminous X-ray sources in nearby galaxies. *MNRAS*, 349(4):1193–1210.
- [346] Rodríguez Castillo, G. A., Israel, G. L., Belfiore, A., Bernardini, F., Esposito, P., Pintore, F., De Luca, A., Papitto, A., Stella, L., Tiengo, A., Zampieri, L., Bachetti, M., Brightman, M., Casella, P., D’Agostino, D., Dall’Osso, S., Earnshaw, H. P., Fürst, F., Haberl, F., Harrison, F. A., Mapelli, M., Marelli, M., Middleton, M., Pinto, C., Roberts, T. P., Salvaterra, R., Turolla, R., Walton, D. J., and Wolter, A. (2019). Discovery of a 2.8 s pulsar in a 2 d orbit High-Mass X-ray Binary powering the Ultraluminous X-ray source ULX-7 in M51. *arXiv e-prints*, page arXiv:1906.04791.
- [347] Ross, R. R. and Fabian, A. C. (2005). A comprehensive range of X-ray ionized-reflection models. *MNRAS*, 358(1):211–216.
- [348] Rupke, D. S. N., Gültekin, K., and Veilleux, S. (2017). Quasar-mode Feedback in Nearby Type 1 Quasars: Ubiquitous Kiloparsec-scale Outflows and Correlations with Black Hole Properties. *ApJ*, 850(1):40.
- [349] Rupke, D. S. N. and Veilleux, S. (2011). Integral Field Spectroscopy of Massive, Kiloparsec-scale Outflows in the Infrared-luminous QSO Mrk 231. *ApJ*, 729(2):L27.
- [350] Sako, M., Kahn, S. M., Behar, E., Kaastra, J. S., Brinkman, A. C., Boller, T., Puchnarewicz, E. M., Starling, R., Liedahl, D. A., Clavel, J., and Santos-Lleo, M. (2001). Complex resonance absorption structure in the X-ray spectrum of <ASTROBJ>IRAS 13349+2438</ASTROBJ>. *A&A*, 365:L168–L173.
- [351] Sana, H., de Mink, S. E., de Koter, A., Langer, N., Evans, C. J., Gieles, M., Gosset, E., Izzard, R. G., Le Bouquin, J. B., and Schneider, F. R. N. (2012). Binary Interaction Dominates the Evolution of Massive Stars. *Science*, 337(6093):444.
- [352] Sathyaprakash, R., Roberts, T. P., and Siwek, M. M. (2019a). Observational limits on the X-ray emission from the bubble nebula surrounding Ho IX X-1. *MNRAS*, 488(4):4614–4622.
- [353] Sathyaprakash, R., Roberts, T. P., Walton, D. J., Fuerst, F., Bachetti, M., Pinto, C., Alston, W. N., Earnshaw, H. P., Fabian, A. C., Middleton, M. J., and Soria, R. (2019b). The discovery of weak coherent pulsations in the ultraluminous X-ray source NGC 1313 X-2. *MNRAS*, 488(1):L35–L40.
- [354] Scargle, J. D. (1973). The production of discrete, quantized outflow velocities by radiation pressure in stars, Seyfert nuclei, and quasi-stellar objects. *ApJ*, 179:705.
- [355] Schechter, P. (1976). An analytic expression for the luminosity function for galaxies. *ApJ*, 203:297–306.
- [356] Schmidt, M. (1963). 3C 273 : A Star-Like Object with Large Red-Shift. *Nature*, 197(4872):1040.
- [357] Schulz, N. S., Hasinger, G., and Truemper, J. (1989). Spectral classification of low-mass X-ray binary (LMXB) energy spectra with color-color diagrams. *A&A*, 225:48–68.

- [358] Schwarzschild, K. (1916). On the Gravitational Field of a Mass Point According to Einstein's Theory. *Abh. Konigl. Preuss. Akad. Wissenschaften Jahre 1906,92, Berlin,1907*, 1916:189–196.
- [359] Scott, D. M., Leahy, D. A., and Wilson, R. B. (2000). The 35 Day Evolution of the Hercules X-1 Pulse Profile: Evidence for a Resolved Inner Disk Occultation of the Neutron Star. *ApJ*, 539:392–412.
- [360] Serafinelli, R., Tombesi, F., Vagnetti, F., Piconcelli, E., Gaspari, M., and Saturni, F. G. (2019). Multiphase quasar-driven outflows in PG 1114+445. I. Entrained ultra-fast outflows. *A&A*, 627:A121.
- [361] Seward, F., Grindlay, J., Seaquist, E., and Gilmore, W. (1980). Diffuse X-ray emission from the jets of SS433. *Nature*, 287(5785):806–808.
- [362] Seyfert, C. K. (1943). Nuclear Emission in Spiral Nebulae. *ApJ*, 97:28.
- [363] Shakura, N. I. and Sunyaev, R. A. (1973). Reprint of 1973A&A....24..337S. Black holes in binary systems. Observational appearance. *A&A*, 500:33–51.
- [364] Shapiro, S. L. and Teukolsky, S. A. (1983). *Black holes, white dwarfs, and neutron stars : the physics of compact objects*.
- [365] Sidoli, L., Parmar, A. N., Oosterbroek, T., and Lumb, D. (2002). Discovery of complex narrow X-ray absorption features from the low-mass X-ray binary GX 13+1 with XMM-Newton. *A&A*, 385:940–946.
- [366] Silk, J. and Rees, M. J. (1998). Quasars and galaxy formation. *A&A*, 331:L1–L4.
- [367] Smith, R. K., Abraham, M., Allured, R., Bautz, M., Bookbinder, J., Bregman, J., Brenneman, L., Brickhouse, N. S., Burrows, D., Burwitz, V., Cheimets, P. N., Costantini, E., Dawson, S., DeRoo, C., Falcone, A., Foster, A. R., Gallo, L., Grant, C. E., Günther, H. M., Heilmann, R. K., Hertz, E., Hine, B., Huenemoerder, D., Kaastra, J. S., Kreykenbohm, I., Madsen, K. K., McEntaffer, R., Miller, E., Miller, J., Morse, E., Mushotzky, R., Nandra, K., Nowak, M., Paerels, F., Petre, R., Poppenhaeger, K., Ptak, A., Reid, P., Sanders, J., Schattenburg, M., Schulz, N., Smale, A., Temi, P., Valencic, L., Walker, S., Willingale, R., Wilms, J., and Wolk, S. J. (2017). Arcus: exploring the formation and evolution of clusters, galaxies, and stars. In *Proc. SPIE*, volume 10397 of *Society of Photo-Optical Instrumentation Engineers (SPIE) Conference Series*, page 103970Q.
- [368] Staubert, R., Klochkov, D., Vasco, D., Postnov, K., Shakura, N., Wilms, J., and Rothschild, R. E. (2013). Variable pulse profiles of Hercules X-1 repeating with the same irregular 35 d clock as the turn-ons. *A&A*, 550:A110.
- [369] Staubert, R., Klochkov, D., and Wilms, J. (2009). Updating the orbital ephemeris of Hercules X-1; rate of decay and eccentricity of the orbit. *A&A*, 500(2):883–889.
- [370] Staubert, R., Shakura, N. I., Postnov, K., Wilms, J., Rothschild, R. E., Coburn, W., Rodina, L., and Klochkov, D. (2007). Discovery of a flux-related change of the cyclotron line energy in Hercules X-1. *A&A*, 465:L25–L28.

- [371] Staubert, R., Trümper, J., Kendziorra, E., Klochkov, D., Postnov, K., Kretschmar, P., Pottschmidt, K., Haberl, F., Rothschild, R. E., Santangelo, A., Wilms, J., Kreykenbohm, I., and Fürst, F. (2019). Cyclotron lines in highly magnetized neutron stars. *A&A*, 622:A61.
- [372] Steenbrugge, K. C., Kaastra, J. S., Crenshaw, D. M., Kraemer, S. B., Arav, N., George, I. M., Liedahl, D. A., van der Meer, R. L. J., Paerels, F. B. S., Turner, T. J., and Yaqoob, T. (2005). Simultaneous X-ray and UV spectroscopy of the Seyfert galaxy NGC 5548. II. Physical conditions in the X-ray absorber. *A&A*, 434:569–584.
- [373] Steenbrugge, K. C., Kaastra, J. S., de Vries, C. P., and Edelson, R. (2003). XMM-NEWTON High resolution spectroscopy of NGC 5548. *A&A*, 402:477–486.
- [374] Stobbart, A.-M., Roberts, T. P., and Wilms, J. (2006). XMM-Newton observations of the brightest ultraluminous X-ray sources. *MNRAS*, 368:397–413.
- [375] Strohmayer, T. E. and Mushotzky, R. F. (2003). Discovery of X-Ray Quasi-periodic Oscillations from an Ultraluminous X-Ray Source in M82: Evidence against Beaming. *ApJ*, 586(1):L61–L64.
- [376] Strohmayer, T. E. and Mushotzky, R. F. (2009). Evidence for an Intermediate-mass Black Hole in NGC 5408 X-1. *ApJ*, 703(2):1386–1393.
- [377] Strohmayer, T. E., Mushotzky, R. F., Winter, L., Soria, R., Uttley, P., and Cropper, M. (2007). Quasi-periodic Variability in NGC 5408 X-1. *ApJ*, 660(1):580–586.
- [378] Strüder, L., Briel, U., Dennerl, K., Hartmann, R., Kendziorra, E., Meidinger, N., Pfeiffermann, E., Reppin, C., Aschenbach, B., Bornemann, W., Bräuninger, H., Burkert, W., Elender, M., Freyberg, M., Haberl, F., Hartner, G., Heuschmann, F., Hippmann, H., Kastelic, E., Kemmer, S., Kettenring, G., Kink, W., Krause, N., Müller, S., Oppitz, A., Pietsch, W., Popp, M., Predehl, P., Read, A., Stephan, K. H., Stötter, D., Trümper, J., Holl, P., Kemmer, J., Soltau, H., Stötter, R., Weber, U., Weichert, U., von Zanthier, C., Carathanassis, D., Lutz, G., Richter, R. H., Solc, P., Böttcher, H., Kuster, M., Staubert, R., Abbey, A., Holland, A., Turner, M., Balasini, M., Bignami, G. F., La Palombara, N., Villa, G., Buttler, W., Gianini, F., Lainé, R., Lumb, D., and Dhez, P. (2001). The European Photon Imaging Camera on XMM-Newton: The pn-CCD camera. *A&A*, 365:L18–L26.
- [379] Sturm, E., González-Alfonso, E., Veilleux, S., Fischer, J., Graciá-Carpio, J., Hailey-Dunsheath, S., Contursi, A., Poglitsch, A., Sternberg, A., Davies, R., Genzel, R., Lutz, D., Tacconi, L., Verma, A., Maiolino, R., and de Jong, J. A. (2011). Massive Molecular Outflows and Negative Feedback in ULIRGs Observed by Herschel-PACS. *ApJ*, 733(1):L16.
- [380] Sutton, A. D., Roberts, T. P., and Middleton, M. J. (2013). The ultraluminous state revisited: fractional variability and spectral shape as diagnostics of super-Eddington accretion. *MNRAS*, 435:1758–1775.
- [381] Swartz, D. A., Soria, R., Tennant, A. F., and Yukita, M. (2011). A Complete Sample of Ultraluminous X-ray Source Host Galaxies. *ApJ*, 741(1):49.

- [382] Takahashi, T., Mitsuda, K., Kelley, R., Aarts, H., Aharonian, F., Akamatsu, H., Akimoto, F., Allen, S., Anabuki, N., Angelini, L., Arnaud, K., Asai, M., Audard, M., Awaki, H., Azzarello, P., Baluta, C., Bamba, A., Bando, N., Bautz, M., Blandford, R., Boyce, K., Brown, G., Cackett, E., Chernyakova, M., Coppi, P., Costantini, E., de Plaa, J., den Herder, J.-W., DiPirro, M., Done, C., Dotani, T., Doty, J., Ebisawa, K., Eckart, M., Enoto, T., Ezoe, Y., Fabian, A., Ferrigno, C., Foster, A., Fujimoto, R., Fukazawa, Y., Funk, S., Furuzawa, A., Galeazzi, M., Gallo, L., Gandhi, P., Gendreau, K., Gilmore, K., Haas, D., Haba, Y., Hamaguchi, K., Hatsukade, I., Hayashi, T., Hayashida, K., Hiraga, J., Hirose, K., Hornschemeier, A., Hoshino, A., Hughes, J., Hwang, U., Iizuka, R., Inoue, Y., Ishibashi, K., Ishida, M., Ishimura, K., Ishisaki, Y., Ito, M., Iwata, N., Iyomoto, N., Kaastra, J., Kallman, T., Kamae, T., Kataoka, J., Katsuda, S., Kawahara, H., Kawaharada, M., Kawai, N., Kawasaki, S., Khangaluyan, D., Kilbourne, C., Kimura, M., Kinugasa, K., Kitamoto, S., Kitayama, T., Kohmura, T., Kokubun, M., Kosaka, T., Koujelev, A., Koyama, K., Krimm, H., Kubota, A., Kunieda, H., LaMassa, S., Laurent, P., Lebrun, F., Leutenegger, M., Limousin, O., Loewenstein, M., Long, K., Lumb, D., Madejski, G., Maeda, Y., Makishima, K., Marchand, G., Markevitch, M., Matsumoto, H., Matsushita, K., McCammon, D., McNamara, B., Miller, J., Miller, E., Mineshige, S., Minesugi, K., Mitsuishi, I., Miyazawa, T., Mizuno, T., Mori, H., Mori, K., Mukai, K., Murakami, T., Murakami, H., Mushotzky, R., Nagano, H., Nagino, R., Nakagawa, T., Nakajima, H., Nakamori, T., Nakazawa, K., Namba, Y., Natsukari, C., Nishioka, Y., Nobukawa, M., Nomachi, M., O'Dell, S., Odaka, H., Ogawa, H., Ogawa, M., Ogi, K., Ohashi, T., Ohno, M., Ohta, M., Okajima, T., Okamoto, A., Okazaki, T., Ota, N., Ozaki, M., Paerels, F., Paltani, S., Parmar, A., Petre, R., Pohl, M., Porter, F. S., Ramsey, B., Reis, R., Reynolds, C., Russell, H., Safi-Harb, S., Sakai, S.-i., Sameshima, H., Sanders, J., Sato, G., Sato, R., Sato, Y., Sato, K., Sawada, M., Serlemitsos, P., Seta, H., Shibano, Y., Shida, M., Shimada, T., Shinozaki, K., Shirron, P., Simionescu, A., Simmons, C., Smith, R., Sneiderman, G., Soong, Y., Stawarz, L., Sugawara, Y., Sugita, H., Sugita, S., Szymkowiak, A., Tajima, H., Takahashi, H., Takeda, S.-i., Takei, Y., Tamagawa, T., Tamura, T., Tamura, K., Tanaka, T., Tanaka, Y., Tashiro, M., Tawara, Y., Terada, Y., Terashima, Y., Tombesi, F., Tomida, H., Tsuboi, Y., Tsujimoto, M., Tsunemi, H., Tsuru, T., Uchida, H., Uchiyama, Y., Uchiyama, H., Ueda, Y., Ueno, S., Uno, S., Urry, M., Ursino, E., de Vries, C., Wada, A., Watanabe, S., Werner, N., White, N., Yamada, T., Yamada, S., Yamaguchi, H., Yamasaki, N., Yamauchi, S., Yamauchi, M., Yatsu, Y., Yonetoku, D., Yoshida, A., and Yuasa, T. (2012). *The ASTRO-H X-ray Observatory*, volume 8443 of *Society of Photo-Optical Instrumentation Engineers (SPIE) Conference Series*, page 84431Z.
- [383] Takahashi, T., Mitsuda, K., Kelley, R., Aharonian, F., Akimoto, F., Allen, S., Anabuki, N., Angelini, L., Arnaud, K., Awaki, H., Bamba, A., Bando, N., Bautz, M., Blandford, R., Boyce, K., Brown, G., Chernyakova, M., Coppi, P., Costantini, E., Cottam, J., Crow, J., de Plaa, J., de Vries, C., den Herder, J.-W., DiPirro, M., Done, C., Dotani, T., Ebisawa, K., Enoto, T., Ezoe, Y., Fabian, A., Fujimoto, R., Fukazawa, Y., Funk, S., Furuzawa, A., Galeazzi, M., Gandhi, P., Gendreau, K., Gilmore, K., Haba, Y., Hamaguchi, K., Hatsukade, I., Hayashida, K., Hiraga, J., Hirose, K., Hornschemeier, A., Hughes, J., Hwang, U., Iizuka, R., Ishibashi, K., Ishida, M., Ishimura, K., Ishisaki, Y., Isobe, N., Ito, M., Iwata, N., Kaastra, J., Kallman, T., Kamae, T., Katagiri, H., Kataoka, J., Katsuda, S., Kawaharada, M., Kawai, N., Kawasaki, S., Khangaluyan, D., Kilbourne, C., Kinugasa, K., Kitamoto,

- S., Kitayama, T., Kohmura, T., Kokubun, M., Kosaka, T., Kotani, T., Koyama, K., Kubota, A., Kunieda, H., Laurent, P., Lebrun, F., Limousin, O., Loewenstein, M., Long, K., Madejski, G., Maeda, Y., Makishima, K., Markevitch, M., Matsumoto, H., Matsushita, K., McCammon, D., Miller, J., Mineshige, S., Minesugi, K., Miyazawa, T., Mizuno, T., Mori, K., Mori, H., Mukai, K., Murakami, H., Murakami, T., Mushotzky, R., Nakagawa, Y., Nakagawa, T., Nakajima, H., Nakamori, T., Nakazawa, K., Namba, Y., Nomachi, M., O'Dell, S., Ogawa, H., Ogawa, M., Ogi, K., Ohashi, T., Ohno, M., Ohta, M., Okajima, T., Ota, N., Ozaki, M., Paerels, F., Paltani, S., Parmar, A., Petre, R., Pohl, M., Porter, S., Ramsey, B., Reynolds, C., Sakai, S.-I., Sambruna, R., Sato, G., Sato, Y., Serlemitsos, P., Shida, M., Shimada, T., Shinozaki, K., Shirron, P., Smith, R., Sneiderman, G., Soong, Y., Stawarz, L., Sugita, H., Szymkowiak, A., Tajima, H., Takahashi, H., Takei, Y., Tamagawa, T., Tamura, T., Tamura, K., Tanaka, T., Tanaka, Y., Tanaka, Y., Tashiro, M., Tawara, Y., Terada, Y., Terashima, Y., Tombesi, F., Tomida, H., Tozuka, M., Tsuboi, Y., Tsujimoto, M., Tsunemi, H., Tsuru, T., Uchida, H., Uchiyama, Y., Uchiyama, H., Ueda, Y., Uno, S., Urry, M., Watanabe, S., White, N., Yamada, T., Yamaguchi, H., Yamaoka, K., Yamasaki, N., Yamauchi, M., Yamauchi, S., Yatsu, Y., Yonetoku, D., and Yoshida, A. (2010). The ASTRO-H Mission. In *Space Telescopes and Instrumentation 2010: Ultraviolet to Gamma Ray*, volume 7732 of *Proc. SPIE*, page 77320Z.
- [384] Takano, M., Mitsuda, K., Fukazawa, Y., and Nagase, F. (1994). Properties of M33 X-8, the Nuclear Source in the Nearby Spiral Galaxy. *ApJ*, 436:L47.
- [385] Takeuchi, S., Ohsuga, K., and Mineshige, S. (2013). Clumpy Outflows from Supercritical Accretion Flow. *PASJ*, 65:88.
- [386] Tanaka, Y., Nandra, K., Fabian, A. C., Inoue, H., Otani, C., Dotani, T., Hayashida, K., Iwasawa, K., Kii, T., Kunieda, H., Makino, F., and Matsuoka, M. (1995). Gravitationally redshifted emission implying an accretion disk and massive black hole in the active galaxy MCG-6-30-15. *Nature*, 375(6533):659–661.
- [387] Tananbaum, H., Gursky, H., Kellogg, E. M., Levinson, R., Schreier, E., and Giacconi, R. (1972). Discovery of a Periodic Pulsating Binary X-Ray Source in Hercules from UHURU. *ApJ*, 174:L143.
- [388] Tarter, C. B., Tucker, W. H., and Salpeter, E. E. (1969). The Interaction of X-Ray Sources with Optically Thin Environments. *ApJ*, 156:943.
- [389] Thorne, K. S. (1974). Disk-Accretion onto a Black Hole. II. Evolution of the Hole. *ApJ*, 191:507–520.
- [390] Titarchuk, L. (1994). Generalized Comptonization Models and Application to the Recent High-Energy Observations. *ApJ*, 434:570.
- [391] Tolman, R. C. (1939). Static Solutions of Einstein's Field Equations for Spheres of Fluid. *Physical Review*, 55(4):364–373.
- [392] Tombesi, F., Cappi, M., Reeves, J. N., Nemmen, R. S., Braitto, V., Gaspari, M., and Reynolds, C. S. (2013). Unification of X-ray winds in Seyfert galaxies: from ultra-fast outflows to warm absorbers. *MNRAS*, 430(2):1102–1117.

- [393] Tombesi, F., Cappi, M., Reeves, J. N., Palumbo, G. G. C., Yaqoob, T., Braitto, V., and Dadina, M. (2010a). Evidence for ultra-fast outflows in radio-quiet AGNs. I. Detection and statistical incidence of Fe K-shell absorption lines. *A&A*, 521:A57.
- [394] Tombesi, F., Meléndez, M., Veilleux, S., Reeves, J. N., González-Alfonso, E., and Reynolds, C. S. (2015). Wind from the black-hole accretion disk driving a molecular outflow in an active galaxy. *Nature*, 519(7544):436–438.
- [395] Tombesi, F., Sambruna, R. M., Reeves, J. N., Braitto, V., Ballo, L., Gofford, J., Cappi, M., and Mushotzky, R. F. (2010b). Discovery of Ultra-fast Outflows in a Sample of Broad-line Radio Galaxies Observed with Suzaku. *ApJ*, 719(1):700–715.
- [396] Tomsick, J. A., Parker, M. L., García, J. A., Yamaoka, K., Barret, D., Chiu, J.-L., Clavel, M., Fabian, A., Fürst, F., Gandhi, P., Grinberg, V., Miller, J. M., Pottschmidt, K., and Walton, D. J. (2018). Alternative Explanations for Extreme Supersolar Iron Abundances Inferred from the Energy Spectrum of Cygnus X-1. *ApJ*, 855(1):3.
- [397] Tremaine, S., Gebhardt, K., Bender, R., Bower, G., Dressler, A., Faber, S. M., Filippenko, A. V., Green, R., Grillmair, C., Ho, L. C., Kormendy, J., Lauer, T. R., Magorrian, J., Pinkney, J., and Richstone, D. (2002). The Slope of the Black Hole Mass versus Velocity Dispersion Correlation. *ApJ*, 574(2):740–753.
- [398] Truemper, J., Pietsch, W., Reppin, C., Voges, W., Staubert, R., and Kendziorra, E. (1978). Evidence for strong cyclotron line emission in the hard X-ray spectrum of Hercules X-1. *ApJ*, 219:L105–L110.
- [399] Tsygankov, S. S., Mushtukov, A. A., Suleimanov, V. F., and Poutanen, J. (2016). Propeller effect in action in the ultraluminous accreting magnetar M82 X-2. *MNRAS*, 457(1):1101–1106.
- [400] Turner, M. J. L., Abbey, A., Arnaud, M., Balasini, M., Barbera, M., Belsole, E., Bennie, P. J., Bernard, J. P., Bignami, G. F., Boer, M., Briel, U., Butler, I., Cara, C., Chabaud, C., Cole, R., Collura, A., Conte, M., Cros, A., Denby, M., Dhez, P., Di Coco, G., Dowson, J., Ferrando, P., Ghizzardi, S., Gianotti, F., Goodall, C. V., Gretton, L., Griffiths, R. G., Hainaut, O., Hochedez, J. F., Holland, A. D., Jourdain, E., Kendziorra, E., Lagostina, A., Laine, R., La Palombara, N., Lortholary, M., Lumb, D., Marty, P., Molendi, S., Pigot, C., Poindron, E., Pounds, K. A., Reeves, J. N., Reppin, C., Rothenflug, R., Salvétat, P., Sauvageot, J. L., Schmitt, D., Sembay, S., Short, A. D. T., Spragg, J., Stephen, J., Strüder, L., Tiengo, A., Trifoglio, M., Trümper, J., Vercellone, S., Vigroux, L., Villa, G., Ward, M. J., Whitehead, S., and Zonca, E. (2001). The European Photon Imaging Camera on XMM-Newton: The MOS cameras. *A&A*, 365:L27–L35.
- [401] Turner, T. J. and Miller, L. (2009). X-ray absorption and reflection in active galactic nuclei. *A&ARv*, 17(1):47–104.
- [402] Ueda, Y., Asai, K., Yamaoka, K., Dotani, T., and Inoue, H. (2001). Discovery of an Iron K Absorption Line in the Low-Mass X-Ray Binary GX 13+1. *ApJ*, 556(2):L87–L90.

- [403] Ueda, Y., Inoue, H., Tanaka, Y., Ebisawa, K., Nagase, F., Kotani, T., and Gehrels, N. (1998). Detection of Absorption-Line Features in the X-Ray Spectra of the Galactic Superluminal Source GRO J1655-40. *ApJ*, 492(2):782–787.
- [404] Ueda, Y., Murakami, H., Yamaoka, K., Dotani, T., and Ebisawa, K. (2004). Chandra High-Resolution Spectroscopy of the Absorption-Line Features in the Low-Mass X-Ray Binary GX 13+1. *ApJ*, 609:325–334.
- [405] Urry, C. M. and Padovani, P. (1995). Unified Schemes for Radio-Loud Active Galactic Nuclei. *PASP*, 107:803.
- [406] Ustyugova, G. V., Koldoba, A. V., Romanova, M. M., Chechetkin, V. M., and Lovelace, R. V. E. (1999). Magnetocentrifugally Driven Winds: Comparison of MHD Simulations with Theory. *ApJ*, 516:221–235.
- [407] van der Klis, M. (2000). Millisecond Oscillations in X-ray Binaries. *ARA&A*, 38:717–760.
- [408] Veilleux, S., Meléndez, M., Sturm, E., Gracia-Carpio, J., Fischer, J., González-Alfonso, E., Contursi, A., Lutz, D., Poglitsch, A., Davies, R., Genzel, R., Tacconi, L., de Jong, J. A., Sternberg, A., Netzer, H., Hailey-Dunsheath, S., Verma, A., Rupke, D. S. N., Maiolino, R., Teng, S. H., and Polisensky, E. (2013). Fast Molecular Outflows in Luminous Galaxy Mergers: Evidence for Quasar Feedback from Herschel. *ApJ*, 776(1):27.
- [409] Vestergaard, M. and Peterson, B. M. (2006). Determining Central Black Hole Masses in Distant Active Galaxies and Quasars. II. Improved Optical and UV Scaling Relationships. *ApJ*, 641(2):689–709.
- [410] Villar, V. A., Berger, E., Chornock, R., Margutti, R., Laskar, T., Brown, P. J., Blanchard, P. K., Czekala, I., Lunnan, R., and Reynolds, M. T. (2016). The Intermediate Luminosity Optical Transient SN 2010da: The Progenitor, Eruption, and Aftermath of a Peculiar Supergiant High-mass X-Ray Binary. *ApJ*, 830:11.
- [411] Volonteri, M. (2010). Formation of supermassive black holes. *A&ARv*, 18(3):279–315.
- [412] Volonteri, M., Silk, J., and Dubus, G. (2015). The Case for Supercritical Accretion onto Massive Black Holes at High Redshift. *ApJ*, 804(2):148.
- [413] Walter, R. and Fink, H. H. (1993). The ultraviolet to soft X-ray bump of Seyfert 1 type active galactic nuclei. *A&A*, 274:105.
- [414] Walton, D. J., Fürst, F., Harrison, F. A., Stern, D., Bachetti, M., Barret, D., Brightman, M., Fabian, A. C., Middleton, M. J., Ptak, A., and Tao, L. (2018a). Super-Eddington accretion on to the neutron star NGC 7793 P13: Broad-band X-ray spectroscopy and ultraluminous X-ray sources. *MNRAS*, 473:4360–4376.
- [415] Walton, D. J., Fürst, F., Heida, M., Harrison, F. A., Barret, D., Stern, D., Bachetti, M., Brightman, M., Fabian, A. C., and Middleton, M. J. (2018b). Evidence for Pulsar-like Emission Components in the Broadband ULX Sample. *ApJ*, 856(2):128.

- [416] Walton, D. J., Harrison, F. A., Grefenstette, B. W., Miller, J. M., Bachetti, M., Barret, D., Boggs, S. E., Christensen, F. E., Craig, W. W., Fabian, A. C., Fuerst, F., Hailey, C. J., Madsen, K. K., Parker, M. L., Ptak, A., Rana, V., Stern, D., Webb, N., and Zhang, W. W. (2014). Broadband X-Ray Spectra of the Ultraluminous X-Ray Source Holmberg IX X-1 Observed with NuSTAR, XMM-Newton, and Suzaku. *ApJ*, 793:21.
- [417] Walton, D. J., Middleton, M. J., Pinto, C., Fabian, A. C., Bachetti, M., Barret, D., Brightman, M., Fuerst, F., Harrison, F. A., Miller, J. M., and Stern, D. (2016a). An Iron K Component to the Ultrafast Outflow in NGC 1313 X-1. *ApJ*, 826(2):L26.
- [418] Walton, D. J., Middleton, M. J., Rana, V., Miller, J. M., Harrison, F. A., Fabian, A. C., Bachetti, M., Barret, D., Boggs, S. E., Christensen, F. E., Craig, W. W., Fuerst, F., Grefenstette, B. W., Hailey, C. J., Madsen, K. K., Stern, D., and Zhang, W. (2015). NuSTAR, XMM-Newton, and Suzaku Observations of the Ultraluminous X-Ray Source Holmberg II X-1. *ApJ*, 806(1):65.
- [419] Walton, D. J., Nardini, E., Fabian, A. C., Gallo, L. C., and Reis, R. C. (2013). Suzaku observations of ‘bare’ active galactic nuclei. *MNRAS*, 428(4):2901–2920.
- [420] Walton, D. J., Nardini, E., Gallo, L. C., Reynolds, M. T., Ricci, C., Dauser, T., Fabian, A. C., García, J. A., Harrison, F. A., Risaliti, G., and Stern, D. (2019a). A low-flux state in IRAS 00521-7054 seen with NuSTAR and XMM-Newton: relativistic reflection and an ultrafast outflow. *MNRAS*, 484(2):2544–2555.
- [421] Walton, D. J., Pinto, C., Nowak, M., Bachetti, M., Sathyaprakash, R., Kara, E., Roberts, T. P., Soria, R., Brightman, M., Canizares, C. R., Earnshaw, H. P., Fuerst, F., Heida, M., Middleton, M. J., Stern, D., Tao, L., Webb, N., Alston, W. N., Barret, D., Fabian, A. C., Harrison, F. A., and Kosec, P. (2019b). The Unusual Broadband X-ray Spectral Variability of NGC 1313 X-1 seen with *XMM-Newton*, *Chandra* and *NuSTAR*. *arXiv e-prints*, page arXiv:1911.09622.
- [422] Walton, D. J., Tomsick, J. A., Madsen, K. K., Grinberg, V., Barret, D., Boggs, S. E., Christensen, F. E., Clavel, M., Craig, W. W., Fabian, A. C., Fuerst, F., Hailey, C. J., Harrison, F. A., Miller, J. M., Parker, M. L., Rahoui, F., Stern, D., Tao, L., Wilms, J., and Zhang, W. (2016b). The Soft State of Cygnus X-1 Observed with NuSTAR: A Variable Corona and a Stable Inner Disk. *ApJ*, 826:87.
- [423] Webb, N., Cseh, D., Lenc, E., Godet, O., Barret, D., Corbel, S., Farrell, S., Fender, R., Gehrels, N., and Heywood, I. (2012). Radio Detections During Two State Transitions of the Intermediate-Mass Black Hole HLX-1. *Science*, 337:554.
- [424] Webster, B. L. and Murdin, P. (1972). Cygnus X-1-a Spectroscopic Binary with a Heavy Companion ? *Nature*, 235(5332):37–38.
- [425] Weymann, R. J., Morris, S. L., Foltz, C. B., and Hewett, P. C. (1991). Comparisons of the Emission-Line and Continuum Properties of Broad Absorption Line and Normal Quasi-stellar Objects. *ApJ*, 373:23.

- [426] Wheaton, W. A., Doty, J. P., Primini, F. A., Cooke, B. A., Dobson, C. A., Goldman, A., Hecht, M., Howe, S. K., Hoffman, J. A., Scheepmaker, A., Tsiang, E. Y., Lewin, W. H. G., Matteson, J. L., Gruber, D. E., Baity, W. A., Rotschild, R., Knight, F. K., Nolang, P., and Peterson, L. E. (1979). An absorption feature in the spectrum of the pulsed hard X-ray flux from 4U0115 + 63. *Nature*, 282(5736):240–243.
- [427] White, N. E., Swank, J. H., and Holt, S. S. (1983). Accretion powered X-ray pulsars. *ApJ*, 270:711–734.
- [428] Wijnands, R. and van der Klis, M. (1998). A millisecond pulsar in an X-ray binary system. *Nature*, 394(6691):344–346.
- [429] Wiktorowicz, G., Sobolewska, M., Lasota, J.-P., and Belczynski, K. (2017). The Origin of the Ultraluminous X-Ray Sources. *ApJ*, 846(1):17.
- [430] Wilms, J., Allen, A., and McCray, R. (2000). On the Absorption of X-Rays in the Interstellar Medium. *ApJ*, 542(2):914–924.
- [431] Woosley, S. E. and Weaver, T. A. (1995). The Evolution and Explosion of Massive Stars. II. Explosive Hydrodynamics and Nucleosynthesis. *ApJS*, 101:181.
- [432] Wu, X.-B., Wang, F., Fan, X., Yi, W., Zuo, W., Bian, F., Jiang, L., McGreer, I. D., Wang, R., Yang, J., Yang, Q., Thompson, D., and Beletsky, Y. (2015). An ultraluminous quasar with a twelve-billion-solar-mass black hole at redshift 6.30. *Nature*, 518(7540):512–515.
- [433] XRISM Science Team (2020). Science with the X-ray Imaging and Spectroscopy Mission (XRISM). *arXiv e-prints*, page arXiv:2003.04962.
- [434] Yuan, F. and Narayan, R. (2014). Hot Accretion Flows Around Black Holes. *ARA&A*, 52:529–588.
- [435] Zampieri, L. and Roberts, T. P. (2009). Low-metallicity natal environments and black hole masses in ultraluminous X-ray sources. *MNRAS*, 400(2):677–686.
- [436] Zane, S., Ramsay, G., Jimenez-Garate, M. A., Willem den Herder, J., and Hailey, C. J. (2004). XMM-Newton EPIC and Optical Monitor observations of Her X-1 over the 35-d beat period. *MNRAS*, 350:506–516.
- [437] Zoghbi, A., Fabian, A. C., Uttley, P., Miniutti, G., Gallo, L. C., Reynolds, C. S., Miller, J. M., and Ponti, G. (2010). Broad iron L line and X-ray reverberation in 1H0707-495. *MNRAS*, 401:2419–2432.
- [438] Zoghbi, A., Miller, J. M., Walton, D. J., Harrison, F. A., Fabian, A. C., Reynolds, C. S., Boggs, S. E., Christensen, F. E., Craig, W., Hailey, C. J., Stern, D., and Zhang, W. W. (2015). NuSTAR Reveals Relativistic Reflection But No Ultra-Fast Outflow in the Quasar Pg~1211+143. *ApJ*, 799(2):L24.



# Appendix A

## Complete Gaussian line search results from chapter 2

In this appendix we plot all the results from the RGS Gaussian line scan analysis of ULXs from chapter 2. All ULXs with usable RGS data are shown.

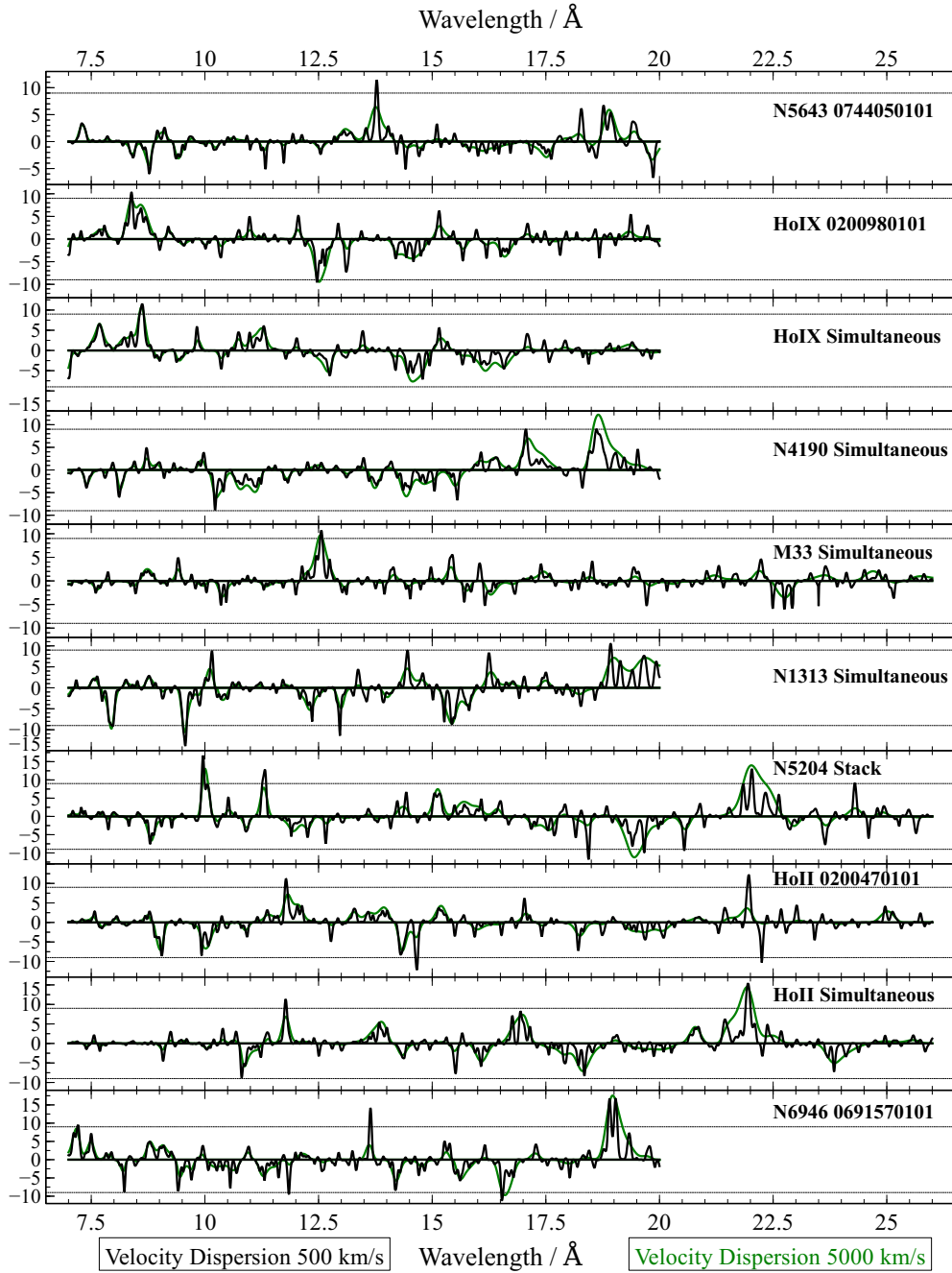


Fig. A.1 The Gaussian line search performed on the RGS spectra of ULXs in our sample. The wavelength is on the X-axis and the obtained  $\Delta C$ -stat value on the Y axis for each source or observation analysed. The objects are ordered by their hardness the same way as in Fig. 3.1, starting from the hardest source, NGC 5643 X-1, ending with the softest source, NGC 6946 X-1. The Y axis is defined as  $\Delta C$ -stat times the sign of the line normalisation to show the difference between absorption and emission residuals.

# Appendix B

## Additional short *XMM-Newton* observation of PG 1448+273 - no evidence for UFO absorption

There is also a second, much shorter observation of PG 1448+273 in the *XMM-Newton* archive, with a raw exposure of 22 ks (ID: 0152660101, taken in 2003). We followed the same steps from Sect. 5.2 to reduce and prepare this observation for analysis. The statistics were naturally much worse compared to the long exposure analysed above, albeit the AGN was brighter in 2003. The average EPIC pn count rate was 4 ct/s, and the average MOS 1/2 count rate was 0.9 ct/s. Since EPIC pn was operated in Large Window mode (with a pile-up limit of 3 ct/s), it is possible that the pn data are affected by pile-up. MOS was operated in Large Window mode (pile-up limit of 1.5 ct/s) and its data should not be affected. Nevertheless, we do not observe any significant differences between pn and MOS spectra. We ignored EPIC data below 1.7 keV, only using RGS data in the soft X-ray band, following the same procedure as with the main dataset.

We apply the same continuum model as used in Sect. 5.3.1. Due to a lower data quality, we fix the blurred iron K line parameters to the best-fitting parameters from the final fit in Sect. 5.3.3, which included the broadband continuum as well as the ultrafast and warm absorption. We find that the coronal powerlaw slope is much higher with  $\Gamma = 2.38 \pm 0.04$ , and the average 2-10 keV luminosity is  $(2.16 \pm 0.07) \times 10^{43}$  erg/s.

Due to the lower data quality, the addition of neutral absorption intrinsic to the AGN is not significant. The best-fitting spectrum is shown in Fig. B.1 (EPIC data) and Fig. B.2 (RGS data). The data are of lower quality than from the other observation, but we do not notice any strong absorption features at 7 keV or at 18 Å as seen in the

previous dataset, or any other absorption signature of a UFO. Interestingly, it appears that an emission feature is present at  $18 \text{ \AA}$  instead (Fig. B.2), this could be due to Fe XVII emission (rest-frame wavelength  $17.1 \text{ \AA}$ ).

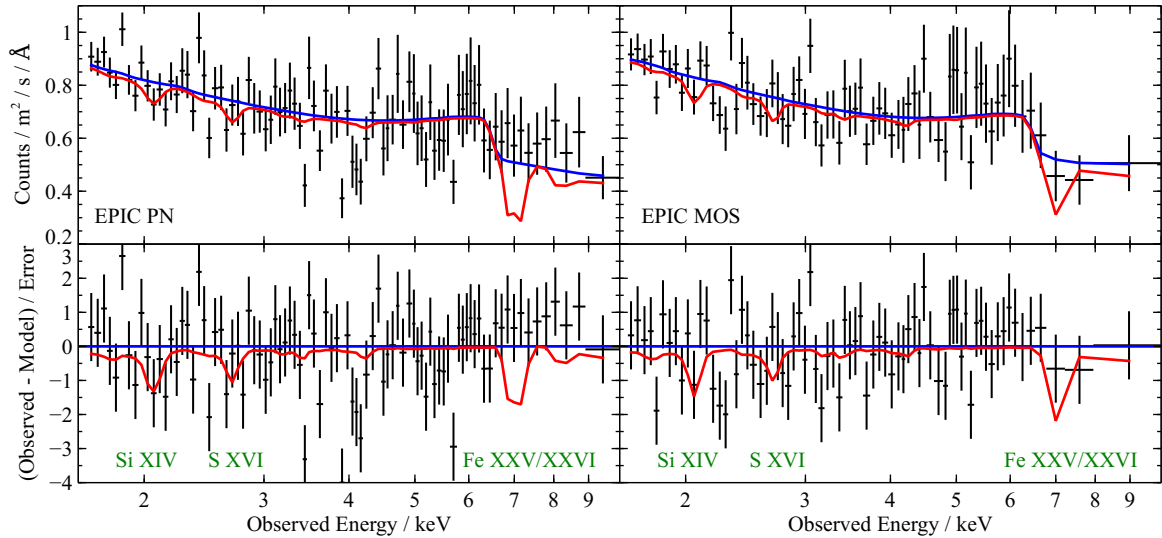


Fig. B.1 EPIC pn (left subplots) and MOS (right subplots) data ( $1.7 - 10 \text{ keV}$ ) of the second, short observation of PG 1448+273 fitted with the baseline continuum model from Appendix B (blue colour). The model in red colour is the best-fitting baseline continuum plus one UFO component with the parameters of the outflow detected in the long *XMM-Newton* observation (Sect. 5.3.3). The top subplots show the fitted spectra, the bottom subplots contain the residuals. Green labels name the strongest absorption lines of the UFO absorption.

As a further check, we add the same UFO absorption as observed in the long exposure dataset to the baseline continuum of the short observation. We use the best-fitting UFO parameters from Sect. 5.3.3. The resulting spectral model is shown in Fig. B.1 and B.2 (red colour), and is clearly rejected by the data. The  $1\sigma$  upper limit on the column density of such absorber is just  $1.7 \times 10^{22} \text{ cm}^{-2}$ , more than 10 times lower than the column density observed in the other *XMM-Newton* observation. We cannot exclude a possibility that a UFO of the same column density is present, but with a higher ionisation parameter. However, the change in the ionisation parameter would have to be significant, with a lower limit on the ionisation parameter of about  $\log(\xi/\text{erg cm s}^{-1}) \approx 5$ . Such a large change in the ionisation parameter ( $10\times$  higher) would require a non-linear response between the absorber and the ionising luminosity of PG 1448+273.

Finally, we apply the same systematic wind search from Sect. 5.3.2 to locate any potential absorption with parameters different to that of the UFO observed in the

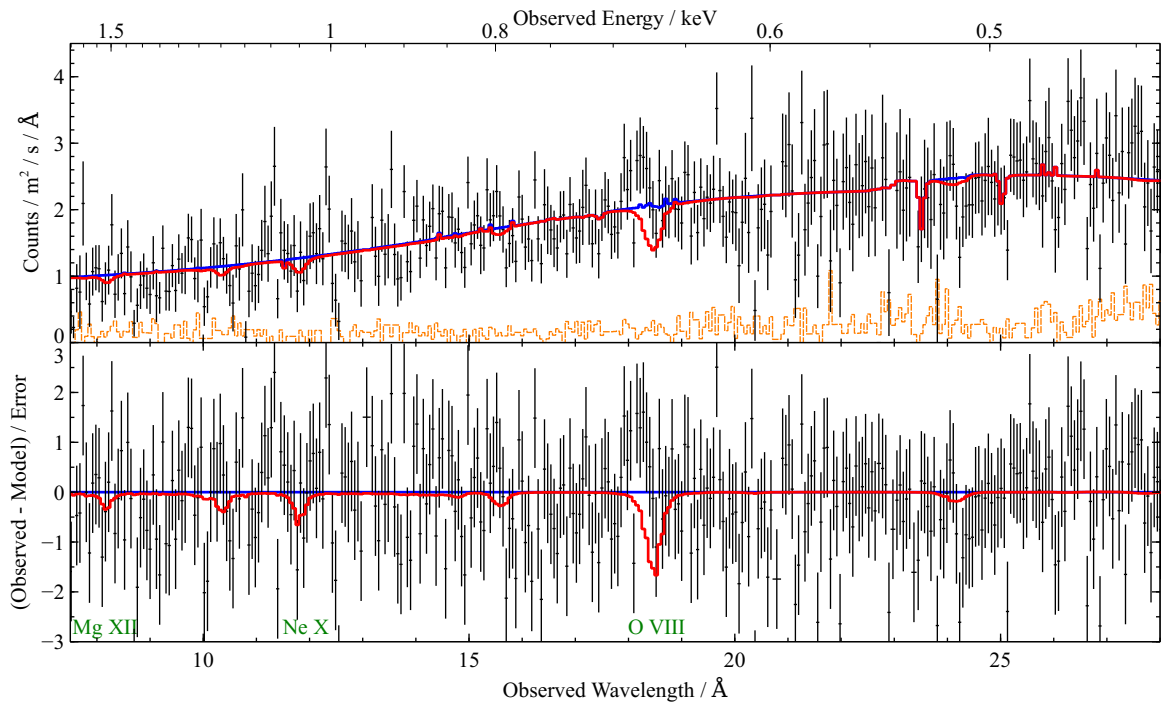


Fig. B.2 RGS data between  $7.5 \text{ \AA}$  ( $1.7 \text{ keV}$ ) and  $28 \text{ \AA}$  ( $0.4 \text{ keV}$ ) of the second, short observation of PG 1448+273, stacked and overbinned for plotting purposes only, fitted with the baseline continuum model from Appendix B (blue colour). The model in red colour is the best-fitting baseline continuum plus one UFO component with the parameters of the outflow detected in the long *XMM-Newton* observation (Sect. 5.3.3). The top subplot shows the fitted spectra, the bottom subplot contains the residuals. Green labels name the strongest absorption lines of the UFO absorption.

other observation. As the data quality is much lower compared to the first exposure, do not find any significant detections ( $\Delta C\text{-stat} > 15$ ).



# Appendix C

## Pile-up in *XMM-Newton* Her X-1 observations

One important issue in the analysis of Her X-1 observations which needs to be discussed is that of pile-up. Table 7.1 shows that the count rates in both RGS and EPIC pn during most of the observations are indeed very high. Count rates of up to  $\sim 800$  counts/s in pn are reached during some of the observations, which is close to the pile-up limit for Timing mode observations. Furthermore, this does not take into account any variability and especially pulsations of the source. It is therefore not surprising to expect some pile-up in the higher flux observations.

The count rates observed in the RGS cameras are also high, with up to about 20 counts/s per camera. The pile-up threshold in RGS is usually defined by a maximum count rate per CCD in RGS 1 or 2. Its effect is to move first order events to the second order and thus degrade both of these spectra. The threshold is roughly 12 counts/s per CCD in RGS 1 and 6 counts/s per CCD in RGS2 (because one of the two read-out nodes in RGS 2 is disabled)<sup>1</sup>. This is the maximum summed count rate of all orders per CCD.

Fig. C.1 shows the count rate per  $\text{\AA}$  for both orders and RGS detectors in observation 0673510801, the observation with the highest RGS flux. The figure also shows the approximate CCD edge positions and the width of each chip in  $\text{\AA}$ . The total count rate per CCD can be calculated as the sum of the count rates per  $\text{\AA}$  for each order times the width of each CCD in  $\text{\AA}$  (which is different in each order, and the width in the second order is half that of the first order). The figure shows that multiple CCDs between CCD 3 and CCD 7 could be affected by pile-up. The approximate fluxes per CCD are: CCD 8 - 2.5 cts/s, CCD 7 - 4.4 cts/s, CCD 6 - 4.6 cts/s, CCD 5 - 4.5 cts/s,

---

<sup>1</sup>[www.cosmos.esa.int/web/xmm-newton/sas-thread-pile-up-in-the-rgs](http://www.cosmos.esa.int/web/xmm-newton/sas-thread-pile-up-in-the-rgs)

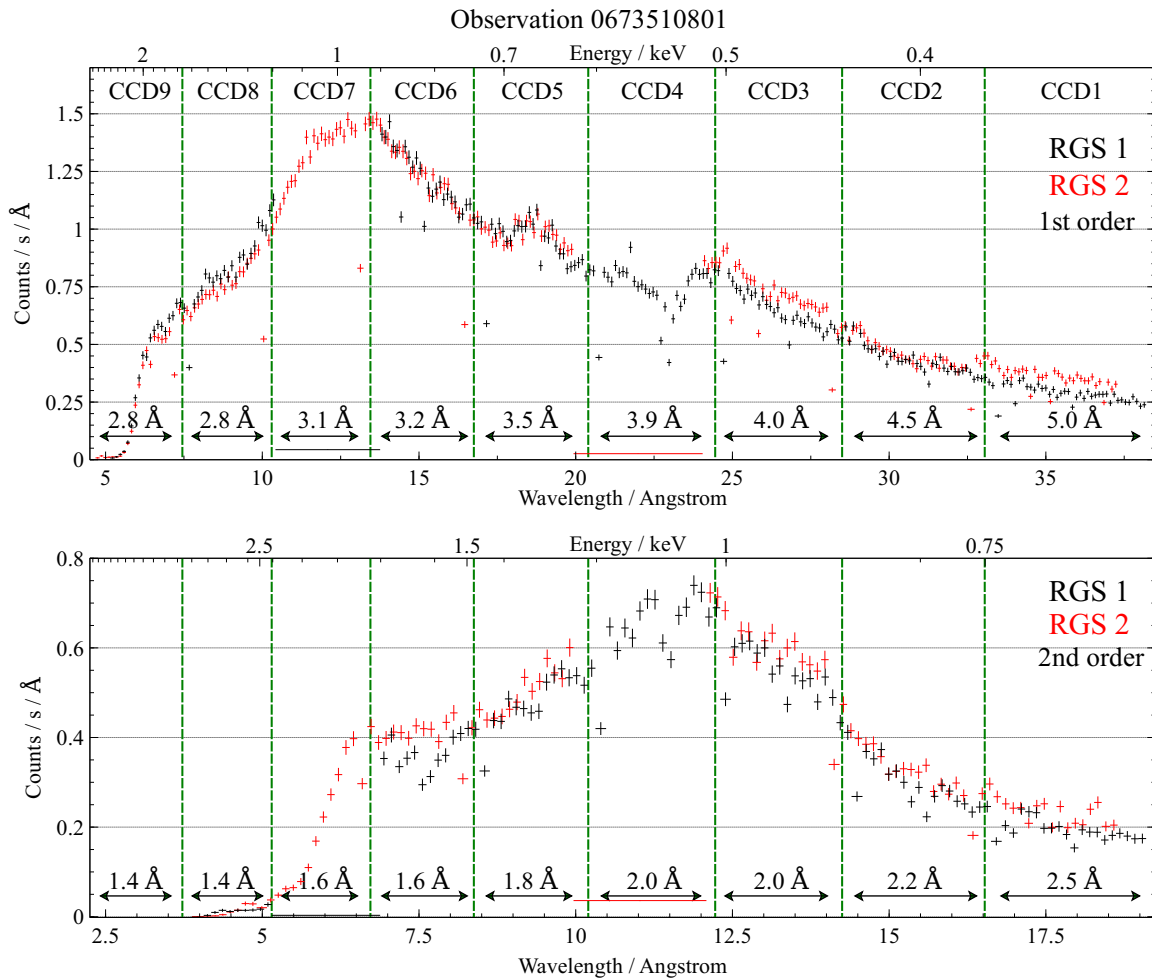


Fig. C.1 The average count rate per  $\text{\AA}$  in the first and the second order of both RGS 1 and 2 instruments during the highest count rate observation 0673510801. The top plot contains the first order count rates and the bottom plot contains the second order count rates. RGS 1 data are in black, while RGS 2 data are red. Green vertical dashed lines show the approximate positions of chip gaps and the labels list the approximate chip sizes in  $\text{\AA}$ . CCD numbers are listed on the top of the figure. The count rate per CCD can be approximated as the sum of the count rates per  $\text{\AA}$  times the CCD width (in  $\text{\AA}$ ) of both orders.

CCD 4 - 4.5 cts/s, CCD 3 - 4.2 cts/s and CCD 2 - 2.8 cts/s. These values are hence below the 6 cts/s RGS 2 limit, but again, they are only the average count rates for a variable and pulsating source. It is not inconceivable to imagine a 50 per cent flux spike (e.g. during the pulse) during which the count rate in some CCDs would exceed 6 cts/s. We thus conclude that while RGS 1 should be unaffected by pile-up, RGS 2 might be partially affected in the highest flux observations (but probably less than pn).

It is unlikely that pile-up could introduce a series of narrow absorption features in both the pn and the RGS spectra that line-up in velocity space. Nevertheless, we perform two checks to show that the wind features are indeed real in at least some of the observations in this study. First, we exclude pn data from the analysis and only look at RGS1 and RGS 2 (first order) data, performing a similar fit as described in 7.3.2. Secondly, we also exclude RGS 2 from the analysis and only use the RGS 1 first and second order data to show that the wind is still significantly present at least in one observation with the highest data quality.

## C.1 Analysis with RGS 1 and 2

The spectral model has to be modified after ignoring the pn data. The hard band (3-10 keV) data are unavailable and hence the overall broadband spectral shape cannot be constrained. We thus replace the COMT Comptonisation continuum model with a simpler POWERLAW. Naturally the 6.6 keV Gaussian line is omitted as it is out of the current energy band (0.35-1.8 keV). The remaining model components are identical as before. The continuum model is therefore:  $\text{HOT} \times (\text{POWERLAW} + \text{BB} + 4 \times \text{GAUSS} + \text{CIE})$ . Since we do not have access to a broadband 0.3-10 keV SED while only using the RGS data, we also have to resort to using the XABS photoionisation absorption model with the default SED.

The data are first fitted with the continuum model, after which we add the wind absorption. We fit for the wind parameters and also recover the fit improvement. The results are listed in Table C.1. For this check we only use the 5 observations with the strongest significance of the wind detection. It is evident that while for some observations, there is a large decrease of significance after ignoring the pn dataset, multiple still show strong evidence for the wind absorption. Most importantly, observations 0673510501 and 0783770601 show a  $\Delta\text{C}$ -stat of more than 40 which confirms the reality of the absorption features.

We also notice (Table C.1) that the RGS only analysis predicts very high ionisation levels of the outflowing gas, much higher than the full broadband analysis. This is because of the absence of the crucial Fe K band containing the Fe XXV and Fe XXVI ions. These transitions are necessary for putting upper limits to the ionisation parameter of plasma at high ionisation levels.

Table C.1 Best-fitting wind parameters for 5 observations of Her X-1 using only RGS 1 and RGS 2 instruments. The first column contains the observation ID. The remaining columns show the properties of the disc wind such as its column density, ionisation parameter, turbulent velocity and systematic velocity, as well as the statistical fit improvement of the final model compared to the baseline continuum spectral model.

Obs. ID	Column density $10^{24} \text{ cm}^{-2}$	$\log \xi$ $\text{erg cm s}^{-1}$	Turbulent velocity $\text{km s}^{-1}$	Outflow velocity $\text{km s}^{-1}$	$\Delta\text{C-stat}$
0673510501	$3.04 \pm 0.12$	$5.05^{+0.06}_{-0.10}$	$250 \pm 170$	$-940 \pm 130$	40.89
0673510601	$0.17^{+0.34}_{-0.08}$	$4.79^{+0.14}_{-0.12}$	$30^{+200}_{-30}$	$-330 \pm 150$	8.02
0673510901	$0.11^{+0.14}_{-0.07}$	$4.28^{+0.08}_{-0.06}$	$160^{+130}_{-100}$	$-610^{+140}_{-130}$	23.46
0783770501	$0.0026^{+0.0023}_{-0.0013}$	$3.01^{+0.12}_{-0.13}$	$150^{+140}_{-80}$	$-730^{+210}_{-170}$	14.17
0783770601	$2.4^{+1.5}_{-0.8}$	$4.54 \pm 0.12$	$80^{+30}_{-50}$	$-380^{+90}_{-100}$	54.79

## C.2 Analysis with RGS 1 only

The most stringent test is to only use RGS 1 data, which is the instrument the least affected by pile-up. Unfortunately, CCD 7 is disabled in RGS 1 so the important 10–13 Å waveband containing the Ne X absorption line is lost. We therefore also use the second order RGS 1 data, which has access to this part of the spectrum, although we note that the data quality is significantly lower.

Here we only use data from observation 0673510501 (which has the strongest wind features) to show that even in the worst case of pile-up, there is at least one observation with a statistically significant wind detection. We use the same continuum and wind spectral models as in the previous section. The best-fitting spectra are shown in Fig. C.2. The recovered wind parameters are: column density of  $(0.16 \pm 0.04) \times 10^{24} \text{ cm}^{-2}$ , ionisation parameter of  $\log \xi = 4.2 \pm 0.2$ , systematic velocity of  $-1140 \pm 120 \text{ km/s}$  and a turbulent velocity of  $280^{+120}_{-90} \text{ km/s}$ . The fit improvement  $\Delta\text{C-stat}$  is 33.12. This is a large enough fit improvement to consider the wind detection significant (although we note that extensive Monte Carlo simulations would be necessary to prove it rigorously).

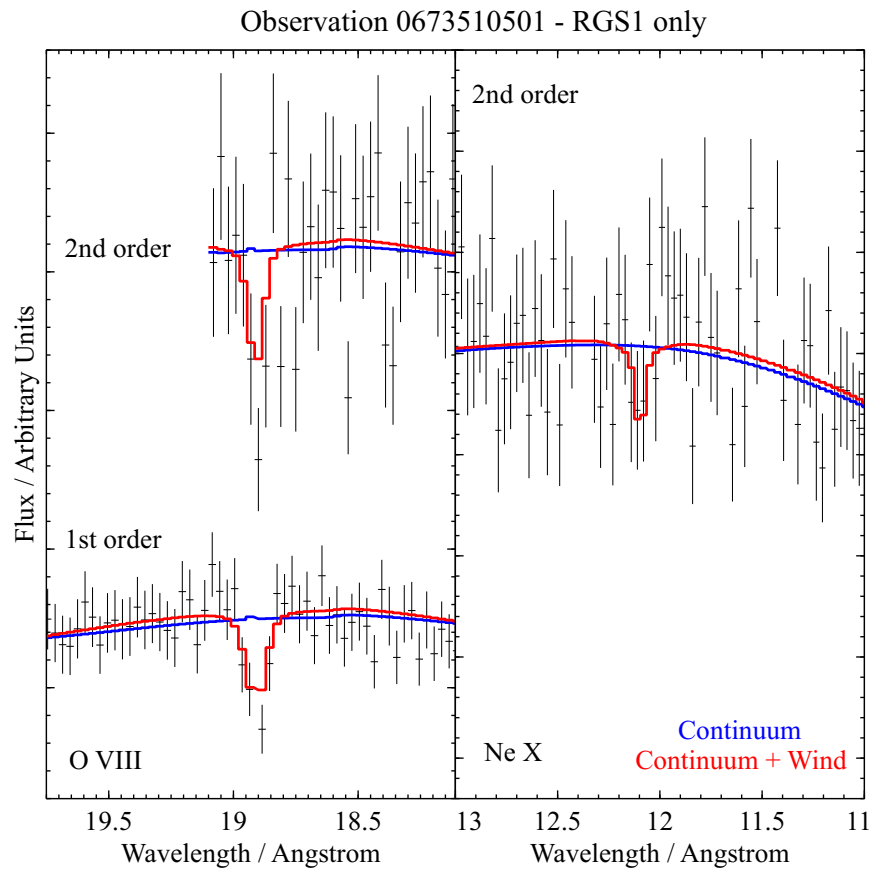


Fig. C.2 The best-fitting spectral models for observation 0673510501 using only RGS 1 first and second order data. Only the O VIII and Ne X bands are shown as the N VII signature is insignificant in this case. The best-fitting baseline continuum is shown in blue and the final wind solution in red.

